

附件 2 浙江水利水电学院“南浔青年学者”申请表

姓 名	吕姚	出生年月年龄 (年龄)	1990 年 11 月 岁 ( 33 岁)	参加工作时间	2017 年 07 月
现所在单位 (部门)	浙江水利水电学院 (机械与汽车工程 学院)	最高学历/学位	博士研究生/博士	专业技术职务	讲师
符合条款	符合科研类：发表 3 类论文 3 篇，5 类论文 1 篇，总绩点 170。				
所涉业绩	教学类 绩点：_____				
	科研类 绩点：170	[1] Lv Y, Huang S, Lu S, et al. Engineering of cobalt-free Ni-rich cathode material by dual element modification to enable 4.5 V-class high-energy-density lithium-ion batteries. <i>Chemical Engineering Journal</i> , 2023, 455:140652. (Sci top 中科院一区)			
		[2] Lv Y, Huang S, Lu S, et al. B <sub>2</sub> O <sub>3</sub> /LiBO <sub>2</sub> dual-modification layer stabilized Ni-rich cathode for lithium-ion battery. <i>Journal of Power Sources</i> , 2022, 536: 231510. (Sci top 中科院二区)			
		[3] Lv Y, Huang S, et al. A review of nickel-rich layered oxide cathodes: synthetic strategies, structural characteristics, failure mechanism, improvement approaches and prospects. <i>Applied Energy</i> . 2022, 305, 117849. (Sci top 中科院一区)			
		[4] Huang S, Lv Y (共同一作), et al. Three-dimensional hierarchical porous hard carbon for excellent sodium/potassium storage and mechanism investigation. <i>Materials Today Energy</i> . 2021, 20, 100673 (Sci 中科院三区).			
	人才称号类 绩点：_____				
	总绩点	170			
备注：请严格按照《浙江水利水电学院“南浔青年学者”实施办法（试行）》（浙水院（2022）114号）附件《业绩成果绩点赋值项目库》的类目、分类、等级（等次）、绩点填写。					
个人承诺	本人承诺上述所填内容真实、准确；如有不实，本人承担相应责任。 <div>签名：吕姚 时间：2023.11.14</div>				
以上部分由申请人填写，所在单位审核。以下由单位（部门）和学校填写。					
所在单位 (部门) 意见	1.经审核，申请人所填内容： <input type="checkbox"/> 属实 <input type="checkbox"/> 不属实； 2.是否符合所申请的类别： <input type="checkbox"/> 符合 <input type="checkbox"/> 不符合； 3.是否同意推荐： <input type="checkbox"/> 同意 <input type="checkbox"/> 不同意。 <div>负责人签名： (部门盖章) ____年____月____日</div>				
科技处 审核意见	负责人签名： (部门盖章) ____年____月____日	教务处 审核意见	负责人签名： (部门盖章) ____年____月____日		

其他相关职能部门审核意见	<div>负责人签名：____年____月____日</div> <div>(部门盖章)</div>
学校意见	<div>(学校盖章)</div> <div>____年____月____日</div>

备注：表格请用 A4 纸打印，有关佐证材料附后。



# Engineering of cobalt-free Ni-rich cathode material by dual-element modification to enable 4.5 V-class high-energy-density lithium-ion batteries

Yao Lv<sup>a,b,1</sup>, Shifei Huang<sup>b,c,1</sup>, Sirong Lu<sup>d</sup>, Tianqi Jia<sup>b,c</sup>, Yanru Liu<sup>b,c</sup>, Wenbo Ding<sup>c</sup>, Xiaoliang Yu<sup>e</sup>, Feiyu Kang<sup>b,c</sup>, Jiujuun Zhang<sup>a,\*</sup>, Yidan Cao<sup>b,c,\*</sup>

<sup>a</sup> College of Sciences and Institute for Sustainable Energy, Shanghai University, Shanghai, China

<sup>b</sup> Shenzhen Geim Graphene Center, Institute of Materials Research, Shenzhen International Graduate School, Tsinghua University, Shenzhen, China

<sup>c</sup> Tsinghua-Berkeley Shenzhen Institute, Tsinghua University, Shenzhen, China

<sup>d</sup> Shenzhen Institute for Quantum Science and Engineering, Southern University of Science and Technology, Shenzhen, China

<sup>e</sup> Department of Mechanical Engineering, The Hong Kong Polytechnic University, Hong Kong, China

## ARTICLE INFO

### Keywords:

Ni-rich Co-free cathode  
High voltage  
Dual-element modification  
High-energy-density  
Lithium battery

## ABSTRACT

Ni-rich Co-free cathodes have attracted extensive attention for high-energy-density lithium ion batteries (LIBs). However, structural and interfacial instability in these cathodes accelerates capacity degradation under high-voltage operation. Herein, Ni-rich Co-free In/Sn dual-element modified cathode (InSn-LiNi<sub>0.85</sub>Mn<sub>0.09</sub>Al<sub>0.06</sub>O<sub>2</sub>, InSn-NMA85) was synthesized through a one-step sintering strategy. Dual-element doping along with the in-situ induced LiInO<sub>2</sub> interphase synergistically prolongs the cycle life of the Ni-rich Co-free cathode under high voltage ( $\geq 4.5$  V) as well as high temperature ( $\geq 45$  °C). Comprehensive characterizations combined with DFT calculation confirm that In/Sn dual-element modification effectively increases Li<sup>+</sup>/Ni<sup>2+</sup> mixing energy and oxygen release energy, stabilizes the lattice structure, and improves the electrochemical performance. Meanwhile, in-situ formed coating of LiInO<sub>2</sub> effectively protects the cathode from redundant cathode-electrolyte side reactions, preserves the layered phase, and further inhibits the generation of microcracks after cycles. The modified cathode maintains superior capacity retention of  $\sim 100$  % and  $\sim 90$  % within the voltage range of 2.7–4.5 V at 30 °C and 45 °C, respectively, after 100 cycles. The modification strategy enables the Ni-rich Co-free layered NMA85 cathode to deliver comparable battery performance with NCM and NCA cathodes, which provides promising approaches for the application of Ni-rich Co-free cathode in 4.5 V-class high-energy-density LIBs.

## 1. Introduction

With the ever-rising demand for high-energy-density lithium-ion batteries (LIBs) nowadays, the development of high-voltage cathode materials with high capacity has attracted considerable attention [1–3]. Ni-rich cathode materials, including LiNi<sub>1-x-y</sub>Co<sub>x</sub>Mn<sub>y</sub>O<sub>2</sub> (NCM) and LiNi<sub>1-x-y</sub>Co<sub>x</sub>Al<sub>y</sub>O<sub>2</sub> (NCA) ( $1-x-y > 0.5$ ), with the  $\alpha$ -NaFeO<sub>2</sub> structure (R $\bar{3}m$ , space group) have high capacity and excellent electrochemical kinetic characteristics, and show great potential in reducing cost and improving energy density [4–6]. Co has been considered as an indispensable component because it efficiently reduces Li<sup>+</sup>/Ni<sup>2+</sup> mixing, facilitates 2D diffusion in the Li<sup>+</sup> plane, and improves the rate capability of the cathode [7,8]. However, Co resources are scarce, expensive, and

highly toxic, which motivates researchers to research on Ni-rich Co-free cathode materials [9]. Currently, Ni-rich Co-free cathodes still face problems including surface residual alkali, deficient rock salt phase formation and high-order Li<sup>+</sup>/Ni<sup>2+</sup> mixing [10–12]. These issues severely damage the stability of cathodes, leading to structural collapse, transition metal dissolution, irreversible phase transformation, and lattice oxygen release, as a result, capacity dramatically degrades. Meanwhile, high temperature and high cut-off voltage operating conditions are necessary to realize a wide range of environmental practicability and elevated energy density. However, the structural stability of Ni-rich Co-free cathodes is poor when cycling at high temperature and high cut-off voltage. The high valence nickel ions are prone to irreversible reaction with the electrolyte, and the surface will be gradually corroded by the

\* Corresponding authors at: Shenzhen Geim Graphene Center, Institute of Materials Research, Shenzhen International Graduate School, Tsinghua University, Shenzhen, China (Y. Cao).

E-mail addresses: [jiujun.zhang@i.shu.edu.cn](mailto:jiujun.zhang@i.shu.edu.cn) (J. Zhang), [yidanco@sz.tsinghua.edu.cn](mailto:yidanco@sz.tsinghua.edu.cn) (Y. Cao).

<sup>1</sup> These authors contributed equally to this work.

electrolyte. As a result, the layered structure is gradually destroyed from the inside out and the electrolyte is gradually consumed, eventually leading to rapid battery failure [13]. So far, the application of the Ni-rich Co-free cathodes is still quite challenging.

Doping is a low-cost and efficient strategy to alleviate the above-mentioned problems and enhance the structural stability and electrochemical performance of NCM and NCA cathodes [14–16]. Usually, the incorporation of high valence ions (such as  $\text{Zr}^{4+}$ ,  $\text{Ti}^{4+}$ ,  $\text{Ta}^{5+}$ ,  $\text{Nb}^{5+}$ ,  $\text{W}^{6+}$ ,  $\text{Mo}^{6+}$ ) can form strong interaction with lattice oxygen. It effectively prevents the release of lattice oxygen during cycling and induces the formation of lithium vacancies, thus greatly improving the diffusion efficiency of lithium ions [17,18].  $\text{Sn}^{4+}$  has larger ion radius and higher valence state, which can effectively regulate lattice parameters and reduce lithium ion diffusion barrier to improve lithium ion diffusion efficiency, and it is a candidate element to inhibit the contraction of lattice parameters in the  $c$  direction under high charge state, inhibit the migration of nickel ions, and reduce the release of oxygen [19]. Additionally, dual-ion co-doped Ni-rich cathodes exhibit improved performance due to synergetic improvement effect compared with single ion doping [20,21]. However, there are few studies on the synergistic effect of  $\text{Sn}^{4+}$  and other transition metals ions in Ni-rich cathodes, especially in the Ni-rich Co-free cathode system for high voltage ( $\geq 4.5$  V) and high temperature ( $\geq 45^\circ\text{C}$ ) applications. Besides, the engineered surface

structure of cathode, which is robust and stable, also plays a key role in reducing the cathode/electrolyte interfacial side reactions and improving the cyclability of the cathode materials [22]. In-situ formed stable interphase is quite attractive to enable highly reversible cathode, and various materials, like  $\text{Li}_3\text{PO}_4$  [23],  $\text{Li}_2\text{MnO}_3$  [24], and  $\text{Li}_2\text{SiO}_3$  [25] have been utilized to establish stable interphase on the cathode. Moreover, it is imperative to understand the modification mechanism of the Ni-rich Co-free cathode by cation doping.

In this work, we report a one-step sintering strategy to introduce In/Sn dual-element modification in the Ni-rich Co-free cathode ( $\text{LiNi}_{0.85}\text{Mn}_{0.09}\text{Al}_{0.06}\text{O}_2$ , NMA85) and get the InSn-NMA85 cathode material. Structural evolutions of NMA85 and InSn-NMA85 cathodes during cycling are investigated by high-resolution transmission electron microscopy (HRTEM), in-situ XRD, and DFT calculations, etc. to reveal the modification effects at the atomic scale. In/Sn dual-element modification results in homogeneous doping in the NMA85 cathode, which not only effectively inhibits  $\text{Li}^+/\text{Ni}^{2+}$  mixing and stabilizes the lattice oxygen to mitigate the Ni dissolution in the Ni-rich Co-free cathode, but also improves the lithium ion diffusion efficiency and synergistically improves the electrochemical performance of NMA85. Meanwhile, the dual-element modification simultaneously facilitates an in-situ formed  $\text{LiInO}_2$  coating layer on the surface. The in-situ formed  $\text{LiInO}_2$  layer successfully protects the NMA85 particles from the erosion of

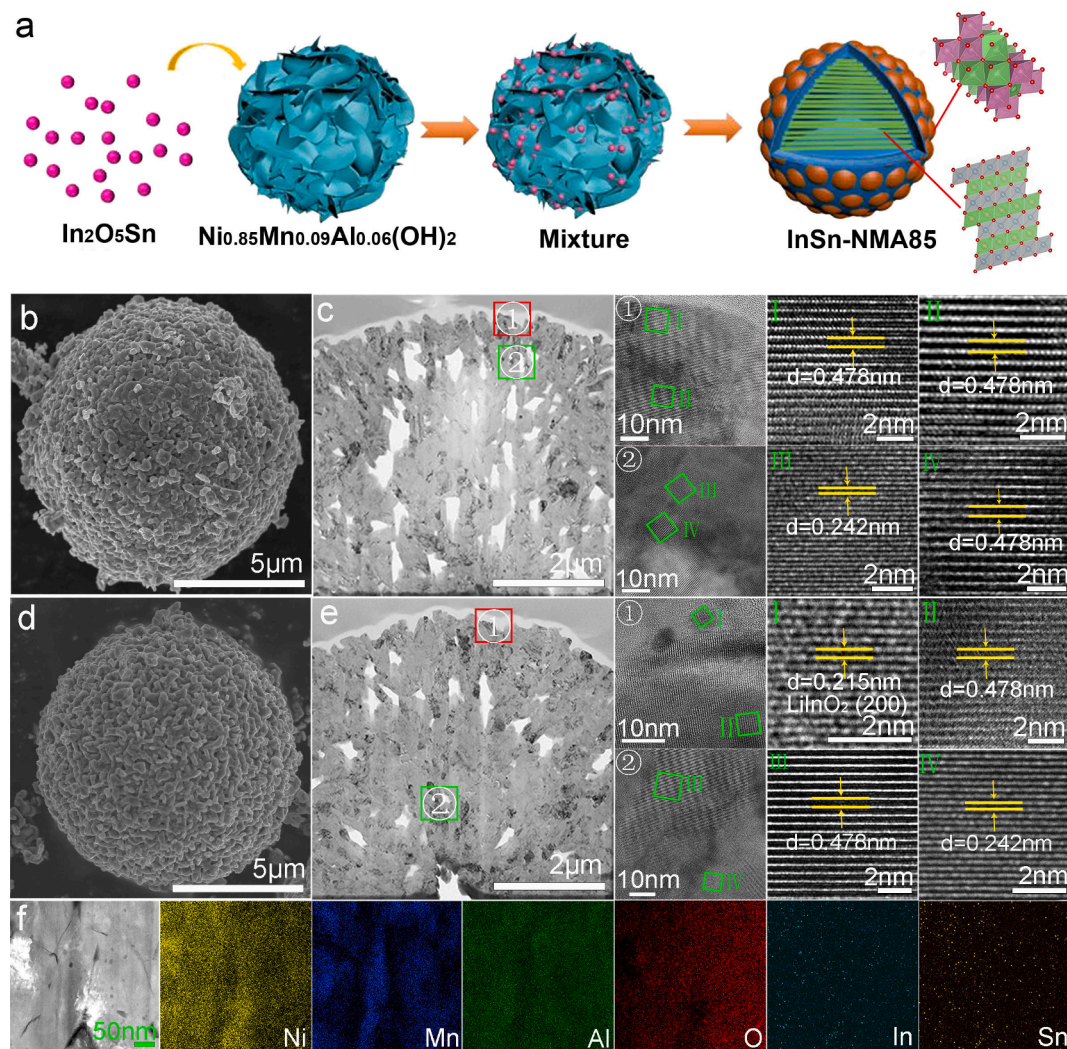


**Fig. 1. Schematic illustration of synthesis, morphology and elemental distribution.** (a) Schematic illustration of the synthesis route of the InSn-NMA85. (b) SEM image of the NMA85. (c) Cross-sectional HRTEM images of the NMA85. (d) SEM image of the InSn-NMA85. (e) Cross-sectional HRTEM images of the InSn-NMA85. (f) HAADF mapping images of the InSn-NMA85.



detrimental species generated by electrolyte decomposition and stabilizes the cathode/electrolyte interface. The irreversible phase transformation of NMA85 and redundant cathode/electrolyte interfacial side reactions during cycling are greatly suppressed by the synergistic effect of the in-situ formed  $\text{LiInO}_2$  layer together with the doping in the lattice. This work provides an insightful strategy on the development of Co-free Ni-rich cathodes for the high-energy-density rechargeable lithium battery with prolonged cycle life.

## 2. Results and discussion

### 2.1. Synthesis and characterizations

The InSn-NMA85 cathode was synthesized via a one-step sintering strategy. Briefly, as shown in Figure S1, the  $\text{LiNi}_{0.85}\text{Mn}_{0.09}\text{Al}_{0.06}(\text{OH})_2$  with spherical particles of  $\sim 11\ \mu\text{m}$  was selected as the precursor. The modified cathode was synthesized by calcinating uniformly mixed  $\text{Ni}_{0.85}\text{Mn}_{0.09}\text{Al}_{0.06}(\text{OH})_2$ ,  $\text{LiOH}\cdot\text{H}_2\text{O}$  and  $\text{In}_2\text{O}_5\text{Sn}$ , denoted as InSn-NMA85. As shown in Fig. 1a,  $\text{In}_2\text{O}_3$  in  $\text{In}_2\text{O}_5\text{Sn}$  reacts with  $\text{LiOH}$  and forms  $\text{LiInO}_2$  layer on the surface of materials ( $\text{In}_2\text{O}_3 + 2\text{LiOH} \rightarrow 2\text{LiInO}_2 + \text{H}_2\text{O}$ ) [26]. In addition, In and Sn enter the lattice of cathodes as doping through high-temperature calcination [27], which will be further clarified in the following characterization. For comparison, a control sample calcined at the same temperature was obtained without adding  $\text{In}_2\text{O}_5\text{Sn}$ , denoted as NMA85. The detailed synthesis procedure is presented in the Experimental section.

SEM images (Fig. 1b, 1d) illustrate that both NMA85 and InSn-NMA85 cathodes consist of spherical secondary particles with average diameters of  $\sim 11\ \mu\text{m}$  and are composed of primary particles less than  $1\ \mu\text{m}$ . Apparently, the introduction of  $\text{In}_2\text{O}_5\text{Sn}$  in the InSn-NMA85 does not bring about discernable morphology differences from the NMA85. Cross-sectional SEM images (Figure S2) also show similar morphology without any fractures. Energy dispersive X-ray spectroscopy (EDS) mapping of InSn-NMA85 in Figure S3 (Top-view) and Figure S4 (Cross sectional-view) demonstrates that the Ni, Mn, Al, O, In, and Sn elements are well distributed throughout InSn-NMA85.

X-ray photoelectron spectroscopy (XPS) was employed to analyze the chemical states of the elements in the samples, and the results are shown in Figure S5. There is no noticeable change of the peak position around 872 eV and 855 eV, corresponding to  $\text{Ni}2\text{p}_{1/2}$  and  $\text{Ni}2\text{p}_{3/2}$ , respectively [28–30], in the Ni 2p spectra for both samples. However, the proportion of  $\text{Ni}^{2+}$  in InSn-NMA85 (38.2 %) is lower than that in NMA85 (42.8 %), which is beneficial to the formation of a more stable surface structure with a lower  $\text{Li}^+/\text{Ni}^{2+}$  mixing [31]. XPS spectra of In 3d and Sn 3d further confirm that In and Sn co-exist in InSn-NMA85. Deconvolution of the In 3d spectra shows that the main peaks (444.1 eV and 451.7 eV) can be attribute to the  $\text{LiInO}_2$  species [26,32], confirming the existence of  $\text{LiInO}_2$  on the surface of InSn-NMA85 and the occurrence of the above-mentioned reaction between  $\text{In}_2\text{O}_3$  and  $\text{LiOH}$ . The X-ray diffraction (XRD) patterns of both cathodes are presented in Figure S6a. The results show that NMA85 and InSn-NMA85 can be completely indexed with a well hexagonal  $\alpha\text{-NaFeO}_2$  structure ( $R\bar{3}m$ , space group) [33]. The apparent splitting of (006)/(012) and (018)/(110) peaks indicate a well-formed layered structure with high crystallinity [34–36]. In addition, the (003) diffraction peak shifts towards lower  $2\theta$  angles with the In/Sn dual-element modification (a shift of  $0.0205^\circ$  as shown in Figure S6b). Lattice parameters  $a$  and  $c$  of InSn-NMA85 are significantly increased according to the Rietveld refinement results in Figure S7 and Table S1, likely owing to the addition of large ion radius of  $\text{In}^{3+}$  and  $\text{Sn}^{4+}$  ( $r_{\text{In}^{3+}}=0.8\ \text{\AA}$ ,  $r_{\text{Sn}^{4+}}=0.69\ \text{\AA}$ ), which indicates that In and Sn are successfully incorporated into the NMA85 cathode lattice. Moreover, with increasing  $\text{In}_2\text{O}_5\text{Sn}$  content (InSn2-NMA85 in Figure S6a), the characteristic peak of  $\text{LiInO}_2$  at  $\sim 22.6^\circ$  (101) becomes apparent [37], which reveals the existence of  $\text{LiInO}_2$  and further confirms the occurrence of reaction between  $\text{In}_2\text{O}_5\text{Sn}$  and  $\text{LiOH}$  to form  $\text{LiInO}_2$  in InSn-NMA85,

consistent with the XPS analysis. In addition, the  $\text{Li}^+/\text{Ni}^{2+}$  cation mixing in the InSn-NMA85 is greatly reduced and the  $I_{003}/I_{104}$  ratio is increased (Table S1). The above results demonstrate that the In/Sn dual-element modification effectively increases the crystallinity of the cathode material by entering the lattice of NMA85 as well as induces in-situ formed  $\text{LiInO}_2$  species.

The cross-sectional TEM and HRTEM were carried out at the surface and bulk regions of NMA85 and InSn-NMA85 to further reveal the distribution of In/Sn and investigate the effects of In/Sn dual-element introduction. As shown in Fig. 1c, the cross-sectional HRTEM images in region ①, i.e. the surface region, of NMA85 show interplanar spacing of 0.478 nm (part ①-I and part ①-II), corresponding to the (003) planes of layered structure [38]. By contrast, the surface region ① in InSn-NMA85 (Fig. 1e) show two sets of interplanar spacing of 0.215 nm (part ①-I) and 0.478 nm (part ①-II), corresponding to (101) planes of  $\text{LiInO}_2$  and the (003) planes of layered structure [26], respectively. It demonstrates that the in-situ formed  $\text{LiInO}_2$  islands distribute on the surface of the NMA85 particles in InSn-NMA85, which may be beneficial to protect the cathode from corrosion by the electrolyte. The cross-sectional HRTEM images in the bulk regions ② for both NMA85 and InSn-NMA85 exhibit clear interplanar spacing of 0.478 nm and 0.242 nm (part ②-III and ②-IV in Fig. 1c and 1e), which are the crystal planes of (003) and (101) belong to the well-ordered  $R\bar{3}m$  layered structure. It indicates that the dual-element modification does not affect the crystallization of the cathodes, which is consistent with the above XRD results. Additionally, cross-sectional high-angle annular dark-field imaging (HAADF) mapping further reveals that the Ni, Mn, Al, O, In and Sn elements are well distributed throughout the InSn-NMA85 cathode, demonstrating successful doping of In and Sn into the inner lattice of the crystal (Fig. 1f). Overall, based on the above analysis, it can be concluded that the In and Sn have been concurrently doped into the NMA85 lattice by the one-step sintering method, which effectively increases the crystallinity of NMA85 cathode. Moreover, island coating of  $\text{LiInO}_2$  is in-situ formed along with the doping during the material synthesis.  $\text{LiInO}_2$  possesses a similar layered structure to the Ni-rich cathode [26], thus  $\text{LiInO}_2$  can easily combine with the cathode, effectively maintain the layered structure, and distribute on the surface of the cathode as coating.

### 2.2. Electrochemical performance

The electrochemical performance of the NMA85 and InSn-NMA85 cathodes was evaluated in half cells at various temperatures, i.e.  $30^\circ\text{C}$  and  $45^\circ\text{C}$  with a cut-off voltage of 4.5 V. Such conditions enable us to comprehend the advantages of In/Sn dual-element modification in alleviating H2-H3 phase transitions and inhibiting cathode/electrolyte interfacial erosion at high temperature and high voltage. Fig. 2a-b shows the charge/discharge curves of the NMA85 and InSn-NMA85 cathodes at 0.5C in 2.7–4.5 V at  $45^\circ\text{C}$ . Both cathodes exhibit voltage plateaus corresponding to phase transitions of H1-H2-H3. The phase transition plateaus of NMA85 cathode decay faster than those of InSn-NMA85 cathode with cycling, especially for the H2-H3 phase transition plateau at 4.2–4.3 V, which nearly disappears in the 80th and 100th cycles in NMA85 cathode. Moreover, it is worth noting that the current of both cathodes gradually decreases during trickle charge. Consequently, the capacity loss caused by overpotential can be partially restored, and a platform appears at 4.5 V. This constant voltage platform is correlated with the overpotential generated by the polarization of the electrode. The constant voltage charging platforms in the InSn-NMA85 cathode is more stable and correspond to way lower capacity than those in the NMA85 cathode even after 100 cycles (10.5 vs 22.7 mAh  $\text{g}^{-1}$ ), indicating much reduced electrode polarization for the InSn-NMA85 cathode due to InSn dual-element modification. The voltage curves at  $30^\circ\text{C}$  (Figure S8) show similar trends, suggesting the advantage of the dual-element modification in the InSn-NMA85.

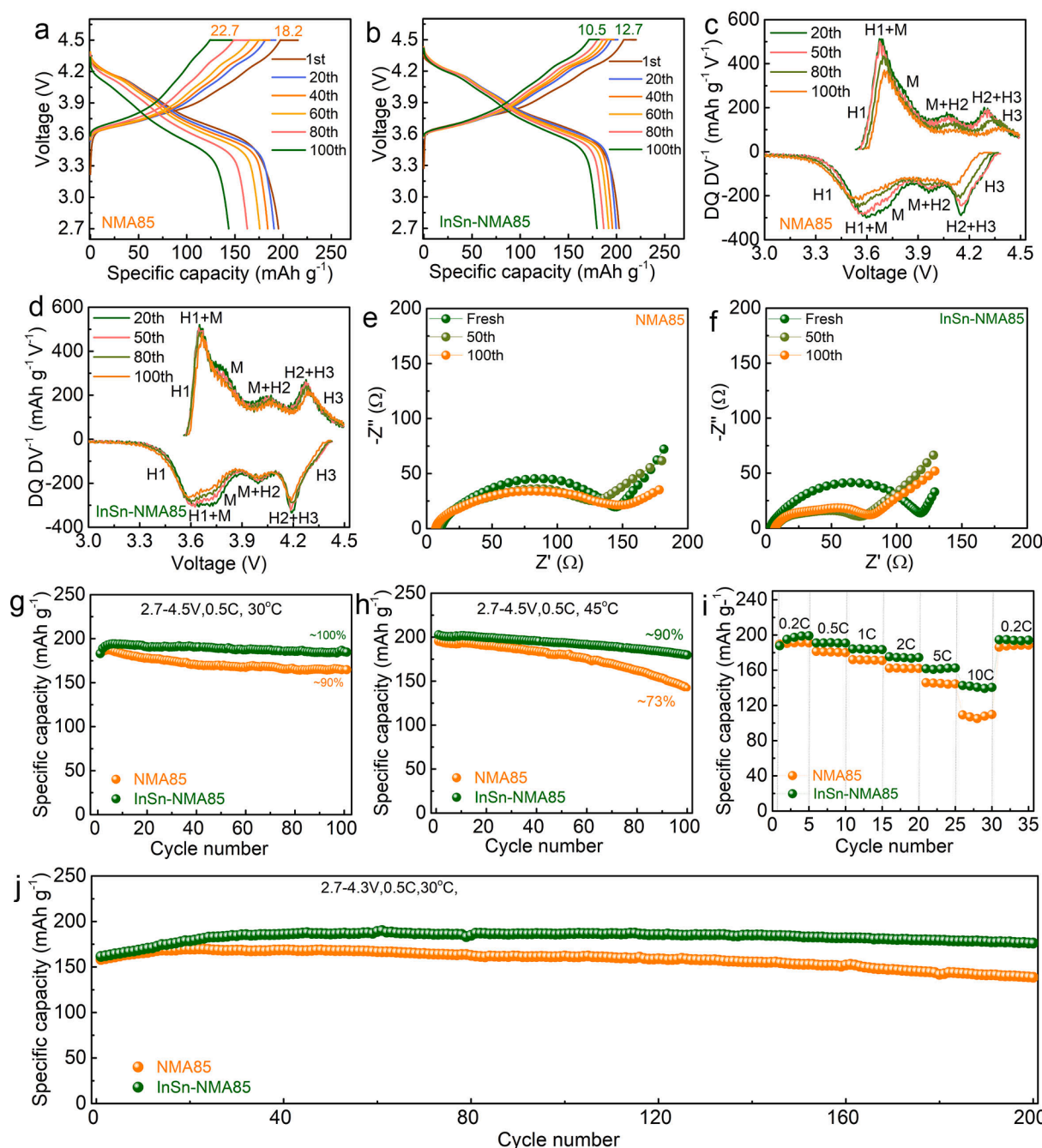


**Fig. 2. Electrochemical characterization.** (a–b) Charge/discharge voltage curves for the NMA85 (a) and InSn-NMA85 (b) cathodes at 45 °C. (c–d) dQ/dV curves of the NMA85 (c) and InSn-NMA85 (d) cathodes at 45 °C. (e–f) EIS curves of the fresh and cycled NMA85 (e) and InSn-NMA85 (f) cathodes in discharge state. (g–h) Cycling performance of the NMA85 and InSn-NMA85 cathodes at 30 °C (g) and 45 °C (h). (i) Rate performance of the NMA85 and InSn-NMA85 cathodes at 30 °C. (j) Cycling performance of the NMA85 and InSn-NMA85 cathodes in full cell with graphite anode cycled between 2.7 and 4.3 V at 0.5C at 30 °C.

Differential capacity profiles ( $dQ/dV^{-1}$ ) were plotted by differentiating the 20th, 50th, 80th, and 100th voltage curves to further understand the reversibility of the electrochemical reaction and phase transition in both cathodes during cycling, as shown in Fig. 2c–d. Both cathodes undergo a series of phase transformation, from hexagonal (H1) through monoclinic (M) to hexagonal (H2 and H3) during the delithiation, and vice versa during lithiation [39–41]. It is reported that the redox peaks around 4.2–4.3 V are related to the H2–H3 phase transition, which results in a sudden unit cell lattice contraction in the c-direction, and the cathodes are subjected to a severe mechanical strain with an anisotropic volume shrinkage that eventually deteriorates during cycling [27,42,43]. From the 20th to the 100th cycle, the voltage of

the H2 → H3 peak in the NMA85 cathode is 4.317 V, 4.318 V, 4.337 V and 4.371 V, respectively, and the voltage of the H2–H3 peak in the InSn-NMA85 cathode is 4.275 V, 4.271 V, 4.275 V, and 4.287 V, respectively. The obvious shift of the H2 → H3 phase transition voltage in the NMA85 suggests obvious attenuation with cycling. The degradation is related to the severe structural changes of the cathode caused by the mechanical strain during the H2 → H3 phase transition. The increase of delithiation/lithiation voltage polarization (potential gap between cathodic peak and anodic peak), especially for the H2 → H3 → H2 phase transition, indicates degraded reversibility and increased charge transfer resistance, which could be caused by the accumulation of cathode electrolyte interphase [44,45], irreversible surface structure transformation [46],

and micro-crack generation [47], etc. By contrast, the delithiation/lithiation peaks of the InSn-NMA85 cathode are well maintained with only slight variations during cycling, demonstrating that the In and Sn dual-element modification can effectively suppress the structural changes of the NMA85 cathode.

Electrochemical impedance spectroscopy (EIS) of the as-prepared and cycled cathodes was tested to further understand the interfacial changes and  $\text{Li}^+$  ions transport kinetics during cycling. Fig. 2e-f show Nyquist curves of both electrodes with different cycles. The Nyquist curves of both NMA85 and InSn-NMA85 cathodes in the fresh cells exhibit one semicircle at high frequency regions corresponding to the interfacial charge transfer resistance ( $R_{ct}$ ) and a slash at low-frequency regions relates to the mass transfer controlled Warburg impedance ( $Z_w$ ) [48,49]. For the fresh samples, compared to the NMA85, the InSn-NMA85 shows lower interfacial charge transfer resistance and faster mass transfer kinetics, indicating that the dual-element modification not only efficiently reduces the interfacial resistance but also facilitates the  $\text{Li}^+$  transport. After cycles, additional semicircle in the high-frequency region appears, which corresponds to the resistance of cathode electrolyte interphase (CEI,  $R_f$ ) [50]. The CEI resistance ( $R_f$ ) and charge transfer resistance ( $R_{ct}$ ) are greatly reduced in the InSn-NMA85 after cycling, indicating a more conductive CEI layer is formed due to the dual-element modification, which may be related to the promoted  $\text{Li}^+$  diffusion by the in-situ formed  $\text{LiInO}_2$  layer [51]. With increasing cycle numbers, the impedance of the NMA85 and InSn-NMA85 cathodes increases gradually, especially for the NMA85 cathode, owing to the structural collapse of the cathode particles and continuous formation of CEI layer. Compared with the NMA85 electrode, the InSn-NMA85 electrode exhibits much lower impedance ( $R_f + R_{ct}$ ) even after 100 cycles, indicating much better structural stability after In and Sn dual-element modification in the sample.

The cycling stability of the InSn-NMA85 is notably superior to that of the NMA85 cathode with the cutoff voltage of 4.5 V, as shown in Fig. 2g-h. The InSn-NMA85 cathode possesses discharge capacity of 185.2 mAh  $\text{g}^{-1}$  at 30 °C after 100 cycles, and capacity retention of  $\sim 100\%$  of its initial capacity, which is superior to the NMA85 cathode (164.8 mAh  $\text{g}^{-1}$  and  $\sim 90\%$ ) (Fig. 2g). It demonstrates that the InSn-NMA85 cathode owns more stable structure than the NMA85 cathode to bear a high cutoff voltage. Initially, some particles in the bulk are not accessible at the beginning of the cycle, which is limited by the diffusion of lithium ions. With prolonged cycling, the electrolyte gradually penetrates into the electrode and lithium ion diffusion is facilitated, all active materials are accessible and participate in the electrode reaction, so the specific capacity has an upward trend at the initial stage, and similar phenomena have been found in previous reports [52–54]. Additionally, the InSn-NMA85 cathode delivers a stable and promising material-level specific energy density of 708.5 Wh  $\text{kg}^{-1}$  at 0.5C and 30 °C after 100 cycles with retention of  $\sim 99\%$  (Figure S9), while the NMA85 cathode delivers specific energy density of 596.2 Wh  $\text{kg}^{-1}$  and inferior retention of  $\sim 88\%$ . Furthermore, the InSn-NMA85 cathode can attain capacity retention of  $\sim 90\%$ , (179.7 mAh  $\text{g}^{-1}$ ) after 100 cycles even at high temperatures of 45 °C, higher than  $\sim 73\%$  (142.4 mAh  $\text{g}^{-1}$ ) capacity retention of the NMA85 cathode (Fig. 2h). The significantly enhanced cycling stability at high temperature and high voltage is another benefit resulting from the In/Sn dual-element modification, which stabilizes the cathode/electrolyte interface and ensures prolonged cycling life. The rate performance for the NMA85 and InSn-NMA85 cathodes is further studied to evaluate the influences of the dual-element modification on  $\text{Li}^+$  transportation with various rates from 0.2C to 10C in the range of 2.7–4.5 V (Fig. 2i). With the rate increase from 0.2C to 10C, the discharge capacity decrease for both cathodes and the capacity of NMA85 cathode exhibit a much faster decrease than that of InSn-NMA85 cathode. At 10C, the discharge capacity of InSn-NMA85 is around 140 mAh  $\text{g}^{-1}$ , which is much higher than that of the NMA85 cathode ( $\sim 120$  mAh  $\text{g}^{-1}$ ). Moreover, when the current density returns to 0.2C, the discharge capacity of both cathodes can recover to the original value, suggesting the structure of the samples

are highly reversible after cycling at varying current densities. The charge–discharge curves of the NMA85 and InSn-NMA85 at various current densities are shown in Figure S10. It is clear that the voltage attenuation of NMA85 is more severe than that for InSn-NMA85 cathode. The drop of reaction platform at high current density is suppressed to some extent. This drop is related to the significantly increased polarization in the cathode and the capacity of the electrode cannot be fully utilized, which are caused by reduced ion diffusion efficiency and increased interfacial resistance at high current density. It suggests that the In/Sn dual-element modification in InSn-NMA85 cathode may facilitate the  $\text{Li}^+$  transport and account for the increased rate performance and reversible capacity retention, even under the harsh conditions of high voltage and high temperature. The full cell consisting of the NMA85 and InSn-NMA85 cathodes and graphite anode was fabricated to further investigate the electrochemical performances of cathodes. As shown in Fig. 2j, remarkably, the InSn-NMA85 cell maintained a reversible capacity of 176.2 mAh  $\text{g}^{-1}$  after 200 cycles with an exceptional capacity retention of 100 % of its initial capacity, while the capacity retention of NMA85 cathode retains only 138.6 mAh  $\text{g}^{-1}$ .

### 2.3. Investigation of structure and Cathode/Electrolyte interphase changes

The detailed structural evolutions, especially against the H2-H3 phase transition, of the NMA85 and InSn-NMA85 cathodes during initial lithiation/delithiation were characterized by in-situ XRD (Fig. 3) to investigate their contributions to the improved electrochemical performance of InSn-NMA85. Fig. 3a-b show the initial charge/discharge curves of the cathodes and corresponding contour maps of the (003), (101), (104) and (018)/(110) reflections derived from the in-situ XRD results. The NMA85 and InSn-NMA85 cathodes experience similar H1  $\rightarrow$  H2  $\rightarrow$  H3 phase evolution upon charging (delithiation), consistent with the voltage curves and differential capacity profiles in Fig. 2 a-d. During the initial delithiation of the two electrodes, (003), (101), (104), and (018)/(110) peaks illustrate a well layered structure and show a noticeable shift due to the initial phase transition from hexagonal (H1) through monoclinic (M) to hexagonal. The (003) peaks shift to lower 2 $\theta$  angles before arriving at the local minimum at  $\sim 4.2$  V, corresponding to the H1-H2 phase transition, indicating an enlargement of lattice along the c-axis, which is related to the increase of a stronger repulsive force between oxygen atoms caused by the diminishing lithium-screening effect within the Li slab in the layered structure [55]. Afterwards, the (003) peaks shift backward to higher 2 $\theta$  angles to 4.5 V, which corresponds to the H2-H3 phase transition with the lattice shrinkage along the c-axes direction. Compared to the NMA85 with a maximum angle shift of 0.32° during H2-H3 transition, the (003) peak of InSn-NMA85 only shifts by a lower maximum angle of 0.2°, illustrating that the contraction along the c-axis of the InSn-NMA85 is reduced. The lattice shrinkage along c-axis is attributed to the continuous removal of  $\text{Li}^+$  which weakens the pillaring effect and accelerates the abrupt variation in the interslab distance and structure collapse [50]. In addition, the continuous shift of the (101) peaks to higher 2 $\theta$  angles during charging up to 4.5 V indicates shrinkage of lattice along the a-axis owing to the oxidation of  $\text{Ni}^{3+}$  to  $\text{Ni}^{4+}$  ions [56]. The results demonstrate that the InSn-NMA85 possesses relatively more stable structure, especially at high voltages. Fig. 3c-d summarizes the changes of lattice parameters derived from in-situ XRD data for the two electrodes upon charging. Initially, when the  $\text{Li}^+$  ions are delithiated from the cathode, lattice parameter c gradually increases (Fig. 3d), which enhances the electrostatic repulsive force in the adjacent oxygen plate slabs. At the same time, the cation oxidation compensates for the charge variation, which is then followed by the decreased ionic radius in the transition metal layers, causing the a-parameter to decrease (Fig. 3c). Specifically, the NMA85 and InSn-NMA85 display shrinkage of 1.98 % and 1.77 % along the a-axes, respectively. For the NMA85 electrode, when charging to voltages higher than 4.2 V, the c-parameter decreases sharply due to



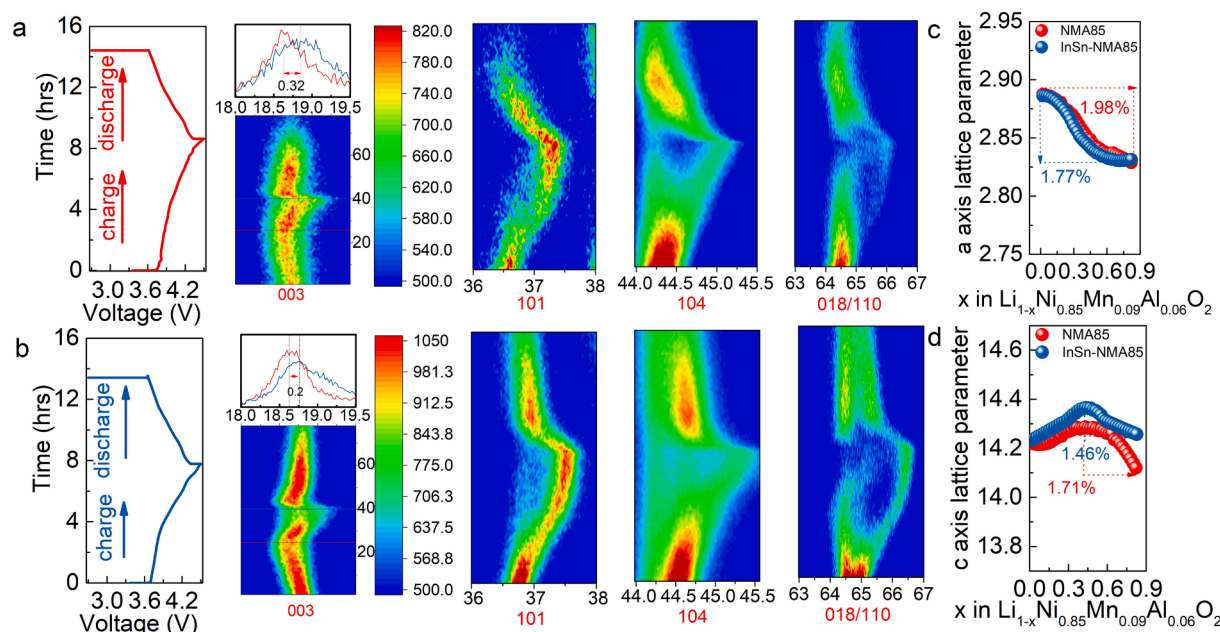


**Fig. 3.** In situ XRD characterizations during initial delithiation/lithiation of the (a) NMA85 and (b) InSn-NMA85, showing recorded charge/discharge curves and contour plots of 003,101,104 and 018/110 reflections. (c) The variation of the a-axis parameter during delithiation for the NMA85 and InSn-NMA85. (d) The variation of the c-axis parameter during delithiation for the NMA85 and InSn-NMA85.

irreversible oxygen loss and the associated transition metal migration associating with the H2 → H3 phase transition. The c parameter of NMA85 dramatically decreases to 14.07 Å at 4.5 V, while that of InSn-NMA85 slightly drops to 14.22 Å. The maximum variation of c parameter in the InSn-NMA85 (1.46 %) is way smaller than that in the NMA85 (1.71 %). The significant c-axis contraction of the NMA85 under high voltage would lead to serious structure degradation. Severe lattice changes are thought to be one of the major reasons for the rapid capacity fade of Ni rich cathodes, and alleviating the lattice contraction is an effective way to improve the capacity retention. For the InSn-NMA85 cathode, the greatly reduced lattice contraction during cycling contribute to more reversible phase transition, as revealed in Fig. 2b and 2d. The variation of the shape and position of the (003) reflection is greatly reduced, which may be ascribed to the inhibition of lattice mismatch between reconstructed surface and interior bulk under high voltage. The structural/volume changes, which is directly responsible for the particle cracking/pulverization, associated with the phase transitions can be effectively suppressed during cycling in the InSn-NMA85. In addition, the lattice shrinkage along c-axes during H2-H3 transition is less aggressive and slower in the modified InSn-NMA85, which would be beneficial to avoid accumulation of internal strain and particle fracture/cracks.

The structural evolution of cycled NMA85 and InSn-NMA85 electrodes after 100 cycles at 2.7–4.5 V and 45 °C were analyzed by cross-sectional SEM and HRTEM, as shown in Fig. 4a–d, to further understand the relationship between structural degradation and microcrack generation. Cracks and particle fractures can be clearly observed in the NMA85 electrode (Fig. 4a and Figure S11a), exposing additional surfaces which would further accelerate the electrolyte penetration and parasitic reactions through the intergranular gaps. In contrast, the InSn-NMA85 electrode is mechanically intact without visible cracks (Fig. 4c and Figure S11b). As discussed above, the improved structural integrity of the InSn-NMA85 is associated with the effectively suppressed irreversible phase transitions during cycling. More detailed observation of the irreversible phase transformation from ordered layered to disordered rock salt structure in the NMA85 and InSn-NMA85 electrodes was obtained by HRTEM. Fig. 4b shows that there is a thick rock-salt NiO layer of ~ 20 nm, i.e., region A indexed by the (200) plane of Fm3m

rock-salt phase, at the surface of the particle with layered phase (region B indexed by (003) plane of layer NMA structure), after 100 cycles, indicating severe structural degradation of the cycled NMA85 electrode. By contrast, the interplanar spacing of 0.230 nm, which corresponds to (012) plane of layer structure, in both region A and B in Fig. 4d suggests that the R3m structure are well-preserved in the cycled InSn-NMA85 electrode. The rock-salt phase formed on the surface of the cathodes during cycling indicates a structural collapse of the cathodes, which would increase the interfacial resistance and elevates the barrier for Li<sup>+</sup> transport [21]. In/Sn dual-element modification for NMA85 electrode effectively promotes the electrochemically and structurally stability even at high-voltage circulation to avoid detrimental phase formation.

The improved structural stability of NMA85 by In/Sn dual-element modification is expected to alleviate the detrimental interfacial side reactions between NMA85 cathode and the electrolyte as well as enhance the reversibility of NMA85 electrode during cycling. The chemical compositions of the cathode-electrolyte interphase (CEI) layer in the cycled NMA85 and InSn-NMA85 electrodes were examined by XPS (Fig. 4e–h) to reveal the amelioration effect of the dual element modification on CEI formation and interfacial reactions. The XPS survey spectra demonstrate the presence of C, O, F and P elements in the CEI (Figure S12). The peaks corresponding to C–C, C–H, C–O, C=O, and OCO<sub>2</sub> bonds are observed in the C 1s spectra for both NMA85 and InSn-NMA85 electrodes. The presence of C–C (284.8 eV) and C–H (285.4 eV) bonds is attributed to acetylene black and polyvinylidene fluoride (PVDF) binder, respectively, while C–O (286.6 eV), C=O (287.7 eV), and OCO<sub>2</sub> bonds (290.3 eV) are associated with lithium alkyl carbonates (ROCO<sub>2</sub>Li), ROLi, and Li<sub>2</sub>CO<sub>3</sub> which are the decomposition products of carbonate electrolyte solvents [57] (Fig. 4e). Compared to the NMA85 electrode, the contribution related to the C–O, C=O, and OCO<sub>2</sub> species in the InSn-NMA85 electrode is reduced, especially for the OCO<sub>2</sub> species, suggesting less organic species produced by electrolyte decomposition due to the In/Sn dual-element modification. Moreover, the M–O, Li<sub>2</sub>CO<sub>3</sub> and ROCO<sub>2</sub> Li species are observed in the O 1s spectra for both NMA85 and InSn-NMA85 electrodes (Fig. 4f). The peaks of Li<sub>2</sub>CO<sub>3</sub> (531.6 eV) and ROCO<sub>2</sub>Li (533.2 eV) are related to lithium alkyl carbonates as the decomposition of carbonate electrolyte solvents. Compared with the NMA85 electrode, the peaks of Li<sub>2</sub>CO<sub>3</sub> and ROCO<sub>2</sub>Li are detected for the



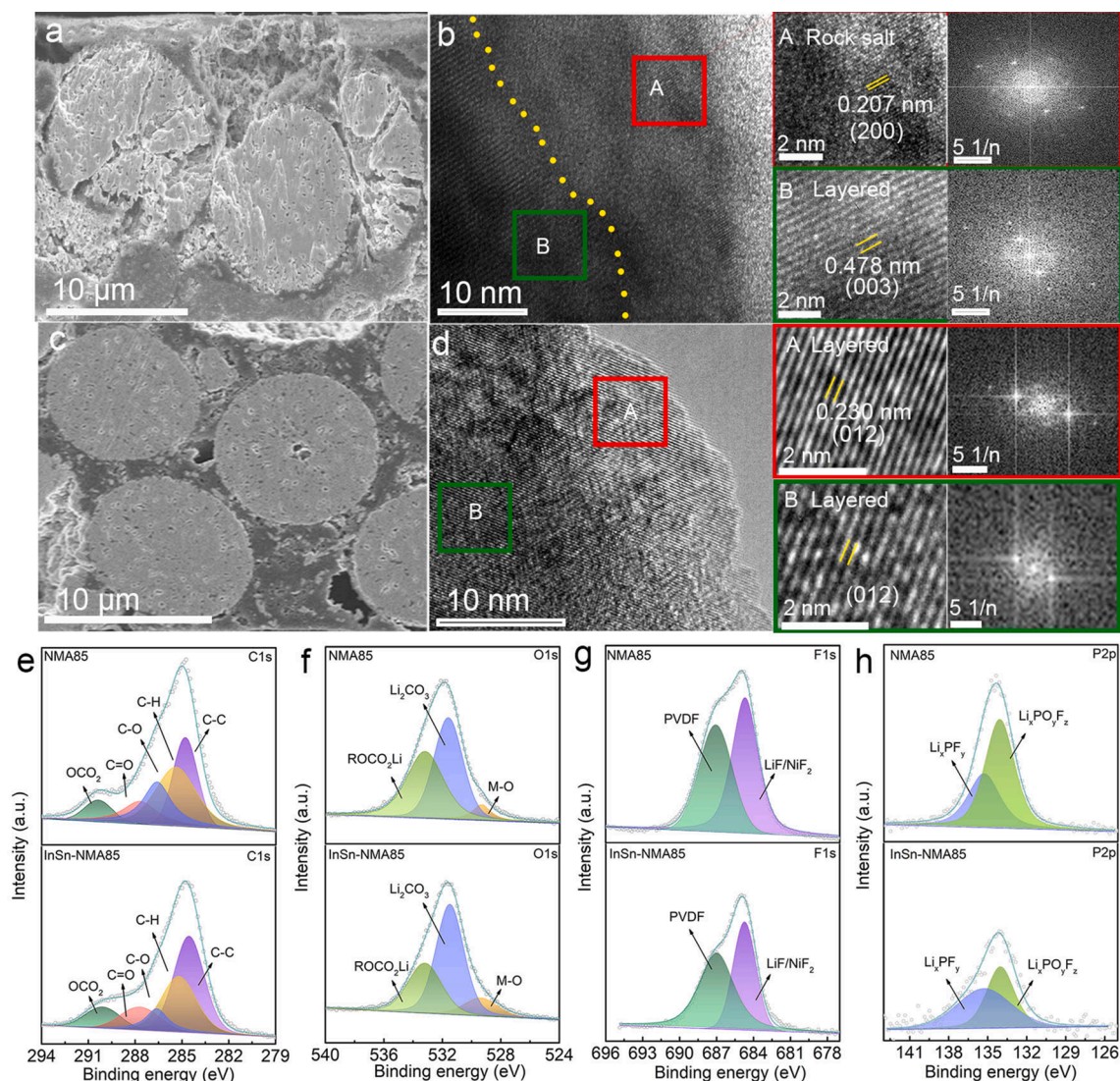


**Fig. 4.** (a) Cross sectional SEM images of NMA85 electrode after 100 cycles at 45 °C. (b) HRTEM images and the corresponding FFT images of the cycled NMA85 electrode. (c) Cross sectional SEM images of the InSn-NMA85 electrode after 100 cycles at 45 °C. (d) HRTEM images and the corresponding FFT images of the cycled InSn-NMA85 electrode. XPS spectra of (e) C 1s, (f) O 1s, (g) F 1s and (h) P 2p elements in the cycled NMA85 and InSn-NMA85 electrodes after 100 cycles at 45 °C.

InSn-NMA85 electrode with reduced content, which further validates the suppressed carbonate decomposition accumulation on the inter-phase between cathode and electrolyte [58–60].

Meanwhile, the O 1s peaks at 529.3 eV is typically assigned to the lattice oxygen (M–O) in the cathode. The larger lattice oxygen content detected on the surface of InSn-NMA85 (11.95 %) electrode than that of NMA85 (5.64 %) electrode implies the formation of a thinner CEI layer in InSn-NMA85 after cycling (Fig. 4f), which may be related to the improved particle integrity and reduced cathode/electrolyte side reactions as demonstrate above. In terms of the F 1s spectra, as presented in Fig. 4g, the peaks located at 685 eV and 687.5 eV are attributed to the LiF/NiF<sub>2</sub> and PVDF binder, respectively [61,62]. LiF/NiF<sub>2</sub> species are originated from the decompositions products of LiPF<sub>6</sub> salts in the electrolyte and dissolved transition metals (TMs) cations from the cathode that caused by acidic species attack. Compared with the NMA85 electrode, the decreased peak intensities of LiF/NiF<sub>2</sub> are deducted on the InSn-NMA85 electrode, which indicates that acid corrosion and TMs dissolution are effectively inhibited. Moreover, a stronger peak of PVDF binder is shown for the InSn-NMA85 electrode, which validates the reduced electrolyte and electrode side reactions. In addition, the peaks of P 2p spectra corresponding to Li<sub>x</sub>PO<sub>y</sub>F<sub>z</sub> (134.1 eV) and Li<sub>x</sub>PF<sub>y</sub> (135.3 eV) bonds are shown Fig. 4h for both NMA85 and InSn-NMA85

electrodes. Compared with the NMA85 electrode, a weaker Li<sub>x</sub>PO<sub>y</sub>F<sub>z</sub> peak shows up, which is beneficial to the formation of a stable CEI layer that can prevent the cathode from being damaged by the electrolyte. As a result, the continuous electrolyte consumption along with the interfacial side reactions and microcrack growth along with the phase transition/TMs dissolution, which are associated with the increase of interfacial impedance and, are successfully suppressed by the stable CEI on InSn-NMA85 to avoid severe deterioration of the electrochemical performances, consistent with the observed results in Fig. 2.

#### 2.4. Electron density of state analysis

To further analyze the positive effects of In/Sn dual-element modification on the crystal structure and electrochemical performance, the density functional theory (DFT) was used to calculate the Li/Ni exchange energies and the oxygen vacancy formation energies based on substituting transition metal ion with In and Sn ions in InSn-NMA85 cathode. Firstly, the doping sites of In ions are determined by calculating the formation energy of In doping in the Li (-0.08444 eV) or Ni (-3.24057 eV) site in the lattice structure, and it turns out that In in the Ni site is energetically more favorable. The atomic configuration of the NMA85 used for the calculation is shown in Fig. 5a-b and Figure S13.

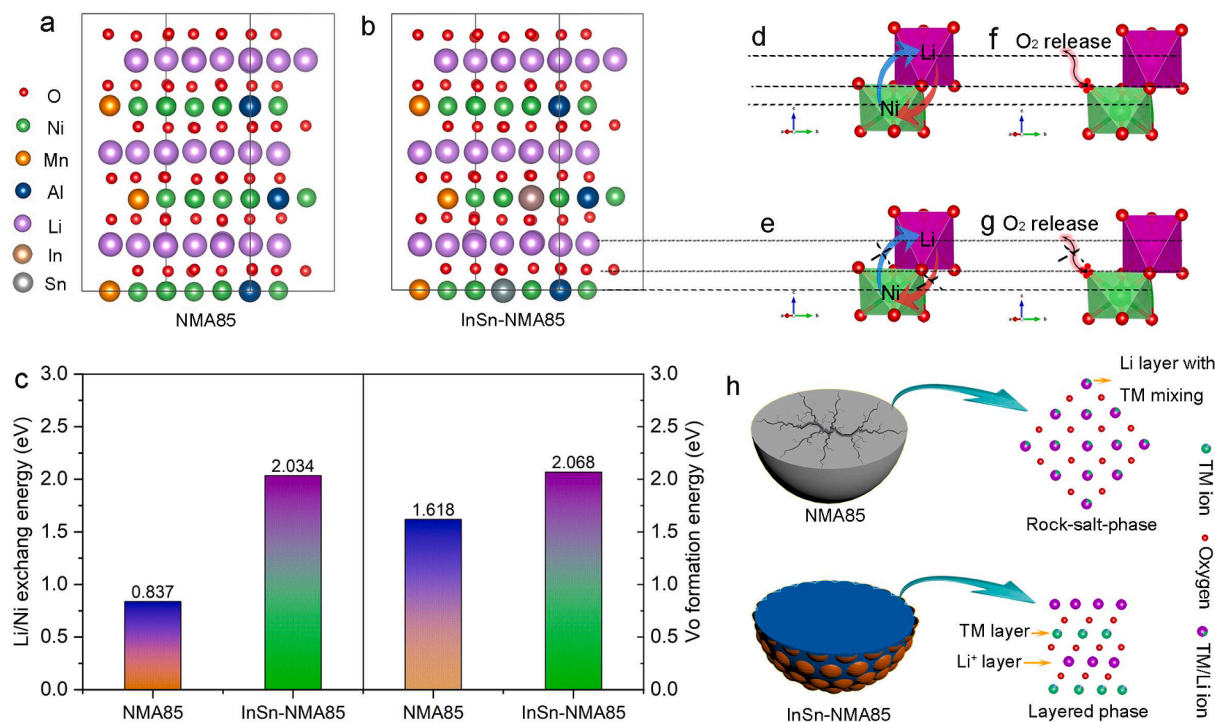


**Fig. 5.** Structural model for the NMA85 (a) and the InSn-NMA85 (b) cathode used in DFT simulation. (c) Li/Ni exchange energies and oxygen vacancy formation energies in NMA85 and InSn-NMA85. Schematic illustration of Li/Ni exchange energies for the NMA85 (d) and the InSn-NMA85 (e) cathodes. Schematic illustration of oxygen vacancy formation energies for the NMA85 (f) and the InSn-NMA85 (g) cathodes. (h) Schematic illustration of crack evolution and the phase transformation for both cathodes.

As depicted in Fig. 5c, the Li/Ni exchange energy is increased from 0.837 eV to 2.034 eV by the In/Sn dual-element modification, which would effectively inhibit the Li-Ni cation mixing [63]. Specifically, due to the similar ionic radius of Li<sup>+</sup> (0.76 Å) and Ni<sup>2+</sup> (0.69 Å), the Ni<sup>2+</sup> in TMs layers can easily migrate to Li<sup>+</sup> sites in the Li<sup>+</sup> layers during synthesis and cycling, leading to the Li/Ni mixing [64]. The removal of Li<sup>+</sup> in the NMA85 cathode, which possesses low cation mixing energy barrier, more likely leads to Li-Ni cation mixing during delithiation (Fig. 5d). When Ni<sup>2+</sup> occupies the Li<sup>+</sup> sites, such cationic mixing triggers the phase transition from the layered phase (R $\bar{3}m$ ) to the rock-salt phase (Fm $\bar{3}m$ ) during cycling, facilitates the lattice structural collapse and generation of micro-cracks, further inducing severe cathode-electrolyte side reactions and transition metal dissolution [65]. These changes in turn increase the impedance and retard the diffusion of Li<sup>+</sup>, resulting in poor cycle stability [66], which have been revealed in Fig. 2e and Fig. 4. By contrast, the increased energy barrier of Li-Ni cation mixing enables a more stabilized layered structure and integrated microstructure of InSn-NMA85 even cycled at high voltage and high temperature (Fig. 5e). It can be related to the In/Sn dopants with relatively larger radius (0.8 Å and 0.69 Å) compared with Ni<sup>3+</sup> (0.56 Å) and Al<sup>3+</sup> (0.53 Å). Combined with the results of EDS, HRTEM and XPS, it is proved that Sn has been successfully introduced into the lattice of NMA85 cathode, which act as “pillar” during delithiation to avoid the migration of Ni to the Li inter-slab [21]. In addition, Sn<sup>4+</sup> has higher valence state, which can effectively inhibit the contraction of lattice parameters in the c direction under high charge state, inhibit the migration of nickel ions and improve the structural stability. As a result, the integrity of the lattice structure can be well preserved, as revealed above, resulting in improved electrochemical performance and prolonged cycle life.

Furthermore, the formation energy of oxygen vacancies in both cathodes was also calculated. The oxygen vacancy formation energy in the InSn-NMA85 cathode is 2.068 eV, which is way higher than that in the NMA85 cathode (1.618 eV). Due to the energy band overlap between transition metal ions and O<sup>2-</sup> (such as the 3d orbital in Ni and the 2p

orbital in oxygen), O<sup>2-</sup> tends to be oxidized in the high delithiated state (i.e., high charged state) with the increase of applied voltage [67]. The lower oxygen vacancy formation energy in NMA85 makes it easy to release lattice oxygen during repeated lithium removal/insertion, resulting in an irreversible phase transition from layered structure to surface spinel and rock salt phase combination (Fig. 5f). Once the oxygen atom is released and reacts with the electrolyte, the TM-O bonds are broken up. The transition metal ions will be reduced to the divalent oxidation state and diffuse from the octahedral site of the transition metal layer to the lithium layer [68], especially at high voltage and high temperature. This harmful surface recombination will not only consume active lithium sites but also form an insulating surface layer, which will hinder the diffusion of lithium [69]. The lattice oxygen activity in InSn-NMA85 is effectively inhibited by its higher oxygen vacancy formation energy, and series of adverse effects caused by oxygen release will also be suppressed (Fig. 5g). The bond energy of In-O (360 kJ mol<sup>-1</sup>) is similar to that of Ni-O (391 kJ mol<sup>-1</sup>). However, Sn-O bond possesses way higher bond energy of 548 kJ mol<sup>-1</sup>, which elevates the barrier for the dissociation of oxygen atoms from the bulk in the sample and ensures a more stable O<sup>2-</sup> anion skeleton in the InSn-NMA85 cathode [31]. Therefore, the InSn-NMA85 cathode possesses improved structural stability at elevated voltage and temperature, enabling the excellent electrochemical performance. The detailed illustration of the internal structural evolution for both cathodes is described in Fig. 5h. For the NMA85 cathode, the lower Li/Ni exchange energy and the oxygen vacancy formation energy triggers the phase transition from the layered phase (R $\bar{3}m$ ) to the rock-salt phase (Fm $\bar{3}m$ ) during cycling, which facilitates the lattice structural collapse and generation of micro-cracks, further inducing severe cathode-electrolyte side reactions and transition metal dissolution. These changes in turn increase the impedance and retard the diffusion of Li<sup>+</sup>, resulting in poor cycle stability. On the contrary, for InSn-NMA85 cathode, the increased energy barrier of Li/Ni exchange energies and the oxygen vacancy formation enables a more stabilized layered structure and integrated microstructure,



resulting in much improved electrochemical performance.

### 3. Conclusion

In summary, we synthesized a Ni-rich Co-free In/Sn dual-element modified cathode through a one-step sintering strategy. Comprehensive structural and electrochemical characterizations provide clear insights into the correlation between the microstructure of Ni-rich cathodes and the corresponding capacity performance and mechanism. In/Sn dual-element modification improves the structural and interfacial stability in the Ni-rich Co-free cathode. Specifically, the In/Sn dual-element modification not only effectively inhibits  $\text{Li}^+/\text{Ni}^{2+}$  mixing but also stabilizes the lattice oxygen. Meanwhile, the in-situ formed  $\text{LiInO}_2$  layer successfully protects the cathode from the erosion of detrimental species generated by electrolyte decomposition and stabilizes the cathode/electrolyte interface. As a result, the modified cathode maintains superior capacity retention of  $\sim 100\%$  ( $185.2 \text{ mAh g}^{-1}$ ) and  $\sim 90\%$  ( $179.7 \text{ mAh g}^{-1}$ ) in 2.7–4.5 V at  $30^\circ\text{C}$  and  $45^\circ\text{C}$  after 100 cycles, respectively. The full cell exhibits a remarkable capacity retention of  $100\%$  after 200 cycles at 4.3 V with an exceptional discharge capacity of  $176.2 \text{ mAh g}^{-1}$ . The key findings of this work highlight the development of high energy density and the superior cycling stability of Ni-rich Co-free cathodes under high voltage.

### Declaration of Competing Interest

The authors declare that they have no known competing financial interests or personal relationships that could have appeared to influence the work reported in this paper.

### Data availability

Data will be made available on request.

### Acknowledgement

This work was supported by Guangdong Basic and Applied Basic Research Foundation (2022A1515010486), China Postdoctoral Science Foundation (2021M691750), Shenzhen Science and Technology Program (JCYJ20210324140804013, RCBS20200714115000219-Doctoral Startup Project), and Tsinghua Shenzhen International Graduate School (QD2021005N, JC2021007).

### Appendix A. Supplementary data

Supplementary data to this article can be found online at <https://doi.org/10.1016/j.cej.2022.140652>.

### References

- [1] T. Dong, P. Mu, S. Zhang, H. Zhang, W. Liu, G. Cui, How do polymer binders assist transition metal oxide cathodes to address the challenge of high-voltage lithium battery applications? *Electrochem Energy Rev.* 4 (3) (2021) 545–565.
- [2] C.S. Yoon, U.H. Kim, G.T. Park, S.J. Kim, K.H. Kim, J. Kim, Y.K. Sun, Self-passivation of a  $\text{LiNiO}_2$  cathode for a lithium-ion battery through Zr doping, *ACS Energy Lett.* 3 (7) (2018) 1634–1639.
- [3] R. Reddy, X. Lin, A. Zeb, C.Y. Su, Metal-organic frameworks and their derivatives as cathodes for lithium-ion battery applications: A review, *Electrochem Energy Rev.* 5 (2022) 312–347.
- [4] Y. Lv, S.F. Huang, Y.F. Zhao, S. Roy, X.G. Lu, Y.L. Hou, J.J. Zhang, A review of nickel-rich layered oxide cathodes: synthetic strategies, structural characteristics, failure mechanism, improvement approaches and prospects, *Appl. Energy* 305 (2022), 117849.
- [5] Y. Lai, Z. Li, W. Zhao, X. Cheng, S. Xu, X. Yu, Y. Liu, An ultrasound-triggered cation chelation and reassembly route to one-dimensional Ni-rich cathode material enabling fast charging and stable cycling of Li-ion batteries, *Nano Res.* 13 (12) (2020) 3347–3357.
- [6] Y. Lv, S.F. Huang, S.R. Lu, W.B. Ding, X.L. Yu, G.M. Liang, J.S. Zou, F.Y. Kang, J. J. Zhang, Y.D. Cao,  $\text{B}_2\text{O}_3/\text{LiBO}_2$  dual-modification layer stabilized Ni-rich cathode for lithium-ion battery, *J. Power Sources* 536 (2022), 231510.
- [7] W.D. Li, S. Lee, A. Manthiram, High-nickel NMA: a cobalt-free alternative to NMC and NCA cathodes for lithium-ion batteries, *Adv. Mater.* 32 (33) (2020) 2002718.
- [8] A. Aishova, G.T. Park, C.S. Yoon, Y.K. Sun, Cobalt-free high-capacity Ni-rich layered  $\text{Li}[\text{Ni}_{0.9}\text{Mn}_{0.1}]\text{O}_2$  cathode, *Adv. Energy Mater.* 10 (4) (2020) 1903179.
- [9] D. Rathore, C.X. Geng, N. Zaker, I. Hamam, Y.L. Liu, P.H. Xiao, G.A. Botton, J. Dahn, C.Y. Yang, Tungsten infused grain boundaries enabling universal performance enhancement of Co-free Ni-rich cathode materials, *J. Electrochem. Soc.* 168 (12) (2021), 120514.
- [10] L. Mu, Z. Yang, L. Tao, C.K. Waters, Z. Xu, L. Li, F. Lin, The sensitive surface chemistry of Co-free, Ni-rich layered oxides: identifying experimental conditions that influence characterization results, *J. Mater. Chem. A* 8 (34) (2020) 17487–17497.
- [11] L. Ni, R. Guo, S. Fang, J. Chen, J. Gao, Y. Mei, X. Ji, Crack-free single-crystalline Co-free Ni-rich  $\text{LiNi}_{0.95}\text{Mn}_{0.05}\text{O}_2$  layered cathode, *eScience* 2 (1) (2022) 116–124.
- [12] A. Liu, N. Zhang, J. Stark, P. Arab, H. Li, J.R. Dahn, Synthesis of Co-free ni-rich single crystal positive electrode materials for lithium ion batteries: part i. two-step lithiation method for Al- or Mg-doped  $\text{LiNiO}_2$ , *J. Electrochem. Soc.* 168 (4) (2021), 040531.
- [13] X. Zhang, L.L. Kong, T.Y. Gao, H.T. Li, X.H. Yao, F.X. Li, Analysis and improvement of cycle performance for Ni-rich lithium ion battery, *Energy Storage Science and Technology* 9 (3) (2020) 813.
- [14] J. Li, M. Zhang, D. Zhang, Y. Yan, Z. Li, An effective doping strategy to improve the cyclic stability and rate capability of Ni-rich  $\text{LiNi}_{0.8}\text{Co}_{0.1}\text{Mn}_{0.1}\text{O}_2$  cathode, *Chem. Eng. J.* 402 (2020), 126195.
- [15] Y. Cheng, Y. Sun, C. Chu, L. Chang, Z. Wang, D. Zhang, L. Wang, Stabilizing effects of atomic Ti doping on high-voltage high-nickel layered oxide cathode for lithium-ion rechargeable batteries, *Nano Res.* 15 (5) (2022) 4091–4099.
- [16] Z.H. Cui, Q. Xie, A. Manthiram, A cobalt- and manganese-free high-nickel layered oxide cathode for long-life, safer lithium-ion batteries, *Adv. Energy Mater.* 11 (41) (2021) 2102421.
- [17] G.T. Park, B. Namkoong, S.B. Kim, J. Liu, C.S. Yoon, Y.K. Sun, Introducing high-valence elements into cobalt-free layered cathodes for practical lithium-ion batteries, *Nat. Energy* (2022) 1–9.
- [18] L. Ni, S. Zhang, A. Di, W. Deng, G. Zou, H. Hou, X. Ji, Challenges and strategies towards single-crystalline Ni-rich layered cathodes, *Adv. Energy Mater.* 12 (31) (2022) 2201510.
- [19] D.H. Kim, J.H. Song, C.H. Jung, D. Eum, B. Kim, S.H. Hong, K. Kang, Adv. Energy Mater., Stepwise dopant selection process for high-nickel layered oxide cathodes, 2022, p. 2200136.
- [20] J. Yan, H. Huang, J. Tong, W. Li, X. Liu, H. Zhang, W. Zhou, Recent progress on the modification of high nickel content NCM: Coating, doping, and single crystallization, *Interdisciplinary Mater.* 1 (3) (2022) 330–353.
- [21] Z. Zhang, B. Hong, M.Y. Yi, X.M. Fan, Z.A. Zhang, X.B. Huang, Y.Q. Lai, In situ co-doping strategy for achieving long-term cycle stability of single-crystal Ni-rich cathodes at high voltage, *Chem. Eng. J.* 445 (2022), 136825.
- [22] T. Deng, X.L. Fan, L.S. Cao, J. Chen, S. Hou, J. Xiao, L. Chen, S. Li, X.Q. Zhou, E. Y. Hu, D. Su, X.Q. Yang, C.S. Wang, Designing in-situ-formed interphases enables highly reversible cobalt-free  $\text{LiNiO}_2$  cathode for Li-ion and Li-metal batteries, *Joule* 3 (10) (2019) 2550–2564.
- [23] J. Zhu, Y. Li, L.L. Xue, Y.X. Chen, T.X. Lei, S.Y. Deng, G.L. Cao, Enhanced electrochemical performance of  $\text{Li}_3\text{PO}_4$  modified  $\text{Li}[\text{Ni}_{0.8}\text{Co}_{0.1}\text{Mn}_{0.1}]\text{O}_2$  cathode material via lithium-reactive coating, *J. Alloy. Compd.* 773 (2019) 112–120.
- [24] X. Huang, W.C. Zhu, J.Y. Yao, L.M. Bu, X.Y. Li, K. Tian, H. Lu, C.X. Quan, S.G. Xu, K.H. Xu, Z.K. Jiang, X. Zhang, L.J. Gao, J.Q. Zhao, Suppressing structural degradation of Ni-rich cathode materials towards improved cycling stability enabled by a  $\text{Li}_2\text{MnO}_3$  coating, *J. Mater. Chem. A* 8 (34) (2020) 17429–17441.
- [25] R.C. Qian, Y.L. Liu, T. Cheng, P.P. Li, R.M. Chen, Y.C. Lyu, B.K. Guo, Enhanced surface chemical and structural stability of Ni-rich cathode materials by synchronous lithium-ion conductor coating for lithium-ion batteries, *ACS Appl. Mater. Inter.* 12 (12) (2020) 13813–13823.
- [26] Y. Liu, L.B. Tang, H.X. Wei, X.H. Zhang, Z.J. He, Y.J. Li, J.C. Zheng, Enhancement on structural stability of Ni-rich cathode materials by in-situ fabricating dual-modified layer for lithium-ion batteries, *Nano Energy* 65 (2019), 104043.
- [27] T.T. Nguyen, U.H. Kim, C.S. Yoon, Y.K. Sun, Enhanced cycling stability of Sn-doped  $\text{Li}[\text{Ni}_{0.90}\text{Co}_{0.05}\text{Mn}_{0.05}]\text{O}_2$  via optimization of particle shape and orientation, *Chem. Eng. J.* 405 (2021), 126887.
- [28] J.C. Zheng, Z. Yang, Z.J. He, H. Tong, W.J. Yu, J.F. Zhang, In situ formed  $\text{LiNi}_{0.8}\text{Co}_{0.15}\text{Al}_{0.05}\text{O}_2/\text{Li}_4\text{SiO}_4$  composite cathode material with high rate capability and long cycling stability for lithium-ion batteries, *Nano Energy* 53 (2018) 613–621.
- [29] C.C. Fu, G.S. Li, D. Luo, Q. Li, J.M. Fan, L.P. Li, Nickel-rich layered microspheres cathodes: lithium/nickel disordering and electrochemical performance, *ACS Appl. Mater. Inter.* 6 (18) (2014) 15822–15831.
- [30] Y.C. Li, W. Xiang, Z.G. Wu, C.L. Xu, Y.D. Xu, Y. Xiao, Z.G. Yang, C.J. Wu, G.P. Lv, X. D. Guo, Construction of homogeneously  $\text{Al}^{3+}$  doped Ni rich Ni-Co-Mn cathode with high stable cycling performance and storage stability via scalable continuous precipitation, *Electrochim. Acta* 291 (2018) 84–94.
- [31] Z. Feng, S. Zhang, R. Rajagopalan, X.B. Huang, Y.R. Ren, D. Sun, H.Y. Wang, Y. G. Tang, Dual-element-modified single-crystal  $\text{LiNi}_{0.6}\text{Co}_{0.2}\text{Mn}_{0.2}\text{O}_2$  as a highly stable cathode for lithium-ion batteries, *ACS Appl. Mater. Inter.* 13 (36) (2021) 43039–43050.
- [32] X.C. Zhang, D.F. Xu, D. Huang, F. Liu, K.Q. Xu, H.X. Wang, S.Y. Zhang, Enhanced visible-light-driven photocatalytic activities of  $\text{LiInO}_2$  by  $\text{Mo}^{6+}$ -doping strategy, *J. Am. Ceram. Soc.* 100 (7) (2017) 2781–2789.

- [33] L.Z. You, B.B. Chu, G.X. Li, T. Huang, Y. Aishui,  $\text{H}_3\text{BO}_3$  washed  $\text{LiNi}_{0.8}\text{Co}_{0.1}\text{Mn}_{0.1}\text{O}_2$  with enhanced electrochemical performance and storage characteristics, *J. Power Sources* 482 (2021), 228940.
- [34] F. Zhang, S. Lou, S. Li, Z. Yu, Q. Liu, A. Dai, C. Cao, M.F. Toney, M. Ge, X. Xiao, W. K. Lee, Y. Yao, J. Deng, T. Liu, Y. Tang, G. Yin, J. Lu, D. Su, J. Wang, Surface regulation enables high stability of single-crystal lithium-ion cathodes at high voltage, *Nat. Commun.* 11 (1) (2020) 1–11.
- [35] L. Yao, F.Q. Liang, J. Jin, B. Chowdari, J.H. Yang, Z.Y. Wen, Improved electrochemical property of Ni-rich  $\text{LiNi}_{0.6}\text{Co}_{0.2}\text{Mn}_{0.2}\text{O}_2$  cathode via in-situ  $\text{ZrO}_2$  coating for high energy density lithium ion batteries, *Chem. Eng. J.* 389 (2020), 124403.
- [36] S.H. Guo, B. Yuan, H.M. Zhao, D. Hua, Y. Shen, C.C. Sun, T.M. Chen, W. Sun, J. S. Wu, B. Zheng, W.N. Zhang, S. Li, F.W. Huo, Dual-component  $\text{Li}_2\text{TiO}_3/\text{silica}$  functional coating in one layer for performance enhanced  $\text{LiNi}_{0.6}\text{Co}_{0.2}\text{Mn}_{0.2}\text{O}_2$  cathode, *Nano Energy* 58 (2019) 673–679.
- [37] Y.J. Hsiao, S.C. Chang, Photoluminescent properties of  $\text{LiInO}_2$  nanocrystals, *Mater. Lett.* 65 (19–20) (2011) 2920–2922.
- [38] Y.G. Zou, H.C. Mao, X.H. Meng, Y.H. Du, H.S. Sheng, X.Q. Yu, J.L. Shi, Y.G. Guo, Mitigating the kinetic hindrance of single-crystalline Ni-rich cathode via surface gradient penetration of tantalum, *Angew. Chem.* 133 (51) (2021) 26739–26743.
- [39] L. Qiu, W. Xiang, W. Tian, C.L. Xu, Y.C. Li, Z.G. Wu, T.R. Chen, K. Jia, D. Wang, F. R. He, X.D. Guo, Polyanion and cation co-doping stabilized Ni-rich Ni-Co-Al material as cathode with enhanced electrochemical performance for Li-ion battery, *Nano Energy* 63 (2019), 103818.
- [40] H.H. Ryu, K.J. Park, D.R. Yoon, A. Aishova, C.S. Yoon, Y.K. Sun, Li  $[\text{Ni}_{0.9}\text{Co}_{0.09}\text{W}_{0.01}]\text{O}_2$ : a new type of layered oxide cathode with high cycling stability, *Adv. Energy Mater.* 9 (44) (2019) 1902698.
- [41] K.J. Park, H.G. Jung, L.Y. Kuo, P. Kaghazchi, C. Yoon, Y.K. Sun, Improved cycling stability of  $\text{Li}[\text{Ni}_{0.90}\text{Co}_{0.05}\text{Mn}_{0.05}]\text{O}_2$  through microstructure modification by boron doping for Li-ion batteries, *Adv. Energy Mater.* 8 (25) (2018) 1801202.
- [42] N.Y. Park, H.H. Ryu, G.T. Park, T.C. Noh, Y.K. Sun, Optimized Ni-rich NCMA cathode for electric vehicle batteries, *Adv. Energy Mater.* 11 (9) (2021) 2003767.
- [43] G.W. Nam, N.Y. Park, K.J. Park, J.H. Yang, J. Liu, C. Yoon, Y.K. Sun, Capacity fading of Ni-rich NCA cathodes: Effect of microcracking extent, *ACS Energy Lett.* 4 (12) (2019) 2995–3001.
- [44] X. Fan, X. Ou, W. Zhao, Y. Liu, B. Zhang, J. Zhang, Y. Yang, In situ inorganic conductive network formation in high-voltage single-crystal Ni-rich cathodes, *Nat. Commun.* 12 (1) (2021) 1–13.
- [45] S. Wang, A. Dai, Y. Cao, H. Yang, A. Khalil, J. Lu, X. Ai, Enabling stable and high-rate cycling of a Ni-rich layered oxide cathode for lithium-ion batteries by modification with an artificial  $\text{Li}^+$ -conducting cathode-electrolyte interphase, *J. Mater. Chem. A* 9 (19) (2021) 11623–11631.
- [46] F. Xin, H. Zhou, Y. Zong, M. Zuba, Y. Chen, N.A. Chernova, M.S. Whittingham, What is the role of Nb in nickel-rich layered oxide cathodes for lithium-ion batteries? *ACS Energy Lett.* 6 (4) (2021) 1377–1382.
- [47] U.H. Kim, J.H. Park, A. Aishova, R.M. Ribas, R.S. Monteiro, K.J. Griffith, Y.K. Sun, Microstructure engineered Ni-rich layered cathode for electric vehicle batteries, *Adv. Energy Mater.* 11 (25) (2021) 2100884.
- [48] C.H. Jung, D.H. Kim, D. Eum, K.H. Kim, J. Choi, J. Lee, S.H. Hong, New insight into microstructure engineering of Ni-rich layered oxide cathode for high performance lithium ion batteries, *Adv. Funct. Mater.* 31 (18) (2021) 2010095.
- [49] L.C. Zeng, K.X. Shi, B. Qiu, H.Y. Liang, J.H. Li, W. Zhao, S.L. Li, W.G. Zhang, Z. P. Liu, Q.B. Liu, Hydrophobic surface coating against chemical environmental instability for Ni-rich layered oxide cathode materials, *Chem. Eng. J.* 437 (2022) 135276.
- [50] C.F. Zhang, J.J. Wan, X. Li, S.Y. Zheng, K. Zhou, D.H. Wang, D.F. Wang, C.Y. Hong, Z.L. Gong, Y. Yang, Restraining the polarization increase of Ni-rich and low-Co cathodes upon cycling by Al-doping, *J. Mater. Chem. A* 8 (14) (2020) 6893–6901.
- [51] F.Y. Cheng, X.Y. Zhang, Y.G. Qiu, J.X. Zhang, Y. Liu, P. Wei, M.Y. Ou, S.X. Sun, Y. Xu, Q. Li, C. Fang, J.T. Han, Y.H. Huang, Tailoring electrolyte to enable high-rate and super-stable Ni-rich NCM cathode materials for Li-ion batteries, *Nano Energy* 88 (2021), 106301.
- [52] L. Zou, J. Li, Z. Liu, G. Wang, A. Manthiram, C. Wang, Lattice doping regulated interfacial reactions in cathode for enhanced cycling stability, *Nat. Commun.* 10 (1) (2019) 1–11.
- [53] P. Wang, H. Li, Y. Wei, D. Zhao, L. Mao, X. Cui, S. Li, Truncated octahedral  $\text{LiNi}_{0.5}\text{Mn}_{1.5}\text{O}_4$  with excellent electrochemical properties for lithium-ion batteries prepared by a graphite assisted calcination method, *New J. Chem.* 43 (38) (2019) 15396–15404.
- [54] S. Yang, Q. Fan, Z. Shi, L. Liu, J. Liu, X. Ke, Z. Guo, Superior stability secured by a four-phase cathode electrolyte interface on a Ni-rich cathode for lithium ion batteries, *ACS Appl Mater Inter.* 11 (40) (2019) 36742–36750.
- [55] S.H. Song, M. Cho, I. Park, J.G. Yoo, K.T. Ko, J. Hong, J. Kim, S.K. Jung, M. Avdeev, S. Ji, S. Lee, J. Bang, H. Kim, High-voltage-driven surface structuring and electrochemical stabilization of Ni-rich layered cathode materials for Li rechargeable batteries, *Adv. Energy Mater.* 10 (23) (2020) 2000521.
- [56] Q.M. Gan, N. Qin, Z.Y. Wang, Z.Q. Li, Y.H. Zhu, Y.Z. Li, S. Gu, H.M. Yuan, W. Luo, L. Lu, Z.H. Xu, Z.G. Lu, Revealing mechanism of  $\text{Li}_3\text{PO}_4$  coating suppressed surface oxygen release for commercial Ni-rich layered cathodes, *ACS Appl Energy Mater.* 3 (8) (2020) 7445–7455.
- [57] X.M. Fan, G.R. Hu, B. Zhang, X. Ou, J.F. Zhang, W.B. Zhao, H.P. Jia, L.F. Zou, P. Li, Y. Yang, Crack-free single-crystalline Ni-rich layered NCM cathode enable superior cycling performance of lithium-ion batteries, *Nano Energy* 70 (2020), 104450.
- [58] F. Wu, J.Y. Dong, L. Chen, L.Y. Bao, N. Li, D.Y. Cao, Y. Lu, R.X. Xue, N. Liu, L. Wei, Z.R. Wang, S. Chen, Y.F. Su, High-voltage and high-safety nickel-rich layered cathode enabled by a self-reconstructive cathode/electrolyte interphase layer, *Energy Storage Mater.* 41 (2021) 495–504.
- [59] J. Yu, J.L. Zhang, Y.Y. Zhang, Z.H. Wang, Z.J. Chen, A.M. Gao, J.F. Zhang, Y. Wang, R.R. Zhao, Electrostatic adsorption facilitating dual-layer coating for stabilized cathode-electrolyte interphases and boosted lithium intercalation thereof in  $\text{LiNi}_{0.8}\text{Co}_{0.1}\text{Mn}_{0.1}\text{O}_2$  cathode, *Appl Surface Sci.* 577 (2022), 151716.
- [60] Q.H. Li, Y. Wang, X.L. Wang, X.R. Sun, J.N. Zhang, X.Q. Yu, H. Li, Investigations on the fundamental process of cathode electrolyte interphase formation and evolution of high-voltage cathodes, *ACS Appl. Mater. Inter.* 12 (2) (2020) 2319–2326.
- [61] Y.G. Zou, F. Meng, D.D. Xiao, H. Sheng, W.P. Chen, X.H. Meng, Y.H. Du, L. Gu, J. L. Shi, Y.G. Guo, Constructing a stable interfacial phase on single-crystalline Ni-rich cathode via chemical reaction with phosphomolybdic acid, *Nano Energy* 87 (2021), 106172.
- [62] J. Ahn, J. Im, H. Seo, S. Yoon, K.Y. Cho, Enhancing the cycling stability of Ni-rich  $\text{LiNi}_{0.83}\text{Co}_{0.11}\text{Mn}_{0.06}\text{O}_2$  cathode at 4.5 V via 2,4-difluorobiphenyl additive, *J. Power Sources* 512 (2021), 230513.
- [63] Z. Feng, R. Rajagopalan, S. Zhang, D. Sun, Y.G. Tang, Y. Ren, H.Y. Wang, A Three in one strategy to achieve zirconium doping, boron doping, and interfacial coating for stable  $\text{LiNi}_{0.8}\text{Co}_{0.1}\text{Mn}_{0.1}\text{O}_2$  cathode, *Adv. Sci.* 8 (2) (2021) 2001809.
- [64] S. Gao, X.W. Zhan, Y.T. Cheng, Structural, electrochemical and Li-ion transport properties of Zr-modified  $\text{LiNi}_{0.8}\text{Co}_{0.1}\text{Mn}_{0.1}\text{O}_2$  positive electrode materials for Li-ion batteries, *J. Power Sources* 410 (2019) 45–52.
- [65] B. Han, S. Xu, S. Zhao, G.X. Lin, Y.Z. Feng, L.B. Chen, D.G. Ivey, P. Wang, W.F. Wei, Enhancing the structural stability of Ni-rich layered oxide cathodes with a preformed Zr-concentrated defective nanolayer, *ACS Appl. Mater. Inter.* 10 (46) (2018) 39599–39607.
- [66] Z.C. Ye, L. Qiu, W. Yang, Z.G. Wu, Y.X. Liu, G.K. Wang, Y. Song, B.H. Zhong, X. D. Guo, Nickel-rich layered cathode materials for lithium-ion batteries, *Chem-Eur J.* 27 (13) (2021) 4249–4269.
- [67] P. Hou, J.M. Yin, M. Ding, J.Z. Huang, X.J. Xu, Surface/interfacial structure and chemistry of high-energy nickel-rich layered oxide cathodes: Advances and Perspectives, *Small* 13 (45) (2017) 1701802.
- [68] S.W. Li, Z.P. Liu, Y. Lu, X. Shen, Q.Y. Liu, Z.W. Hu, Q.Y. Kong, J. Ma, J.D. Li, H. J. Lin, C.T. Chen, X.F. Wang, R.C. Yu, Z.X. Wang, L.Q. Chen, Anionic redox reaction and structural evolution of Ni-rich layered oxide cathode material, *Nano Energy* 98 (2022), 107335.
- [69] C.G. Shi, X.X. Peng, P. Dai, P.H. Xiao, W.C. Zheng, H.Y. Li, H. Li, S. Indris, S. Mangold, Y.H. Hong, C.X. Luo, C.H. Shen, Y.M. Wei, L. Huang, S. g., Sun, investigation and suppression of oxygen release by  $\text{LiNi}_{0.8}\text{Co}_{0.1}\text{Mn}_{0.1}\text{O}_2$  cathode under overcharge conditions, *Adv. Energy Mater.* 12 (20) (2022) 2200569.





# B<sub>2</sub>O<sub>3</sub>/LiBO<sub>2</sub> dual-modification layer stabilized Ni-rich cathode for lithium-ion battery

Yao Lv<sup>a,b</sup>, Shifei Huang<sup>b,c</sup>, Sirong Lu<sup>d</sup>, Wenbo Ding<sup>c</sup>, Xiaoliang Yu<sup>e</sup>, Gemeng Liang<sup>f</sup>, Jinshuo Zou<sup>f</sup>, Feiyu Kang<sup>b,c</sup>, Jiujuan Zhang<sup>a,\*\*</sup>, Yidan Cao<sup>b,c,\*</sup>

<sup>a</sup> College of Sciences and Institute for Sustainable Energy, Shanghai University, Shanghai, China

<sup>b</sup> Institute of Materials Research, Shenzhen International Graduate School, Tsinghua University, Shenzhen, China

<sup>c</sup> Tsinghua-Berkeley Shenzhen Institute, Tsinghua University, Shenzhen, China

<sup>d</sup> Shenzhen Institute for Quantum Science and Engineering, Southern University of Science and Technology, Shenzhen, China

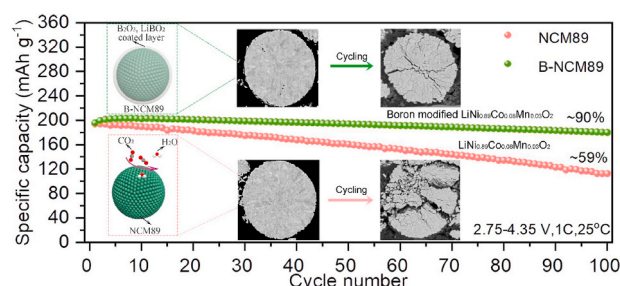
<sup>e</sup> Department of Mechanical Engineering, The Hong Kong Polytechnic University, Hong Kong, China

<sup>f</sup> School of Chemical Engineering & Advanced Materials, The University of Adelaide, Adelaide, SA, 5005, Australia

## HIGHLIGHTS

- Ni-rich cathode with B<sub>2</sub>O<sub>3</sub>/LiBO<sub>2</sub> dual-modification layer is synthesized.
- The boron modification effectively reduces residual lithium.
- The modification effectively prohibits side reactions and facilitate stable CEI.
- Severe lattice changes and particle rupture are avoided in modified cathode.

## GRAPHICAL ABSTRACT



## ARTICLE INFO

### Keywords:

Ni-rich layered oxide  
Interfacial stability  
Capacity degradation  
Dual-modification layer  
Boron  
Structural stability

## ABSTRACT

Ni-rich layered oxide material with high theoretical capacity and low cost is one of the most promising cathode candidates for high-energy-density lithium-ion battery. However, increase of Ni content triggers structural instability and fast capacity degradation, which severely impedes the practical application of Ni-rich materials. Here, a surface dual-modification layer of B<sub>2</sub>O<sub>3</sub> & LiBO<sub>2</sub> is introduced to Ni-rich material LiNi<sub>0.89</sub>Co<sub>0.08</sub>Mn<sub>0.03</sub>O<sub>2</sub> (NCM89), which successfully stabilizes the layered structure of NCM89 during cycling as well as removes residual lithium in NCM89. The in-situ X-ray diffraction and cross-sectional scanning electron microscopy results demonstrate effectively improved structural reversibility and stability of the cathode. Moreover, the dissolution of transition metals and decomposition of electrolyte at the cathode/electrolyte interface are successfully suppressed, resulting in beneficial cathode electrolyte interphase (CEI) layer. As a result, the boron modified cathode exhibits a high capacity of 180.4 mAh g<sup>-1</sup> along with an excellent capacity retention of 90% after 100 cycles at 1C in 2.75–4.35 V at 25 °C, while the pristine NCM89 cathode only retains 59% of its initial capacity after 100 cycles. Furthermore, the capacity retention of full cell after 350 cycles is improved from 52.5% to 90%.

\* Corresponding author. Institute of Materials Research, Shenzhen International Graduate School, Tsinghua University, Shenzhen, China.

\*\* Corresponding author.

E-mail addresses: [jiujuan.zhang@i.shu.edu.cn](mailto:jiujuan.zhang@i.shu.edu.cn) (J. Zhang), [yidanco@sz.tsinghua.edu.cn](mailto:yidanco@sz.tsinghua.edu.cn) (Y. Cao).

## 1. Introduction

Growing markets of portable electronics and electric vehicles create tremendous demand for advanced lithium ion batteries (LIBs) with high power and energy density, and developing battery electrodes with high capacity and energy density is one of the keys for next-generation LIBs [1–6]. Ni-rich cathode material has attracted extensive attention owing to its superior theoretical capacity ( $>200 \text{ mA g}^{-1}$ ) [7] and energy density ( $\sim 800 \text{ Wh kg}^{-1}$ ) [8]. Besides, it has impressive performance in achieving capacity at high voltage range ( $>4.3 \text{ V}$ ) and reducing the usage of cobalt metals to reduce cathode cost [9]. However, Ni-rich cathode material suffers from some critical problems which impede its application [10]. The Ni-rich cathodes have a high affinity to  $\text{H}_2\text{O}$  and  $\text{CO}_2$  in the atmosphere [11], and the surface remaining lithium oxides ( $\text{Li}_2\text{O}$ ,  $\text{Li}_2\text{O}_2$ , etc) would react with  $\text{H}_2\text{O}$  and  $\text{CO}_2$  in the air and generate lithium compounds ( $\text{LiOH}$  and  $\text{Li}_2\text{CO}_3$ ), which is commonly referred to as “residual lithium” [12]. The residual lithium ( $\text{LiOH}$  and  $\text{Li}_2\text{CO}_3$ ) on the surface result in potential safety issues, such as  $\text{CO}_2$  generation during lithiation and  $\text{O}_2$  release during delithiation, which not only deteriorates the electrochemical performance but also could cause catastrophic thermal runaway even explosion [13]. In addition, the direct contact between the cathode and electrolyte causes parasitic interfacial reactions, including severe depletion of electrolyte [14], production of gases [15], element dissolution of Ni/Co/Mn [16], and highly resistive cathode electrolyte interphase (CEI) layer. These are the main causes of the structural instability, cracks generation and capacity degradation of Ni-rich cathodes [17]. Stabilizing the lattice structure and alleviating parasitic reactions would benefit the long-term cyclability of Ni-rich cathodes.

Surface coating of Ni-rich cathode materials can effectively improve the chemical and structural stability, and then enhance the electrochemical performance. Inorganic oxides ( $\text{ZrO}_2$  [18],  $\text{TiO}_2$  [19],  $\text{MgO}$  [20],  $\text{Al}_2\text{O}_3$  [21],  $\text{SiO}_2$  [22],  $\text{CeO}_2$  [23]) have been widely investigated as surface coatings for Ni-rich cathodes. The inorganic oxide coating can form a stable interface layer between the cathode and the electrolyte, reducing the occurrence of side reactions and enhancing the structural stability of the cathodes [24]. Strategies that utilize chemical compounds to react with residual lithium ( $\text{LiOH}$  and  $\text{Li}_2\text{CO}_3$ ) on the surface of Ni-rich cathodes have also been reported. For example, Zhu et al. [25] reported a  $\text{Li}_3\text{PO}_4$  coating layer to reduce the contents of surface residual lithium through the reaction between surface residual lithium and  $(\text{NH}_4)_2\text{HPO}_4$ . Similarly,  $\text{Li}_4\text{SiO}_4$  with a small amount of Al was introduced to modify  $\text{LiNi}_{0.8}\text{Co}_{0.15}\text{Al}_{0.05}\text{O}_2$  by wet-chemical and solid-state methods, leading to improved rate and cycle performance [11]. Recently, Liu et al. [26] reported a dual-modified approach to in-situ synthesize an  $\text{In}_2\text{O}_3$  &  $\text{LiInO}_2$  layer on the surface of Ni-rich cathodes, which can improve the stability of Ni-rich cathode and reduce lithium impurity on the surface of the material. Despite all the progress, it is still challenging and critical to seek for appropriate modification material for Ni-rich cathode in practical LIBs.

Herein, we report a facile wet coating strategy to synthesize dual-modification layer of  $\text{B}_2\text{O}_3$  &  $\text{LiBO}_2$  on the Ni-rich oxide materials ( $\text{LiNi}_{0.89}\text{Co}_{0.08}\text{Mn}_{0.03}\text{O}_2$ , NCM89). With the help of chemical titration, in-situ X-ray diffraction (XRD) and XPS analysis, etc., it is found that the modification effectively reduces residual lithium, enhances the structural integrity of the NCM89, and improves the cathode/electrolyte interfacial stability. The  $\text{B}_2\text{O}_3$  &  $\text{LiBO}_2$  dual-modifications prohibit successive side reactions between the cathode and electrolyte. Structures of the cathode can be well maintained without any severe irreversible phase transitions and particle ruptures. As a result, the boron modified  $\text{LiNi}_{0.89}\text{Co}_{0.08}\text{Mn}_{0.03}\text{O}_2$  (hereafter termed as B-NCM89) delivers a high capacity of  $180.4 \text{ mA/g}$  at  $1\text{C}$  with  $90\%$  capacity retention after 100 cycles. In full cell paired with graphite, the capacity retention is improved from  $52.5\%$  (NCM89) to  $90\%$  (B-NCM89) after 350 cycles.

## 2. Experimental section

### 2.1. Materials preparation

$\text{Ni}_{0.887}\text{Co}_{0.09}\text{Mn}_{0.04}(\text{OH})_2$  precursor (Shaanxi Coal & Chemical Industry) was mixed with  $\text{LiOH}\cdot\text{H}_2\text{O}$  (Aladdin, analytical grade,  $98\%$ ) in a molar ratio of  $1:1.03$ , and then calcined at  $740^\circ\text{C}$  for  $9 \text{ h}$  in oxygen flow to get  $\text{LiNi}_{0.89}\text{Co}_{0.08}\text{Mn}_{0.03}\text{O}_2$  (NCM89).  $1 \text{ wt}\%$   $\text{B}(\text{OH})_3$  (Macklin, analytical grade,  $99.9\%$ ) was dissolved into the anhydrous ethanol solution and then NCM89 was added into the above solution. The mixture was continuously stirred at  $80^\circ\text{C}$  until the solvent was completely evaporated. The obtained product was calcined at  $300^\circ\text{C}$  for  $10 \text{ h}$  in oxygen flow to get the desired boron modified NCM89 (B-NCM89).

### 2.2. Material characterization

The crystalline structure of the samples was characterized by X-ray diffractometer (XRD Bruker D8 Advance) with  $\text{Cu-K}\alpha$  radiation ( $\lambda = 1.5406 \text{ \AA}$ ) in the  $2\theta$  range of  $10^\circ$ – $80^\circ$  at a step rate of  $5^\circ \text{ min}^{-1}$ . The Rietveld refinement was performed using the GSAS software. Surface morphology and cross-sections of the cathodes polished by argon ion milling (IB–19530CB, JEOL) were characterized under a SEM (HITACHI SU8010) equipped with an EDS detector. The surface chemistry of the samples were characterized by X-ray photoelectron spectroscopy (XPS) on an ESCALAB250Xi spectrometer with  $\text{Al K}\alpha$  radiation source ( $1486.6 \text{ eV}$ ). The residual lithium content of both samples were determined by a chemical titration method. Briefly,  $1 \text{ g}$  of cathode material was added to  $100 \text{ mL}$  ( $A_1$ ) of de-ionized water and then stirred for  $5 \text{ min}$ . Afterwards, the resulting suspension was filtered through a vacuum filtration system.  $50 \text{ mL}$  ( $A_2$ ) of the filtered solution was titrated with  $0.05 \text{ M}$   $\text{HCl}$  solution with methyl orange and phenolphthalein as indicators. When phenolphthalein changed color, the reaction was suspended and the added volume of  $\text{HCl}$  was marked as  $V_1$ . The reaction in this process was  $\text{LiOH} + \text{HCl} = \text{LiCl} + \text{H}_2\text{O}$  and  $\text{Li}_2\text{CO}_3 + \text{HCl} = \text{LiHCO}_3 + \text{LiCl}$ . As the methyl orange changed color again, the reaction was terminated, and the used volume of  $\text{HCl}$  was labeled as  $V_2$ . The reaction in this process was  $\text{LiHCO}_3 + \text{HCl} = \text{LiCl} + \text{H}_2\text{O}$ . The contents of the residual lithium compounds can be calculated based on the consumed amount of  $\text{HCl}$  solution with the formula below:

$$\text{LiOH (wt.\%)} = \frac{(2V_1 - V_2) \times C_{\text{HCl}} \times M_{\text{LiOH}}}{1000 \times W} \times \frac{A_1}{A_2} \times 100(\text{wt.\%}) \quad (1)$$

$$\text{Li}_2\text{CO}_3 \text{ (wt.\%)} = \frac{(V_2 - V_1) \times C_{\text{HCl}} \times M_{\text{Li}_2\text{CO}_3}}{1000 \times W} \times \frac{A_1}{A_2} \times 100(\text{wt.\%}) \quad (2)$$

$$\text{Li (ppm)} = (\text{Li}_2\text{CO}_3\% \times 0.1879 + \text{LiOH}\% \times 0.29) \times 10000 \quad (3)$$

### 2.3. Electrochemical measurements

The cathode slurries were prepared by mixing the active material, carbon black (super-P), and polyvinylidene fluoride (PVDF) (weight ratio =  $8:1:1$ ) in N-methyl-2-pyrrolidone (NMP). The slurries were coated onto Al foil with an active material loading of  $3\text{--}5 \text{ mg cm}^{-2}$  and then dried in a vacuum oven at  $120^\circ\text{C}$  for  $12 \text{ h}$ .  $1.2 \text{ M}$   $\text{LiPF}_6$  in ethylene carbonate (EC)/ethylmethyl carbonate (EMC) ( $3:7$  by weight) with  $2 \text{ wt}\%$  vinylene carbonate (VC) was used as electrolyte. The CR2032 half cells were assembled in an Ar-filled glove box (both  $\text{O}_2$  and  $\text{H}_2\text{O}$  levels below  $0.01 \text{ ppm}$ ) using Li-metal, Celgard 2325 separator, electrolyte and cathode electrode. Cells were cycled galvanostatically with Land (CT3001A, Wuhan) between  $2.75 \text{ V}$  and  $4.35 \text{ V}$  at  $\text{C}/2$  or  $1\text{C}$  rate with a trickle charge at  $4.35 \text{ V}$ . The rate capability was evaluated by cycling at various rates ( $\text{C}/5$ ,  $\text{C}/2$ ,  $1\text{C}$ ,  $2\text{C}$ ,  $5\text{C}$ ,  $10\text{C}$ , and  $15\text{C}$ ) for  $5$  cycles respectively. Electrochemical impedance spectroscopy (EIS) was measured by using a CHI760 electrochemical workstation with the frequency from  $0.01 \text{ Hz}$  to  $1 \text{ M Hz}$  and with a  $5 \text{ mV}$  amplitude by using half cells before

and after cycles. The electrode was equilibrated for 1 h before the EIS measurements, and the impedance data were analyzed using Z-view software. For the galvanostatic intermittent titration technique (GITT) measurement, a 600 s galvanostatic discharge pulse (C/10) was applied, followed by an open-circuit relaxation of 3600 s. The galvanostatic discharge pulse and relaxation test were maintained until the cutoff voltage of 2.75 V. The diffusion coefficient was calculated according to equation.

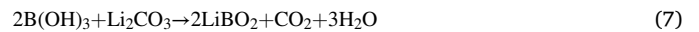
$$D = \frac{4}{\pi\tau} \left( \frac{m_B V_M}{M_B S} \right)^2 \left( \frac{\Delta E_s}{\Delta E_t} \right)^2 \quad (4)$$

where  $\tau$  is the time of the galvanostatic current pulses,  $S$  represents the contact area between the active material and electrolyte,  $\Delta E_t$  is the change of the transient potential before and after the current pulses, and  $\Delta E_s$  is the change of the steady-state voltage. In addition,  $V_M$ ,  $M_B$  and  $m_B$  are the molar volume, molar mass and mass of the electrode material, respectively. Full cells were cycled at 1C between 2.7 and 4.2 V at 25 °C with a constant current-constant voltage charging mode.

### 3. Result and discussion

#### 3.1. Microstructure of the materials

The schematics in Fig. 1a illustrate the formation process of the dual-modification layer on the NCM89.  $B(OH)_3$  was introduced followed by pyrolysis to establish the modification layer on the NCM89 material. The amount of  $LiOH$  (Fig. S1) is decreased by  $\sim 9.8\%$ , with an obvious drop of  $Li_2CO_3$  content by  $\sim 44.1\%$ , due to the reaction between  $B(OH)_3$  and residual lithium compounds. Dual-modification layer of  $LiBO_2$  &  $B_2O_3$ , which will be further characterized below, on the surface of NCM89 material is expected through the following reactions (5)–(7).



The SEM images in Fig. 1b and c and Fig. 1e and f displays that both NCM89 and B-NCM89 have spherical secondary particles with a diameter of  $\sim 10 \mu m$ , consisting of  $\sim 500$  nm primary particles. It demonstrates that the microstructure of NCM89 is well maintained after the introduction of boron species. The HRTEM images of NCM89 and B-NCM89 are shown in Fig. 1d, g. The interplanar spacing in Fig. 1d is

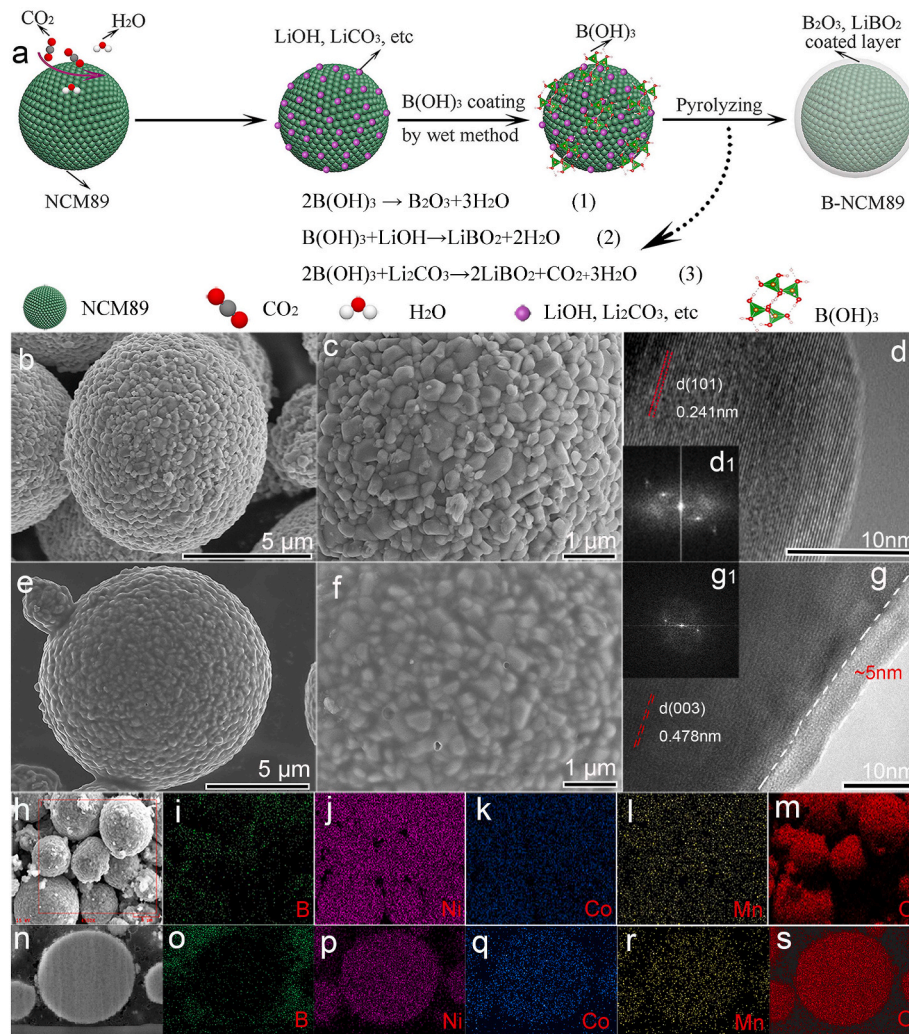


**Fig. 1.** (a) Schematic illustration of the formation of  $B_2O_3$  &  $LiBO_2$  dual-modification layer on NCM89. (b–c) SEM images of NCM89. (d) HRTEM images of NCM89 and corresponding FFT pattern (inset d1). (e–f) SEM images of B-NCM89. (g) HRTEM images of B-NCM89 and corresponding FFT pattern (inset g1). (h–m) EDS mapping of B, Ni, Co, Mn and O in B-NCM89. (n–s) EDS mapping of the cross-sectional structure of B, Ni, Co, Mn and O in B-NCM89.



0.241 nm, which is the (101) plane of NCM89. The interplanar spacing in Fig. 1g is 0.478 nm, which is the (003) plane of B-NCM89. Compared to NCM89, an amorphous layer with an average thickness of  $\sim 5$  nm disperses on the surface of B-NCM89, suggesting the existence of modification layer on the surface of NCM89 particles. The EDS mapping images in Fig. 1h–m shows a homogeneous distribution of the B, Ni, Co, Mn and O elements on the surface of B-NCM89. In addition, the EDS mapping (Fig. 1n–s) of the cross sections of B-NCM89 demonstrate that boron species mainly exists on the surface layer.

The structure of the NCM89 and B-NCM89 was characterized by XRD (Fig. 2a–c). The diffraction peaks in NCM89 and B-NCM89 belong to the rhombohedral  $\alpha$ -NaFeO<sub>2</sub> structure with the space group of  $R\bar{3}m$ , and there is not any extra impurity peak. Both of them show clear peak splittings around 37.5–39.0° and 64.0–65.5°, which are corresponding to (006)/(102) and (018)/(110), respectively. The peak splitting suggests both samples have high crystallinity and well-formed layered structure [27]. The Rietveld refinement results of NCM89 and B-NCM89 are shown in Fig. 2d and e with the lattice parameters listed in Table S1. The  $c/a$  value of both samples is greater than 4.9 and the intensity ratio of (003)/(104) peaks is greater than 1.2, which indicates that both samples have highly ordered layered structure and low degree of Li/Ni cation mixing [14,28]. There is no obvious change of the lattice parameters, and the unit cell volume of B-NCM89 is comparable to that of NCM89, suggesting that boron species mainly exist on the surface rather

than occupy the NCM89 lattice. Deconvoluted XPS spectra of B1s, C1s, O1s, Ni2p shown in Fig. 2f–i provide more information about the surface chemistry of the NCM89 and B-NCM89. The peaks at 191.7 eV and 192.7 eV corresponding to LiBO<sub>2</sub> and B<sub>2</sub>O<sub>3</sub> species [29,30], respectively, are observed in B 1s spectra in B-NCM89 (Fig. 2f), consistent with equations (5–7). The C1s spectra consist of peaks corresponding to CO<sub>3</sub><sup>2-</sup> (288.8 eV), C–O (286.6 eV) and C–C (284.7 eV) [31]. The contribution of CO<sub>3</sub><sup>2-</sup> is decreased from 16.4% to 13.7% with boron addition (Fig. 2g), confirming the reduced amount of Li<sub>2</sub>CO<sub>3</sub> on the surface of the B-NCM89 cathode [32], which agrees well with the chemical titration results. The O 1s spectra in Fig. 2h include peaks corresponding to the O<sub>impurity</sub> (531.1 eV) and O<sub>lattice</sub> (528.7 eV) [33]. The O<sub>impurity</sub> mainly relates to the reactive oxygen species including O<sup>-</sup>, O<sup>2-</sup> and CO<sub>3</sub><sup>2-</sup> in LiOH/Li<sub>2</sub>CO<sub>3</sub> [34]. The O<sub>lattice</sub> is derived from lattice oxygen O<sup>2-</sup> in M–O (M = Ni, Co, Mn) bond. The amount of oxygen impurities is greatly reduced (84.3%→77.5%) by boron modification, which aligns with the reduced amount of residual lithium by chemical titration and C 1s spectra. Meanwhile, Fig. 2i demonstrates that more Ni<sup>3+</sup> appears on the surface of B-NCM89 than on NCM89, which could be related to the electron-deficient property of boron. The increased content of Ni<sup>3+</sup> has been proved to be beneficial to promote the structural stability of Ni-rich cathodes [35].

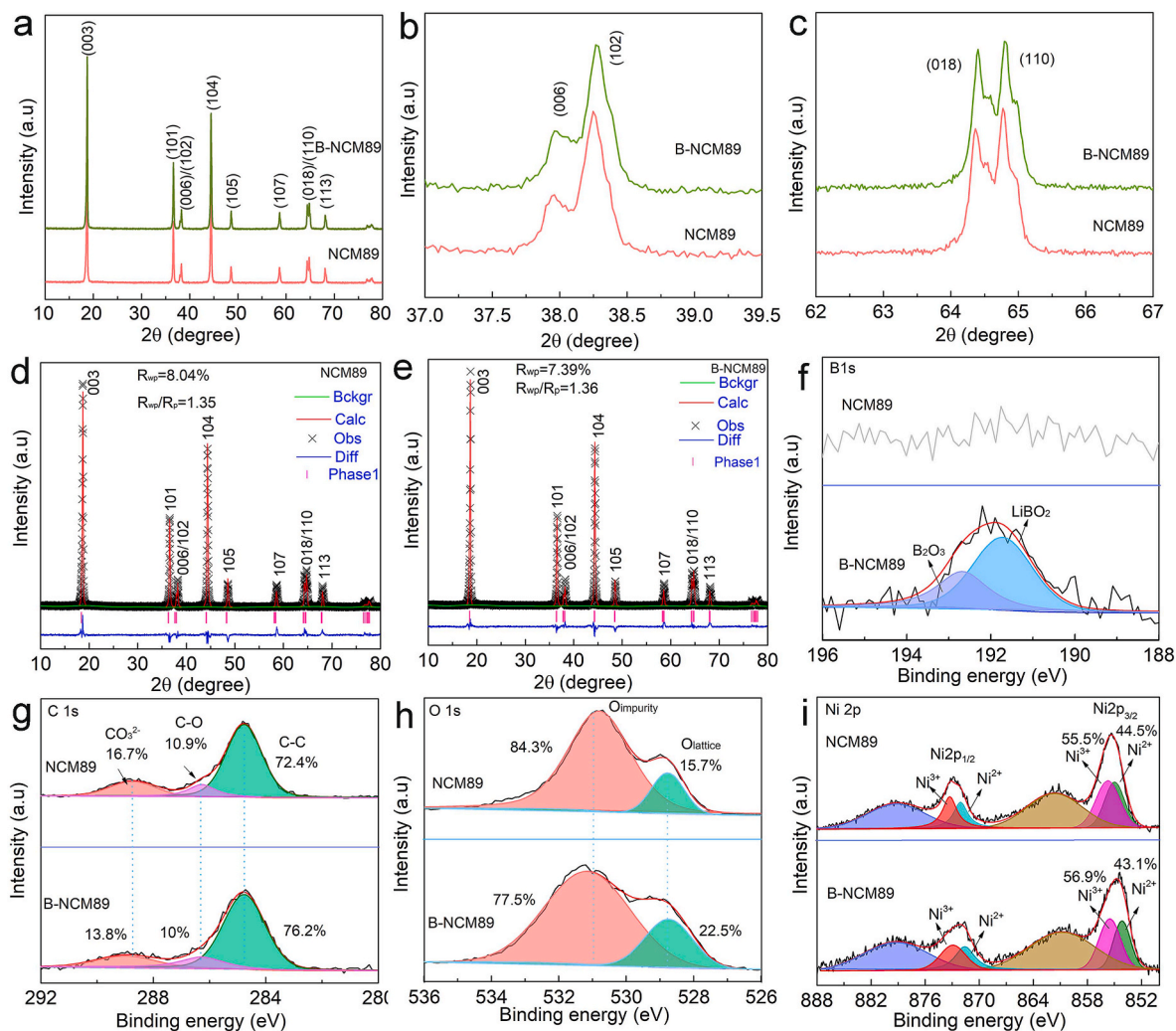


**Fig. 2.** (a–c) XRD results of NCM89 and B-NCM89. (d–e) Rietveld XRD refinement of NCM89 and B-NCM89. (f–i) XPS spectra of B1s (f), C1s (g), O1s (h), Ni2p (i) in NCM89 and B-NCM89.



### 3.2. Electrochemical performance

Electrochemical performance of the NCM89 and B-NCM89 were evaluated in both half cells (vs  $\text{Li}/\text{Li}^+$ ) and full cells (vs graphite), and the results are shown in Fig. 3. Fig. 3a and b shows the voltage curves of the NCM89 and B-NCM89 over the cycling of 100 cycles at 1C. During the initial cycle, both samples clearly display voltage plateaus corresponding to H1–H2–H3 phase transitions. However, the plateaus of NCM89 decay much more rapidly than those of B-NCM89 over cycling, especially for the H2–H3 phase transition plateau around  $\sim 4.2$  V which almost disappears after 100 cycles in NCM89. The rapid fade in voltage profiles results from the increase in impedance upon cycling, which may be related to the transition metal dissolution and the thickening of CEI layers (further discussion in the following section) [36]. The average voltage difference between the charge and discharge voltages in NCM89 is 0.7404 V, which is much higher than the 0.1982 V in B-NCM89 after 100 cycles. Compared to NCM89, the voltage curves of the B-NCM89 remain stable even after 100 cycles with slight changes, suggesting a quite small increase of impedance in B-NCM89 and much better structural stability over NCM89. In addition, it should be noted that the current gradually decreases in the process of trickle charge (i.e. constant voltage charge at 4.35 V), as a result, the capacity loss caused by polarization can be partially restored and a platform presents at 4.35 V in the voltage curves. This constant voltage platform is related to the overpotential generated by the electrode polarization. The capacity change related to this platform in Fig. 3a is  $19.7 \text{ mA g}^{-1}$  after 10 cycles and  $40.1 \text{ mAh g}^{-1}$  after 100 cycles, respectively, indicating severe electrode polarization in NCM89 cathode after cycles. By contrast, the

platforms account for only  $4 \text{ mA g}^{-1}$  after 10 cycles and  $27.9 \text{ mA g}^{-1}$  after 100 cycles (Fig. 3b) in the B-NCM89 cathode, which suggests that the introduction of B in the Ni-rich cathodes can effectively alleviate the increase of electrode polarization. Charge/discharge voltage profiles at 0.5C are shown in Fig. S2 and demonstrate a similar trend to those in Fig. 3a and b).

Corresponding differential capacity curves were plotted in Fig. 3c–d and Fig. S3 to further understand the redox reactions and the phase transitions in NCM89 and B-NCM89 during cycling. As shown in Fig. 3c and d, both of the NCM89 and the B-NCM89 profiles consist of three pairs of redox peaks, which are associated with a series of phase transitions in NCM materials through hexagonal (H1)  $\rightarrow$  monoclinic (M)  $\rightarrow$  hexagonal (H2)  $\rightarrow$  hexagonal (H3) during charging (delithiation) and the transitions in reverse order during discharging (lithiation) [3,27]. The redox peaks around 4.1–4.35 V are related to the H2–H3 phase transition, which is known to be responsible for capacity fading [37,38]. The final H2  $\rightarrow$  H3 phase transition leads to a sudden contraction of the unit cell in the c-direction, as a result, the cathode materials are subjected to a mechanically strained state that subsequently deteriorates its rechargeability. The delithiation peaks of the NCM89 gradually attenuate with cycling and the delithiation/lithiation voltage polarization increases, especially for the H2  $\rightarrow$  H3 phase transition. The phase transition peaks of the NCM89 totally distort after 100 cycles, indicating poor reversibility, which is consistent with the voltage profiles. The decay and distortion of the redox peaks are due to the deteriorating reversibility of the cathode, which is likely caused by the structural degradation of the cathode arising from the H2  $\rightarrow$  H3 phase transition. By contrast, the reversibility of the redox peaks and phase transitions in the

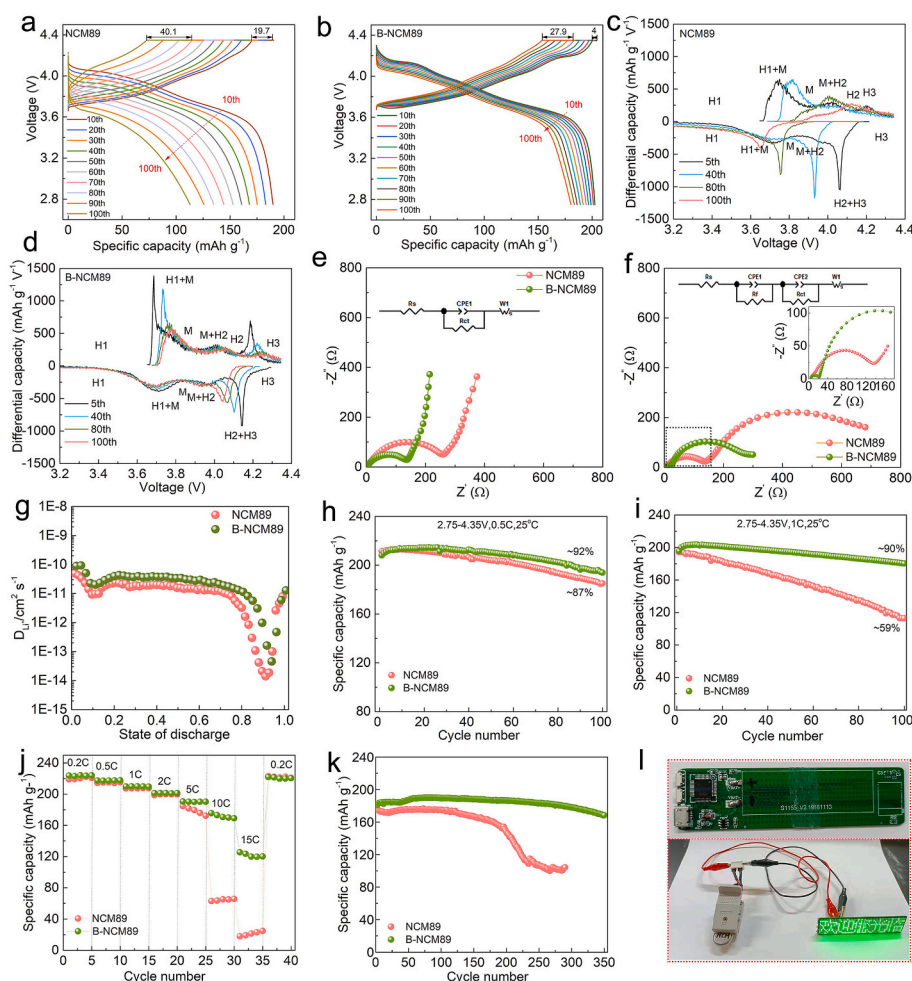


**Fig. 3.** (a–d) Voltage curves (a–b) and corresponding differential capacity profiles (c–d) of NCM89 and B-NCM89 at 1C. (e–f) Nyquist plots of NCM89 and B-NCM89 cathodes before (e) and after (f) 100 cycles. (g)  $\text{Li}^+$  diffusion coefficient ( $D_{\text{Li}^+}$ ) of the NCM89 and B-NCM89 as function of the state of discharge. (h–i) Cycling performance of NCM89 and B-NCM89 at 0.5C (h) and 1C (i) in the range of 2.75–4.35 V. (j) Rate performance of NCM89 and B-NCM89 in the range of 2.75–4.35 V. (k) Cycling performance of NCM89 and B-NCM89 in full cell with graphite anode cycled between 2.7 and 4.2 V at 1C. (l) Light plate demonstration powered by a full cell with B-NCM89.

B-NCM89 is well maintained during cycling with only slight increased delithiation/lithiation voltage polarizations, indicating an increased structural stability of the cathode by boron modification.

EIS measurement for as-prepared and cycled cathodes was carried out to further understand the relationship between the electrochemical degradation and the interfacial evolutions during cycling. Fig. 3e and f shows the Nyquist plots of the electrodes and corresponding equivalent circuits at the fresh cells and after 100 cycles. For the as-prepared cells, the intercepts at high frequency, which are assigned to the solution resistance ( $R_s$ ), for NCM89 and B-NCM89 are comparable (2.83  $\Omega$  and 3.11  $\Omega$ , respectively). The semicircle is related to the charge transfer resistance ( $R_{ct}$ ) and the followed slope line relates to the Warburg impedance ( $Z_w$ ) [39]. The charge transfer resistance is reduced from 247.4  $\Omega$  to 137.8  $\Omega$  due to the boron modification, indicating that the surface modification layer can facilitate the interfacial charge transfer to some extent. After cycling, as shown in Fig. 3f, an increased semicircle in the high-frequency region arises, which can be ascribed to the interfacial resistance ( $R_f$ ) due to the formation of cathode electrolyte interphase (CEI) layer during cycling [40]. There is no obvious change of the internal solution resistance after cycling. The CEI resistance (inset in Fig. 3f,  $R_f$ ) is greatly reduced from 157.3  $\Omega$  to 22.53  $\Omega$  due to the boron modification, indicating that a more conductive CEI layer is formed in B-NCM89. The  $R_{ct}$  of NCM89 increases dramatically to 643.6  $\Omega$ , which is way higher than that of the B-NCM89 (276.5  $\Omega$ ), implying the better structural stability with the boron modification. Additionally, the mass transfer controlled low-frequency regions in the fresh cells indicate a faster kinetic in the boron modified B-NCM89 case. The diffusion behavior of  $\text{Li}^+$  in both samples were further evaluated by galvanostatic intermittent titration technique (GITT). GITT results (Fig. 3g, GITT discharge curves of both samples are plotted in Fig. S4) demonstrate that the NCM89 and B-NCM89 show a similar change in conductivity magnitude. The  $D_{\text{Li}}^+$  values in the B-NCM89 are higher than those in the NCM89, indicating that the introduction of B facilitates the migration and diffusion of lithium ions at the cathode/electrolyte interface, in accordance with the EIS results in Fig. 3e. As demonstrated above, B(OH)<sub>3</sub> transforms to  $\text{B}_2\text{O}_3$  and  $\text{LiBO}_2$  after reacting with surface lithium residuals, and the formed modification layer would remarkably improve the ionic conductivity and reduce the impedance increase during cycling. The GITT and EIS results demonstrate that the B-NCM89 exhibit better kinetic behavior, which can be related to the outstanding structural stability by the modification of boron species.

Fig. 3h and i shows the cycling performance of NCM89 and B-NCM89 material. Upon cycling at 0.5C, the B-NCM89 delivers a high discharge capacity of 193  $\text{mA g}^{-1}$  and capacity retention of 92% after 100 cycles, superior to the 184  $\text{mA g}^{-1}$  and 87% of NCM89. Additionally, the B-NCM89 cathode retains 90% of its initial capacity after 100 cycles at 1C (180.4  $\text{mA g}^{-1}$ ), much higher than 59% of the NCM89. In addition, a series of cathode materials with different amount of boron were synthesized by adjusting the addition of B(OH)<sub>3</sub> to 0 wt%, 0.5 wt%, 1.0 wt%, 1.5 wt% and 2.0 wt%, respectively. As shown in Fig. S5, the reversible capacity and capacity retention follow a volcano-shape relationship with the boron contents. Therefore, the addition of 1.0 wt% was selected to achieve the best modification effect. According to the reaction equations (5-7), the addition of a large amount of B(OH)<sub>3</sub> would lead to a significant increase in the amount of the  $\text{B}_2\text{O}_3/\text{LiBO}_2$  and the percent of  $\text{B}_2\text{O}_3$ , which not only affects the transmission rate of  $\text{Li}^+$  but also reduces the content of active components, resulting in a certain decline in the specific capacity and capacity retention [41]. Fig. 3j illustrates the rate performance of both samples at different current densities in 2.75–4.35 V. At relatively low current densities of 0.2C, 0.5C, 1C and 2C, both samples exhibit similar discharge capacity. However, when the current density is greater than 5C, the discharge capacity of B-NCM89 is much higher than that of NCM89. At 15C, B-NCM89 cathode delivers a superior discharge capacity of  $\sim 120 \text{ mA g}^{-1}$ , about 53.5% of the discharge capacity at 0.2C, which is much higher than that of NCM89. As shown in Fig. S6, the lithiation plateaus,

which nearly vanish in high voltage ranges in NCM89 at high current densities, are well maintained in B-NCM89. Cycling results of half cells at 5C in Fig. S7 further demonstrate the excellent cycling performance of the B-NCM89 at high current density. As discussed above, the interfacial charge transfer resistance is greatly reduced and the lithium-ion diffusion coefficient is increased due to the existence of  $\text{B}_2\text{O}_3/\text{LiBO}_2$  modification layer in B-NCM89. As a result, the reaction kinetics at the cathode/electrolyte are facilitated, leading to an improved rate performance at high current density. Lastly, the NCM89 and B-NCM89 cathodes were used in full cells paired with a graphite anode to illustrate their practical viability. As shown in Fig. 3k, there is not obvious capacity degradation during the first 300 cycles in cells with B-NCM89, and 93% capacity can be well reserved after 350 cycles. However, the capacity of the NCM89 decays substantially after 200 cycles, and the retention is less than 50% after 300 cycles. The full cell consisting B-NCM89 was used to light up a light board and can provide stable power supply (Figure S1l).

### 3.3. Investigation of structure and cathode/electrolyte interphase change

The structural and phase evolution during delithiation/lithiation was studied using in situ XRD measurements to investigate their possible contributions to the enhanced electrochemical stability of B-NCM89. Fig. 4a and b illustrate initial charge/discharge curves of NCM89 and B-NCM89 electrodes, together with contour maps of the characteristic (003), (101), (104) and (018)/(110) reflections based on the recorded XRD patterns in Fig. S8. Both NCM89 and B-NCM89 exhibit a similar phase evolution upon charging ( $\text{H1} \rightarrow \text{H2} \rightarrow \text{H3}$ ), which is consistent with the voltage curves and differential capacity profiles in Fig. 3a–d. During an early stage of delithiation, the (003)<sub>H1</sub> peak gradually shifts to lower 2 $\theta$  angles for both samples and finally evolves into (003)<sub>H2</sub> at  $\sim 4.1 \text{ V}$ , which indicates an enlargement of lattice along the c-axes. The expansion is attributed to the increase of oxygen-oxygen repulsion due to a diminishing lithium-screening effect within the Li slab. Upon further delithiation, the (003)<sub>H2</sub> peak rapidly shifts backward to a higher 2 $\theta$  angle, accompanied by the H2–H3 phase transition, which implies the lattice shrinkage along the c-axes direction [42]. The B-NCM89 electrode exhibits a peak shift of 0.72° at high SOC, whereas a larger peak shift of 0.86° and phase separation were observed for the NCM89 electrode. The (110) peak as well as (101) and (104) peaks monotonically shifts to a higher angle during the delithiation process, indicating the lattice shrinkage along the a- and b-axes, which relates to the oxidation of transition-metal ions (such as  $\text{Ni}^{3+}$  to  $\text{Ni}^{4+}$ ) [43]. During lithiation (discharge) process, the peaks returned to the initial 2 $\theta$  position and the peak variations are in good accordance with previous reports [44,45]. However, there is an obvious peak widening in NCM89 which does not occur in the fully discharged B-NCM89, indicating that the reversibility of NCM89 crystalline structure is improved in B-NCM89 [46].

The detailed evolution of lattice parameters derived from Fig. 4a and b are shown in Fig. 4c and d. The NCM89 and B-NCM89 display shrinkage of 2.2% and 2.4% along the a-axes, respectively. The maximum variation of c parameter in the B-NCM89 (4.6%) is smaller than that in the NCM89 (4.9%). Severe anisotropic lattice changes are thought to be one of the major reasons for the rapid capacity fading of high-Ni cathodes, and alleviating the lattice contraction has been proven effective in improving the capacity retention. The in-situ XRD analysis demonstrates that the B-NCM89 electrode can effectively alleviate the severe lattice changes at high SOC, suggesting that the introduction of boron containing modification layer can effectively mitigate the intrinsic structural change associated with the phase transitions during cycling [44]. The volume change during cycling is directly responsible for the integrity of particles. Secondary particle cracking and pulverization in high-Ni cathodes is considered to be caused by dramatic lattice changes during cycling [47]. Notably, the lattice shrinkage along the c-axes in Fig. 4d is much quicker and more aggressive during H2–H3 transition than the expansion during initial delithiation of H1–H2

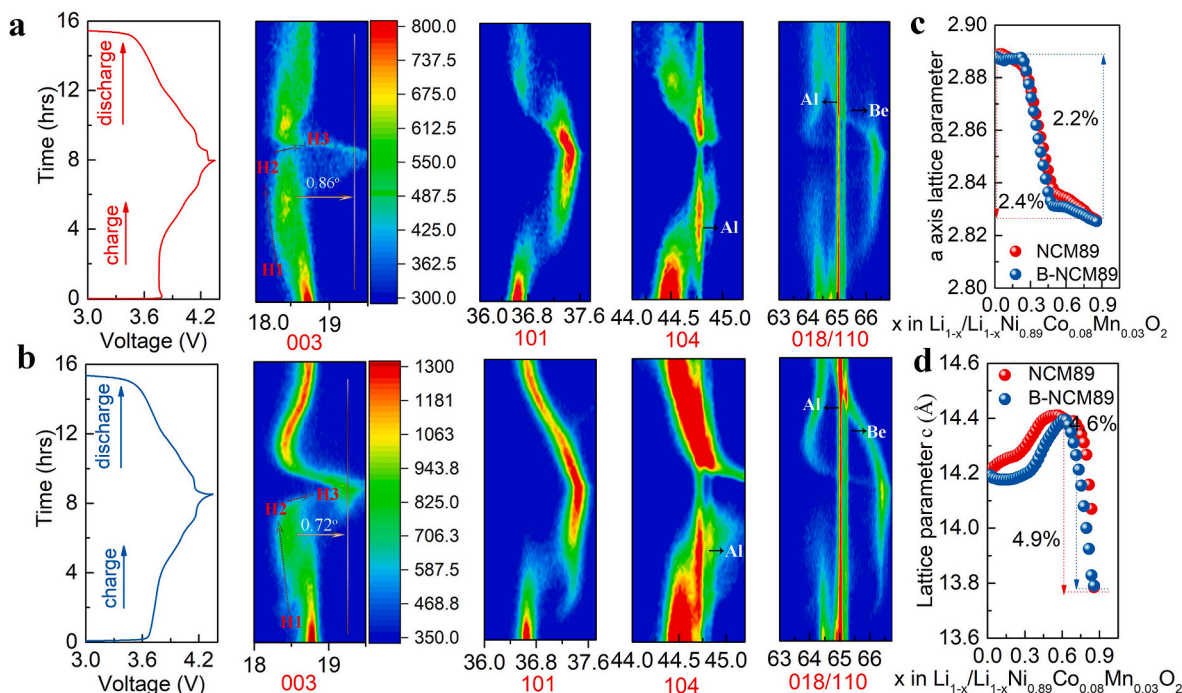


**Fig. 4.** In situ XRD examinations during charging/discharging of (a) NCM89 and (b) B-NCM89 in the first cycle, showing recorded charge/discharge curves and contour plots of 003, 101, 104 and 018/110 reflections. (c) The variation of the a-axis parameter during charging for NCM89 and B-NCM89. (d) The variation of the c-axis parameter during charging for NCM89 and B-NCM89.

transition, especially in NCM89 and this would cause severe accumulation of internal strain and particle rupture.

In view of this, cross-sectional SEM investigations were performed on the pristine and cycled cathodes. The uncycled cross-sectional SEM images indicate that the overall primary particle array in both cathodes is radial and there is no significant difference in the secondary particle microstructure before cycling (Fig. 5a and d). However, NCM89 and B-NCM89 display quite different features after cycling. Some of the NCM89 particles fracture into fragments and totally lose their original secondary particle morphology (Fig. 5b and c), which is responsible for the electrical contact lost with the current collector and CEI accumulation at the interface. The particle rupture is caused by dramatic lattice changes and the repeated strain from the abrupt volume contraction and expansion during cycling, as demonstrated above in Fig. 4. The interfacial impedance would be elevated, and lithium-ion diffusion as well as charge transfers would slow down. By contrast, the secondary particles of the B-NCM89 are well maintained after cycling, with only small cracks inside (Fig. 5e and f). The SEM images of the electrodes after 100 cycles in half cell and after 350 cycles in full cell are also shown in Fig. S9 and Fig. S10. The secondary particles of NCM89 were crushed into fragments, while secondary particles of B-NCM89 remained intact. These results clearly testify that the B-NCM89 is more resistant to microcracking. In addition, the structural integrity and stability are greatly improved which contribute to the improved electrochemical performance of B-NCM89. As a result, the cycling degradation is suppressed in the B-NCM89 cell compared with the NCM89 one.

XPS spectra of (a) C 1s, (b) O 1s, (c) F 1s and (d) B 1s elements for NCM89 and B-NCM89 cathodes after 100 cycles from 2.75 V to 4.35 V.

Additionally, XPS analysis on the cycled NCM89 and B-NCM89 further demonstrate the function of boron modification layer on the CEI construction and the interfacial structural stability during cycling. For C1s spectra (Fig. 5g), abundant carbonaceous species for cycled NCM89 and B-NCM89 on the surfaces were observed. Carbonaceous species corresponding to C–C (284.4 eV), C–H (285.1 eV), C–O (286.2 eV), C=O (288.4 eV) and OCO<sub>2</sub> (290.3 eV) can be attributed to the acetylene black, PVDF binder, and carbonate electrolyte decomposition products

[48]. Compared to the NCM89, weaker peak intensities are observed for the peaks associated with C–O, C=O, and OCO<sub>2</sub> of the B-NCM89, suggesting lower electrolyte decomposition amount on the surface of the boron modified B-NCM89 material. Moreover, the O 1s spectra (Fig. 5h) include peaks corresponding to the M–O (529.3 eV), Li<sub>2</sub>CO<sub>3</sub> (531.6 eV) and ROCO<sub>2</sub>Li (533.2 eV) [49]. The amount of M–O (metal-oxide) derived from the active material decreases from 44.4% to 24.5%, indicating a thinner CEI layer may be formed on the surface of B-NCM89. In terms of the F 1s XPS (Fig. 5i), there is a dramatic suppression in the formation of highly resistive LiF and NiF<sub>2</sub> species in the CEI layer after boron modification. Meanwhile, strong B 1s (Fig. 5j) signals were observed in the cycled B-NCM89, which indicates the B surface layer is not covered by thick CEIs even after prolonged cycling. The observations above suggest that the boron modification can prohibit successive side reactions between the cathode and electrolyte, suppress transition metal dissolution, and facilitate more stable thin CEI layer on the B-NCM89 during cycling. The interfacial structure and its stability greatly contribute to the improved cycling performance of the B-NCM89.

#### 4. Conclusion

In summary, this work proposes a modification strategy by B<sub>2</sub>O<sub>3</sub>&LiBO<sub>2</sub> dual modification layer to improve the structural stability and electrochemical performance of the Ni-rich LiNi<sub>0.89</sub>Co<sub>0.08</sub>Mn<sub>0.03</sub>O<sub>2</sub> cathode material. The chemical analysis shows that the boron modification can effectively reduce residual lithium and further enhance the interfacial stability. With the help of in-situ X-ray diffraction (XRD), cross-sectional SEM and XPS analysis, it is found that B<sub>2</sub>O<sub>3</sub> and LiBO<sub>2</sub> species are present on boron modified LiNi<sub>0.89</sub>Co<sub>0.08</sub>Mn<sub>0.03</sub>O<sub>2</sub> (hereafter termed as B-NCM89). Severe lattice changes and particle ruptures of the Ni-rich cathodes are successfully avoided in B-NCM89 while the layered



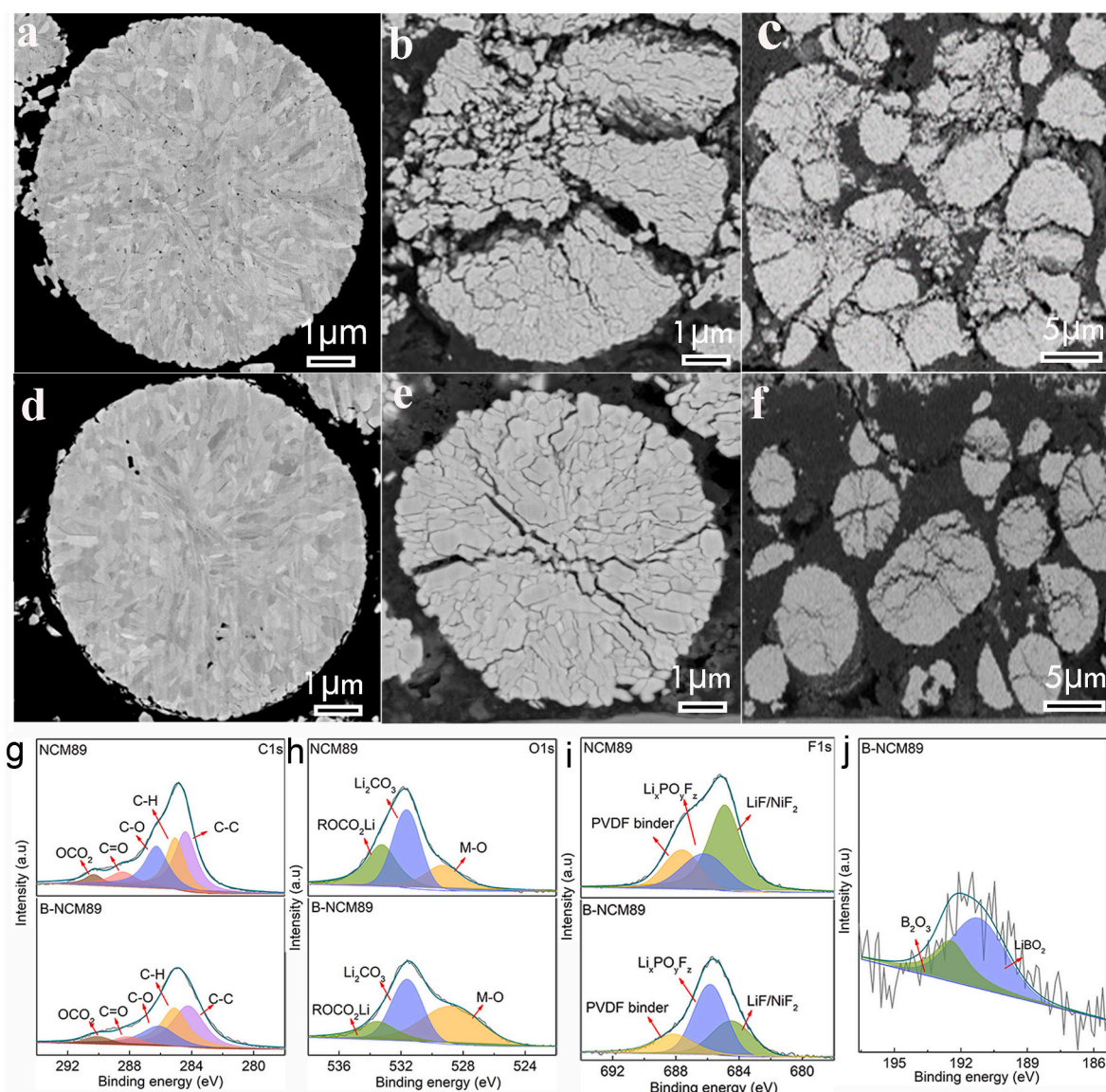


**Fig. 5.** Cross-section SEM images of NCM89 (a) and B-NCM89 (d). Cross section SEM images of NCM89 (b–c) and B-NCM89 (e–f) after 100 cycles between 2.75 and 4.35 V (discharged state).

structure is well maintained during cycling. The B<sub>2</sub>O<sub>3</sub>&LiBO<sub>2</sub> modifications can effectively prohibit successive side reactions between the cathode and electrolyte and facilitate more stable CEI. As a result, B-NCM89 delivers a high capacity of 193 mA g<sup>-1</sup> and capacity retention of 92% at 0.5C, 180.4 mA g<sup>-1</sup> with 90% capacity retention at 1C after 100 cycles. For full cell paired B-NCM89 with graphite, there is not obvious capacity degradation during the first 300 cycles in cells with B-NCM89 cathode, and 93% capacity can be well reserved after 350 cycles. However, the capacity of the NCM89 containing full cell decays substantially after 200 cycles, and the retention is less than 50% after 300 cycles. This work enhances the understanding of the boron modification effects on the Ni-rich oxide cathodes and provides insight for further improvements to the state-of-the-art Li ion battery cathode materials.

#### CRediT authorship contribution statement

**Yao Lv:** Conceptualization, Methodology, Investigation, Writing – original draft. **Shifei Huang:** Data curation, Writing – review & editing. **Sirong Lu:** Formal analysis, Visualization, Investigation. **Wenbo Ding:** Investigation, Writing – review & editing. **Xiaoliang Yu:** Validation, Data curation. **Gemeng Liang:** Data curation. **Jinshuo Zou:**

Visualization. **Feiyu Kang:** Resources, Writing – review & editing. **Jiujun Zhang:** Resources, Supervision, Project administration. **Yidan Cao:** Conceptualization, Formal analysis, Writing – review & editing, Project administration, Supervision, Funding acquisition.

#### Declaration of competing interest

The authors declare that they have no known competing financial interests or personal relationships that could have appeared to influence the work reported in this paper.

#### Acknowledgments

This work was supported by Guangdong Basic and Applied Basic Research Foundation (2019A1515110530), China Postdoctoral Science Foundation (2021M691750), Shenzhen Science and Technology Program (JCYJ20210324140804013, RCBS20200714115000219-Doctoral Startup Project), and Tsinghua Shenzhen International Graduate School (QD2021005N, JC2021007).

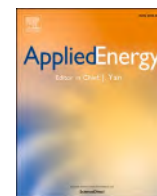


## Appendix A. Supplementary data

Supplementary data to this article can be found online at <https://doi.org/10.1016/j.jpowsour.2022.231510>.

## References

- [1] K. Park, H. Jung, L. Kuo, P. Kaghazchi, C. Yoon, Y. Sun, Improved cycling stability of  $\text{Li}[\text{Ni}_{0.9}\text{Co}_{0.05}\text{Mn}_{0.05}]\text{O}_2$  through microstructure modification by boron doping for Li-ion batteries, *Adv. Energy Mater.* 8 (25) (2018), 1801202.
- [2] Y. Yang, R. Xu, K. Zhang, S. Lee, L. Mu, P. Liu, C. Wei, et al., Quantification of heterogeneous degradation in Li-ion batteries, *Adv. Energy Mater.* 9 (25) (2019), 1900674.
- [3] H. Ryu, K. Park, D.R. Yoon, A. Aishova, C. Yoon, Y. Sun,  $\text{Li}[\text{Ni}_{0.9}\text{Co}_{0.09}\text{W}_{0.01}]\text{O}_2$ : a new type of layered oxide cathode with high cycling stability, *Adv. Energy Mater.* 9 (44) (2019), 1902698.
- [4] U. Kim, G. Park, B. Son, G.W. Nam, J. Liu, L. Kuo, P. Kaghazchi, C. Yoon, Y.K. Sun, Heuristic solution for achieving long-term cycle stability for Ni-rich layered cathodes at full depth of discharge, *Nat. Energy* 5 (11) (2020) 860–869.
- [5] K. Wu, J. Wang, Q. Li, Y. Yang, X. Deng, R. Dang, M. Wu, Z. Wu, X. Xiao, X. Yu, In situ synthesis of a nickel concentration gradient structure of Ni-rich  $\text{LiNi}_{0.8}\text{Co}_{0.15}\text{Al}_{0.05}\text{O}_2$  with promising superior electrochemical properties at high cut-off voltage, *Nanoscale* 12 (20) (2020) 11182–11191.
- [6] Y. Lv, S. Huang, Y. Zhao, S. Roy, X. Lu, Y. Hou, J. Zhang, A review of nickel-rich layered oxide cathodes: synthetic strategies, structural characteristics, failure mechanism, improvement approaches and prospects, *Appl. Energy* 305 (2022), 117849.
- [7] P. Hou, J. Yin, M. Ding, J. Huang, X. Xu, Surface/interfacial structure and chemistry of high-energy nickel-rich layered oxide cathodes: advances and perspectives, *Small* 13 (45) (2017), 1701802.
- [8] Q. Tao, L. Wang, C. Shi, J. Li, G. Chen, Z. Xue, S. Wang, H. Jin, Understanding the Ni-rich layered structure materials for high-energy density lithium-ion batteries, *Mater. Chem. Front.* 5 (6) (2021) 2607–2622.
- [9] C. Jung, D. Kim, D. Eum, K. Kim, J. Choi, J. Lee, H. Kim, K. Kang, S. Hong, New insight into microstructure engineering of Ni-rich layered oxide cathode for high performance lithium ion batteries, *Adv. Funct. Mater.* 31 (18) (2021), 2010095.
- [10] J.U. Choi, N. Voronina, Y. Sun, S. Myung, Recent progress and perspective of advanced high-energy Co-less Ni-rich cathodes for Li-ion batteries: yesterday, today, and tomorrow, *Adv. Energy Mater.* 10 (42) (2020), 2002027.
- [11] J. Zheng, Z. Yang, Z. He, W. Yu, H. Tong, J. Zhang, In situ formed  $\text{LiNi}_{0.8}\text{Co}_{0.15}\text{Al}_{0.05}\text{O}_2@ \text{Li}_4\text{SiO}_4$  composite cathode material with high rate capability and long cycling stability for lithium-ion batteries, *Nano Energy* 53 (2018) 613–621.
- [12] Q. Xie, W. Li, A. Dolocan, A. Manthiram, Insights into boron-based polyanion-tuned high-nickel cathodes for high-energy-density lithium-ion batteries, *Chem. Mater.* 31 (21) (2019) 8886–8897.
- [13] L. Qiu, W. Xiang, W. Tian, C. Xu, Y. Li, Z. Wu, T.-Chen, K. Jia, D. Wang, F. He, X. Guo, Polyanion and cation co-doping stabilized Ni-rich Ni-Co-Al material as cathode with enhanced electrochemical performance for Li-ion battery, *Nano Energy* 63 (2019), 103818.
- [14] F. Xin, H. Zhou, X. Chen, M. Zuba, N. Chernova, G. Zhou, M. Whittingham, Li-Nb-O coating/substitution enhances the electrochemical performance of the  $\text{LiNi}_{0.8}\text{Mn}_{0.1}\text{Co}_{0.1}\text{O}_2$  (NMC 811) cathode, *ACS Appl. Mater. Interfaces* 11 (38) (2019) 34889–34894.
- [15] S.S. Zhang, Problems and their origins of Ni-rich layered oxide cathode materials, *Energy Storage Mater.* 24 (2020) 247–254.
- [16] T. Li, X. Yuan, L. Zhang, D. Song, K. Shi, C. Bock, Degradation mechanisms and mitigation strategies of nickel-rich NMC-based lithium-ion batteries, *Electrochemical Energy Reviews* 3 (1) (2020) 43–80.
- [17] H.M.K. Sari, X. Li, Controllable cathode-electrolyte interface of  $\text{Li}[\text{Ni}_{0.8}\text{Co}_{0.1}\text{Mn}_{0.1}]\text{O}_2$  for lithium ion batteries: a review, *Adv. Energy Mater.* 9 (39) (2019), 1901597.
- [18] W. Bao, G. Qian, L. Zhao, Y. Yu, L. Su, X. Cai, H. Zhao, Y. Zuo, Y. Zhang, H. Li, Z. Peng, L. Li, J. Xie, Simultaneous enhancement of interfacial stability and kinetics of single-crystal  $\text{LiNi}_{0.6}\text{Mn}_{0.2}\text{Co}_{0.2}\text{O}_2$  through optimized surface coating and doping, *Nano Lett.* 20 (12) (2020) 8832–8840.
- [19] Q. Fan, K. Lin, S. Yang, S. Guan, J. Chen, S. Feng, J. Liu, L. Liu, J. Li, Z. Shi, Constructing effective  $\text{TiO}_2$  nano-coating for high-voltage Ni-rich cathode materials for lithium ion batteries by precise kinetic control, *J. Power Sources* 477 (2020), 228745.
- [20] M.R. Laskar, D.H.K. Jackson, S. Xu, R.J. Hamers, D. Morgan, Atomic layer deposited MgO: a lower overpotential coating for  $\text{Li}[\text{Ni}_{0.5}\text{Mn}_{0.3}\text{Co}_{0.2}]\text{O}_2$  cathode, *ACS Appl. Mater. Interfaces* 9 (12) (2017) 11231–11239.
- [21] K. Du, H. Xie, G. Hu, Z. Peng, Y. Cao, F. Yu, Enhancing the thermal and upper voltage performance of Ni-rich cathode material by a homogeneous and facile coating method: spray-drying coating with nano- $\text{Al}_2\text{O}_3$ , *ACS Appl. Mater. Interfaces* 8 (27) (2016) 17713–17720.
- [22] S. Lee, G. Park, S. Sim, B. Jin, H. Kim, Improved electrochemical performances of  $\text{LiNi}_{0.8}\text{Co}_{0.1}\text{Mn}_{0.1}\text{O}_2$  cathode via  $\text{SiO}_2$  coating, *J. Alloys Compd.* 791 (2019) 193–199.
- [23] S. Dong, Y. Zhou, C. Hai, J. Zeng, Y. Sun, Y. Shen, X. Li, X. Ren, G. Qi, X. Zhang, L. Ma, Ultrathin  $\text{CeO}_2$  coating for improved cycling and rate performance of Ni-rich layered  $\text{LiNi}_{0.7}\text{Co}_{0.2}\text{Mn}_{0.1}\text{O}_2$  cathode materials, *Ceram. Int.* 45 (1) (2019) 144–152.
- [24] U. Nisar, N. Muralidharan, R. Essehli, R. Amin, I. Belharouak, Valuation of surface coatings in high-energy density lithium-ion battery cathode materials, *Energy Storage Mater.* 38 (2021) 309–328.
- [25] J. Zhu, Y. Li, L. Xue, Y. Chen, T. Lei, S. Deng, G. Cao, Enhanced electrochemical performance of  $\text{Li}_3\text{PO}_4$  modified  $\text{Li}[\text{Ni}_{0.8}\text{Co}_{0.1}\text{Mn}_{0.1}]\text{O}_2$  cathode material via lithium-reactive coating, *J. Alloys Compd.* 773 (2019) 112–120.
- [26] Y. Liu, L. Tang, H. Wei, X. Zhang, Z. He, Y. Li, J. Zheng, Enhancement on structural stability of Ni-rich cathode materials by in-situ fabricating dual-modified layer for lithium-ion batteries, *Nano Energy* 65 (2019), 104043.
- [27] L. Qiu, W. Xiang, W. Tian, C. Xu, Y. Li, Z. Wu, T. Chen, K. Jia, D. Wang, F. He, X. Guo, Polyanion and cation co-doping stabilized Ni-rich Ni-Co-Al material as cathode with enhanced electrochemical performance for Li-ion battery, *Nano Energy* 63 (2019), 103818.
- [28] L. Tian, K. Liang, X. Wen, J. Zheng, Enhanced cycling stability and rate capability of  $\text{LiNi}_{0.8}\text{Co}_{0.15}\text{Al}_{0.05}\text{O}_2$  cathode material by a facile coating method, *J. Electroanal. Chem.* 812 (2018) 22–27.
- [29] J. Li, Z. Liu, Y. Wang, R. Wang, Investigation of facial  $\text{B}_2\text{O}_3$  surface modification effect on the cycling stability and high-rate capacity of  $\text{LiNi}_{1/3}\text{Co}_{1/3}\text{Mn}_{1/3}\text{O}_2$  cathode, *J. Alloys Compd.* 834 (2020), 155150.
- [30] W. Hu, C. Zhang, H. Jiang, M. Zheng, Q. Wu, Q. Dong, Improving the electrochemistry performance of layer  $\text{LiNi}_{0.5}\text{Mn}_{0.3}\text{Co}_{0.2}\text{O}_2$  material at 4.5 V cutoff potential using lithium metaborate, *Electrochim. Acta* 243 (2017) 105–111.
- [31] Y. Liu, Y. Qiao, G. Wei, S. Li, Z. Lu, X. Wang, X. Lou, Sodium storage mechanism of N, S co-doped nanoporous carbon: experimental design and theoretical evaluation, *Energy Storage Mater.* 11 (2018) 274–281.
- [32] C. Lv, Z. Li, X. Ren, K. Li, J. Ma, X. Duan, Revealing the degradation mechanism of Ni-rich cathode materials after ambient storage and related regeneration method, *J. Mater. Chem.* 9 (7) (2021) 3995–4006.
- [33] L. Mu, Z. Yang, L. Tao, C.K. Waters, Z. Xu, L. Li, S. Sainio, Y. Du, H. Xin, D. Nordlund, F. Lin, The sensitive surface chemistry of Co-free, Ni-rich layered oxides: identifying experimental conditions that influence characterization results, *J. Mater. Chem.* 8 (34) (2020) 17487–17497.
- [34] B. Huang, D. Liu, K. Qian, L. Zhang, K. Zhou, Y. Liu, F. Kang, B. Li, A simple method for the complete performance recovery of degraded Ni-rich  $\text{LiNi}_{0.7}\text{Co}_{0.15}\text{Mn}_{0.15}\text{O}_2$  cathode via surface reconstruction, *ACS Appl. Mater. Interfaces* 11 (15) (2019) 14076–14084.
- [35] J. Wang, Y. Nie, C. Miao, Y. Tan, M. Wen, W. Xiao, Enhanced electrochemical properties of Ni-rich layered cathode materials via  $\text{Mg}^{2+}$  and  $\text{Ti}^{4+}$  co-doping for lithium-ion batteries, *J. Colloid Interface Sci.* 601 (2021) 853–862.
- [36] J. Kasnatscheew, M. Evertz, B. Streipert, R. Wagner, S. Nowak, I.C. Laskovic, M. Winter, Changing established belief on capacity fade mechanisms: thorough investigation of  $\text{LiNi}_{1/3}\text{Co}_{1/3}\text{Mn}_{1/3}\text{O}_2$  (NCM111) under high voltage conditions, *J. Phys. Chem. C* 121 (3) (2017) 1521–1529.
- [37] N. Park, H. Ryu, G. Park, T. Noh, Y. Sun, Optimized Ni-rich NCMA cathode for electric vehicle batteries, *Adv. Energy Mater.* 11 (9) (2021), 2003767.
- [38] T. Nguyen, U. Kim, C.S. Yoon, Y. Sun, Enhanced cycling stability of Sn-doped  $\text{Li}[\text{Ni}_{0.9}\text{Co}_{0.05}\text{Mn}_{0.05}]\text{O}_2$  via optimization of particle shape and orientation, *Chem. Eng. J.* 405 (2021), 126887.
- [39] C. Zhou, P. Wang, B. Zhang, L. Tang, H. Tong, Z. He, J. Zheng, Formation and effect of residual lithium compounds on Li-rich cathode material  $\text{Li}_{1.35}[\text{Ni}_{0.35}\text{Mn}_{0.65}]\text{O}_2$ , *ACS Appl. Mater. Interfaces* 11 (12) (2019) 11518–11526.
- [40] X. Qu, H. Huang, T. Wan, L. Hu, Z. Yu, Y. Liu, A. Dou, Y. Zhou, M. Su, X. Peng, H. Wu, T. Wu, D. Chu, An integrated surface coating strategy to enhance the electrochemical performance of nickel-rich layered cathodes, *Nano Energy* 91 (2022), 106665.
- [41] Y. Su, L. Li, L. Chen, L. Wang, Y. Lu, Q. Zhang, L. Bao, F. Wu, Enhanced electrochemical performance of Ni-rich cathode materials with an in situ-formed  $\text{LiBO}_2/\text{B}_2\text{O}_3$  hybrid coating layer, *ACS Appl. Energy Mater.* 5 (2022) 2231–2241.
- [42] C. Jung, Q. Li, D. Kim, D. Eum, D. Ko, J. Choi, J. Lee, K. Kim, K. Kang, W. Yang, S. Hong, Revisiting the role of Zr doping in Ni-rich layered cathodes for lithium-ion batteries, *J. Mater. Chem.* 9 (32) (2021) 17415–17424.
- [43] J. Li, A. Manthiram, A comprehensive analysis of the interphasial and structural evolution over long-term cycling of ultrahigh-nickel cathodes in lithium-ion batteries, *Adv. Energy Mater.* 9 (45) (2019), 1902731.
- [44] X. Fan, X. Ou, W. Zhao, Y. Liu, B. Zhang, J. Zhang, L. Zou, L. Seidl, Y. Li, G. Hu, C. Battaglia, Y. Yang, In situ inorganic conductive network formation in high-voltage single-crystal Ni-rich cathodes, *Nat. Commun.* 12 (1) (2021) 1–13.
- [45] X. Huang, W. Zhu, J. Yao, L. Bu, X. Li, K. Tian, H. Lu, C. Quan, S. Xu, K. Xu, Z. Jiang, X. Zhang, L. Gao, J. Zhao, Suppressing structural degradation of Ni-rich cathode materials towards improved cycling stability enabled by a  $\text{Li}_2\text{MnO}_3$  coating, *J. Mater. Chem.* 8 (34) (2020) 17429–17441.
- [46] S. Song, M. Cho, I. Park, G.J. Yoo, K. Ko, J. Hong, J. Kim, S. Jun, M. Avdeev, S. Ji, S. Lee, J. Bang, H. Kim, High-voltage-driven surface structuring and electrochemical stabilization of Ni-rich layered cathode materials for Li rechargeable batteries, *Adv. Energy Mater.* 10 (23) (2020), 2000521.
- [47] G. Nam, N. Park, K. Park, J. Yang, J. Liu, C. Yoon, Y. Sun, Capacity fading of Ni-rich NCA cathodes: effect of microcracking extent, *ACS Energy Lett.* 4 (12) (2019) 2995–3001.
- [48] Y. Zou, F. Meng, D. Xiao, H. Sheng, W. Chen, X. Meng, Y. Du, L. Gu, J. Shi, Y. Guo, Constructing a stable interfacial phase on single-crystalline Ni-rich cathode via chemical reaction with phosphomolybdic acid, *Nano Energy* 87 (2021), 106172.
- [49] F. Wu, J. Dong, L. Chen, L. Bao, N. Li, D. Cao, Y. Lu, R. Xue, N. Liu, L. Wei, Z. Wang, S. Chen, Y. Su, High-voltage and high-safety nickel-rich layered cathode enabled by a self-reconstructive cathode/electrolyte interphase layer, *Energy Storage Mater.* 41 (2021) 495–504.



# A review of nickel-rich layered oxide cathodes: synthetic strategies, structural characteristics, failure mechanism, improvement approaches and prospects

Yao Lv<sup>a</sup>, Shifei Huang<sup>a,\*</sup>, Yufeng Zhao<sup>a,\*</sup>, Swagata Roy<sup>a</sup>, Xionggang Lu<sup>a</sup>, Yanglong Hou<sup>b</sup>, Jiujun Zhang<sup>a,\*</sup>

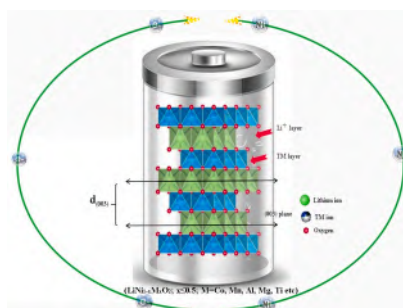
<sup>a</sup> College of Sciences and Institute for Sustainable Energy, Shanghai University, Shanghai 200444, China

<sup>b</sup> Department of Materials Science and Engineering, College of Engineering, Peking University, Beijing 100871, China

## HIGHLIGHTS

- The capacity failure mechanisms are emphatically summarized and discussed.
- The improvement measures of nickel-rich cathodes in recent years are summarized.
- The prospects of nickel-rich materials are summarized.

## GRAPHICAL ABSTRACT



## ARTICLE INFO

### Keywords:

Lithium-ion batteries  
Nickel-rich layered oxide cathode materials  
Capacity failure mechanism  
Strategies  
Perspectives

## ABSTRACT

Nickel-rich layered oxide cathode materials have high specific capacity and are environmentally-benign, hence they are considered as the most relevant next-generation positive-electrode materials for lithium-ion batteries, particularly for powering plug-in hybrid electric vehicles and battery electric vehicles. The rich nickel content in layered oxides is highly beneficial in improving the energy density, but the cycle ability, rate capability and thermal stability inevitably decrease with the increase of nickel percentage, leading to the gradual failure of lithium-ion batteries. Therefore, it is an essential requisite to give a thorough review of previous research, thereby providing a clear understanding of the relationships between the material structure and their electrochemical activities, and improving the electrochemical performances of nickel-rich layered oxide cathode materials through reasonable modifications. In this article, the structural characteristics and synthetic methods are systematically reviewed. Particularly, the capacity failure mechanism and the corresponding improvement strategies of nickel-rich layered oxides are emphasized and discussed from atomic scale to macro-scale along with the latest literature review. A brief analysis of the perspectives is also presented with several possible research directions for technical and commercial success of nickel-rich layered oxide cathodes.

\* Corresponding authors.

E-mail addresses: [huangsf2020@sz.tsinghua.edu.cn](mailto:huangsf2020@sz.tsinghua.edu.cn) (S. Huang), [yufengzhao@shu.edu.cn](mailto:yufengzhao@shu.edu.cn) (Y. Zhao), [jiujun.zhang@i.shu.edu.cn](mailto:jiujun.zhang@i.shu.edu.cn) (J. Zhang).

## 1. Introduction

Over the past century, the wide application of fossil energy, such as oil, natural gas, coal and nuclear energy, has provided a strong driving force for the development of human society and the world economy. [1–9] Despite producing more and more energy from renewables each year, the global energy mix is still dominated by coal, oil, and gas. Not only does most of our energy  $\sim 84\%$  of it come from fossil fuels, we continue to burn more each year: total production has increased from 116,214 to 136,761 TWh in the last 10 years (Fig. 1a–b). However, the earth's resources are limited. With the continuous consumption of resources, these resources will gradually dry up in the next 50–150 years (Fig. 1c). With the global energy crisis and environmental pollution becoming increasingly prominent, the development of energy-saving and environmental protection related industries has been highly valued, and the development of new energy vehicles has formed a consensus all over the world. In 2020, the global sales volume of new energy vehicles increased from 140,000 in 2012 to 3.07 million, with an annual compound growth rate of 47%; Permeability increased from 0.2% to 4%. In the short and medium term, the global energy conservation and emission reduction policies will drive the rapid increase of the penetration rate of new energy vehicles. In the long run, intelligent upgrading will bring a subversive revolution to the automobile industry and bring greater growth space to the new energy automobile industry. In this context, the global sales volume of new energy vehicles is expected to reach 10 million in 2025 and  $\sim 25$  million in 2030, and the future market capacity growth is expected to exceed ten times (Fig. 1d). Due to the requirement of high energy density, the batteries used in electric vehicles are basically lithium-ion batteries. Battery system is the component with the highest cost in new energy vehicles, and its cost accounts for nearly 40%. With the popularity of new energy vehicles, the scale of power battery industry is expected to grow rapidly. In 2020, the global lithium battery output will be 747 GWh. Lithium ion battery super factory predicts that the global lithium battery output will reach 2492 GWh in 2025, and the compound growth rate from 2020 to 2025 will exceed 27% (Fig. 1e).

Further enhancement of the energy and power density of LIBs are being highly focused in order to inflate their application in the EV market, as well as in the renewable energy involving wind and solar energy grid storage applications [10]. Electrode materials (cathodes and

anodes) have a significant influence on the electrochemical performance of LIBs such as volumetric/gravimetric energy density, cycle performance, output potential and safety [11–21]. However, when compared with the industrialized anode materials having high specific capacity, such as graphite ( $372 \text{ mAh g}^{-1}$ ), especially silicon carbon anode (greater than  $600 \text{ mAh g}^{-1}$ ), it has been observed that the cathode materials chiefly restrict the energy density and power density of LIBs. Over the past two decades, conventional cathode materials such as  $\text{LiCoO}_2$  [22] with hexagonal layered structure and  $\text{LiFePO}_4$  [23] with polyanionic olivine structure, as well as  $\text{LiMn}_2\text{O}_4$  [24] with spinel structure have been extensively studied. Among them,  $\text{LiCoO}_2$  ( $140 \text{ mAh g}^{-1}$ ) [25] is widely used in traditional 3C field, but its application in large-scale energy storage system is limited due to the lack of cobalt resources, radioactivity, high price, poor overcharge resistance and cycle performance of lithium cobalt oxide batteries [26]. The lithium ions in olivine  $\text{LiFePO}_4$  ( $140 \text{ mAh g}^{-1}$ ) [27,28] form a continuous linear chain with two dimensional mobility, stable oxidation state, good safety, high temperature performance and long cycle life, but their electronic as well as ionic conductivities are low. Therefore, their rate performance needs to be improved.  $\text{LiMn}_2\text{O}_4$  ( $120 \text{ mAh g}^{-1}$ ) is a low cost material, having stable structure, excellent electronic and ionic conductivity as well as safety but it suffers from capacity decay due to the structural distortion upon charge/discharge cycles [29]. Till date, traditional cathode materials are mostly used in PHEVs and EVs, but cathode materials can only deliver around  $120\text{--}160 \text{ mAh g}^{-1}$ , which have significantly hindered the far-ranging application of LIBs due to the limited specific energy. Consequently, it will be difficult to satisfy the demand for passenger cars in the future. Clearly, the pursuit for high specific energy is a key research and development direction of LIBs in PHEVs and EVs. Recently, the new generation of layered oxide cathodes, particularly the Ni-rich oxides ( $\text{LiNi}_{1-x-y}\text{M}_x\text{N}_y\text{O}_2$ ;  $x + y \leq 0.5$ ; M, N = Co, Mn, Al, Mg, Ti etc.) have attracted intensive attention due to their higher reversible capacity (greater than  $200 \text{ mAh g}^{-1}$ ) and specific energy ( $\sim 800 \text{ Wh kg}^{-1}$ ) as compared to  $\text{LiCoO}_2$  ( $140 \text{ mAh g}^{-1}$  and  $570 \text{ Wh kg}^{-1}$ ) and  $\text{LiMn}_2\text{O}_4$  ( $120 \text{ mAh g}^{-1}$  and  $440 \text{ Wh kg}^{-1}$ ), and are entrusted with heavy task to achieve the target of  $350 \text{ Wh kg}^{-1}$  cell-level specific energy and long endurance mileage by 2025 or sooner. Notably, Ni-rich oxide cathodes like  $\text{LiNi}_x\text{Co}_y\text{Mn}_z\text{O}_2$  and  $\text{LiNi}_x\text{Co}_y\text{Al}_z\text{O}_2$  have solidified their status in EVs. The 18650-type LIBs which utilized  $\text{LiNi}_{0.8}\text{Co}_{0.15}\text{Al}_{0.05}\text{O}_2$  (NCA) as

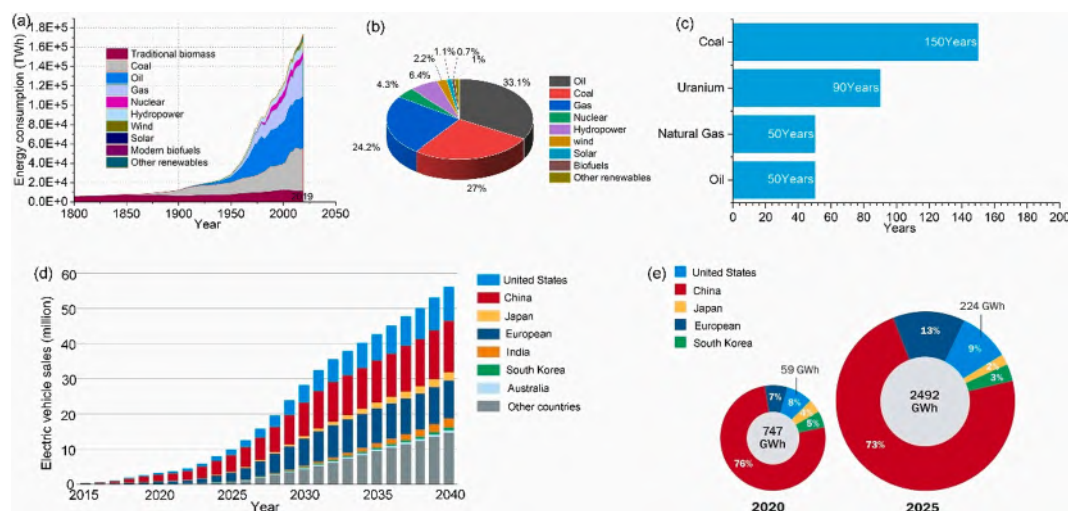


**Fig. 1.** (a) Global primary energy consumption by source (Primary energy is calculated based on the 'substitution method' which takes account of the inefficiencies in fossil fuel production by converting non-fossil energy into the energy inputs required if they had the same conversion losses as fossil fuels.) (Source: Vaclav Smil (2017) & BP Statistical Review of World Energy). (b) Global primary energy consumption by source for 2019 (Our World in Data based on BP Statistical Review of World Energy (2020)). (c) Industry estimates of economically viable fossil fuel reserves (Source: World Coal Association, World Nuclear Association, International Gas Union Global Gas Report 2020, British Petroleum Statistical Review of world Energy 2020). (d) Annual sales of passenger pure electric vehicle (EV) and plug-in hybrid electric vehicle (PHEV) (Source: Bloomberg, electric vehicle outlook 2019). (e) Battery manufacturing capacity (Source: "lithium ion battery super factory evaluation", benchmark mineral intelligence, March 2021).



cathode materials have already been successfully used in Tesla Model 3 for EV application, with an advantage of more than 200 miles of ranges per charge. The above two cathodes were derived from  $\text{LiNiO}_2$ , which have a high theoretical capacity of  $278 \text{ mAh g}^{-1}$ . Multiple phase transitions rapidly deteriorate the discharge capacity of  $\text{LiNiO}_2$  during delithiation while the intrinsic structural instability seriously hinders its commercial application. In order to prevent multiple phase transitions,  $\text{Li}[\text{Ni}_{0.8}\text{Co}_{0.15}\text{Al}_{0.05}]\text{O}_2$  cathode materials were prepared by introducing  $\text{Co}^{3+}$  and  $\text{Al}^{3+}$  into  $\text{LiNiO}_2$  to stabilize the structure. In another example, Ni was partially replaced by Co and Mn to form  $\text{Li}[\text{Ni}_{0.8}\text{Co}_{0.1}\text{Mn}_{0.1}]\text{O}_2$  with a good capacity retention.

Till date, many researchers have shown great interest in Ni-rich layered materials, and numerous types of Ni-rich materials have been studied. Sun et al. synthesized Ni-rich  $\text{LiNi}_x\text{Co}_y\text{B}_z\text{O}_2$  (NCB) [30] and  $\text{LiNi}_x\text{Co}_y\text{W}_z\text{O}_2$  (NCW) [31] cathode materials by replacing Mn with B and W. Again, cobalt is highly expensive (\$9000/ton) and also it is scarcely available in the earth's crust. Thereby, reducing or eliminating Co in Ni-rich materials has gradually become a consensus in the industry. In recent years, a renewed interest in  $\text{LiNiO}_2$  with substitutions of cations other than Co, viz.,  $\text{LiNi}_{0.9}\text{Mn}_{0.1}\text{O}_2$  [32],  $\text{LiNi}_{0.95}\text{Mg}_{0.05}\text{O}_2$  [33],  $\text{LiNi}_{0.94}\text{Al}_{0.05}\text{Mg}_{0.01}\text{O}_2$  [34], and  $\text{LiNi}_{0.96}\text{Mg}_{0.02}\text{Ti}_{0.02}\text{O}_2$  [35] have also been reported. However, the electrochemical performance and the control of element composition in cobalt free materials are not satisfactory. There are only a few long-term test reports that meet commercial standards. Good electrochemical performance, cost efficacy and high voltage are the notable features which have impelled high nickel and ultra-high nickel rich cathodes to be the major research interests as the next-generation of high energy density cathodes in the medium and long tenure. At the same time, some new cobalt free (LNMO:  $\text{LiNi}_{0.5}\text{Mn}_{1.5}\text{O}_4$ , NMA:  $\text{LiNi}_x\text{Mn}_y\text{Al}_z\text{O}_2$ ) and lithium rich (LMR:  $\text{Li}_{1+n}\text{M}_{1-n}\text{O}_2$ ) cathodes are still in their initial stage of investigation [36].

Compared with Ni-rich cathodes, Li-rich layered oxide cathodes (LMR) can be represented by  $x\text{Li}_2\text{MnO}_3 \cdot (1-x)\text{LiMO}_2$  ( $M = \text{Mn, Ni, Co, Fe, etc.}$ ), which are generally considered to be composed of  $\text{LiMO}_2$  and  $\text{Li}_2\text{MnO}_3$  component.  $\text{LiMO}_2$  have a typical rhombohedral crystal structure with  $R\bar{3}m$  space group,  $\text{Li}^+$  occupies octahedral 3b sites and TMs (Ni, Co and Mn) occupy octahedral 3a sites. The structure of  $\text{Li}_2\text{MnO}_3$  (space group  $\text{C2/m}$ ) is similar to  $\text{LiMO}_2$ , but one-third of the TM sites are occupied by  $\text{Li}^+$  ions [37]. The structural transformation caused by cation migration during charge and discharge, and the activation of low potential  $\text{Mn}^{4+}/^{3+}$  redox pairs caused by the redox process of irreversible oxygen (lattice oxygen release,  $\text{O}^{2-} \rightarrow \text{O}_2$ ). Compared with Mn and Co ions, Ni ions have higher and more stable redox potential [38]. The increase of nickel doping can improve the structural stability and oxygen redox reversibility of the material, so it can improve the capacity retention rate, inhibit the voltage attenuation, and obtain high energy density and long cycle stability [39]. In the long run, it is expected to break the monopoly of NCM and NCA in the Ni-rich cathodes and high energy density LIBs (Fig. 2).

The higher Ni content can result in higher charge–discharge capacity, however at the same time it can also be accompanied with accelerated capacity fading and poorer thermal stability as well as safety properties. The main reasons that cause capacity decay for Ni-rich cathodes can generally be summarized as following: 1) environmental factors; 2) intrinsic structural factors; and 3) electrochemical parameters. The increase of nickel content makes the cathode materials more sensitive to temperature, moisture and carbon dioxide in the air, which is detrimental to the intrinsic structure and the stability of the structure during repeated charge/discharge [40]. Owing to the influencing factors of its intrinsic structure, secondary spherical particles formed by the accumulation of primary spherical particles in Ni-rich layered oxide cathode materials may lead to  $\text{Li}^+/\text{Ni}^{2+}$  mixing, thereby formation of,

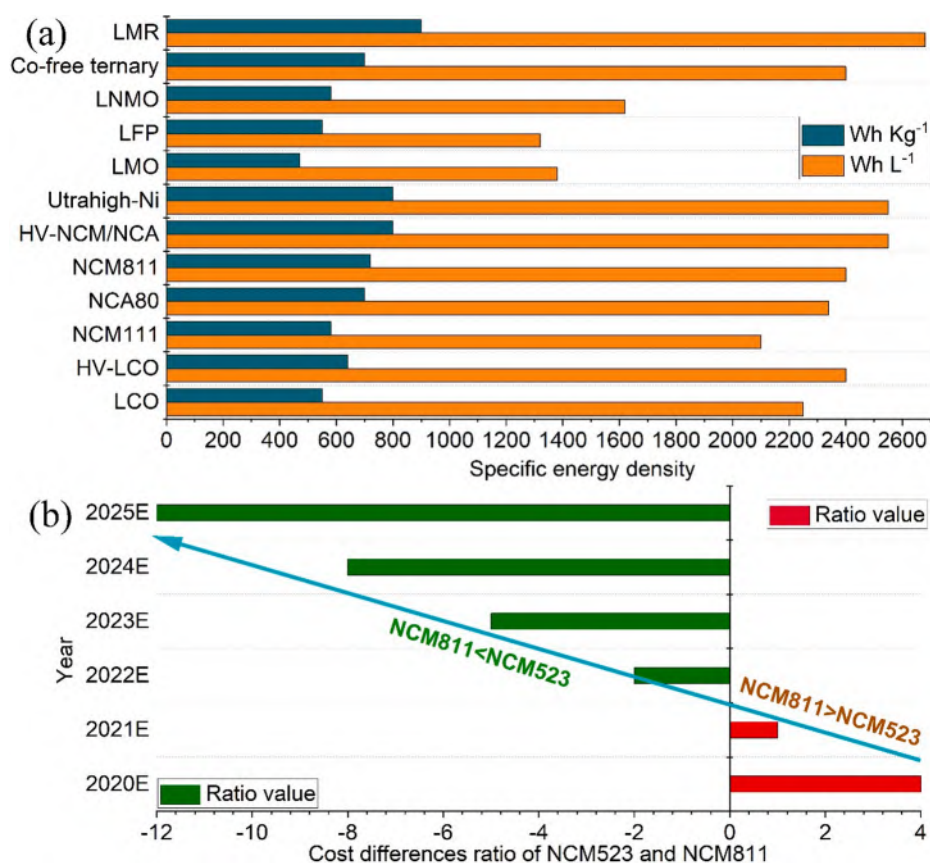


**Fig. 2.** (a) The mass and volume specific energy density for a series commercialized, next-generation and emerging cathodes for LIBs (LNMO:  $\text{LiNi}_{0.5}\text{Mn}_{1.5}\text{O}_4$ ; LMR:  $\text{Li}_{1+n}\text{M}_{1-n}\text{O}_2$ ; HV: high-voltage.). (b) The battery cell cost difference ratio of NCM523 and NCM811 in medium and long term development.

rock salt phase (NiO) and residual alkali (LiOH and  $\text{Li}_2\text{CO}_3$ ) on the surface during the synthesis, diminishing the reversible capacity and stability.

In addition, the continuous  $\text{Li}^+$  conduction channel formed by the radial distribution of grains can reduce the non-uniformity of charge distribution in the secondary particles and improve the stability of NCM during repeated charge/discharge, but it can have adverse effects on the structural integrity of the particles [41,42]. At the same time, a small number of vacancies, dislocations and lattice distortion are found as the intrinsic defects. Unstable structure of nickel-rich cathodes can be held responsible for several degradation phenomena induced by cycle and accompanied by the phase transition of defect chain reaction (DCR) [43]. The electrochemical parameters mainly include the structural degeneration of cathode material which is induced by both cycle process and the influence of discharge depth (DOD). During the cycling process, the phase transition of  $\text{H}_2 \rightarrow \text{H}_3$  occurs, which leads to oxygen release. The change of lattice constant/cell volume results in the occurrence of stress, which further leads to micro cracks and breakage of particles. The electrolyte immerses the particles, which further aggravates the side effects and affects the electrochemical performance. After a certain number of cycles, Ni/Co/Mn metal elements precipitate and dissolve, and the change of material structure leads to the loss of active material and decrease in capacity. Meanwhile, removal of lithium, especially in the deep charged state, involves multiple phase transitions instigating inherent instability of the materials, which hinders the further development of Ni-rich positive electrodes [44,45]. Transition metal ions and  $\text{O}^{2-}$  have energy band overlap (such as 3d orbit of Ni and 2p orbit of

oxygen). Hence, with the increase of applied voltage,  $\text{O}^{2-}$  is oxidized and peroxy species or superoxide species are formed. While the electrode is deoxidized, the transition metal ions form unstable high oxidation by-products resulting in interface phase transition. Besides, the electrolyte oxidation reaction on the electrode surface can have a significant impact on the improvement of their activity (Fig. 3) [46].

The performance degradation of subsequent cycles can be attributed to several causes like complex chemical and mechanical interactions among lithium diffusion, anisotropic lattice strain, surface oxygen consumption and cathode particle deterioration. Among them, the transient performance of particle size of material remains the key factor of diffusion and deterioration process. Once the electrochemical process is interrupted for diffraction measurement, the charge rebalancing will occur, the movement of lithium ions will be along the radial direction of the particles and the anisotropy of the lattice parameters will be masked. Therefore, it is indispensable to use high-resolution experimental technology (such as submicron focused operando synchrotron radiation X-ray diffraction and in situ stacking tomography nano imaging) in time and space dimensions in order to explore the undisturbed charge discharge process for better understanding of the potential decomposition degradation mechanism [42] (Fig. 3). Researchers have carried out a series of improvement strategies such as lattice doping, surface coating, morphology design, regulating the crystal structure and electrolyte modification on the performance degradation mechanism of Ni-rich layered oxide cathode materials. In addition to the conventional doping, coating and electrolyte modification, the current research technologies for large-scale production include single crystal

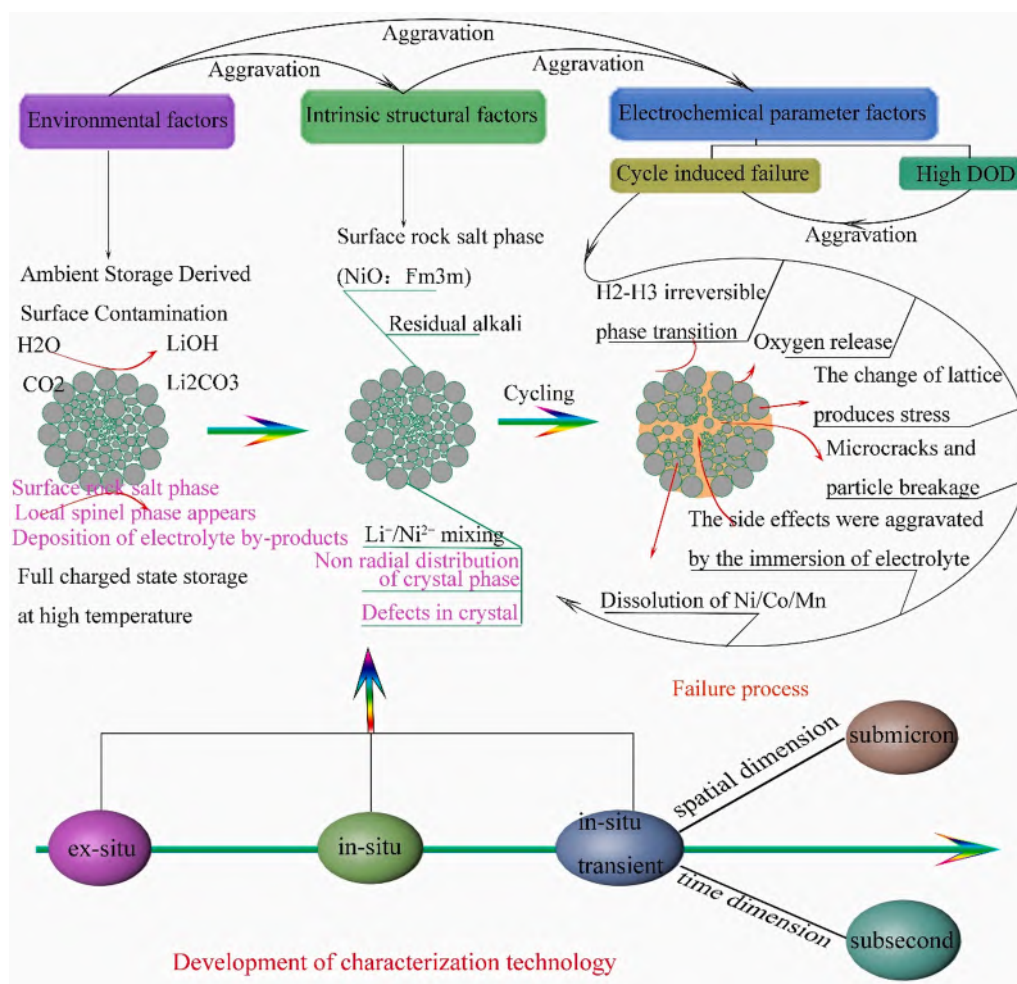


Fig. 3. Schematic diagram of failure factors, evolution process and characterization technology development of Ni-rich layered cathodes.

preparation [47] and regulating the morphology (core-shell, radial primary particles, etc.) [48,49].

In this paper, the synthesis, structure and redox mechanisms of Ni-rich cathode materials are briefly introduced. As a key point, we have mainly focused on the failure mechanism of Ni-rich cathode materials, through a large number of recent research progress analyses. For the first time, the three factors and their mutual influence on the failure of Ni-rich cathode materials have been summarized. Furthermore, combined with some advanced characterization techniques, the latest capacity failure mechanism (such as temperature effect at full charge; charge distribution guided by grain crystallographic orientations in polycrystalline battery materials; structural evolution induced by crystal defects; influence of discharge depth et al.) of Ni-rich cathode materials and the modification approaches to solve these problems are analyzed (Fig. 4). Also, a detailed venation chart, depicting the remaining challenges and perspectives of Ni-rich oxide materials in recent years has been drawn. Finally, the new insights of Ni-rich cathode materials are discussed, which expand the research fields and promote their practical applications.

## 2. Preparation methods and electrochemical performances

The preparation methods have a significant influence on the micro-structure and electrochemical properties of Ni-rich layered materials. High temperature solid phase method, co-precipitation method, sol-gel method, spray drying method and combustion method are the few major synthesis techniques discussed here in detail.

### 2.1. High temperature solid phase method

In high temperature solid state method, the lithium source and the transition metal salt in accordance with the stoichiometric ratio are directly taken in the ball mill. The uniform mixture thus formed is pre-sintered at low temperature followed by sintering of the same at a higher temperature, to obtain the desired powder products. The non-uniformity of reaction during the synthesis has been considered as the major drawback of this method. The morphology and particle size distribution of the prepared materials are quite different. Consequently, only a few researchers use this method to synthesize Ni-rich cathode materials, and it is also not suitable for industrial production. Caballero et al. [50] developed a simple, rapid and direct method for synthesizing nano-crystalline oxides with either layered or spinel structures, including  $\text{LiMn}_2\text{O}_4$ ,  $\text{LiCoO}_2$ ,  $\text{LiNi}_{0.5}\text{Mn}_{1.5}\text{O}_4$ , and  $\text{LiCo}_{0.5}\text{Ni}_{0.5}\text{O}_2$ . The approach is based on the thermal decomposition by one step solid-state metathesis reactions of mixed nano-crystalline oxalates formed by grinding oxalic acid and hydrated salts. Saavedra-Arias et al. [51] synthesized  $\text{LiNi}_{0.8}\text{Co}_{0.1}\text{Mn}_{0.1}\text{O}_2$  cathodes by solid-state reaction route using  $\text{Li}_2\text{O}$ ,  $\text{NiO}$ ,  $\text{Co}_3\text{O}_4$  and  $\text{MnO}_2$ . The reagent mixtures were first ball-milled for 24 h in isopropanol and the resulting mixture was dried at 60 °C. Subsequently, the powder was calcined at 450 °C for 4 h and sintered at higher temperatures. X-ray diffraction (XRD) and Raman scattering (RS) spectra of various stages of lithiation-delithiation processes portrayed that the well layered structure is maintained throughout the electrochemical process along with the systematic change of lattice parameters in the range of 3.0–4.5 V. The initial discharge capacity obtained was 132 mAh g<sup>-1</sup>.

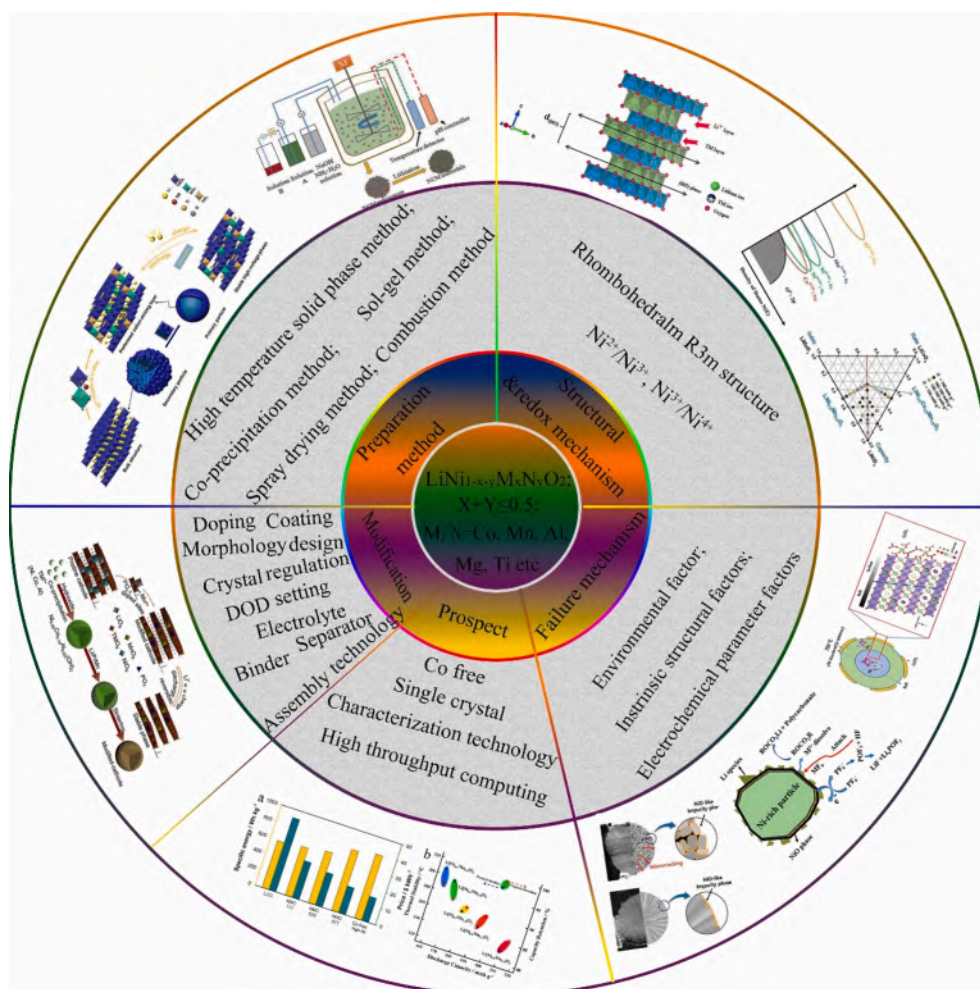


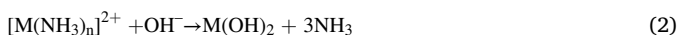
Fig. 4. Schematic diagram of structural characteristics, preparation method, failure mechanisms and modification of Ni-rich layered cathodes.



while the capacity retention rate was 86% after 20 cycles.

## 2.2. Co-precipitation method

Co-precipitation method can address the problems of inhomogeneous mixture and wide particle size distribution which were found in traditional solid-phase method. By controlling the concentration of raw materials, droplet acceleration, stirring speed, pH value and reaction temperature, core-shell structure, spherical, nano flower and other morphologies with uniform particle size distribution can be prepared. The development of Ni-rich materials cannot be separated from the promotion of precursors. At present, Ni-rich materials face problems of secondary spherical particles breaking and pulverizing, which not only prevents it from participating in the charging-discharging process, but also creates more side reactions in the new interface of cracks. The above problems deteriorate the comprehensive performance in LIBs. In order to obtain a stable granular crystal structure and excellent comprehensive performance, it is necessary to design the whole process from the precursors. The co-precipitation method is a feasible approach for industrialized preparation of Ni-rich materials precursors [52]. For better understanding of the growth mechanism of Ni-rich precursors, a brief description of their formation has been provided. The precursor is prepared by mixing Ni, Co and Mn salts together and forming a soluble mixed solution. Hereafter,  $\text{NH}_3$  and  $\text{NaOH}$  are further added to the former solution to form Ni-rich materials precursors by controlled reaction conditions. The reaction equations are as follows.



From the above equation it can be seen that M salt first reacts with the  $\text{NH}_3 \cdot \text{H}_2\text{O}$  to form  $[\text{M}(\text{NH}_3)_n]^{2+}$ , and then  $\text{OH}^-$  replaces to form  $\text{M}(\text{OH})_2$ . In order to show the reaction process more vividly, Yang et al. [53] used the stick model in the above equation. Reaction equations and the stick growth model can provide a clear picture of the growth process of primary particles. By controlling the reaction conditions viz. temperature, pH, stirring and flow rate, the primary particles were gradually agglomerated into spherical secondary particles. Islam et al. [54], through his experiments, offered a better understanding of the influence of reaction conditions on the co-precipitation process.  $\text{LiNi}_{0.6}\text{Mn}_{0.2}\text{Co}_{0.2}\text{O}_2$  materials were synthesized by co-precipitation method and the effects of the synthesis parameters such as stirring speed, pH and sintering temperature on the structural characteristic, particle size, morphology and cyclic stability were discussed in detail. The results show that the pH is the most important factor for the synthesis of precursor, because it affects the tap density and the morphology. The pH value of 10.8 exhibits the highest tap density. Stirring speed has a great impact on the crystallization process. As the stirring speed increases, the particle morphology changes from irregular agglomeration to dense spherical particles. However, when the stirring speed reached 1200 rpm, the particle morphology was destroyed, which resulted in cracking. XRD peaks showed that with the upsurge of sintering temperature from 780 °C to 860 °C, the value of  $I(003)/I(104)$  increased signifying a better layered structure. However, due to Li/Ni mixing, when the temperature escalated to 900 °C, the value of  $I(003)/I(104)$  decreased. The samples, when sintered at 860 °C, exhibited best electrochemical properties (168 mAh g<sup>-1</sup> at 0.5C). Park et al. [55] synthesized  $\text{LiNi}_{0.90}\text{Co}_{0.05}\text{Mn}_{0.05}\text{O}_2$  cathode material by co-precipitation method. The synthesized cathode material was charged and discharged at a current density of 0.1C in the voltage window ranging from 2.7 to 4.3 V. The discharge specific capacity of the composite was found to be 230 mAh g<sup>-1</sup>, and the capacity retention was 89% after 50 cycles.  $\text{LiNi}_{0.95}\text{Co}_{0.05}\text{O}_2$  cathode material was synthesized by Wu et al. [56] via co-precipitation method and exceptional cycle ability with capacity retention of 69.68% after 100 cycles at 0.1C was demonstrated by the material.

## 2.3. Sol-gel method

Sol-gel method is a synthesis technique which involves compounds containing high chemically active components as precursors. These raw materials are mixed in the liquid phase and are hydrolyzed. Thereafter, chemical reactions condense and form a stable sol-gel system/phase. The gel with a three-dimensional spatial network structure is formed by aging and slow aggregation of colloidal particles. The stoichiometric ratio of this method is precisely controlled, and some trace elements can be doped uniformly and quantitatively at the molecular level. The reaction is easy to execute, the required temperature is low, with good morphology [57]. Chandrasekar et al. [58] prepared  $\text{Ni}_{0.7}\text{Co}_{0.15}\text{Mn}_{0.15}(\text{OH})_2$  precursor by a solvothermal method using  $\text{Ni}(\text{CH}_3\text{COO})_2$ ,  $\text{Co}(\text{CH}_3\text{COO})_2$  and  $\text{Mn}(\text{CH}_3\text{COO})_2$ . Stoichiometric amount of metal acetate was first dissolved in 50 ml of anhydrous alcohol and deionized water having a volume ratio of 4:1 and thereby transferred to a teflon-lined stainless-steel autoclave followed by heating at 200 °C for 12 h. Finally, the obtained slurry was filtered and washed with anhydrous alcohol and then dried.  $\text{Li}_2\text{CO}_3$  and the  $\text{Ni}_{0.7}\text{Co}_{0.15}\text{Mn}_{0.15}(\text{OH})_2$  precursor in accordance with the stoichiometric ratio of 1.05:1 were thoroughly blended and the mixture was sintered at 480 °C for 5 h and 800 °C for 12 h in an atmosphere of  $\text{O}_2$ . Lu et al. [59] also prepared NCM811 cathodes by sol-gel and co-precipitation methods. The XRD patterns depicted that NCM811 positive electrode synthesized by these two methods can form a good layered structure. Rietveld refinement revealed some disparity in the degree of cation disorder between the two materials, among which the samples prepared by sol-gel method showed lower Li/Ni cation disorder. SEM and BET measurements revealed that the sol-gel samples were composed of relatively small aggregate particles with larger BET surface area compared to the co-precipitation samples. The electrochemical test showed that the material prepared by sol-gel method delivered better initial discharge capacity of 200 mAh g<sup>-1</sup> with capacity retention rate of 82.2% after 50 cycles at 0.5C.

## 2.4. Spray-drying method

Spray drying method uses atomizing equipment to atomize the reaction solution and leads it into the reactor, so that the solution gets rapidly evaporated and dried. The process is simple, can prepare a large number of precursors in a short time, and the raw materials can be uniformly mixed at atomic level, with extraordinary consistency of particle size and regular morphology making it an efficient synthesis method. Li et al. [60] prepared  $\text{LiNi}_{1/3}\text{Mn}_{1/3}\text{Co}_{1/3}\text{O}_2$  cathodes by a spray dry process between  $\text{Ni}(\text{CH}_3\text{COO})_2 \cdot 4\text{H}_2\text{O}$ ,  $\text{Mn}(\text{CH}_3\text{COO})_2 \cdot 4\text{H}_2\text{O}$ ,  $\text{Co}(\text{CH}_3\text{COO})_2 \cdot 4\text{H}_2\text{O}$  and  $\text{LiNO}_3$ . The stoichiometric amount of metal acetates were first dissolved in deionized water to obtain the starting solution and then was pumped into a spray dry instrument followed by pre-heating at 400 °C and sintering for 15 h in air. Yue et al. [61] also prepared micron-sized  $\text{LiNi}_{0.6}\text{Co}_{0.2}\text{Mn}_{0.2}\text{O}_2$  cathode material at various sintering temperatures by spray drying method with a molar ratio of Li/Me = 1.04, and studied the effect of sintering temperature on the crystal structure, morphology and electrochemical properties of the material. The results showed an enhancement in the volume of a and c with the rise of sintering temperature. The particle prepared at 850 °C was an irregular primary aggregation with a size of 1 μm as well as of low cationic mixing degree. It exhibited a discharge capacity of 173 mAh g<sup>-1</sup> of 0.1C and capacity retention of 89% after 50 cycles, which proved to be better than materials prepared at other temperatures.

## 2.5. Combustion method

The combustion method involves mixing of the raw metal salt with the fuel to form a dry gel at low temperature. Next, the dry gel is heated to a high temperature to make the system undergo combustion and exothermic reaction occurs resulting in the formation of precursor

powder comprising of extremely fine particles. The powder is then roasted at a high temperature to obtain the final product. Ahn et al. [62] prepared micron-sized  $\text{LiNi}_{0.6}\text{Co}_{0.2}\text{Mn}_{0.2}\text{O}_2$  cathode material by this method. Scanning electron microscopy (SEM) showed that a large number of spherical particles with a diameter of 100 nm agglomerated into secondary particles. The ratio of  $\text{Ni}^{3+}/(\text{Ni}^{2+}+\text{Ni}^{3+})$  prepared at 800 °C was found close to their theoretical value. It exhibited a discharge specific capacity of 170.1 mAh g<sup>-1</sup> while the capacity retention rate was 98.2% after 30 cycles.

### 3. Structure and redox mechanisms

The general structure of nickel rich layered oxide cathode materials  $\text{LiNi}_x\text{Co}_y\text{Mn}_z\text{O}_2$  ( $x > 0.6$ ) is in form of a rhombohedral  $\text{R}\bar{3}\text{m}$  structure, which can be derived from the ordered rock-salt structure of  $\alpha\text{-NaFeO}_2$  (Fig. 5) [63,64]. Li occupies octahedral 3b sites and Ni, Co and Mn (TMs) occupy octahedral 3a sites disorderly [65,66]. The formation of the whole crystal is designed by alternate stacking of  $[\text{MO}_6]$  octahedron layer and  $[\text{LiO}_6]$  octahedron layer [67], which is appropriate for lithium ion intercalation and de-intercalation. However, the ionic radius of  $\text{Ni}^{2+}$  (0.069 nm) is approximately similar to that of  $\text{Li}^+$  (0.076 nm). Hence,  $\text{Ni}^{2+}$  can easily occupy  $\text{Li}^+$  slabs and vice versa, resulting in the cationic mixing, increase of cell parameter  $a$ , and the weakening of the intensity of the diffraction peak (003) [68,69]. Cation disordering between these two sites of  $\text{Li}^+$  and  $\text{Ni}^{2+}$  can compromise the structural stability of nickel rich layered oxide cathode materials. This is because during sintering,  $\text{Ni}^{2+}$  is oxidized to  $\text{Ni}^{3+}$  at a high temperature and oxygen atmosphere. However, the energy barrier of  $\text{Ni}^{2+}$  to  $\text{Ni}^{3+}$  is elevated, making it difficult for  $\text{Ni}^{2+}$  to get completely oxidized even in pure oxygen atmosphere. The remaining  $\text{Ni}^{2+}$  will still occupy 3a sites, which will further reduce the cation mixing. In order to preserve the charge balance, part of  $\text{Ni}^{2+}$  will occupy 3b sites. In addition, while charging, the minimal valence nickel in the transition metal layer will migrate to the lithium layer, occupying the lithium vacancy, and form the cation mixing arrangement.

The redox reactions of  $\text{Ni}^{2+}/\text{Ni}^{3+}/\text{Ni}^{4+}$ ,  $\text{Co}^{3+}/\text{Co}^{4+}$  electron pairs mainly take place during the charging and discharging process. Mn has no electrochemical activity and does not participate in the redox reaction, but has a role in stabilizing the materials. Nevertheless, the structure of nickel rich layered oxide cathode materials is very unstable due to the release of a large number of  $\text{Li}^+$ . Material cycle capacity decay and deterioration in its thermal stability can be considered as its two significant outcomes. The ionic radius of  $\text{Ni}^{2+}$  in Li layer is less than that of  $\text{Li}^+$ . This reduces the thickness of inter-wafer and oxidizes it into  $\text{Ni}^{3+}$  or  $\text{Ni}^{4+}$  during charging, resulting in the partial collapse of inter-wafer space. Also, during discharging, it makes the ion embedment of  $\text{Li}^+$  more difficult, thus reducing the reversible capacity of materials. When

$\text{Li}^+$  enters the transition metal layer, the thickness of the main wafer will get enlarged. Thereby, it will be tough to get detached which in turn will depreciate the electrochemical performance of the material. Therefore, the smaller the inter-wafer thickness, the more difficult it is for  $\text{Li}^+$  to be re-embedded. [70-73] The degree of ion mixing can be characterized by  $c/a$  and  $I(003)/I(104)$  value. When  $c/a$  greater than 4.9 and  $I(003)/I(104)$  greater than 1.2, the degree of ion mixing is low. [74,75] In addition, (006)/(102) crystal plane and (108)/(110) crystal plane have two pairs of splitting degree of the diffraction peaks [75,76], which reflect the integrity of the layered structure and have a greater impact on the electrochemical properties of nickel rich layered oxide cathode materials. [77-81] The greater splitting degree of the two pairs of diffraction peaks is accountable for the complete layered structure of  $\text{NaFeO}_2$ , as well as for improved electrochemical properties. Therefore, during synthesis, it is necessary to maintain a suitable  $\text{Li}^+/\text{Ni}^{2+}$  ratio, low mixing degree and complete layered structure for improving the electrochemical performance of nickel rich layered oxide cathode materials. Increasing Ni content can intensify the material capacity but decrease the cycle performance and stability. Increase in Co content can inhibit phase transformation and improve the rate performance. [72,73,82,83] Increasing Mn content can improve the structural stability, but reduce the capacity. Enterprises can reduce the content of Ni and increase the proportion of Co and Mn in the production process in order to enhance the cycle performance and thereby attaining a prolonged product life. [84,85] Moreover, Ni gains and loses electrons in the oxidation-reduction process, while it is difficult for  $\text{Co}^{3+}$  to get oxidized in nickel rich layered oxide cathode materials. The 3 deg energy levels of  $\text{Ni}^{2+}/\text{Ni}^{3+}$ ,  $\text{Ni}^{3+}/\text{Ni}^{4+}$  are higher than those of  $\text{Co}^{3+}/\text{Co}^{4+}$   $3d_{2g}$  (Fig. 6a). [86] Therefore, in the charging process,  $\text{Ni}^{2+}/\text{Ni}^{3+}$ ,  $\text{Ni}^{3+}/\text{Ni}^{4+}$  oxidation process takes place preferentially, and the corresponding HOMO energy levels are higher than  $\text{Co}^{3+}/\text{Co}^{4+}$ . The charge-discharge voltage of nickel rich layered oxide cathode materials is less than  $\text{LiCoO}_2$ . At most 0.8 lithium can be separated from the layered structure under the same voltage [87,88], so high nickel containing materials can transfer more electrons than  $\text{LiCoO}_2$ , that is, their charge-discharge capacity is higher than  $\text{LiCoO}_2$ . [89,90] In addition,  $\text{Co}^{3+}/\text{Co}^{4+}$   $t_{2g}$  overlaps with the top of  $\text{O}^{2-}$  2p energy level, while  $\text{Ni}^{3+}/\text{Ni}^{4+}$  overlaps only by a small part, indicating that  $\text{LiNiO}_2$  is more stable at higher voltage. During the charging and discharging process of nickel-rich layered oxide, the valence state of  $\text{Mn}^{4+}$  remains unchanged, which stabilizes the layered structure of the material, hence, the safety is improved. The capacity is mainly provided by  $\text{Ni}^{2+}/\text{Ni}^{3+}$ ,  $\text{Ni}^{3+}/\text{Ni}^{4+}$  pairs. The addition of Co can improve the conductivity and rate performance from the synergistic effects of Ni, Co and Mn (Fig. 6b) [12].

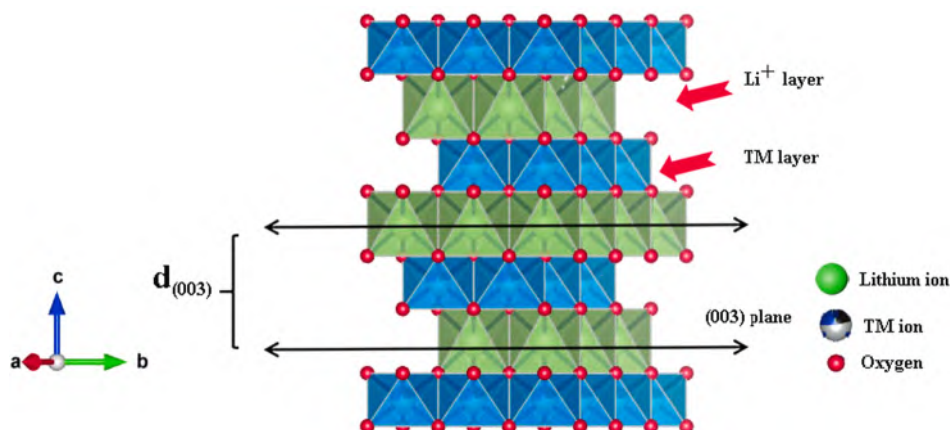


Fig. 5. Crystal structure of layered  $\text{LiNi}_x\text{Co}_y\text{Mn}_z\text{O}_2$  cathodes.

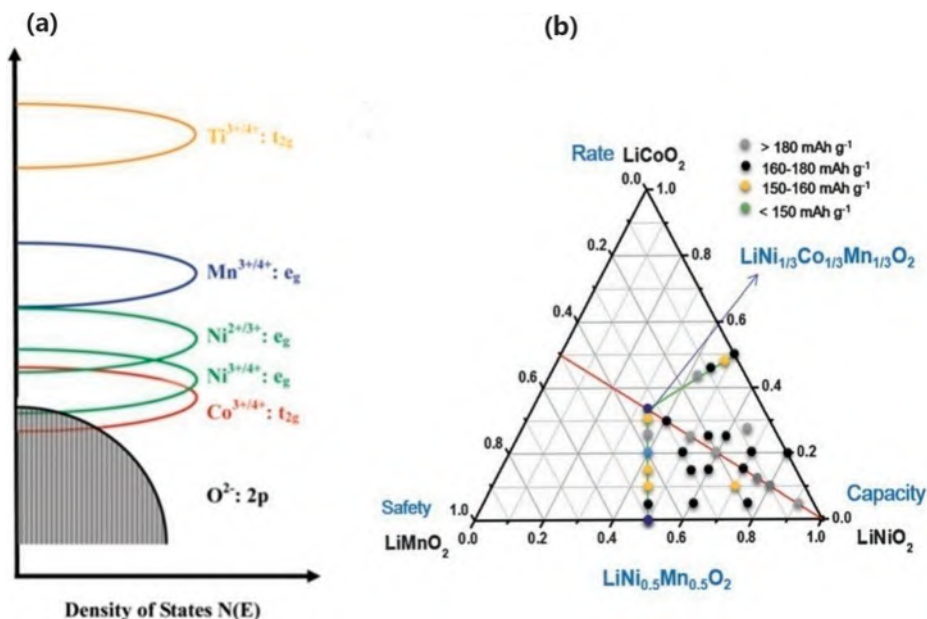


Fig. 6. (a) Schematic diagram of energy levels of layered electrons. Reproduced with permission. [86] Copyright 2011, American Chemical Society. (b) Compositional phase diagrams of lithium stoichiometric-layered transition-metal oxide:  $LiCoO_2$ - $LiNiO_2$ - $LiMnO_2$ . Reproduced with permission. [12] Copyright 2008, Royal Society of Chemistry.

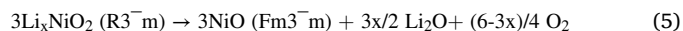
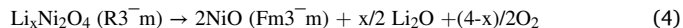
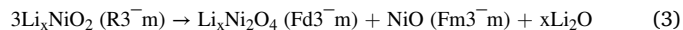
#### 4. Capacity failure mechanism and characterization technology

The failure of nickel rich layered oxide cathode materials are related not only to its surface rock salt phase ( $NiO$ ), residual alkali and its internal structural ( $Li^+/Ni^{2+}$  mixing) characteristics, but also to a series of complex evolution processes during lithiation-delithiation as mentioned above. Further elucidating the failure mechanism has a great significance in the preparation and development of nickel rich cathode materials. With the development of characterization technology, especially in the application of in-situ electrochemical characterization and in-situ electrochemical transient characterization technology, these experimental techniques with high resolution in time and space dimension can demonstrate the potential degradation mechanism at a higher depth.

##### 4.1. $Li^+/Ni^{2+}$ cation mixing

During the preparation of Ni-rich oxide cathodes, a complete oxidation of  $Ni^{2+}$  to  $Ni^{3+}$  is extremely difficult. As a result, there remains a small amount of  $Ni^{2+}$  in Ni-rich oxide cathodes. Furthermore, the radius of  $Ni^{2+}$  (0.069 nm) is very close to that of  $Li^+$  (0.076 nm), and  $Ni^{2+}$  can easily occupy the 3b sites of  $Li^+$ , resulting in the  $Li/Ni$  mixing. [63]  $Li/Ni$  mixing not only occurs in the synthesis of materials, but also during the charge-discharge process, which significantly affects the electrochemical properties including initial capacity, reversible capacity and cycle performance. During first charging,  $Li^+$  in both the lithium layer and the transition metal layer can be deintercalated, but in the first discharge, part of  $Li^+$  cannot return to the positive lattice due to the  $Li^+/Ni^{2+}$  mixing, which results in the lower efficiency (typically less than 90%) and increase in the irreversible capacity. When  $Ni^{2+}$  occupies the lithium layer, the thickness of the inter-granular layer will be reduced, and the redox reaction of  $Ni^{2+}/Ni^{3+}$ ,  $Ni^{3+}/Ni^{4+}$  will occur during the charging process. The ionic radius will be further reduced, which will cause the partial structural collapse of the space of the inter-granular layer, hinder the migration of  $Li^+$  during the charging and discharging process, increase the impedance, and lead to poor cycle stability. When  $Ni^{2+}$  occupies the  $Li^+$  site completely, the space group structure of cathode materials changes from layered phase ( $R3\bar{m}$ ) to the spinel-like phase ( $Fd3\bar{m}$ ) and rock-salt phase ( $Fm3\bar{m}$ ) during cycling at an elevated temperature, which in turn increases the diffusion of  $Li^+$  and

induces poor thermal stability [91]. Cation mixing occurs not only during the synthesis of nickel rich cathode materials but also during the electrochemical cycling process. The processes are represented by the reactions which are as follows [52,92,93]:



New characterization techniques can help to further analyze the structural changes caused by cation mixing. For instance, Kim et al. [94] reported the structural degradation mechanism of  $LiNi_{0.6}Co_{0.2}Mn_{0.2}O_2$  electrode by HAADF-STEM analysis. They realized that the surface crystal structures suffer from an irreversible transition from the pristine rhombohedral structure to a mixture of spinel as well as rock-salt phases as shown in (Fig. 7a-b). In addition, Han et al. [95] also exemplified that  $LiNi_{0.8}Co_{0.8}Mn_{0.1}O_2$  material's surface has a thin cation disordered layer during the synthesis process. Both regions 1 and 2 exhibit an uneven  $NiO$ -type cation mixed layer with a thickness of 1–2 nm (Fig. 7c-d). Zou et al. [96] also observed the crystal structure rearrangement after lithium deintercalation by using transmission electron microscope (TEM). Some regions of the layered surface changed into layered/rock salt mixed structure. The structure gradually changed from the inside to the surface of the material particles, respectively: ordered layered structure ( $\alpha$ - $NaFeO_2$ ), partially ordered structure and disordered rock salt phase structure ( $NiO$ ). This transformation can be attributed to the mixture of transition metal ions and lithium ions along with the formation of rock salt phase as the precursor of particle crack (Fig. 7e-g). Zhao et al. [97] studied the phase transformation caused by mixed cation in the preparation of  $LiNi_{0.8}Co_{0.2}O_2$ , and optimized the sintering process (sintering temperature, sintering atmosphere and holding time), which greatly reduced the loss of Li and the formation of  $NiO$  rock salt phase on the surface of the structure. It also facilitated in obtaining a higher order  $LiNi_{0.8}Co_{0.2}O_2$  layered structure and the mixed discharge rate of  $Ni^{2+}/Li^+$  ions was found to be less than 2%. The specific capacity of the optimized high nickel layered anode material under wide working voltage (2.7–4.6 V) range reached more than 220 mAh  $g^{-1}$ , and the cycle stability was significantly improved (Fig. 7h). Duan et al. [98]



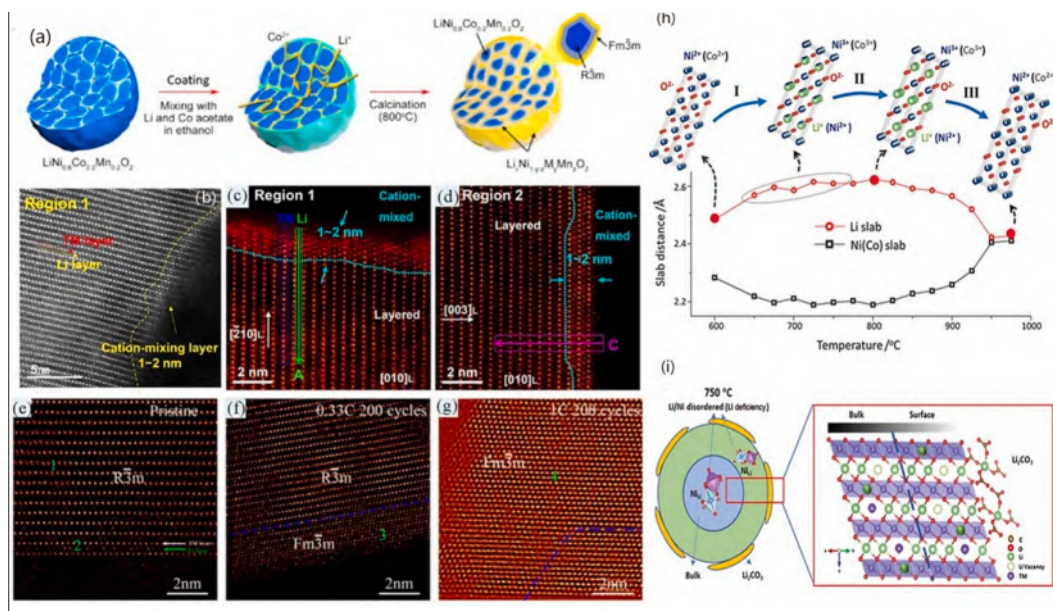


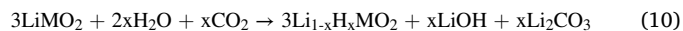
**Fig. 7.** Illustrations of the phase transformation from well-ordered layered structure (R-3 m) to the disordered spinel structure (Fd-3 m) and/or the rock-salt structure (Fm-3 m). (a) Schematic diagram of the surface treatment on the primary particles. (b) HAADF-STEM images of 622. Reproduced with permission.[94] Copyright 2015, American Chemical Society. (c-d) STEM images of pristine 811. Reproduced with permission.[95] Copyright 2018, American Chemical Society. (e) HAADF-STEM image of the pristine sample showing the majority of the bulk maintains R3' m structure. The white and green arrows point to the TM layer and Li layer. (f and g) HAADF-STEM image of the 200-cycle  $\text{LiNi}_{0.76}\text{Co}_{0.10}\text{Mn}_{0.14}\text{O}_2$  at 0.33C and 1C. The blue dashed lines outline the boundary of the converted phase, below and above which are the disordered rock salt and layered structure. Reproduced with permission.[96] Copyright 2018, American Chemical Society. (h) Schematic illustration of the phase evolution, cationic ordering of the intermediates. Reproduced with permission.[97] Copyright 2016, Wiley-VCH. (i) Schematic illustrations of how cationic ordering is coupled to surface reconstruction of NMC71515 under different sintering temperatures. Reproduced with permission.[98] Copyright 2019, The Royal Society of Chemistry. (For interpretation of the references to color in this figure legend, the reader is referred to the web version of this article.)

concluded that surface reactions have substantial impacts on the cationic ordering/disordering kinetics in the bulk. Insufficient sintering temperatures do not provide enough driving force for  $\text{Li}_2\text{CO}_3$  decomposition as well as Li-ion diffusion during the ordering process, leading to the cation mixing  $\text{Li}^+$  and  $\text{Ni}^{2+}$  (Fig. 7i). In order to gain a deeper understanding of the correlation between surface chemistry and performance decay, Zhang et al. [99] synthesized nickel rich single crystal cathode materials and used operando X-ray spectroscopy imaging and nano-tomography to monitor the compositional and structural evolution before and after 200 cycles. The redox reaction occurred along all directions and phase-transition fronts propagated drastically during the initial cycle, indicating a high electrochemical reversibility. Nevertheless, high reversibility failed to survive after 200 cycles. Operando X-ray spectroscopy imaging and nano-tomography chemical phase mapping unambiguously revealed the above outcomes. Four representative regions from the bulk to the surface were selected and the corresponding content of Ni oxidation states was illustrated. The 2D histogram highlights inhomogeneous Ni oxidation state distribution within the single crystal particle. Reaction heterogeneity and high irreversibility are ascribed to the characteristics of surface chemicals rock-salt phase on pristine single crystal cathodes, which may induce heterogeneous internal strain within the particle, and further results in the structural/performance degradation, as evidenced from the chemical composition analysis.

#### 4.2. Surface side reaction

Due to the volatilization of lithium at high-temperature calcination, excessive lithium is often needed in the preparation of nickel-rich layered oxide cathode materials ( $\text{LiNi}_{1-x}\text{M}_x\text{O}_2$ ;  $x \leq 0.5$ ; M = Co, Mn, Al, Mg, Ti etc). The remaining active lithium oxides ( $\text{Li}_2\text{O}$ ,  $\text{Li}_2\text{O}_2$ ) adhere to the surface of the materials, react with  $\text{H}_2\text{O}$  and  $\text{CO}_2$  in the air, and form LiOH and  $\text{Li}_2\text{CO}_3$  layers (Fig. 8) [100]. The Ni content increases by over 70 % and have a dynamic high affinity towards moisture and  $\text{CO}_2$

in ambient air. They primarily react to form LiOH,  $\text{Li}_2\text{CO}_3$  on the surface, which is commonly termed as “residual lithium”. When Ni-rich layered oxide cathode materials ( $\text{LiNi}_{1-x}\text{M}_x\text{O}_2$ ;  $x \leq 0.5$ ; M = Co, Mn, Al, Mg, Ti etc.) are exposed in air, they are more likely to absorb  $\text{CO}_2$  and  $\text{H}_2\text{O}$  in the air to generate  $\text{CO}_3^{2-}$  and  $\text{OH}^-$ , and further react with residual lithium to generate  $\text{Li}_2\text{CO}_3$  and LiOH. In addition, NiO was found to form on the surface of Ni-rich cathodes because of the exhaustion of Li and evolution of lattice oxygen (Fig. 8a). The reactions are stated as follows [101-105]:



The existence of  $\text{Li}_2\text{CO}_3$  and LiOH will cause several complications. (1)  $\text{Li}_2\text{CO}_3$  and LiOH not only consume  $\text{Li}^+$  in the material, but also have no electrochemical activity. This further instigates capacity attenuation. Moreover, dense  $\text{Li}_2\text{CO}_3$  layer on the materials surface will hinder the  $\text{Li}^+$  diffusion, and cause irreversible capacity loss in the process of cyclic charging and discharging. Further decomposition of  $\text{Li}_2\text{CO}_3$  during high-voltage charging generates  $\text{CO}_2$  inside the cell, thus threatening the safe operation of the battery (Fig. 8b-c). (2) LiOH reacts with PVDF and  $\text{LiPF}_6$ , which has a negative effect on battery process and performance. In the preparation of Ni-rich cathodes slurry, PVDF dissolves in NMP and the basic groups on the surface of the material attack the adjacent C-F and C-H bonds. PVDF is also prone to bimolecular elimination reaction, forming a part of C = C bond with the molecular chain. It transforms the slurry into a gel state and restrains from adequate coating. (3) LiOH reacts with Al foil as shown below:

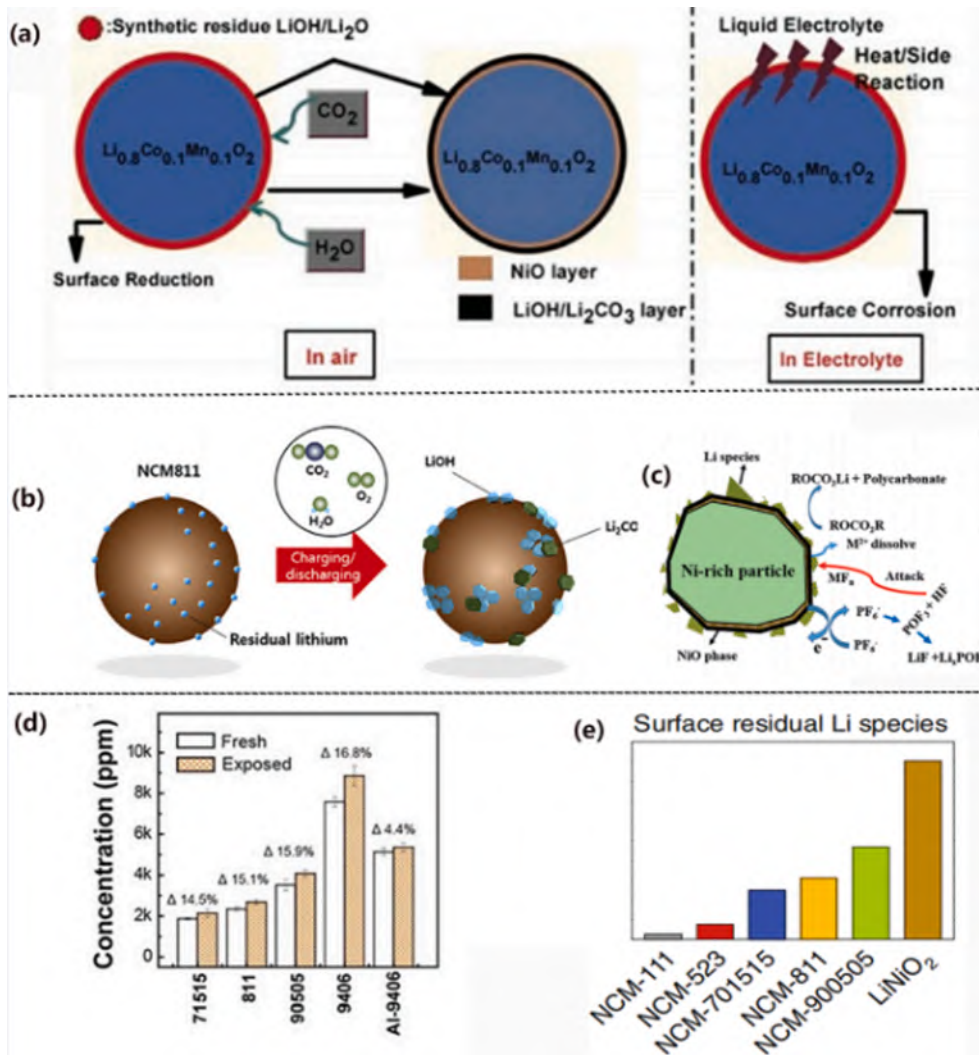
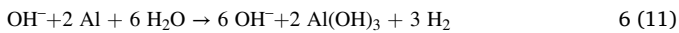
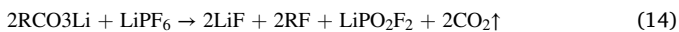
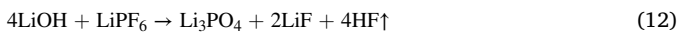


Fig. 8. (a) Scheme of  $\text{Li}(\text{Ni}_{0.8}\text{Mn}_{0.1}\text{Co}_{0.1})\text{O}_2$  and its impact on suppressing unfavorable side reactions at the cathode-electrolyte interface. (b). Residual lithium change of NCM811 during charging/discharging. Reproduced with permission.[107] Copyright 2019, Elsevier. (c) The microstructure and composition of the solid-electrolyte interface at the surface of Ni-rich cathode materials. Reproduced with permission.[12] Copyright 2015, Wiley-VCH. (d) Concentration of residual Li species on high-Ni layered oxides with various nickel contents before and after being exposed to ambient air for 30 days. (e) accumulation of surface residual Li compounds. Reproduced with permission.[106] Copyright 2018, Wiley-VCH.



After the corrosion of Al, the electrochemical performance and safety of the battery is utterly affected. (4)  $\text{LiOH}$  also reacts with  $\text{LiPF}_6$ , which consumes  $\text{Li}^+$  in electrolyte and generates  $\text{HF}$  gas. It can corrode the metal parts inside the battery and cause battery leakage. Moreover,  $\text{HF}$  can destroy SEI and react with SEI continuously.



In summary, degradation caused in the process of material synthesis, storage and charge discharge of lithium-ion batteries initiates from the modification of the surface structure. It is also found that different materials have different reactivity to carbon dioxide and water in the air. You et al. [106] showed that the residual lithium content on the surface of the same composite material increases with the increase in nickel content (71715, 811 and 9055) (Fig. 8d-e).

#### 4.3. Irreversible phase transition

The irreversible phase transformation of Ni-rich layered oxide cathode materials occurs easily in the state of deep lithium intercalation, leading to the degradation of the particle surface structure. In the

process of charging and discharging, phase transformation occurs four times along with the intercalation and deintercalation of lithium ions. When the voltage is less than 4.2 V, the transformation takes place from hexagonal phase H1  $\rightarrow$  monoclinic phase M  $\rightarrow$  hexagonal phase H2; when the voltage is greater than 4.2 V, the transformation takes place from hexagonal phase H1  $\rightarrow$  monoclinic phase M  $\rightarrow$  hexagonal phase H2  $\rightarrow$  H3; when the voltage is greater than 4.2 V, H2  $\rightarrow$  H3 is an irreversible phase transition, which seriously affects the cyclic stability of nickel-rich layered oxide cathode materials.

Zhang et al. [108] introduced the H2-H3 phase transition of  $\text{LiNi}_{0.80}\text{Co}_{0.10}\text{Mn}_{0.10}\text{O}_2$  near 4.1 V, accompanied by the release of lattice oxygen. The precipitated lattice oxygen oxidizes the electrolyte, and transforms the material from layered structure to spinel structure and rock salt structure, resulting in the continuous decline of discharge capacity and voltage platform of  $\text{LiNi}_{0.80}\text{Co}_{0.10}\text{Mn}_{0.10}\text{O}_2$  under high voltage (Fig. 9a-b). In the process of charge and discharge of nickel rich cathode materials, the existence of H3 phase can be used as a performance index to reflect the state of high capacity transmission and high degree of lithium removal. In fact, a large number of Li vacancies in the state of highly deintercalation will weaken the structural stability and induce structural transition. In order to improve the reversibility of H2-H3 phase transformation in nickel-rich layered oxide cathode materials, element of doping radius similar to  $\text{Li}^+$  (0.076 nm) can improve the stability. Wu et al. [56] synthesized  $\text{Ti}^{4+}$  doped  $\text{LiNi}_{0.9}\text{Co}_{0.1}\text{O}_2$  cathode material which not only improved the stability of the structure, but also



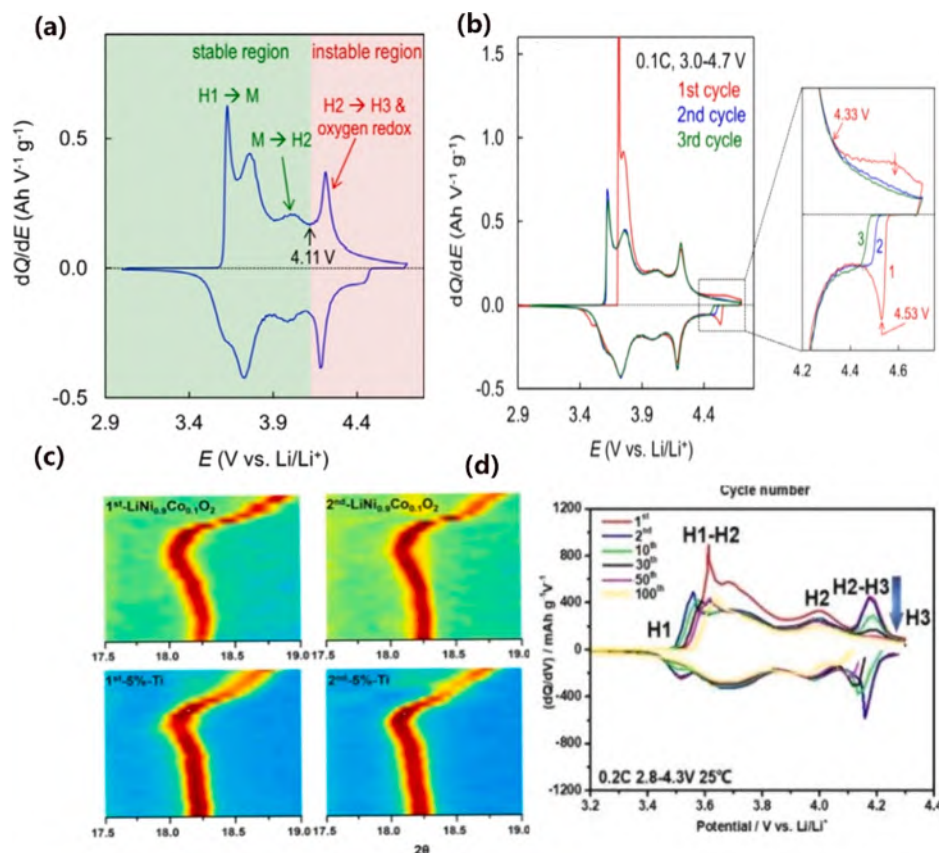


**Fig. 9.** (a) Typical pattern of the differential capacity vs. cell's voltage for Li/NCM811 cells. (b) plot of differential capacity vs. cell voltage. Reproduced with permission.[108] Copyright 2020, Elsevier. (c) In situ XRD (d) plot of differential capacity vs. cell voltage. Reproduced with permission.[56] Copyright 2019, Elsevier.

restrained the irreversible phase transition in the process of charging and discharging. A repeated appearance of the H3 phase during the charge discharge cycle was induced by the improvement in the reversibility of H2-H3 phase transformation. It also maintained a high capacity output. At the same time, H3 phase ensured excellent cycling stability of the material. After 100 weeks at 38 mA g<sup>-1</sup> cycles, the retention rate of modified LiNi<sub>0.9</sub>Co<sub>0.1</sub>O<sub>2</sub> material was significantly increased from 69.7 to 97.9%. In order to observe the phase transition process directly, the undoped and Ti<sup>4+</sup> doped samples were characterized by in-situ XRD. During the second cycle of charging, when charged to 3.9 V, the (003) peak of the sample shifted to a lower angle, and shifted to a higher angle when charged to 4.2 V, corresponding to the formation of H2 and H3 phases respectively (Fig. 9c-d). After 30 cycles, the shift angle of (003) peak of undoped samples decreased, while that of Ti<sup>4+</sup> doped sample did not change significantly. Therefore, it can be concluded that the ion mixing layer in the Ti<sup>4+</sup> doped sample maintained the integrity of H3 phase during the cycle. The hidden hazard of H3 phase formation is that micro cracks may be induced during the cycle. Titanium doped particles showed no micro cracks. After cycling, the layer structure of the undoped samples were destroyed, and Fm-3 m phase, mixed phase and R-3 m phase appeared successively from the surface to the interior. For Ti<sup>4+</sup> doped sample, no obvious structural change was noted. Bak et al. [109] used in-situ XRD, synchrotron radiation and mass spectrometry to test the phase transformation and oxygen production of different components of nickel-rich layered oxide cathode materials during charging and discharging. During heating, mixed discharge of cations resulted in the transformation of R3<sup>-</sup>m to Fm-3<sup>-</sup>m structure, and the subsequent release of oxygen. When heated to a higher temperature, it changed to Fd-3 m structure.

#### 4.4. Generation of micro cracks

At present, nickel rich layered cathode materials are synthesized by co-precipitation method, and the characteristic of co-precipitation is to grow into secondary particles by agglomeration of nano primary particles. In the process of co-precipitation, the primary particles are disorderly distributed and agglomerated due to violent stirring, so there are different degrees of stress and distortion in the secondary particles.

The nickel-rich layered oxide cathodes are composed of two-micron spheres formed by agglomeration of particles. In the process of lithium intercalation, the variation of lattice size results in the formation of micro cracks in the primary particles, which hinders the diffusion of lithium ions. What's more, the change of cell parameters in the process of charge and discharge leads to the repeated expansion and reduction of the crystal, which further leads to the crack between primary particles and destroys the continuity between them. It again obstructs the electronic transmission, penetration of electrolyte and the continuous growth of interface impedance. The generation of micro cracks is also closely related to the change of phase structure. In the range of high cut-off voltage, the micro cracks are generated at the boundary of the lattice due to the change of stress. When the charging voltage of the nickel layered anode material is higher than 4.2 V, the irreversible phase transition from H2 to H3 will occur, causing a large volume change. NiO phase will be produced, which will not only induce the further phase transition of the material, but also lead to the crack in the material. Increase in impedance and decrease of active materials are triggered by the generation of micro cracks. At the same time, the electrolyte permeates into the cracks, and degrades the electrochemical performance. Park et al. [55] explicitly illustrated the degree of mechanical damage sustained by each cathode during cycling. In a severe case, a crack



traverses across the entire particle and nearly fractures the secondary particle, even in its first charged state before cycling (Fig. 10a). Nam et al. [110] summarized the relationship between specific capacity, the capacity retention rate, micro crack degree and thermal stability of NCA and  $\text{LiNiO}_2$  with high nickel content. Though the specific capacity of the cathode increased with the increase in Ni content, the capacity retention and thermal stability decreased. With the increase of Ni content, the propagation degree of micro cracks also got enhanced. Fig. 10b-c shows the SEM of the positive cross section under different SOC and DOD. Micro cracks began to appear at 3.9 V for all three kinds of positive electrodes. At the same voltage, the percentage of micro cracks area in the discharge was higher than that of the charge, which indicated that micro cracks were not completely reversible. The electrolyte entered the secondary particles from micro cracks, accelerated the surface degradation of particles of micro cracks and formed NiO rock salt phase.

#### 4.5. Other newly proposed failure factors

With the continuous development of research and characterization technology, some newer and deeper failure mechanisms have been proposed. Generally, the increase of nickel content in ternary materials will make it easier to react with water and carbon dioxide in the environment. CATL evaluated the NCM811/graphite soft package battery for full charge storage at high temperature, and analyzed the cell disassembly before and after storage to study the mechanism of storage performance degradation. The results show that the thickness of non-electrochemically active rock salt phase on the cathode material surface increases after storage, and spinel phase appears in the local range of grains, which can lead to the attenuation of reversible capacity of Ni-rich materials. At the same time, the deposition of by-products produced by electrolyte side reaction on the surface of cathode materials after high temperature storage can lead to poor interface conductivity and increase the battery polarization.

For a comprehensive understanding of the chemical and physical changes of NCM, and an intense study of the actual changes occurring in electrode materials in the long cycle process, Arumugam et al. [111] used an electron microscope based analysis technique to obtain microstructure images of crystals and electronic structural changes. The results of electron probe microanalysis (EPMA), X-ray energy dispersive

spectroscopy (XEDS) and electron energy loss spectroscopy (EELS) combined with TEM reveal the modifications of Ni content, crystal structure and oxidation state on the surface and bulk cathode. The relationship between the change of high Ni NCM positive electrode and its electrical properties was studied by comparing the original positive electrode and the positive electrode after 500 cycles. The results show that the structure, chemical composition and oxidation state of TMS propagate from the surface to the whole bulk phase in a long cycle time. The continuous formation of  $\text{Ni}^{2+}$  and the loss of  $\text{O}^{2-}$  are the main problems leading to the degradation of high nickel NCM cathode. Yang et al. [112] and Su [43] et al. found that intrinsic crystal defects cause cycle induced degradation of cathode materials. Furthermore, the studies made by Lin et al. [41] also established that the non-radial crystal orientation of the NMC positive electrode is not conducive to the formation of continuous  $\text{Li}^+$  conduction channel, which reduced the inhomogeneity of charge distribution in the secondary particles, and improved the cycling charge discharge stability of NMC. Recently, it has been observed that DOD has an obvious effect on the stability of ternary high nickel cathode materials. Yoon et al. [44] revealed that NCT95 cathode material had a discharge depth of 60% in the high range (3.76–4.3 V), 60% in the low range (2.7–4.0 V), and 100% in the range of 2.7–4.3 V. At the discharge depth of 60% in the high range, NCT95 cathode material had the most of the cracks, the most obvious change of cell volume, and the deterioration of cycle stability was more significant.

#### 5. Approaches to suppress capacity failure

Although the primary nanoparticles of Ni-rich layered materials with high Ni content can enlarge the reaction interface and shorten the diffusion path of  $\text{Li}^+$ , thereby improving the cycle and rate performance of materials, there are also side reactions such as the formation of rock salt phase (NiO). Ni-rich layered materials react with the electrolyte to form solid electrolyte interface (SEI), which increases boundary impedance and leads to rapid capacity decay. [113–116] In addition, when materials are deeply charged at extreme voltage, Li/O vacancies will cause oxidized  $\text{Ni}^{3+}/\text{Ni}^{4+}$  ions to become unstable. It will result in the migration of cations and thereby forming a surface reconstruction layer consisting of NiO phase and spinel phase on the surface of the electrode. [117,118] Appearance of surface reconstruction layer will

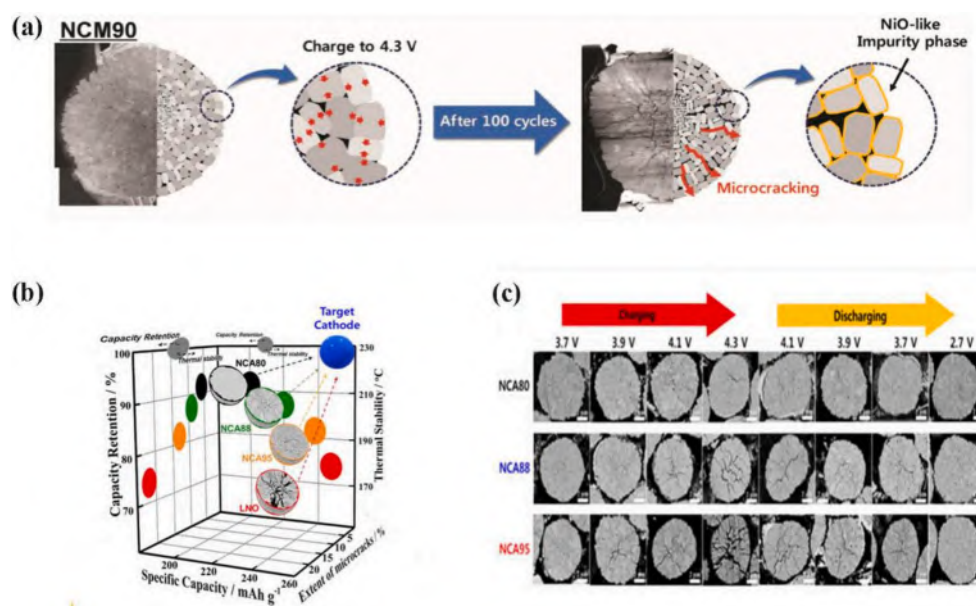


**Fig. 10.** (a) Schematic illustration of the effect of NCM90 cathode's mechanical stability during charge and discharge cycling. Reproduced with permission.[55] Copyright 2018, Wiley-VCH. (b) Diagram of specific capacity, capacity retention rate, micro crack degree and thermal stability of NCA and  $\text{LiNiO}_2$  with high nickel content. (c) SEM comparison of NCA80, NCA88 and NCA95 under different SOC. Reproduced with permission.[110] Copyright 2019, American Chemical Society.

increase the diffusion dynamic resistance of  $\text{Li}^+$  and will lead to capacity degradation. The commercial application of nickel rich layered material is restricted by its poor high temperature performance and low compacting density. Doping, surface coating, crystal and morphology structure regulation, DOD setting, electrolyte, binder, separator modification and assembly technology are deemed to be the main methods for effectively reducing the side reactions and improving the electrochemical properties and thermal stability of the materials (Fig. 11). Table 1 summarizes the various promising approaches in enhancing the electrochemical performances of Ni-rich cathodes.

### 5.1. Elemental doping

Multiple phase transitions occur in Ni rich layered oxide cathodes during the lithiation/delithiation process, especially under deep charge, which will lead to a series of unstable conditions. In order to alleviate these complications, researchers have modified the cathodes by using various doped elements to increase their energy density without sacrificing the cyclic stability. Structural modification via atomic substitution of foreign elements such as cationic doping and anionic doping, as well as co-doping of anion and anion element have been adopted. The commonly used doping elements are  $\text{Zr}^{4+}$ ,  $\text{Ti}^{4+}$ ,  $\text{Al}^{3+}$ ,  $\text{Mg}^{2+}$ ,  $\text{Mo}^{6+}$ ,  $\text{B}^{3+}$  and F. The successful doping helps in restraining the Li/Ni mixture and stabilizes the crystal structure of the materials, further improving their comprehensive performance. Zr has become the most commonly used doping element because of its stabilizing effect on layered cathode materials. Lastly, Choi et al. [119] detected through experiments that Zr doping in  $\text{Li}[\text{Ni}_{0.6}\text{Co}_{0.2}\text{Mn}_{0.2}]\text{O}_2$  can be an effective approach to enhance the cycle as well as rate performance by stabilizing the structure and increasing  $\text{Li}^+$  diffusion rate. The doping of Zr decreased the mixing degree of ions, reduced the structure transition and promoted the diffusion of  $\text{Li}^+$ , further improving the cycle and rate performance (Fig. 12a-c). Gao et al. [120] synthesized NCM811 cathode material by

substituting the transition metals with Zr to mitigate its structural instability and capacity degradation. It exhibited superior electrochemical performance in comparison to the undoped-NCM811 material (Fig. 12d-e).

$\text{Ti}^{4+}$  and  $\text{Al}^{3+}$  are frequently used as promising dopants in stabilizing the material layered structure. Song et al. [121] synthesized Ti-doped  $\text{LiNi}_{0.7}\text{Co}_{0.15}\text{Mn}_{0.15}\text{O}_2$  cathode materials via the following methods; a solution of 0.1 wt% titanium sulfate was dissolved in deionized water.  $\text{Ni}_{0.7}\text{Co}_{0.15}\text{Mn}_{0.15}(\text{OH})_2$  precursor powders were then added to the solution and continuously stirred at  $100^\circ\text{C}$  until the complete evaporation of the solvent. The resulting powder was mixed with  $\text{Li}_2\text{CO}_3$  ( $\text{Li}/\text{M} = 1.03$ ) and sintered at  $800^\circ\text{C}$  for 10 h under an  $\text{O}_2$  atmosphere to produce  $\text{Ti-Ni}_{0.7}\text{Co}_{0.15}\text{Mn}_{0.15}\text{O}_2$ . For comparison, the  $\text{Ni}_{0.7}\text{Co}_{0.15}\text{Mn}_{0.15}\text{O}_2$  was prepared with the same approach without Ti addition. Subsequently, after Ti-doping, the external morphology remains similar, but the lattice parameters of the layered structure were slightly shifted toward larger values.  $\text{Ti-Ni}_{0.7}\text{Co}_{0.15}\text{Mn}_{0.15}\text{O}_2$  cathode material exhibited long cycle life and delivered better retention rate of 95% after 50 cycles at  $60^\circ\text{C}$ . Titanium doping enhanced the structural strength of a high-Ni layered cathode material in lithium ion batteries during high temperature cycling which attributed to the better retention of the compressive strength of the particles. Besides, it also retarded crack formation within the particles (Fig. 13a-f). Zhang et al. [143] found that  $\text{Ti}^{4+}$  doping in Ni-rich cathodes can improve the robustness of the oxygen framework, which further contributes to improve the structural stability and electrochemical performance (Fig. 13g-h).

Among the various dopants,  $\text{Al}^{3+}$  doping can effectively improve the storage stability and prevent the reaction between  $\text{H}_2\text{O}$  and  $\text{CO}_2$  during storage.  $\text{Al}^{3+}$  has been proven to be one of the most potential elements in mitigating the structural degradation. Successful commercialization of  $\text{LiNi}_{0.8}\text{Co}_{0.15}\text{Al}_{0.05}\text{O}_2$  cathodes has revived the interest in Ni rich layered materials comprising Al. Yan et al. [144] synthesized  $\text{LiNi}_{0.8}\text{Co}_{0.1}\text{Mn}_{0.1}\text{O}_2$  and  $\text{LiNi}_{0.78}\text{Co}_{0.1}\text{Mn}_{0.1}\text{Al}_{0.02}\text{O}_2$ , prepared via co-

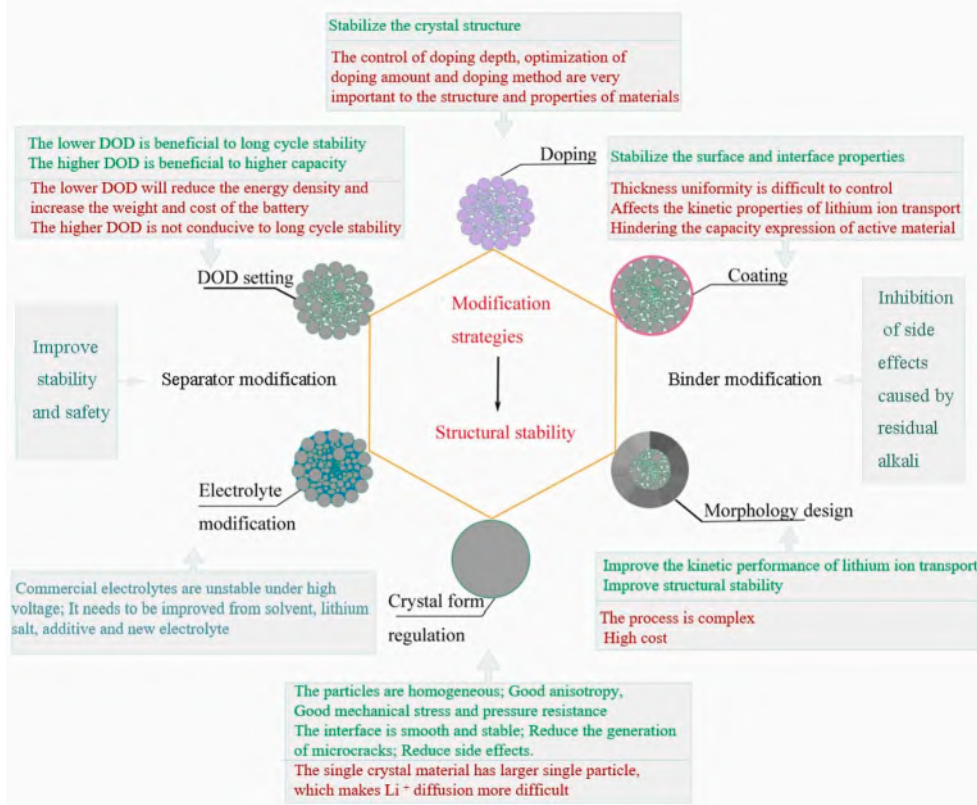
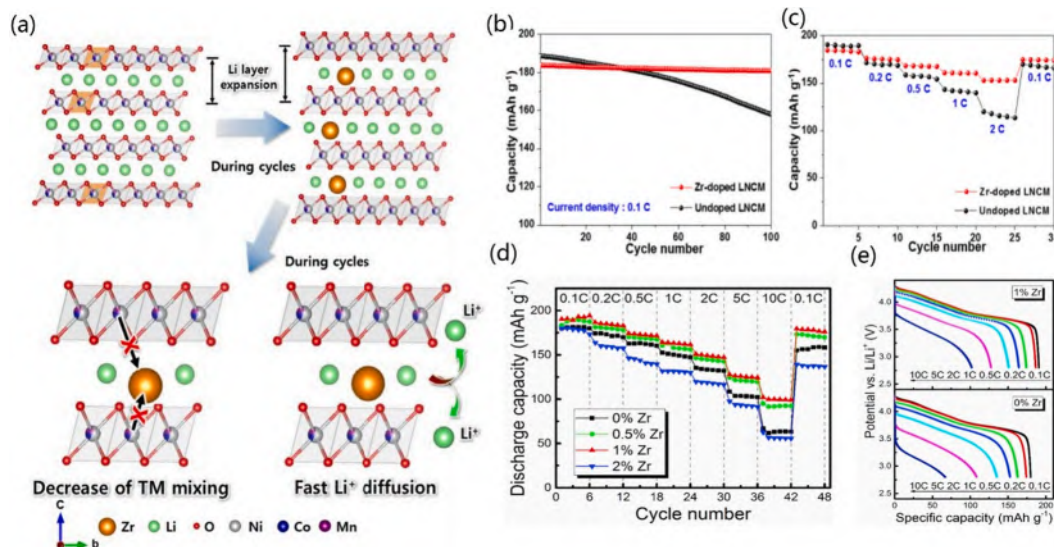


Fig. 11. Schematic diagram of the modification strategies.

**Table 1**

Summaries on the promising strategies in improving the electrochemical performance of Ni-rich cathodes.

Ni content	Strategies	Voltage (V)	Capacity (mAh g <sup>-1</sup> )	Current	Retention		Rate	Capacities		Ref
					Modified	Pristine		Modified	Pristine	
0.6	Zr-doping	4.3	185.2	0.1C	98.4@100th	83.7@100th	2C	152.9	130	2019[119]
0.8	Zr-doping	4.3	183.8	0.2C	84.2@60th	80@60th	2C	163	159	2019[120]
0.7	Ti-doping	4.3	181.05	0.1C	98.82@50th	92.84@50th	5C	150	148	2018[121]
0.82	Ti-doping	4.3	190	0.2C	97.7@200th	75.9@200th	20C	146	120	2019[122]
0.8	Mo-doping	4.6	208.9	0.2C	75@101th	65@101th	2C	180	160	2019[123]
0.94	B-doping	4.4	223(0.1C)	1/3C	85@200th	68@200th	10C	170	170	2019[124]
0.8	Zr-F-doping	4.3	179	1C	90.5@200th	75.8@200th	2C	186.9	192.8	2019[125]
0.9	B-doping	4.3	234(0.1C)	0.5C	90.4@100th	78.8@100th	0.5C	220	212	2020[30]
0.8	Mn-PO <sub>4</sub> <sup>3-</sup> -doping	4.3	210	0.1C	85.5@100th	75@100th	5C	160	140	2019[126]
0.89	Ta-doping	4.3	229(0.1C)	0.5C	94@100th	81@100th	–	–	–	2020[45]
0.9	W-doping	4.3	180.4	0.5C	89@400th	82.4@400th	–	–	–	2020 <sup>11</sup>
0.8	In <sub>2</sub> O <sub>3</sub>	4.3	207(0.1C)	1C	91.3@100th	74@100th	5C	177.1	149.9	2019[127]
	/LiInO <sub>2</sub> coating									
0.8	GN-LPO coating	4.3	184(0.2C)	0.5C	94.3@150th	88.1@150th	10C	122.4	108.5	2019[128]
0.8	LPO coating	4.4	193	1C	92.6@100th	86.1@100th	8C	159.4	144.4	2019[129]
0.8	LiYO <sub>2</sub> coating and inner gradient Y doping	4.5	207.4	0.5C	98.4@100th	83.5@100th	10C	118.4	101.2	2019[130]
0.7	CeO <sub>2</sub> coating	4.3	187	0.5C	86.4@100th	70.6@100th	5C	137.1	95.5	2019[131]
0.8	La-Al doping and coating	4.3	–	1C	86.5@100th	71.3@100th	10C	136	116	2019[132]
0.8	C coating	4.3	182	0.1C	93@40th	86@40th	3C	83	46	2010[133]
0.8	Graphene coating	4.3	185	0.2C	97@80th	91@8th	10C	152	130	2012[134]
0.6	C-Al <sub>2</sub> O <sub>3</sub> coating	4.5	186.6	1C	93.5@100th	–	–	–	–	2019[135]
0.8	LMO coating	4.3	201	0.1C	93@100th	74@100th	2C	150	140	2019[136]
0.8	Core-shell	4.3	192.5	0.2C	95.9@100th	84.9@100th	10C	161.2	100	2019[137]
	concentration gradient									
0.8	radially aligned	4.3	180.9	1C	95.5@300th	84.5@300th	5C	152.7	128.6	2019[48]
0.83	single-crystalline	4.4	200	1C	84.5@150th	63.8@150th	5C	175	177	2020[138]
0.5	p-toluenesulfonyl isocyanate additive	4.5	180	1C	86.2@100th	71.4@100th	10C	–	–	2017[139]
0.8	Silyl-group functionalized organic additive	4.5	200	1C	60.8@100th	41.9@100th	–	–	–	2018[140]
0.7	multi-functionalized additive	4.3	200	0.1C	91.9@100th	71.7@100th	–	–	–	2016[141]
1	fluorinated electrolyte with LiDFOB additive	4.3	216	0.5C	80@400th	65@200th	3C	160	–	2019[142]



**Fig. 12.** (a) Schematic illustration of Zr doping effects in NCM811 cathode. (b) cycling test of undoped and Zr-doped LNCM electrodes at 0.1C. (c) rate capability of undoped and Zr-doped NCM811 electrodes. Reproduced with permission.[119] Copyright 2019, Wiley-VCH. (d) Rate performance of NCM811s with different Zr concentrations. (e) Discharging curves at different C-rates of the raw NCM811 and the 1% Zr-NCM811. Reproduced with permission.[120] Copyright 2018, Elsevier.

precipitation method and followed by sintering. The LiNi<sub>0.78</sub>Co<sub>0.1</sub>Mn<sub>0.1</sub>Al<sub>0.02</sub>O<sub>2</sub> cathode material showed high capacity retention of 96.15% after 50 cycles at 20 °C and of 94.38% after 50 cycles at 60 °C. In addition, Mo doping reduced the Li/Ni mixing and broadened the Li<sup>+</sup> migration channel. Stronger Mo-O bond might suppress precipitation of lattice oxygen and stabilized the material surface. Liu et al. [123] synthesized Mo-doped LiNi<sub>0.6</sub>Co<sub>0.2</sub>Mn<sub>0.2</sub>O<sub>2</sub> cathode material by co-

precipitation method. Electrochemical impedance spectroscopy (EIS) clearly demonstrated that Mo-doped cathode reduced the charge transfer impedance and enhanced the electrochemical reaction activity of Li<sup>+</sup>. When the doping amount of Mo is 0.01 mol, it exhibited an excellent reversible capacity of 208 mA h g<sup>-1</sup> at 0.2C, corresponding to the capacity retention up to 75% even after 101 cycles. Cobalt in NMC and NCA, an expensive and scarce metal is generally considered as the



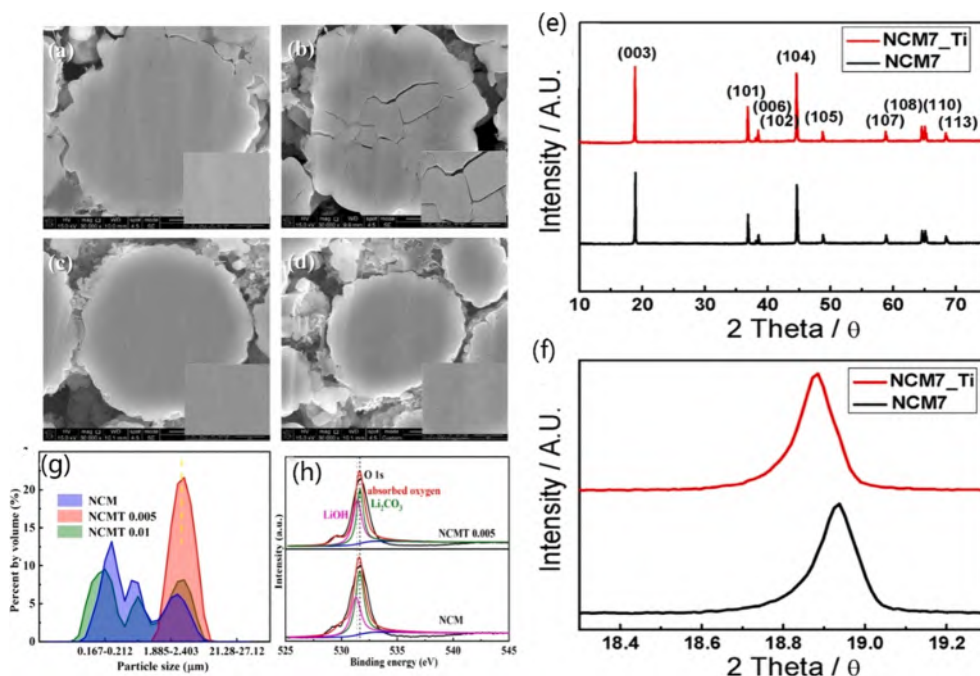


**Fig. 13.** FE-SEM images of polished cross-sections of (a) fresh NCM electrode (b) NCM electrode after 50 cycles. (c) fresh Ti-NCM electrode and (d) Ti-NCM electrode after 50 cycles. XRD patterns for NCM (e) and Ti-NCM (f) powders. Reproduced with permission.[121] Copyright 2018, Elsevier. (g) secondary particle size distribution of the three samples. (h) XPS spectra of the O 1s state for the NCM and NCMT 0.005 samples. Reproduced with permission.[143] Copyright 2019, Elsevier.

key element to inhibit Li/Ni mixing, can further improve the electrochemical performance. Li et al. [33] systematically studied the influence of different cation doping including Al, Mn, Mg and Co doping in Ni-rich layered oxide cathode materials. In-situ X-ray diffraction (XRD) and differential capacity versus voltage exhibited that through the doping of Al, Mn, Mg or Co, multiple phase transition in  $\text{Li}_x\text{Ni}_{0.95}\text{Mn}_{0.05}\text{O}_2$  was restrained during lithiation/delithiation process. This phase transition was attributed to the poor capacity retention of  $\text{LiNiO}_2$ . The addition of 5% Al, Mn and Mg in  $\text{LiNiO}_2$  reduced the Li/Ni mixing and inhibited the irreversible phase transition.

The inherent anisotropic lattice volume variations of randomly oriented primary particles lead to stress concentrations, followed by microcracks of secondary particles. The generation of microcracks causes the electrolyte to penetrate the interior of the particles and attack primary particles, which result in structural degradation and further aggravated capacity attenuation. Recently, Kim et al. [45] introduced Ta dopants into the Ni-rich cathode material  $\text{LiNi}_{0.91}\text{Co}_{0.09}\text{O}_2$  (NC90) by co-precipitation-solid phase method. Ta was introduced into hydroxide precursor and LiOH was used to obtain the material of the ideal radial structure by changing surface energy. As a result, the addition of Ta hindered the coarsening of the particles. The unique microstructure of NCTa90 material led to the dissipation of anisotropic mechanical strain and inhibited the formation and propagation of micro cracks. At the same time, the cyclic stability was achieved by the radial arrangement of primary particles and the crystal structure of [003], which effectively dissipated the internal strain in the deep charge state. It exhibited excellent capacity retention of 95% even after 1000 cycles and exhibited high energy density of  $850 \text{ Wh Kg}^{-1}$  (Fig. 14).

Kim et al. [145] also found that the Nb-doped  $\text{Li}(\text{Ni}_{0.855}\text{Co}_{0.13}\text{Al}_{0.015})\text{O}_2$  (NCA85) cathodes alter the morphology of primary particle to accurately adjust microstructure. With the increase of Nb-dopant content of NCA85 cathodes, the primary particles are elongated and arranged radially, which partially relieve the caused by H2-H3 phase transition during deep charging. The elimination of internal strain significantly improves the cycling stability of NCA85 cathodes even at an elevated temperature. Furthermore, Nb-doping enhances the mechanical stability and further improves the fast charging performance of

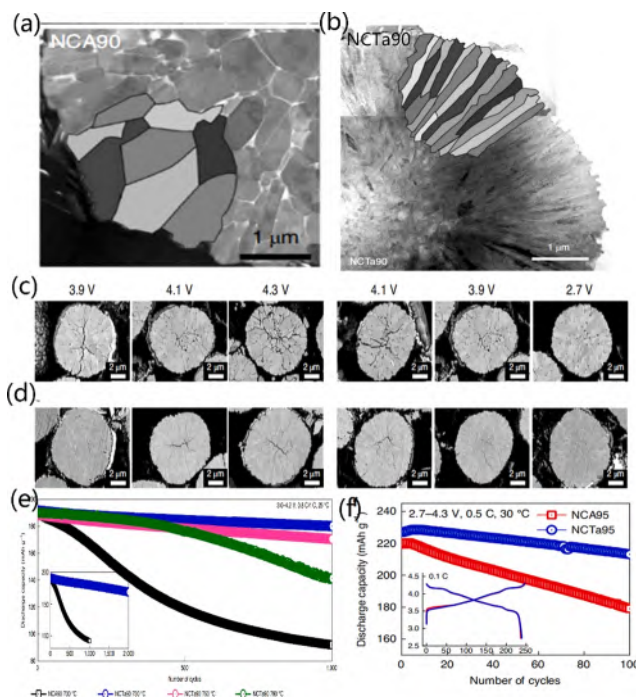


**Fig. 14.** STEM image of a cross-sectional cathode and the corresponding schematic of the primary particles  $\text{LiNi}_{0.90}\text{Co}_{0.09}\text{Al}_{0.01}\text{O}_2$  (a) and  $\text{LiNi}_{0.90}\text{Co}_{0.09}\text{Ta}_{0.01}\text{O}_2$  (b). Cross-sectional SEM images of NCA90 (c) and NCTa90 (d) cathodes at different charge/discharge state during the first cycle. (e) Long-term cycling stability in full cells for NCA90 and NCTa90 cathodes lithiated at different temperatures. (f) Cycling performance (at 0.5C) with the initial charge and discharge curves in the inset for NCA95 and NCTa95 cathodes. Reproduced with permission.[45] Copyright 2020, Nature.

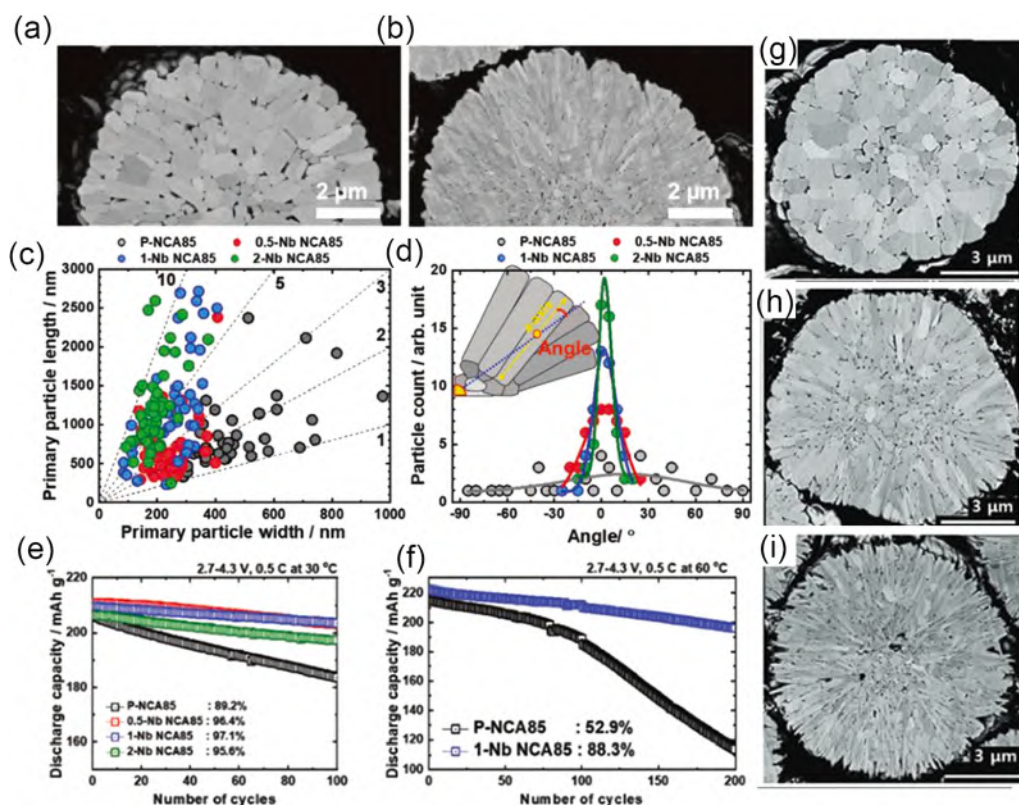


**Fig. 15.** (a) Cross-sectional SEM image of the primary particles of NCA85 cathode. (b) Cross-sectional SEM image of the primary particles of Nb-NCA85 cathode. (c) Aspect ratio of the primary particles. (d) orientation of the primary particles. (e) Cycling performance in half cells at 30 °C. (f) Cycling performance in half cells at 60 °C. Reproduced with permission. [145] Copyright 2021, Wiley-VCH. (g) Cross-sectional SEM image of NC90 cathode. (h) Cross-sectional SEM images of 0.5-NCB90 cathode. (i) Cross-sectional SEM images of 1-NCB90 cathode. Reproduced with permission. [30] Copyright 2021, Wiley-VCH.

batteries. Moreover, The Nb-dopant of NCA85 cathode also shows strong chemical and structural stability under aging and under thermal load (Fig. 15a-f). Furthermore, Ryu et al. [30] proposed B-doped Li (Ni<sub>0.9</sub>Co<sub>0.1</sub>)O<sub>2</sub> cathodes by introducing B<sub>2</sub>O<sub>3</sub>. The synthesized cathodes with B doping show a highly oriented microstructure, and the width of primary particle can be changed by adjusting the boron proportion. Compared with the NC90 cathode without B, NCB cathode effectively inhibits the formation of microcracks and significantly improves the cycling stability. The cathode with wide primary particles delivers a poor stability, which indicates a strong correlation between microcrack formation and microstructure. By changing the primary particles morphology, Ni-rich cathodes with high energy density and long-term life were reasonably designed, which is suitable for the next generation of electric vehicles (Fig. 15g-i). Park et al. [55] used B doping to change the microstructure of Li[Ni<sub>0.90</sub>Co<sub>0.05</sub>Mn<sub>0.05</sub>]O<sub>2</sub> particles and improved the inherent poor cycling performance. Density function theory (DFT) calculations testified that 1 mol % of Li[Ni<sub>0.90</sub>Co<sub>0.05</sub>Mn<sub>0.05</sub>]O<sub>2</sub> with B doping (B-NCM90) altered the surface energy and achieved a well textured microstructure, which further alleviated the intrinsic internal strain generated during the deep charging of NC. 1 mol % B-NCM90 showed extremely high coulombic efficiency of 91% after 100 cycles at 55 °C, however, NCM90 delivered a coulombic efficiency of 76%. By utilizing the differential capacity curve, structural changes of Ni-rich cathode materials were demonstrated during lithiation/delithiation process. It was found that NCM90 underwent a series of phase transitions. The phase transition of H2-H3 caused a sudden contraction in the c axis, further resulting in the mechanical stress and deteriorating cycle performance. Oxidation peak value of H2-H3 significantly decreased during 100 cycles, which indicated poor reversibility, and was related to the serious collapse of material structure caused by mechanical strain. Conversely, 1 mol % B-NCM90 kept good peak strength of H2-H3, which was consistent with the improvement of the cycle stability by B<sup>3+</sup> doping. When compared with NCM90 material, it was noticed that the 1.0 mol % B-NCM90 material had no obvious micro crack, and B<sup>3+</sup> doping significantly reduced the internal strain caused by H2-H3 phase

transformation.

Xie et al. [124] stabilized the Ni-rich cathodes effectively by introducing boron-based polyanions into the LiNi<sub>0.94</sub>Co<sub>0.06</sub>O<sub>2</sub> materials. It delivered long cycling life, retaining a capacity of 223 mAh g<sup>-1</sup> after 400 cycles and the coulombic efficiency was close to 80%. However, the LiNi<sub>0.94</sub>Co<sub>0.06</sub>O<sub>2</sub> (NC) without element doping exhibited a poor coulombic efficiency of 61% after 400 cycles. In addition, further study on the interface showed that a well-passivated boron/phosphorus-rich cathode electrolyte interface was formed, which exhibited excellent cycle stability. Moreover, B-NC had highly enhanced thermal stability and air-exposure as well. After being exposed in air for 30 days, it displayed a superior rate performance of 125 mAh g<sup>-1</sup> at 10C. However, NC showed a rate performance of 80 mAh g<sup>-1</sup> at 10C (Fig. 16).

Zhang et al. [146] also synthesized LiNi<sub>0.6</sub>Co<sub>0.2</sub>Mn<sub>0.2</sub>O<sub>2</sub> cathode materials with B doping via co-precipitation method. As a result, B-LiNi<sub>0.6</sub>Co<sub>0.2</sub>Mn<sub>0.2</sub>O<sub>2</sub> cathode (B-NCM622) delivered a superior reversible capacity of 188.2 mAh g<sup>-1</sup> at 1C and excellent coulombic efficiency of 86% after 200 cycles. High-resolution transmission electron microscopy (HR-TEM) and X-ray photoelectron spectroscopy (XPS) exhibited that the interaction of B<sup>3+</sup> and excess Li<sup>+</sup> led to the reduction of cation mixing, further resulting in rapid kinetics, stable oxygen dense packing structure, which in turn improved the cycling stability. This study has a deep understanding of the effect of B<sup>3+</sup> doping and provides a feasible strategy for the development of practical high energy density ultra-high nickel rich cathodes.

In addition to the cation doping, anion doping has also become a significant approach in improving the structure and electrochemical performance of Ni-rich materials. Woo et al. [147] synthesized LiNi<sub>0.8</sub>Co<sub>0.1</sub>Mn<sub>0.1</sub>O<sub>2-z</sub>F<sub>z</sub> via co-precipitation method. X-ray diffraction (XRD) spectra showed that all peaks were indexed with hexagonal -NaFeO<sub>2</sub> structure with a space group of R3̄m. The lattice constants of a and c were increased by F<sup>-</sup> doping. This can be accredited to the repulsive forces in the oxide matrix formed by the strong bond between Li and F, causing the lattice to expand simultaneously on both a and c axes.

The increase in the initial charging voltage of LiNi<sub>0.8</sub>Co<sub>0.1</sub>Mn<sub>0.1</sub>O<sub>2-z</sub>F<sub>z</sub>



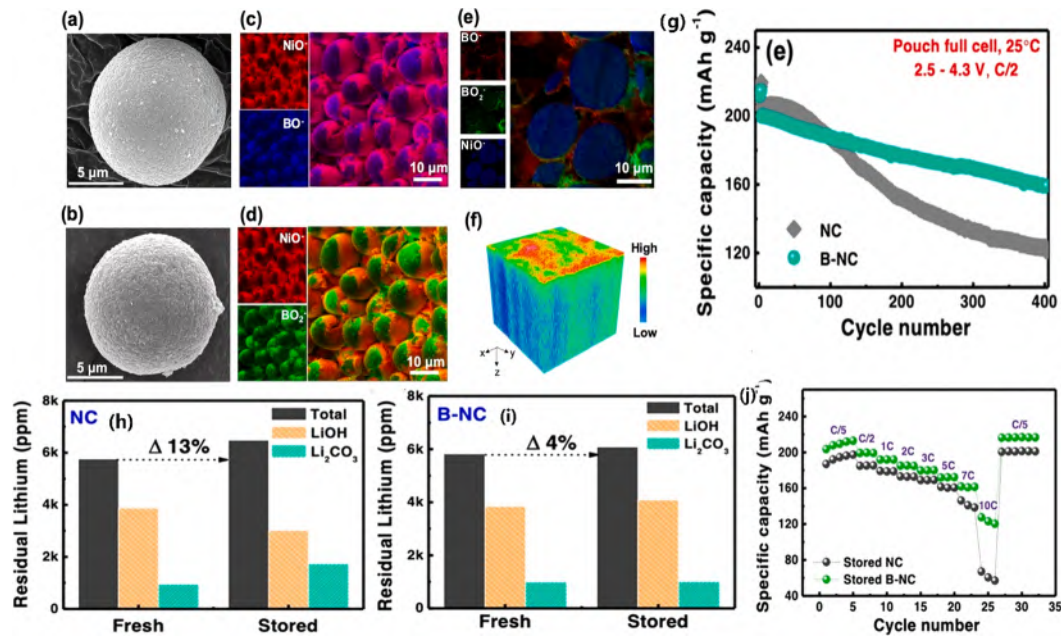


**Fig. 16.** SEM images of (a) fresh NC and (b) fresh B-NC. TOF-SIMS surface mapping of (c) BO<sup>-</sup> and NiO<sup>-</sup> species and (d) BO<sup>2-</sup> and NiO<sup>-</sup> species in fresh B-NC particles. (e) TOF-SIMS cross-section mapping of BO<sup>-</sup>, BO<sup>2-</sup>, and NiO<sup>-</sup> species in the fresh B-NC. (f) TOF-SIMS three dimension depth profiling of BO<sub>x</sub><sup>-</sup> (x = 1 or 2) species in the fresh B-NC. (g) Cycle performance of NC and B-NC cathodes in pouch full cell at 25 °C. Residual lithium content changes (h) NC and (i) B-NC. (j) Rate performance of the 30-day stored NC and B-NC over the course of C/5 to 10C rate. Reproduced with permission. [124] Copyright 2019, American Chemical Society.

material may be related to the interaction caused by the substitution of F for O. The bond energy of Li-F (577 KJ mol<sup>-1</sup>) is much stronger than that of Li-O (341 KJ mol<sup>-1</sup>). Therefore, LiNi<sub>0.8</sub>Co<sub>0.1</sub>Mn<sub>0.1</sub>O<sub>2-2F<sub>z</sub></sub> delivered excellent electrochemical properties such as cycle and rate performance. Generally speaking, single ion doping can only improve one aspect of the performance of Ni-rich materials. In order to improve the comprehensive performance of Ni-rich materials, multi-ion co-doping has become

the research direction of many researchers. Qiu et al. [125] synthesized LiNi<sub>0.8</sub>Co<sub>0.15</sub>Al<sub>0.05</sub>O<sub>2</sub> cathode material by co-doping Zr<sup>4+</sup> and F<sup>-</sup>. X-ray diffraction (XRD), scanning electron microscope (SEM), constant current charge discharge test and cyclic voltammetry (CV) proved that F<sup>-</sup> doping can stabilize the crystal structure but reduces the reversibility of the material. The doping of Zr<sup>4+</sup> effectively stabilized the crystal structure and reduced the strong bond dissociation energy of ZrO. Co-

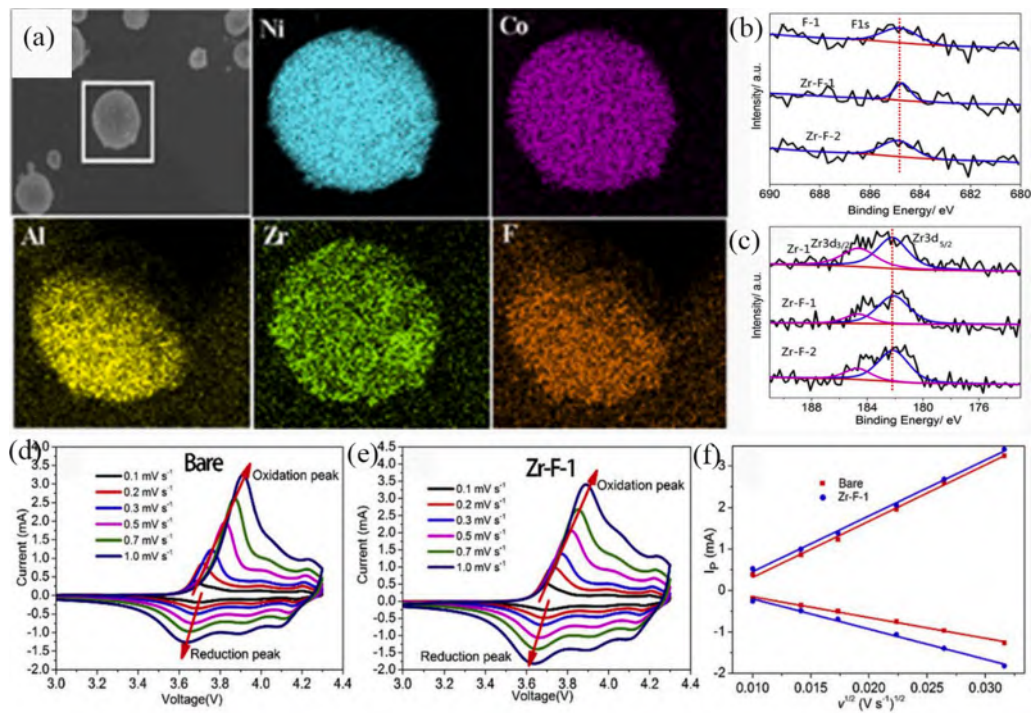


**Fig. 17.** (a) EDS mapping of Zr-F-1 sample. (b) XPS results of F (c) XPS results of Zr. (d) CV curves of bare samples at various scan rates. (e) CV curves of Zr-F-1 samples at various scan rates. (f) the relationship of the peak current (i<sub>p</sub>) and the square root of scan rate (v<sup>1/2</sup>). Reproduced with permission. [125] Copyright 2019, Elsevier.



doping of  $\text{Zr}^{4+}$  and  $\text{F}^-$  stimulated the migration of lithium ions, slowed down the electrochemical polarization and improved the electrochemical performance (Fig. 17). In addition, Qiu et al. [126] studied the effects of the coexistence of  $\text{PO}_4^{3-}$  and  $\text{Mn}^{4+}$  on the crystal structure, phase transition and electrochemical performance during lithiation/delithiation process. Appropriate co-doping of  $\text{PO}_4^{3-}$  content and  $\text{Mn}^{4+}$  increased lithiation/delithiation channel of  $\text{Li}^+$ , reduced the cation mixing and inhibited the structure deterioration during cycle process. When compared with the Ni-rich materials (un-doped), it was noted that the electrochemical performance of the Ni-rich materials with  $\text{PO}_4^{3-}$  and  $\text{Mn}^{4+}$  co-doping got improved. It exhibited an excellent reversible discharge capacity of  $204 \text{ mAh g}^{-1}$  at 0.1C for 2.7–4.3 V and stabilized at  $174 \text{ mAh g}^{-1}$  at 1C after 100 cycles, as well as a coulombic efficiency of 85.5% was achieved.

## 5.2. Coating modification

During the charge–discharge process, especially at higher voltage and higher temperature,  $\text{Ni}^{4+}$  easily reacts with the electrolyte, leading to the destruction of material structure. Surface coating is an effective approach in improving the performance of Ni-rich layered oxides, while coated materials are required to have good  $\text{Li}^+$  and electronic transmission performance. On one hand, it can improve the electronic conductivity [148–151], while on the other hand, the coating materials can reduce the direct contact area between Ni-rich layered oxide cathode materials and electrolyte, hinder the formation probability of HF in the electrolyte and the side reaction and further prevent the collapse of the crystal structure due to corrosion of the cathode materials. All these aspects significantly improve their electrochemical performance.

Previous reports have almost confirmed that Ni-rich layered oxide materials through coating metal oxides can significantly improve the electrochemical stability. Oxides such as  $\text{Al}_2\text{O}_3$ ,  $\text{TiO}_2$ ,  $\text{MgO}$  are often used as coating materials due to their structure stability and electrochemical inertia between coating materials and electrolyte at high voltage, which shows good effects in improving the electrochemical performance. Recently, Fan et al. [152] constructed a highly effective  $\text{TiO}_2$  nano-coating on the surface of  $\text{LiNi}_{0.8}\text{Co}_{0.1}\text{Mn}_{0.1}\text{O}_2$  (NCM811) by accurately controlling the hydrolytic dynamics of  $\text{Ti}^{4+}$  in order to

improve the comprehensive performance of Ni-rich cathodes for LIBs at a higher upper cut-off voltage. A systematic study on the effect of coating layer with  $\text{TiO}_2$  was also executed. As a result, the continuous and uniform coating layer with  $\text{TiO}_2$  offered an exhaustive protection for NCM811 and increased the reversibility of phase transition between H2  $\rightarrow$  H3 during lithiation/delithiation process. This further ensured a superior cycling stability and rate performance under the cut-off voltage of 3.0–4.5 V. High-resolution transmission electron microscopy (HR-TEM) further demonstrated the slight structural decay of the NCM811 material with  $\text{TiO}_2$  coating when compared with the NCM811 material. Electrochemical impedance spectroscopy (EIS) established a stable interface between cathode and electrolyte, as well as fast kinetics at the surface of NCM811 material with  $\text{TiO}_2$  coating. Comparing with NCM811 cathode material, NCM811 material with  $\text{TiO}_2$  coating delivered a superior coulombic efficiency of 72.2% at 1C after 500 cycles with 3.0–4.5 V and 63.4% at 1C after 1000 cycles with 3.0–4.3 V. This work offers a general approach for the preparation of uniform  $\text{TiO}_2$  coatings and provides direction for the precise evaluation of the comprehensive performance of coatings (Fig. 18).

Becker et al. [153] synthesized tungsten oxide ( $\text{WO}_3$ ) coating layer on the surface of  $\text{LiNi}_{0.8}\text{Co}_{0.1}\text{Mn}_{0.1}\text{O}_2$  (NCM-811) via sol–gel method followed by heat treatment. As a result, tungsten oxide ( $\text{WO}_3$ ) coating layer on the surface of  $\text{LiNi}_{0.8}\text{Co}_{0.1}\text{Mn}_{0.1}\text{O}_2$  (NCM-811) delivered a superior capacity retention for the long-term cycling process of  $\text{LiNi}_{0.8}\text{Co}_{0.1}\text{Mn}_{0.1}\text{O}_2$  (NCM-811) based LIBs full cells. Coated electrodes showed superior discharge capacity of  $184 \text{ mAh g}^{-1}$  at 0.1C and excellent capacity retention of 80% after 865 cycles. Furthermore, it was confirmed that tungsten oxide ( $\text{WO}_3$ ) coating composite provides thermal and structure stability. Unlike the uncoated electrode, the particle cracking of the surface modified electrode had improved after cycles. Rare earth oxides can also be used as a promising coating layer for Ni rich cathode materials. Dong et al. [131] synthesized  $\text{LiNi}_{0.7}\text{Co}_{0.2}\text{Mn}_{0.1}\text{O}_2$  (NCM712) cathode materials with  $\text{CeO}_2$  coating by a wet chemical method. X-ray powder diffraction (XRD) analysis and transmission electron microscope (TEM) results demonstrated the structural characteristics, morphology and elemental composition of bare and surface coated NCM712 materials. The  $\text{CeO}_2$ -coated NCM721 exhibited reversible discharge specific capacity of  $202 \text{ mAh g}^{-1}$  at 0.1C and showed excellent capacity

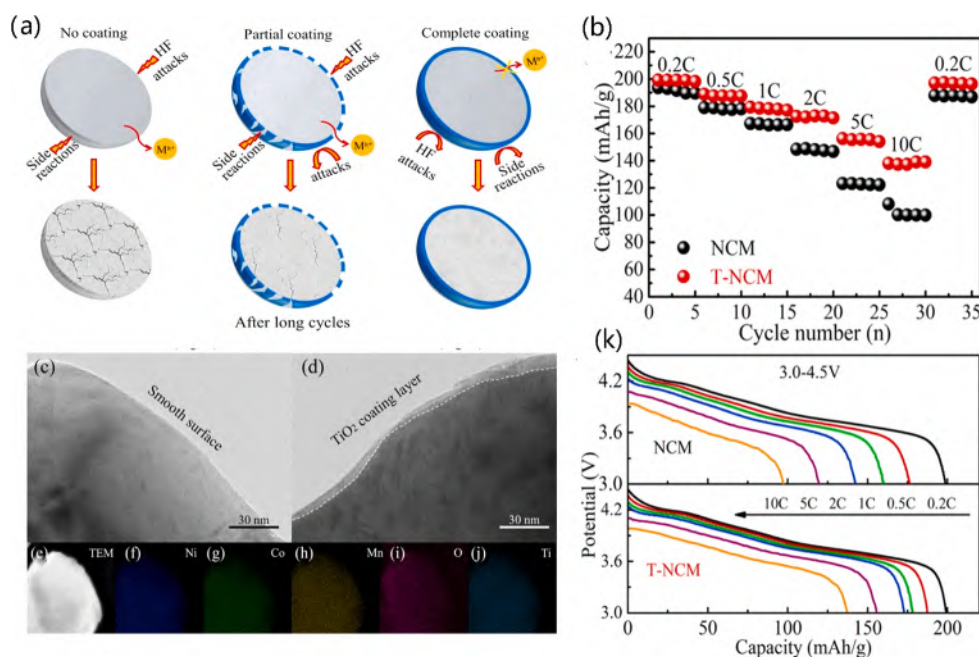


**Fig. 18.** (a) The protection mechanism of the  $\text{TiO}_2$  nano-coating for Ni-rich cathode materials. (b) The rate performance of NCM and T-NCM. TEM images for NCM (c) and T-NCM. (d) TEM image of a primary T-NCM particle. (e) and corresponding elements mapping including Ni (f), Co (g), Mn (h), O (i) and Ti (j). (k) The selected discharge profiles for NCM and T-NCM at different current densities. Reproduced with permission. [152] Copyright 2020, Elsevier.

retention of 86.42% at 0.5C after 100 cycles between 3.0 and 4.3 V as well as decent rate performance of  $137.1 \text{ mAh g}^{-1}$  at 5C. For comparison, NCM721 without coating delivered a reversible discharge specific capacity of  $205.7 \text{ mAh g}^{-1}$  at 0.1C and a coulombic efficiency of 70.64% at 0.5C after 100 cycles between 3.0 and 4.3 V was noted. Again, the rate performance obtained was of  $95.5 \text{ mAh g}^{-1}$  at 5C.

Li et al. [132] constructed La-Al coating and doped co-modified  $\text{LiNi}_{0.8}\text{Co}_{0.1}\text{Mn}_{0.1}\text{O}_2$  by wet coating method followed by calcination. La-Al was uniformly doped in the inner layer and the coated layer of  $\text{La}_2\text{O}_3$  was distributed in the bulk phase. As a result, the doping and coating of La-Al promoted the migration of  $\text{Li}^+$ , decelerated the electrochemical polarization and amplified the reversibility of phase transition between H2  $\rightarrow$  H3 during lithiation/delithiation process. The  $\text{La}_2\text{O}_3$  coating layer offered an exhaustive protection and suppressed the side reactions between materials and electrolyte, further improving the storage stability. During cycling, excellent structural stability of 86.4% at 1C was demonstrated after 100 cycles in the cell within a potential range of 2.7–4.3 V (Fig. 19).

Recently, Yoon et al. [154] prepared  $\text{Co}_x\text{B}$ -NCM811 by a room-temperature synthesis route to construct high-quality coatings. Under the strong driving force of interfacial chemical reaction,  $\text{Co}_x\text{B}$  is not only completely wrapped on the surface of secondary particles, but also injected into the grain boundary of primary particles. As a result,  $\text{Co}_x\text{B}$ -NCM811 cathode dramatically improved the cycling stability and the rate capability, and delivered a superior capacity retention of 95% at 1C after 500 cycles in practical pouch-type full-cells. Mechanically, DFT calculation also identified a strong interfacial binding between NCM and  $\text{Co}_x\text{B}$ , which offers a reasonable explanation for the reactive wetting and inhibited oxygen activity observed in the experiment. Therefore, other transition metal boride coatings may also be suitable for Ni-rich cathodes, which puts forward a simple and feasible method to improve the properties of Ni-rich cathodes (Fig. 20).

Although, coating layers of oxides can reduce the direct contact between the Ni-rich materials and the electrolyte and hinder the occurrence of side effects, most oxides exhibit electrical and electrochemical inactivity. Many researchers have also studied the role of the electronic conductive and  $\text{Li}^+$  conductive matrix as alternative coatings. Materials with electronic conductivity include carbon, graphene oxide and polymer, and materials with  $\text{Li}^+$  conductivity include  $\text{Li}_2\text{ZrO}_3$ ,  $\text{Li}_2\text{SiO}_3$ ,  $\text{LiAlO}_2$  et al. Chung et al. [133] synthesized  $\text{LiNi}_{0.8}\text{Co}_{0.15}\text{Al}_{0.05}\text{O}_2$  (LNCAO/C) material with conductive carbon-coating by addition of surfactant (SDS) and chemical adsorption SAM synthesis techniques. X-ray diffraction (XRD) peaks depicted that LNCAO/C cathode was also in form of a rhombohedral  $\text{R}\bar{3}\text{m}$  structure, which can be derived from the ordered rock-salt structure of  $\alpha\text{-NaFeO}_2$  compared with LNCAO. The field emission transmission electron microscopy (FE-TEM) clearly showed that a distinguishable carbon coating of about 2–3 nm thickness was seen on the surface of LNCAO. The electrochemical performance

such cyclic voltammetry (CV), discharge capacity and cyclic performance demonstrated that the carbon coating with SDS on the surface of LNCAO can effectively prevent the direct contact between electrolyte and cathodes and can avoid being attacked by HF. Further inhibition of the release of oxygen from the lattice as well as exhibition of an excellent initial discharge capacity of  $183 \text{ mAh g}^{-1}$  along with capacity retention of 93% at 1C in 2.8–4.3 V were also the outcomes of the investigation. Yoon et al. [134] obtained  $\text{LiNi}_{0.8}\text{Co}_{0.15}\text{Al}_{0.05}\text{O}_2$ /graphene cathode using a high energy mechanical ball milling process at 200 rpm  $\text{min}^{-1}$  for 30 min under argon atmosphere. It was found to deliver a superior discharge capacity of  $180 \text{ mAh g}^{-1}$  at constant current of  $55.6 \text{ mA g}^{-1}$  and had excellent capacity retention of 97% even after 80 cycles at 25 °C. However,  $\text{LiNi}_{0.8}\text{Co}_{0.15}\text{Al}_{0.05}\text{O}_2$  without coating exhibited first discharge capacity of  $172 \text{ mAh g}^{-1}$  at a constant current of  $55.6 \text{ mA g}^{-1}$  and capacity retention of 91% after 80 cycles. The graphene coating on the  $\text{LiNi}_{0.8}\text{Co}_{0.15}\text{Al}_{0.05}\text{O}_2$  enhanced the conductivity of the cathode material and reduced the polarization of the battery. Unlike other carbon coating experimental approach, this method used graphene for coating which can be directly derived from carbon source without high-temperature sintering. Although this method can save energy and protect the environment, cost-effectiveness and improvement of the homogeneity of graphene coating should be considered. Kong et al. [135] synthesized  $\text{LiNi}_{0.6}\text{Co}_{0.2}\text{Mn}_{0.2}\text{O}_2$  materials with a homogeneous thickness of C- $\text{Al}_2\text{O}_3$  composite. Whilst comparing with  $\text{LiNi}_{0.6}\text{Co}_{0.2}\text{Mn}_{0.2}\text{O}_2$  using the coating of  $\text{Al}_2\text{O}_3$ , it was seen that the dual-functional C- $\text{Al}_2\text{O}_3$  coating on the surface of  $\text{LiNi}_{0.6}\text{Co}_{0.2}\text{Mn}_{0.2}\text{O}_2$  showed a superior reversible discharge capacity of  $186.6 \text{ mAh g}^{-1}$  and excellent capacity retention of 93.5% at 0.1C. The synergistic effect between the amorphous  $\text{Al}_2\text{O}_3$  and conductive carbon improved the structural stability and electrochemical kinetics of  $\text{LiNi}_{0.6}\text{Co}_{0.2}\text{Mn}_{0.2}\text{O}_2$  cathode material. The carbon network in dual-functional C- $\text{Al}_2\text{O}_3$  coating on the surface of  $\text{LiNi}_{0.6}\text{Co}_{0.2}\text{Mn}_{0.2}\text{O}_2$  composite provided high electrical conductivity and reduced the charge transfer resistance on the electrode surface (Fig. 21).

Gan et al. [155] synthesized NCM811@PANI-PVP by polyvinylpyrrolidone (PVP) surfactant-induced homogeneous coating of polyaniline (PANI) on the surface of the NCM811. The coating layer of PANI not only provided a fast channel for electron conduction, but also inhibited direct contact between the electrode materials and the electrolyte. It further hindered side reactions and improved the electrochemical performance. Excellent capacity retention of 88.7% at a constant current of  $200 \text{ mA g}^{-1}$  after 100 cycles and a superior rate performance of  $152 \text{ mAh g}^{-1}$  at  $1000 \text{ mA g}^{-1}$  were achieved. In-situ X-ray diffraction and in-situ Raman spectra investigated the charge-discharge mechanism and the cyclability of NCM811@PANI-PVP upon electrochemical reaction. This surfactant-modulated surface homogeneous coating approach provided a new strategy to stabilize Ni-rich cathodes and improved the electrochemical performance for lithium ion batteries.

Du et al. [156] obtained  $\text{LiNi}_{0.8}\text{Co}_{0.15}\text{Al}_{0.05}\text{O}_2$  with  $\text{LiAlO}_2$  coating by spray-drying coating technique. The study revealed a capacity retention of 90.40% after 150 cycles at 1.0C in 2.8–4.4 V, which was significantly higher than that of the pristine material. This effective coating technology can significantly improve the structural stability, and can be extended to other cathodes, to further obtain a higher safety and better cycle stability for Ni-rich materials. Surface coating on the surface of Ni-rich cathodes is an effective approach to solve the serious problems such as fast energy loss and structure stability in LIBs. Nevertheless, the coating of single and double layers has many serious defects. Herein, Guo et al. [157] synthesized  $\text{Li}_x\text{TiO}_2$  nano-particles embedded in amorphous silica (LTSO) using the strategy of a dual-component in one coating layer by facile approach. The results obtained showed excellent electrochemical performance and improved the ion diffusion kinetics (Fig. 22).

Huang et al. [136] developed an in-situ coating technology, which realized the controllable construction of the material surface coating

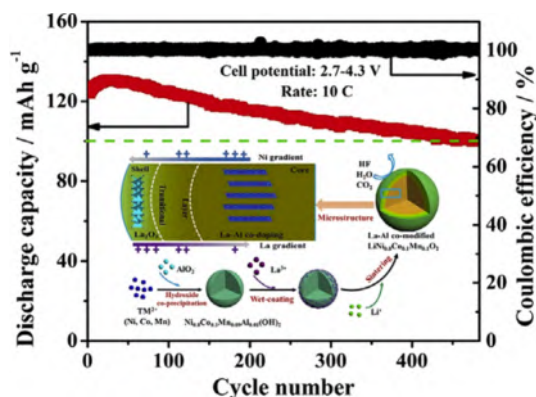
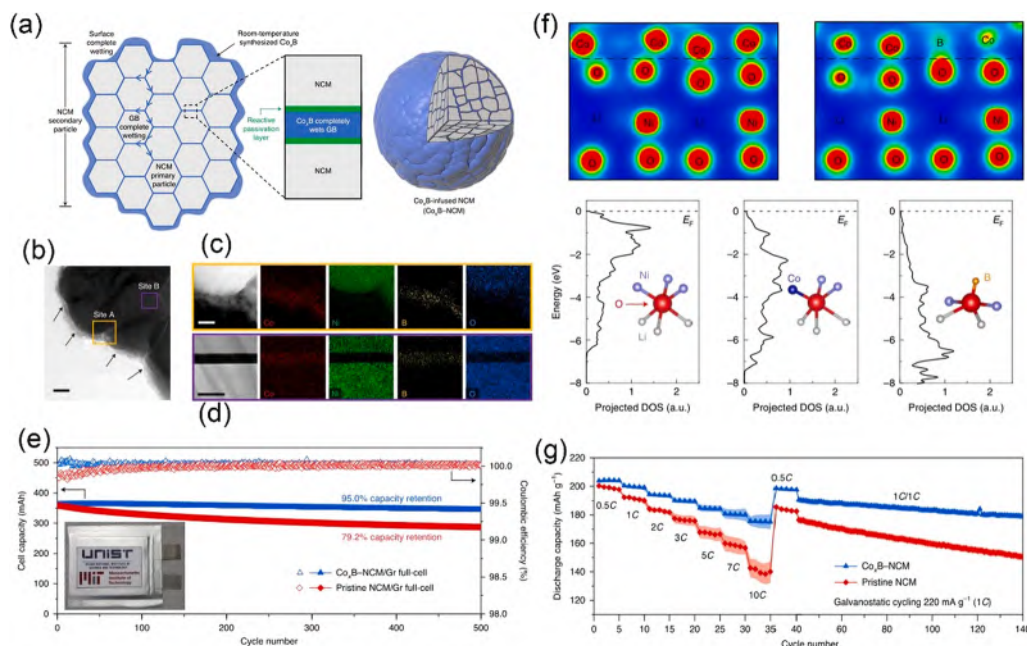
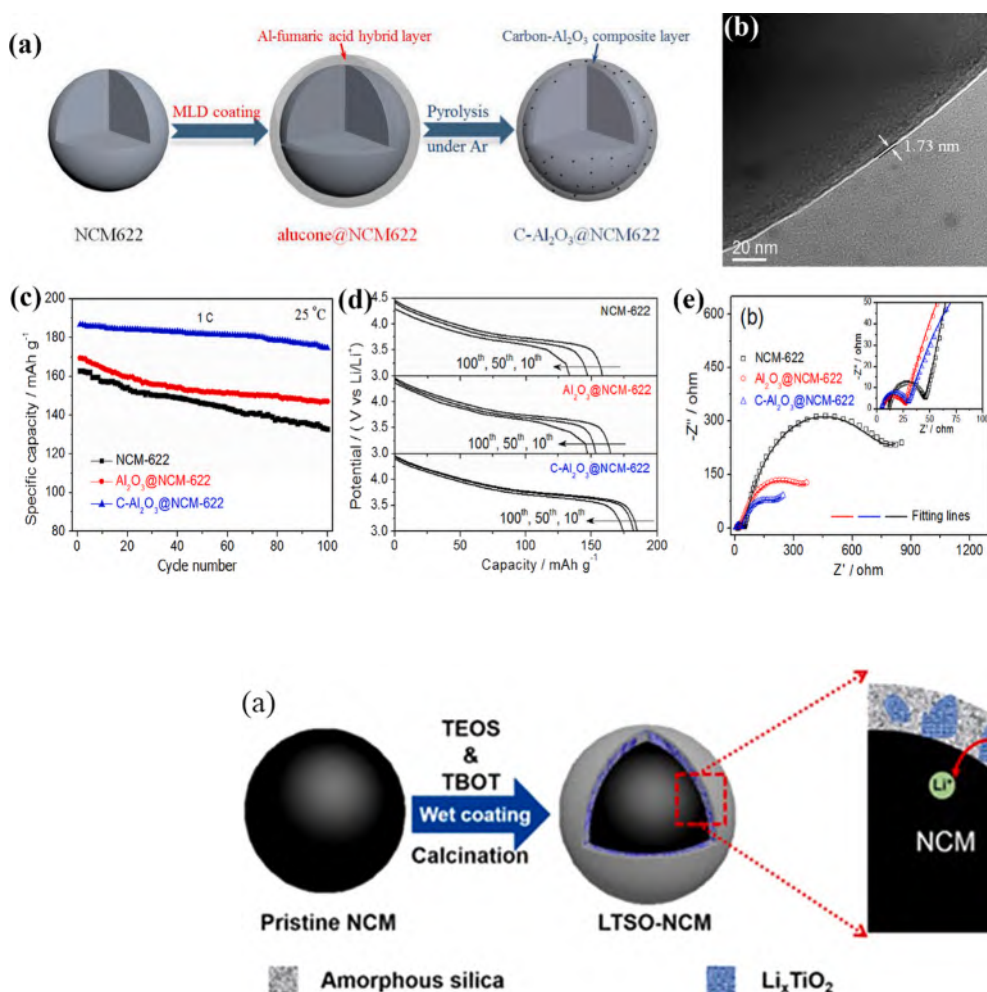


Fig. 19. Illustration for the synthesis and structure of La and Al co-modified Ni rich cathode. Reproduced with permission.[132] Copyright 2019, Elsevier.



**Fig. 20.** (a) Schematic coating-plus-infusion microstructure. (b) TEM images of cross-sectioned  $\text{Co}_x\text{B}$ -NCM cathode. (c) EDS mapping of site A in b. (d) EDS mapping of site B in b. (e) Cycling performance in full-cells at 1C in the range of 2.8–4.3 V. (f) Strong interfacial bonding suppresses oxygen activity. (g) Rate performance of  $\text{Co}_x\text{B}$ -NCM811 and NCM811 cathodes. Reproduced with permission.[154] Copyright 2021, nature.



**Fig. 21.** (a) Schematic illustration for the synthetic procedure of MLD-derived C-Al<sub>2</sub>O<sub>3</sub> coating on the surface of NCM-622. (b) TEM images of C-Al<sub>2</sub>O<sub>3</sub>@NCM-622. (c) cyclic performance of the pristine and coated NCM-622 electrodes at 25 °C, and the corresponding discharge profiles. (d) at the 10th, 50th, and 100th cycles. (e) Nyquist plots of pristine NCM-622, Al<sub>2</sub>O<sub>3</sub>@NCM-622 and C-Al<sub>2</sub>O<sub>3</sub>@NCM-622 electrodes at a charge state of 4.4 V for 50th cycle. Reproduced with permission.[135] Copyright 2019, Elsevier.

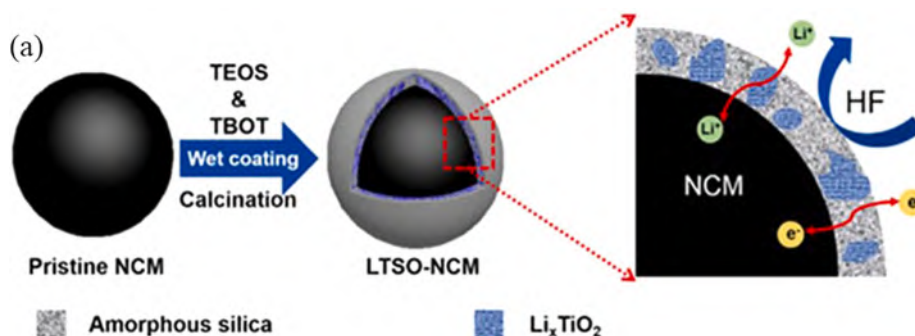


**Fig. 22.** Preparation of dual-component coating NCM by one-pot method. Reproduced with permission.[157] Copyright 2019, Elsevier.

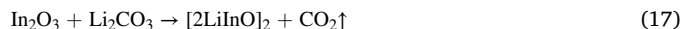
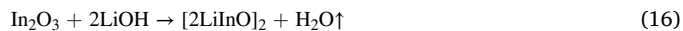


and the regulation of the order degree of the layered structure. At the same time, in situ XRD and electrochemical performance test were performed which revealed the inherent mechanism of the coating layer of  $\text{Li}_2\text{MnO}_3$  which helped to improve the cyclic stability of Ni-rich cathode materials. The results showed that the  $\text{Li}_2\text{MnO}_3$  coating can effectively inhibit the irreversible phase transitions as well as the occurrence of interfacial side reactions during the cycling process, which effectively enhanced the long-cycling stability, rate performance and high-temperature working performance of the Ni-rich cathode materials. This work is expected to be the reference for the preparation of high energy density and Ni-rich cathode materials.

Residue lithium is considered to be one of the most critical factors affecting the electrochemical performances of Ni-rich layered oxide cathode materials. This is because residual lithium ( $\text{Li}_2\text{O}$  and  $\text{Li}_2\text{O}_2$ ) on the surface of Ni-rich layered oxide cathode materials reacts with  $\text{CO}_2$  and  $\text{H}_2\text{O}$  in the air to form  $\text{Li}_2\text{CO}_3$  and  $\text{LiOH}$ .  $\text{Li}_2\text{CO}_3$  and  $\text{LiOH}$  not only consume  $\text{Li}^+$  in materials, but also have no electrochemical activity, which causes capacity degradation. The dense layer of  $\text{Li}_2\text{CO}_3$  on the surface of particles hinders the diffusion of  $\text{Li}^+$ , and further causes irreversible capacity loss during charging and discharging. In addition, the surface  $\text{LiOH}$  reacts with  $\text{LiPF}_6$  to generate  $\text{HF}$ , which results in the deterioration of lithium ion battery performance. In recent years, many researchers have testified that some coating materials can consume  $\text{Li}_2\text{CO}_3$  and  $\text{LiOH}$  on the surface of Ni-rich layered oxide cathode materials and reduce the residual alkalinity as well as improve the electrochemical performance.

Liu et al. [127], for the first time, synthesized Ni-rich

$\text{LiNi}_{0.8}\text{Co}_{0.1}\text{Mn}_{0.1}\text{O}_2$  cathode material with  $\text{In}_2\text{O}_3$  and  $\text{LiInO}_2$  co-coating layer on the surface. During sintering, the surface of  $\text{LiNi}_{0.8}\text{Co}_{0.1}\text{Mn}_{0.1}\text{O}_2$  cathode material formed an  $\text{In}_2\text{O}_3$  coating layer, and then  $\text{In}_2\text{O}_3$  reacted with the residual lithium ( $\text{LiOH}$  and  $\text{Li}_2\text{CO}_3$ ) of  $\text{LiNi}_{0.8}\text{Co}_{0.1}\text{Mn}_{0.1}\text{O}_2$  to form an  $\text{In}_2\text{O}_3$  &  $\text{LiInO}_2$  coating layer. The specific reactions are as follows:



High-resolution transmission electron microscopy (HR-TEM) proved that the surface on the NCM811 formed a homogeneous coating layer of about 12 nm thickness, and two different lattice spacing in the coating layer corresponds to  $\text{In}_2\text{O}_3$  and  $\text{LiInO}_2$ , respectively. Electrochemical performance demonstrated that the NCM811 with the  $\text{In}_2\text{O}_3$ & $\text{LiInO}_2$  co-coating not only exhibited a superior capacity retention of 90% at 1C, but also delivered superb discharge capacity of  $177.1 \text{ mAh g}^{-1}$  at 5C and a capacity retention of 86.4% after 300 cycles (Fig. 23).

In addition, part of  $\text{Li}_2\text{O}$  remains behind in high temperature calcinations.  $\text{H}_3\text{PO}_4$  also reacts with  $\text{Li}_2\text{O}$  material's surface. It is generally believed that it is impossible to completely remove water molecules from commercial electrolytes. The presence of traces of water in the electrolyte results in the decomposition of  $\text{LiPF}_6$ , which is further associated with the formation of  $\text{HF}$ . What's worse, the  $\text{HF}$ , generated from the hydrolysis of  $\text{LiPF}_6$ , accelerates the gradual disintegration of the active materials by dissolving transition metal ions. The reaction equations are as follows [129]:

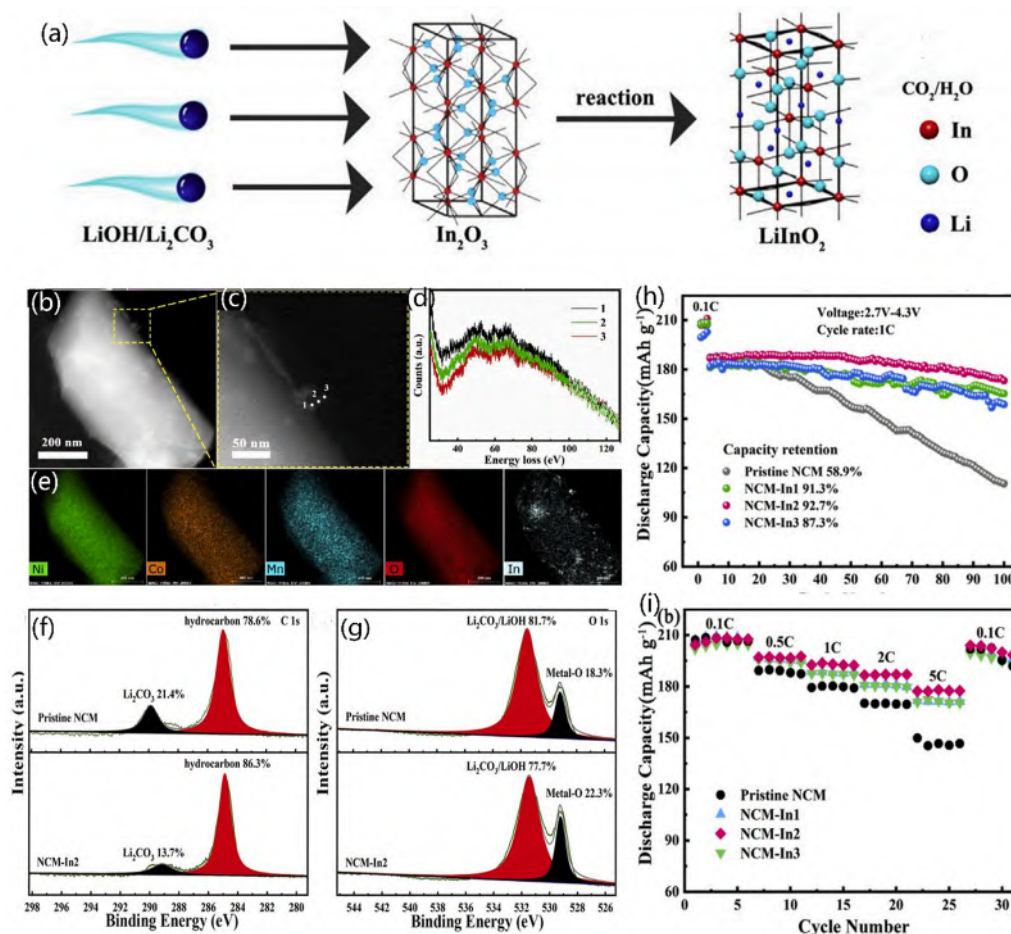
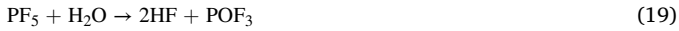
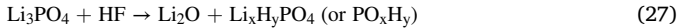
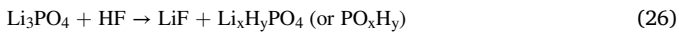
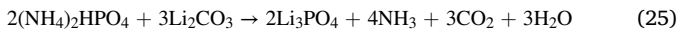
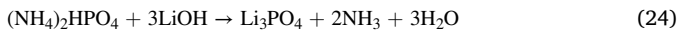


**Fig. 23.** (a) Schematic illustration of the formation of  $\text{LiInO}_2$ . (b-c) HAADF images of NCM-In2. (d) EELS spectra ranging from 25 to 130 eV for NCM-In2 at different points. (e) STEM elemental mapping of NCM-In2. (f) C 1s and (g) O 1s taken from the surface of pristine and NCM-In2 samples. (h) cycling performance of pristine and co-coated samples at 1C. (i) rate performance of pristine and co-coated samples. Reproduced with permission. [127] Copyright 2019, Elsevier.



Fan et al. [128] used wet chemical method to convert  $\text{H}_3\text{PO}_4$ ,  $\text{LiOH}$  and  $\text{Li}_2\text{CO}_3$  on the surface of Ni-rich  $\text{LiNi}_{0.8}\text{Co}_{0.1}\text{Mn}_{0.1}\text{O}_2$  (NCM811) into uniform  $\text{Li}_3\text{PO}_4$  coating layer, and then used high conductivity graphene (GN) to connect the secondary particles of Ni-rich  $\text{LiNi}_{0.8}\text{Co}_{0.1}\text{Mn}_{0.1}\text{O}_2$  (NCM811) together to obtain multi-functional coated materials (GN-LPO-NCM811) with high ionic and electronic conductivities. As a result, the electrochemical performance, safety performance and storage performance of the material have been significantly improved (Fig. 24a-c). Zhu et al. [129] successfully synthesized  $\text{Li}_3\text{PO}_4$ -coated  $\text{LiNi}_{0.8}\text{Co}_{0.1}\text{Mn}_{0.1}\text{O}_2$  (NCM811) cathode material by lithium-reactive coating. The test results showed that the  $\text{Li}_3\text{PO}_4$ -coated NCM811 achieved improved cycling performance at room temperature as well as at elevated temperatures. In addition, there are other functions like (1) removal of residual lithium ( $\text{LiOH}$  and  $\text{Li}_2\text{CO}_3$ ) which impedes  $\text{Li}^+$  migration; (2) protection of the core NCM811 materials from HF attack in the electrolyte; (3) HF scavenger to reduce the level of HF in the electrolyte (Fig. 24d-f). The reaction equations are as follows:



### 5.3. Morphology design

Ni-rich cathodes are generally composed of mixed and disordered arrangements of initial particle reunion of secondary particles. Its structure and characteristics lead to internal stress and complex lithium

ion transport path in the charging/discharging process which further lead to poor cycle stability and rate performance as well as greatly limit the application process. Due to the anisotropic properties of crystal, modification in the morphology in order to improve the stability and rate performance cycles can be realized as an effective strategy. But from the two aspects of structure and morphology, controllable synthesis with excellent cycle stability and rate performance are still a significant challenge, especially in the field of large-scale commercialization. Core-shell and concentration gradient structured materials not only inhibit the reactions between  $\text{Ni}^{4+}$  and electrolyte on the surface, but also reduce the influence of coating on discharge specific capacity and energy density, and further improve the structure stability of Ni-rich cathode materials.

Sun et al. [137] synthesized a  $\text{Li}[(\text{Ni}_{0.8}\text{Co}_{0.1}\text{Mn}_{0.1})_{0.8}(\text{Ni}_{0.5}\text{Mn}_{0.5})_{0.2}]\text{O}_2$  material of spherical core shell structure, namely the high specific capacity  $\text{Li}[\text{Ni}_{0.8}\text{Co}_{0.1}\text{Mn}_{0.1}]\text{O}_2$  (NCM811) cathode, and a good thermally stable  $\text{Li}[\text{Ni}_{0.5}\text{Mn}_{0.5}]\text{O}_2$  regarded as the core and shell, respectively. The  $[(\text{Ni}_{0.8}\text{Co}_{0.1}\text{Mn}_{0.1})_{0.8}(\text{Ni}_{0.5}\text{Mn}_{0.5})_{0.2}](\text{OH})_2$  precursor with spherical core shell structure was initially obtained by a modified hydroxide co-precipitation method, and then uniformly mixed with the stoichiometric amount of  $\text{LiOH}$ . Next, the mixture of  $[(\text{Ni}_{0.8}\text{Co}_{0.1}\text{Mn}_{0.1})_{0.8}(\text{Ni}_{0.5}\text{Mn}_{0.5})_{0.2}](\text{OH})_2$  precursor and  $\text{LiOH}$  were sintered to obtain the  $\text{Li}[(\text{Ni}_{0.8}\text{Co}_{0.1}\text{Mn}_{0.1})_{0.8}(\text{Ni}_{0.5}\text{Mn}_{0.5})_{0.2}]\text{O}_2$  with spherical core-shell structure. Scanning electron microscope (SEM) showed that the inner core was tightly wrapped by the outer shell layer. It delivered a superior long-term cycling performance and capacity retention was relative to the NCM811 at 1C after 500 cycles. A new type of Ni-rich positive cathodes with core shell structured is a major breakthrough in the development of high capacity density LIBs (Fig. 25a-c). Kim et al. [158] designed a new hybrid cathode material,  $\text{LiNi}_{0.886}\text{Co}_{0.049}\text{Mn}_{0.05}\text{Al}_{0.015}\text{O}_2$ , which was synthesized using  $\text{LiNi}_{0.934}\text{Co}_{0.043}\text{Al}_{0.015}\text{O}_2$  encapsulated by  $\text{Li}[\text{Ni}_{0.844}\text{Co}_{0.061}\text{Mn}_{0.080}\text{Al}_{0.015}]\text{O}_2$ . Its core part was Ni-rich  $\text{LiNi}_{0.934}\text{Co}_{0.043}\text{Al}_{0.015}\text{O}_2$  (NCA) and the outer layer shell part was  $\text{Li}[\text{Ni}_{0.886}\text{Co}_{0.049}\text{Mn}_{0.05}\text{Al}_{0.015}]\text{O}_2$ . It exhibited excellent reversibility discharge capacity of  $225 \text{ mAh g}^{-1}$  at 0.1C and a superior capacity retention of 91% at 1C after 1000 cycles. (Fig. 25d-f). In order to achieve high pressure density and excellent velocity performance at the same time, Su et al. [137] synthesized structural gradient  $\text{LiNi}_{0.8}\text{Co}_{0.1}\text{Mn}_{0.1}\text{O}_2$  cathode materials. The gradient Ni-rich cathode material demonstrated excellent electrochemical performance, especially a rate performance of  $160 \text{ mAh g}^{-1}$  at 10C.

Porous electrodes with multi-shell structure have attracted much

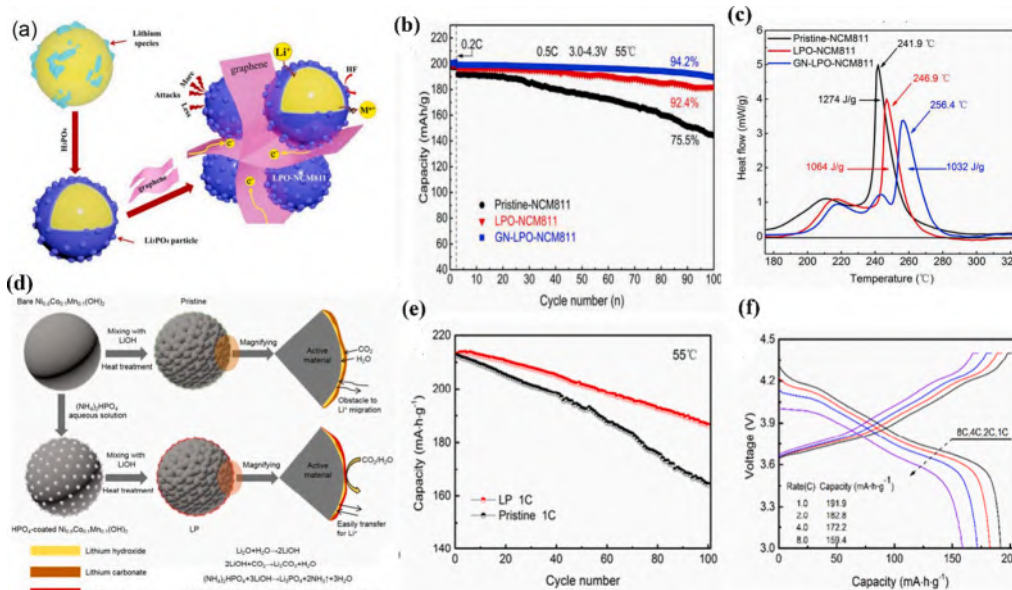


**Fig. 24.** (a) The synthesis schematic and working mechanism of GN-LPO-NCM811. (b) The cycling performance for pristine and modified samples in the voltage range 3.0–4.3 V at 0.5C at 55 °C. (c) The differential scanning calorimetry traces showing heat flow from the reaction of the electrolyte with pristine NCM811, LPO-NCM811, and GN-LPO-NCM811 charged to 4.3 V. Reproduced with permission.[128] Copyright 2019, Elsevier. (d) Schematic illustration of chemistry on the surface. (e) Cycling performance of the as-prepared samples over the voltage range of 3.0 ~ 4.4 V at 55 °C at 1C. (f) rate capability for the LP. Reproduced with permission. [129] Copyright 2019, Elsevier.



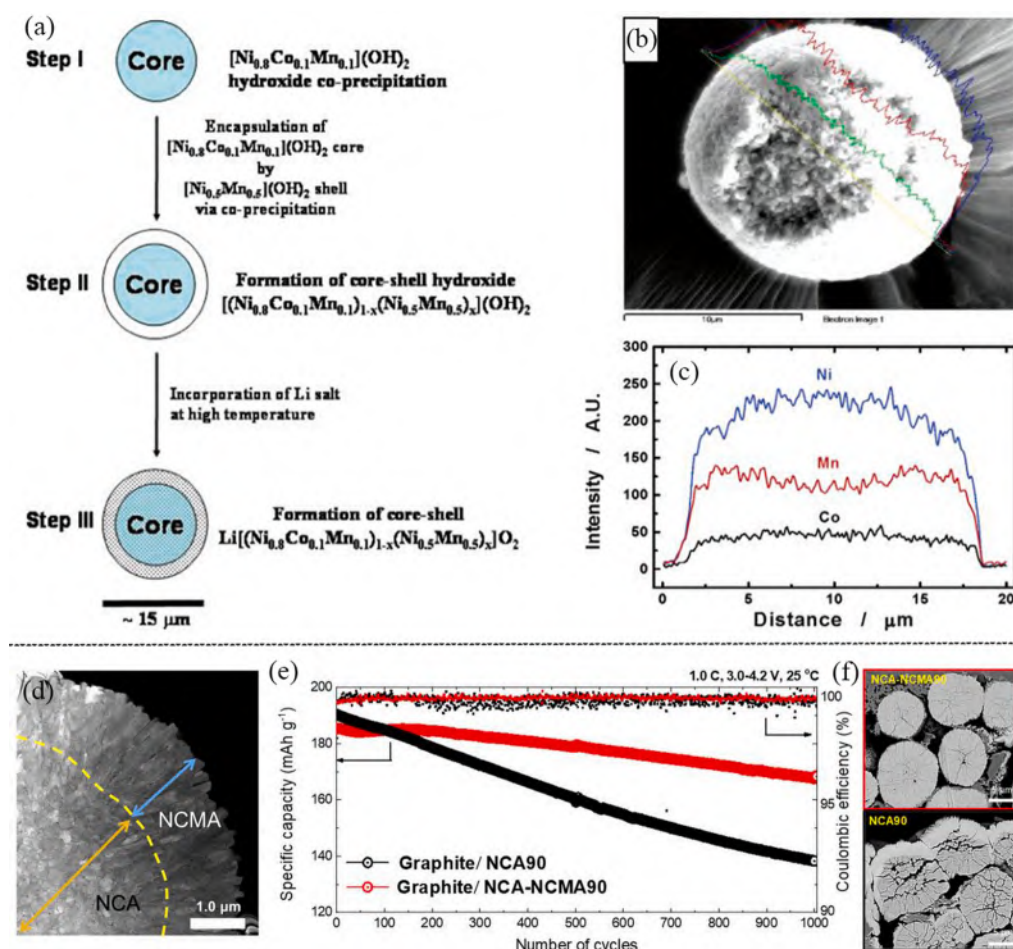


**Fig. 25.** (a). Schematic diagram of the structure of concentration gradient cathode materials and electrochemical performance. (b-c) The energy dispersive spectroscopic (EDS) image of the Li  $[(\text{Ni}_{0.8}\text{Co}_{0.1}\text{Mn}_{0.1})_{0.8}(\text{Ni}_{0.5}\text{Mn}_{0.5})_{0.2}]\text{O}_2$  particle. Reproduced with permission. [137] Copyright 2005, American Chemical Society. (d) TEM image of an NCA-NCMA90 primary particles. (e) Long-term cycling performance of the NCA90 and NCA-NCMA90 cathodes in full cells. (f) Cross-sectional SEM images of the NCA90 and NCA-NCMA90 cathodes from the full cells after 1000 cycles. Reproduced with permission. [158] Copyright 2019, Elsevier.

interest in recent years. First, the porous multi-shell structure provides more lithium ion channels to enhance specific capacity. Second, the multi-shell structure has a lithium ion diffusion path that is very short, leading to good rate performance. As a cathode material for lithium ion batteries, exhibition of high performance is mandatory. Zou et al. [49] synthesized a nickel rich multilayer hollow fiber material with low cation mixing using green algae fiber as template. Compared with the traditional nickel rich materials, the multi-layer hollow fiber materials had lower cationic mixed defects and multi-layer hollow fiber conductive network. Thereby, the materials showed excellent electrochemical performance (Fig. 26a-f). In addition, Xu et al. [48] synthesized secondary spherical Ni-rich cathodes NCM811, which was formed by the primary agglomeration of radially oriented single crystal particles. The surface of the spherical secondary particles were  $\text{Li}^+$  active (010) crystal, which formed three-dimensional  $\text{Li}^+$  transport channels, thus improving the  $\text{Li}^+$  transport rate and rate performance. In addition, the radial primary particles have the same orientation, which significantly reduced the grain boundary stress caused by the anisotropic volume change, further inhibiting the particle breakage and improved the cycle stability (Fig. 26g-i).

#### 5.4. Crystal form regulating

In recent years, many studies have reported that oxide positive electrode can improve specific capacity when charged at high voltage, but the increase in voltage will aggravate the material decomposition and seriously affect the safety performance of the battery. It is generally believed that the transition of nickel rich cathode materials from layered to spinel or completely disordered rock salt structure, as well as the

dissolution, migration and segregation of transition metals (TMs), can cause structural reconstruction, resulting in capacity attenuation. It is observed that the inhomogeneous stress can cause intra-grain cracks during the cycle, which can aggravate the collapse and capacity loss of the nickel rich cathode materials structure. Some traditional modification methods including doping and coating have been reported to inhibit the cation mixing and interface side reactions. But excessive coating and unregulated doping might hinder the migration of  $\text{Li}^+$ , thus affecting the electrochemical performance of the battery. In order to solve these defects, creative strategies must be adopted to improve the structural stability of cathodes. The ideal method is to adjust the structural and morphological characteristics simultaneously in order to impede the structural failure and inter-granular fracture. Compared with traditional polycrystalline particles, single-crystal cathode materials have attracted a solemn attention due to its excellent capacity retention rate in the long cycle. Firstly, the cracking of nickel rich oxides can be inhibited due to the inherent structural integrity and continuous conductive network of single crystal particles. Second, compared with the polycrystalline materials, single crystal electrodes have no grain boundaries in theory, which can improve the antioxidant capacity and structural stability in the process of interacting with electrolytes.

In order to further understand the correlation between surface structure, internal strain, and capacity deterioration, Qian et al. [47] directly observed the correlation between surface chemistry and phase distribution from homogeneity to heterogeneity by using X-ray spectroscopy and nano tomography, which induced heterogeneous internal strain within the particle and structural/performance degradation during cycling. The improved strategy effectively adjusted the performance degradation of single crystal cathode and provided a new idea for



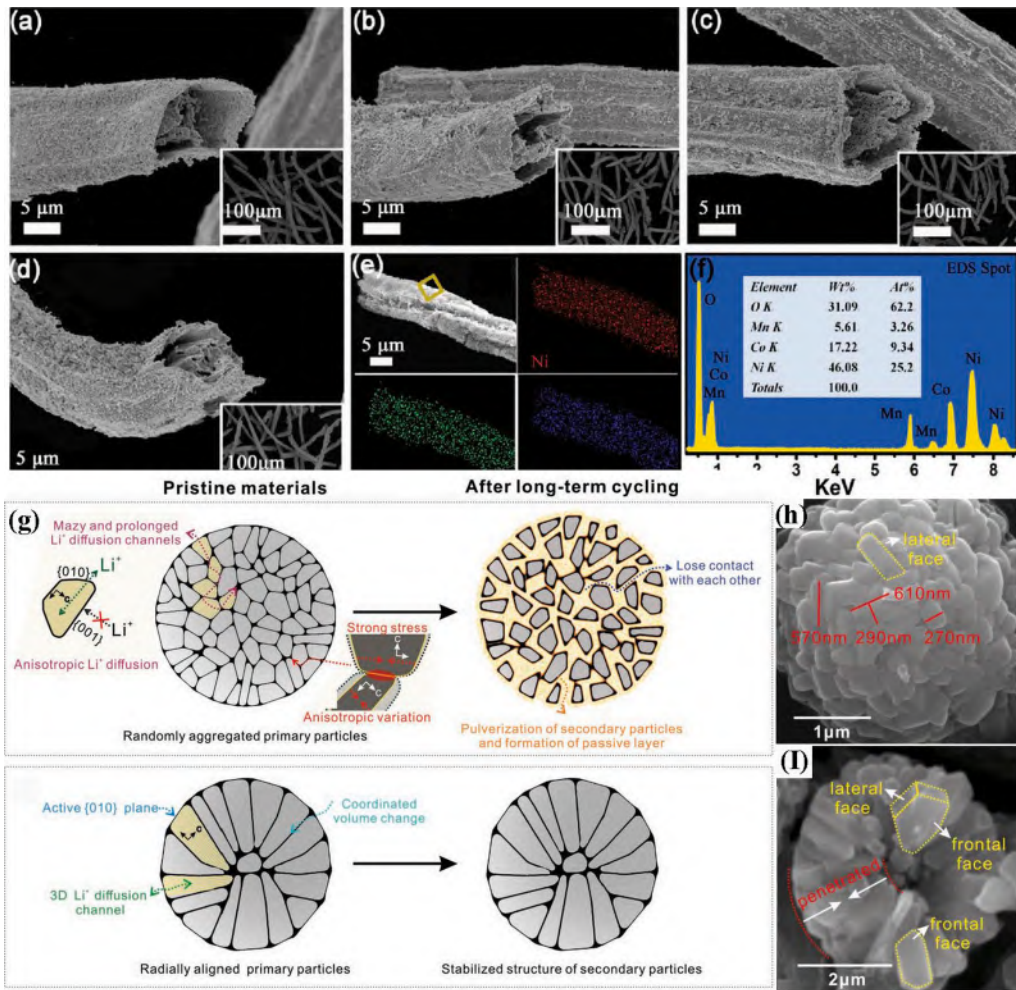


**Fig. 26.** Cross-section SEM images of the multi shelled  $\text{LiNi}_{0.65}\text{Co}_{0.25}\text{Mn}_{0.1}\text{O}_2$  hollow fibers (a)  $x = 0.8$ , (b)  $x = 0.7$ , (c)  $x = 0.65$ , (d)  $x = 0.5$ . (e) SEM image of  $\text{Li}(\text{Ni}_{0.65}\text{Co}_{0.25}\text{Mn}_{0.1})\text{O}_2$  and the corresponding EDS mapping for Ni, Co, Mn elements. (f) EDS spectrum collected from the area in panel (e) of  $\text{Li}(\text{Ni}_{0.65}\text{Co}_{0.25}\text{Mn}_{0.1})\text{O}_2$ . Reproduced with permission.[49] Copyright 2017, Wiley-VCH. (g) Schematic illustration of the structure and characteristics of C-NCM (commercial NCM) and RASC-NCM materials. (h) SEM images of RASC-NCM. (i) cross-sectional SEM images of RASC-NCM. Reproduced with permission.[48] Copyright 2019, WILEY-VCH.

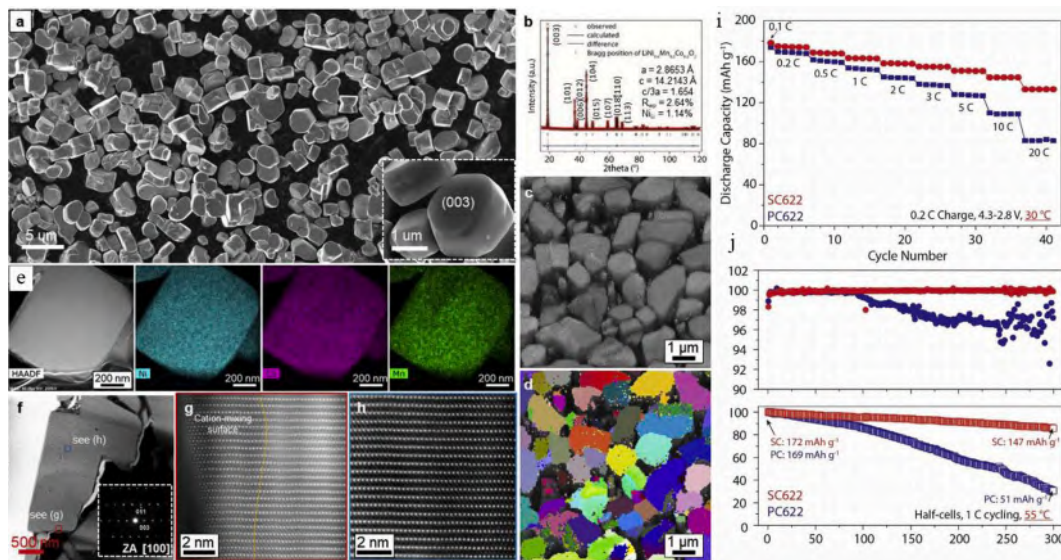


**Fig. 27.** (a) SEM image of the as-synthesized particles. (b) PXRD pattern and the Rietveld refinement results. (c) and (d) are band-contrast EBSD map and the EBSD orientation (Euler angles) map of the particles. Each color in (d) indicates a specific crystal orientation of the grains compared to a chosen reference. (e) STEM-EDS mapping of the particle showing homogeneous distribution of Ni, Co, and Mn elements. (f) STEM image of a particle oriented along the [010] zone axis of  $\text{LiNi}_{0.6}\text{Mn}_{0.2}\text{Co}_{0.2}\text{O}_2$ . (g) and (h) are HAADF-STEM images showing the particle has well-formed layered structure and a surface cation mixing layer of 3–5 nm in thickness. (i) Half-cell rate capability tests of the SC622 cathode and PC622 cathode. (j) half-cell cycling performance of the SC622 and PC622 cathodes at a current density of 1C in 2.8–4.3 V at 55 °C. Reproduced with permission.[47] Copyright 2020, Elsevier.

improving the performance of cathode (Fig. 27). Fan et al. [138] synthesized a single crystal and the secondary particle sample. It has been proved by testing that the sample of secondary particles in the process of charge–discharge cycle process still maintained the R3m-layered structure in the central bulk far away from the nano crack. However, the approached parts gradually deteriorated into disordered layered phase and defect rock-salt phase, which eventually transferred into the disordered rock-salt phase at the nano-crack surface. Compared with the materials with secondary particle morphology, nano/micro cracks were not observed in the synthesized single crystal materials, and the integrity of micron particles was well maintained both inside and outside.

### 5.5. DOD setting

The mechanism of capacity attenuation of high nickel positive electrodes (NCM and NCA) involves the accumulation of mechanical strain caused by the sudden collapse of layered structure during phase transformation, and the formation and development of inter granular micro cracks. A lot of research has been carried out to improve the cycle stability of high nickel positive electrode by coating and doping, but minor results have been perceived. Yoon et al. [44] found that the cycle stability of the cylindrical battery based on NCA positive electrode and graphite negative electrode was poor, and the capacity retention rate was of only 50% after 2000 cycles at 100% discharge depth. However, when the discharge depth was 60%, the cycle performance was found to be better, which indicated that the discharge depth should be limited to 60% in order to achieve long-term cycle stability. However, this reduced the energy density and increased the weight and cost of the battery.

### 5.6. Electrolyte modification

Electrolyte is known as the “blood” of lithium-ion batteries. It plays an important role in the performance of lithium-ion batteries (LIBs), especially in the structure and properties of the interface between electrodes and electrolyte. However, the structural changes and

interface side reactions of cathode materials under high voltage and high temperature bring great challenges to the practical applications in the traditional electrolyte system. It is one of the effective methods to improve the electrochemical performance of lithium-ion battery by developing suitable electrolytes to improve the interface structure between electrode and electrolyte, which has attracted extensive attention in recent times. Since  $\text{LiPF}_6$  decomposes and produces HF at high pressure and high temperature, a series of safety problems are a matter of concern. In  $\text{LiPF}_6$  based electrolytes, the use of additives to establish a uniform cathode electrolyte interface (CEI) and removal of reactive HF and  $\text{PF}_5$ , is considered as a method to maintain the stable electrochemical performance of Ni rich cathodes. Before the decomposition of electrolyte solvents such as ethylene carbonate (EC), dimethyl carbonate (DMC) and lithium salt, the film-forming additives are oxidized on the surface of nickel rich cathode to form uniform CEI. The existence of uniform CEI can inhibit the side reaction of electrolyte at the cathode. Dong et al. [139] introduced p-toluenesulfonyl isocyanate (PTSI) as electrolyte additive. The test showed that the  $\text{Li}/\text{LiNi}_{0.5}\text{Co}_{0.2}\text{Mn}_{0.3}\text{O}_2$  half-cell with PTSI exhibits superior rate capability when compared to that of the baseline electrolyte. The discharge capacity retention is elevated from 71.4% to 86.2% after 100 cycles at room temperature. This can be also attributed to the  $-\text{S}=\text{O}$  group in PTSI which serves as the weak base site to restrain the reactivity of  $\text{PF}_5$ , resulting in the suppression the formation of LIF and HF (Fig. 28).

Phosphite derivatives as additives are an efficient method to make a protective film on high-voltage nickel rich cathodes, to mitigate the hydrolysis reactions of  $\text{LiPF}_6$ , and to eliminate HF. Researchers have aroused their interest to test the effect of phosphate based additives on nickel rich cathode materials. Song et al. [159] carried out a comparative study by using organophosphorus compounds including triphenyl phosphite (TPP), trimethyl phosphite (TMP), tris(2,2,2-trifluoroethyl) phosphite (TFEP), and tris(trimethylsilyl) phosphite(TMSP) in  $\text{Li}/\text{LNMO}$  half cells. It was found that the cycle performance and rate performance of the half-cell were significantly improved under the action of TMP. Moreover, phosphite based additives inhibited the hydrolysis of

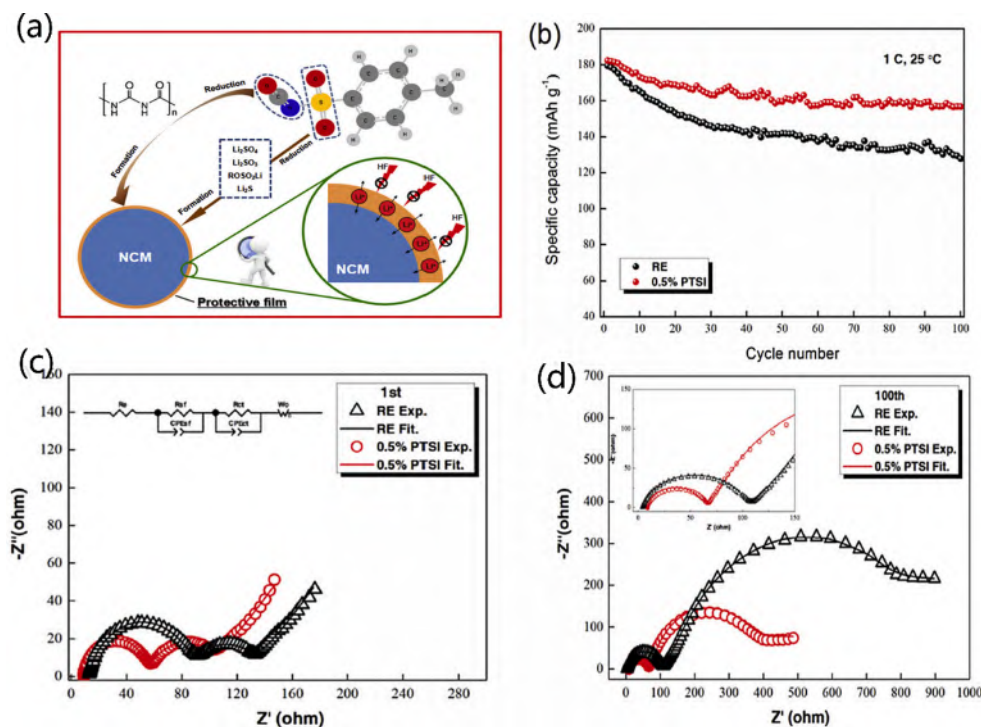


**Fig. 28.** (a) Schematic mechanism on the roles of PTSI to the high voltage electrochemical properties improvement of  $\text{LiNi}_{0.5}\text{Co}_{0.2}\text{Mn}_{0.3}\text{O}_2$  electrode. (b) The cyclic performance at 25 °C. (c) Nyquist curves of  $\text{Li}/\text{LiNi}_{0.5}\text{Co}_{0.2}\text{Mn}_{0.3}\text{O}_2$  half cells in RE and PTSI-containing electrolyte after first cycle and (d) 100 cycles under 55 °C and 1C rate. Reproduced with permission.[139] Copyright 2017, Elsevier.



$\text{LiPF}_6$  and removed HF. Jang et al. [140] proposed silyl-functionalized dimethoxydimethylsilane (DODSi) as a multi-functional additive. In contrast to the typically attempted cathode additive, silyl-functionalized dimethoxydimethylsilane had a wide electrochemical window up to 5.0 V, which indicated that DODSi will not damage the electrochemical stability of traditional carbonate based electrolytes. In terms of cycle performance, the use of DODSi effectively improved the cycle performance and rate performance at higher potential. DODSi removed F from the battery and inhibited the additional side reactions on the surface of NCM811. Presently, Yim et al. [141] showed that DVS oxidized and decomposed on the surface of NCM721 electrode material, forming an inert layer on the surface of positive electrode material and thereby reducing the decomposition of electrolyte on the surface of positive electrode. This resulted in the significant improvement of the cycle stability of NCM721 electrode material. In order to analyze the composition of the inert layer formed on the surface of NCM721 by DVS, the surface composition of NCM721 was characterized by means of FT-IR. Polycarbonate ( $\text{RCO}_2\text{R}$ ) and carbonate ( $\text{Li}_2\text{CO}_3$ ) were observed on the surface after one cycle, from the test results, which mainly come from the decomposition of the solvent. At the same time, the absorption signals ( $1275\text{ cm}^{-1}$  and  $1371\text{ cm}^{-1}$ ) of polyalkyl sulfone and polyolefin functional groups on the surface of NCM721 particles using DVS additive electrolyte were observed, which indicated that DVS did decompose on the surface of NCM721 particles (Fig. 29 a-b). Deng et al. [142] used fluorinated lithium electrolyte (FEC: FEMC: HFE, 2:6:2) and 2% LiDFOB to produce F and B rich cathode/electrolyte interface which was able to withstand the volume expansion of  $\text{LiNiO}_2$ . The  $\text{LiNiO}_2$  with this electrolyte provided discharge capacity of  $210\text{ mAh g}^{-1}$  at 0.5C, and the capacity retention was still maintained at 80% even after 400 cycles (Fig. 29c-d).

### 5.7. Binder

Usually, PVDF is a commonly used binder in cathode materials (used with NMP solvent) with good bond strength, electrochemical stability and insoluble in electrolyte, but its alkali resistance is poor. [160] When high nickel system is selected as the cathode material, the residual alkali content in the material becomes higher and higher with the increase of capacity. Under the strong alkali environment, PVDF will produce decomposition reaction, resulting in the separation of hydrogen fluoride and making the slurry gel (Fig. 30). At the same time, some side reactions will occur on the surface of the high nickel positive electrode,

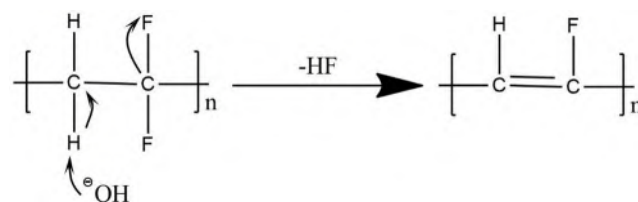


Fig. 30. Reaction formula of PVDF elimination reaction.

which will cause the secondary particles to collapse, resulting in a decrease in the conductivity of the battery. [161] At present, we have summarized the following three points to solve this problem: 1. Reduce alkaline substances. 2. The alkali resistance was improved by PVDF modification. 3. Replace PVDF with new binder. For the treatment of the Ni-rich cathode itself, the optimization of sintering process can reduce the residual alkaline impurities on its surface, but compared with water washing process, this method is not complete. At the same time, water washing will lead to the attenuation of material properties, so these two methods are not applicable. Therefore, coating a layer of stable oxide is a better choice. In addition, the addition of Lewis acid (such as  $\text{LiPF}_6$ ) [162] which can neutralize with free alkali in the Ni-rich cathode has been reported as a feasible method. The application performance of PVDF in high nickel NCM can also be improved by modifying PVDF. For example, Maurizio Biso et al. found that the chemical modification of PVDF by Solef was effective in preventing gelatinization of slurry compared with emulsion polymerization PVDF. [163] Meanwhile, Ki Jae Kim of Korea's Jianguo University and Jang wook Choi of Seoul University reported a high elastic binder spandex (spdx), which can overcome the problems of nickel rich layered cathode materials and significantly improve their electrochemical properties. The high elasticity of spdx enables it to uniformly coat  $\text{LiNi}_{0.8}\text{Co}_{0.1}\text{Mn}_{0.1}\text{O}_2$  particles through shear force during slurry mixing, so as to prevent side reactions in the circulation process of particles, which will greatly promote the wide application of nickel rich cathode materials in the future. [164] Japan's ZEON group also said that it has developed a new fluorine-free binder, which can replace the traditional PVDF too."

### 5.8. Separator

Separator is a kind of functional membrane material with microporous structure, and its thickness is generally  $8 \sim 40\text{ }\mu\text{m}$ . In the battery

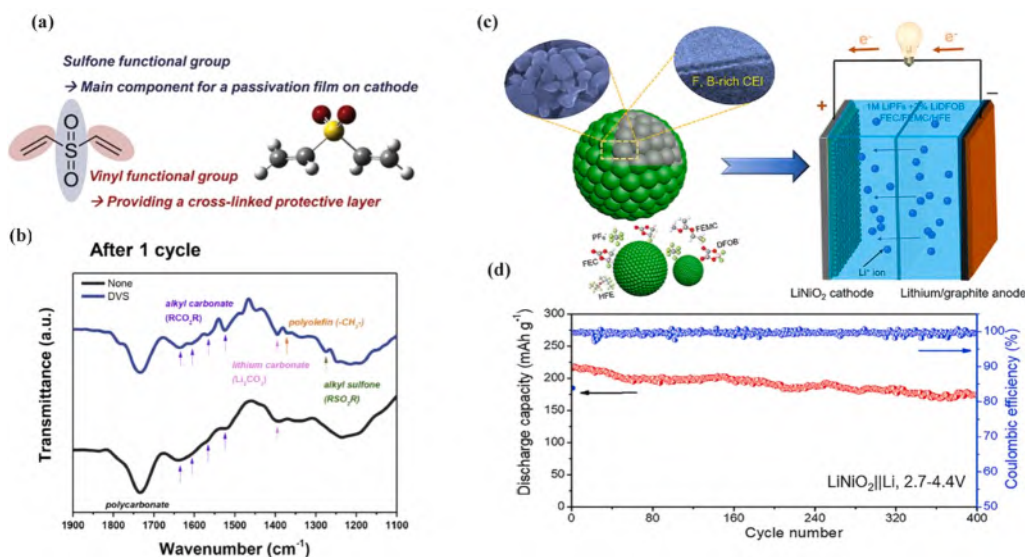


Fig. 29. (a) 2D and 3D molecular structures of DVS. (b) FT-IR analysis results of cycled NCM721 cathode after 1 cycle. Reproduced with permission. [141] Copyright 2015, Elsevier. (c) Synthesis illustrative diagram of  $\text{LiNiO}_2$ . (d) Cycle performance curve of  $\text{LiNiO}_2$ . Reproduced with permission. [142] Copyright 2019, Elsevier.



system, The separator membrane can prevent the short circuit of positive and negative electrodes and provide lithium ion diffusion channel. It can regulate the lithium ion diffusion rate, the retention of electrolyte, the internal resistance of the system and the composition of battery interface structure, so as to affect the electrochemical performance of the battery. However, polypropylene and polyethylene separator currently used commercially will shrink and melt at high temperatures, resulting in short circuit and thermal runaway. The above traditional separator can not meet the current needs of lithium-ion batteries. High porosity, high thermal resistance, high melting point, high strength and good wettability to electrolyte are the development direction of lithium-ion batteries in the future.

According to the development needs of lithium-ion battery technology, researchers have developed a variety of new separators based on the traditional polyolefin membrane. According to the development needs of lithium-ion battery technology, some polymers with better comprehensive performance, such as PVDF, PET and PI et al, have been gradually applied. [165] At the same time, coating inorganic ceramic particle layer or composite polymer layer on the substrate will further improve its comprehensive properties.

For example, Zhao et al. designed a heat-resistant and fireproof double function diaphragm by coating ammonium polyphosphate (APP) particles on a ceramic-coated separator modified with phenol-formaldehyde resin (CCS@PFR). When applied to  $\text{LiNi}_{0.8}\text{Co}_{0.1}\text{Mn}_{0.1}\text{O}_2$ ||SiOx-Gr full battery, it has excellent safety performance, does not catch fire in 30 s combustion test and does not fail in 10 min of high temperature test above 300 °C. [166] So in the long run, the traditional separator of single component may be gradually replaced by composite separator with better comprehensive properties. With the rapid development of solid-state batteries, gel electrolytes or solid electrolytes may completely replace the diaphragm in the future

### 5.9. Assembly technology

Safety performance is the largest luxury of electric vehicles. As one of the core components of electric vehicles, the safety of batteries largely determines the safety performance basis of electric vehicles. The optimization of assembly process has a great impact on the safety of lithium-ion battery. The assembly process of the battery is cumbersome. Before assembly, the diaphragm needs 120 °C heat treatment to increase its barrier performance and safety. The battery shall be vacuum dried for 24 h before cell liquid injection to remove the moisture and moisture in the battery components, so as to prevent  $\text{LiPF}_6$  from reacting with water to form HF and shorten the service life. After the whole battery assembly is completed, the battery shall use X-ray to identify whether the internal structure of the battery is normal, and check the cell misalignment, steel

shell crack, solder joint, short circuit, etc. to eliminate the battery with the above defects and ensure the quality of the battery. At the same time, compared with the wound structure core, the laminated structure has more uniform current density, excellent internal heat dissipation performance, and is more suitable for high-power discharge. For example, BYD blade battery with laminated cell structure shows better cycle characteristics, safety characteristics and energy density. Although the Ni-rich cathode is thermodynamically unstable, it is believed that it will be well solved with the continuous development of assembly technology.

## 6. Prospect

When compared with the traditional layered  $\text{LiCoO}_2$ , nickel-rich layered oxide cathode materials ( $\text{LiNi}_{1-x-y}\text{M}_x\text{N}_y\text{O}_2$ ;  $x + y \leq 0.5$ ; M, N = Co, Mn, Al, Mg, Ti etc.) have the advantages of high reversible specific capacity (greater than  $200 \text{ mAh g}^{-1}$ ), comparably high operating voltage and low cost. These beneficial features are responsible in making them a research hotspot in the arena of materials, energy and other disciplines. Nickel rich layered oxide cathodes have gradually entered the stage of commercial application and have been considered as promising cathode materials for lithium-ion power batteries. In the future, Ni-rich cathodes will have further applications and development in the following aspects (Fig. 31):

### 6.1. Co-free

Due to its scarcity and strategic value, the price of cobalt has remained high for a long time. Reducing cobalt content has become the primary measure to reduce the cost of NCA or NCM cathode materials. At the same time, the redox potential of nickel is relatively high, and the increase of its content can increase the capacity. The development of high nickel and cobalt free materials has become an inevitable trend. Cobalt free high nickel materials have obvious advantages (Fig. 32a) [167]. There are two R & D lines for cobalt free high nickel materials: (1) Reduce the content of CO in NCM/NCA and increase the content of Ni. (2) reduce the content of nickel in  $\text{LiNiO}_2$ . At present, NCM/NCA with 80% Ni content has been reported commercially, and those with more than 80% (90%, 95% et al.) content have also been reported by relevant laboratories, which has been mentioned in the previous part, it will continue to develop towards ultra-high nickel content in the future. For  $\text{LiNiO}_2$ , because  $\text{Ni}^{2+}$  and  $\text{Li}^+$  have the same ion radius,  $\text{Ni}^{2+}$  can easily migrate to the lattice position of Li, thus blocking the migration channel of  $\text{Li}^+$ , greatly reducing the reversible capacity of the material. Ni site doping is a main means to improve the properties of modified materials, including mg, Fe, Al, Mn and other transition metal elements. For

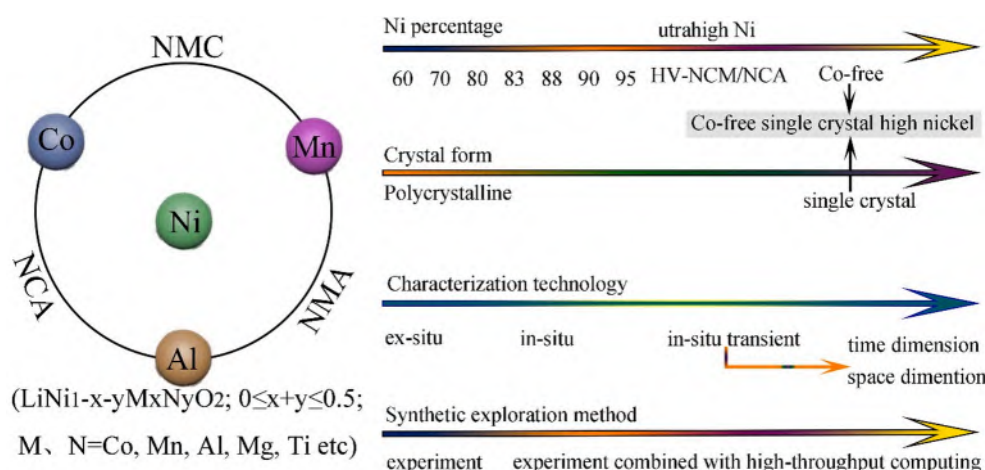
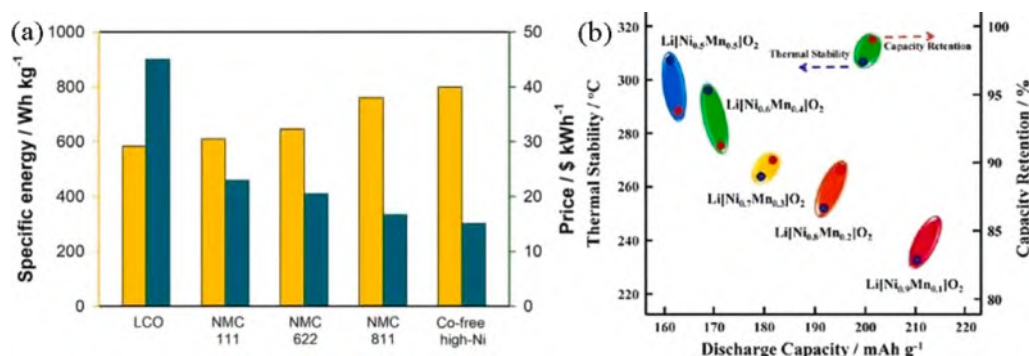


Fig. 31. Further applications and development trends of nickel rich cathodes in the future.



**Fig. 32.** (a) A comparison of specific energy and cost per energy of LCO, NMC111, NMC622, NMC811, and Co-free high-Ni layered oxides. Reproduced with permission. [167] Copyright 2020, Elsevier. (b) Effect of Mn concentration on electrochemical properties and thermal stability of high nickel materials. Reproduced with permission. [168] Copyright 2013, American Chemical Society.

example, Yang kook sun and others found that Mn content is inversely proportional to the capacity of the material, but directly proportional to the capacity retention and thermal stability of the material (Fig. 32b) [168].

## 6.2. Single crystal

Compared with the secondary spherical polycrystalline material of about 10  $\mu\text{m}$  formed by the agglomeration of hundreds of nano-sized primary particles, the single crystal material is directly composed of independent crystals with a diameter of 2–5  $\mu\text{m}$ . Due to the higher crystallinity, more stable layered structure and anisotropy, the single crystal material has both cyclic performance and thermal stability, And gas production are better than the traditional secondary particle NCM materials [169]. At present, high nickel single crystal cathode materials have been studied mainly for single crystal nickel cobalt lithium manganate (NCM) [170] nickel cobalt lithium aluminate (NCA) [171] ternary cathode materials with nickel content of more than 80% and single crystal nickel cobalt lithium manganate (NCMA) [172] quaternary cathode materials. Although single crystal materials contribute to cyclic stability, the low diffusion kinetics of lithium ion limits the multiplier performance and reversible capacity. Therefore, the optimization of single crystal microstructure, particle size and test environment will play a decisive role in achieving rapid charge–discharge. Recently, J. R. Dahn of dalhouse University studied the synthesis of Mg doped cobalt free single crystal LNO by one-step lithium method. Compared with polycrystalline cells cycled at 30 °C, cycling single crystal materials at 55 °C can restore the discharge capacity of about 20 mAh g<sup>-1</sup> and produce similar irreversible capacity. [173] With the development of lithium-ion battery technology, people began to demand a cathode material with large capacity, high voltage and good stability to break through the existing energy density. Cobalt free nickel rich single crystal cathode material is expected to achieve this goal. However, it is still a long way from industrialization, which still needs a lot of efforts and attempts.

## 6.3. Characterization technology

The development of characterization technology is very important to analyze the microstructure morphology and chemical characteristics of electrode materials. Especially in the process of electrochemical charge and discharge, in-situ characterization technology must be introduced to observe the structural transformation of electrode materials, redox process, solid–liquid interface formation, side reactions and lithium ion transport characteristics in real time [174]. In addition, the process of lithium diffusion and decay reaction in high nickel ternary materials depends on the transient properties of material particle size. The performance degradation of subsequent cycles can be attributed to several

causes like complex chemical and mechanical interactions among lithium diffusion, anisotropic lattice strain, surface oxygen consumption and cathode particle deterioration. Amongst them, the transient performance of particle size of material remains the key factor of diffusion and deterioration process. Once the electrochemical process is interrupted for diffraction measurement, the charge rebalancing will occur, the movement of lithium ions will be along the radial direction of the particles and the anisotropy of the lattice parameters will be masked. Therefore, it is indispensable to use high-resolution experimental technology in time (subsecond) and space dimensions (submicro) in order to explore the undisturbed charge discharge process for better understanding of the potential decomposition degradation mechanism. [42]

## 6.4. High-throughput calculations

In the era of big data, high throughput computing method based on material genome and AI technology can quickly determine and select appropriate electrode materials and components and configurations of the whole battery system. Therefore, we also describe the screening and modification of electrode materials by high-throughput calculations. The traditional research and development of battery materials is based on the development mode characterized by “trial and error method”. The cycle from discovery to application is very long, which generally takes 20 years or more. In the process of lithium battery material design and development, the theoretical method of high-throughput computing began with cedar research group. They have carried out research called “genetic engineering of lithium ion battery materials” since 2010. In this method, new compounds are produced by replacing the elements in compounds containing polyanion  $\text{xO}_4$  ( $\text{x} = \text{P}, \text{s}, \text{as}, \text{SI}$ ). The parameters such as energy density, voltage and volume change after Li removal are calculated, and the new materials are selected. Starting from the mineral sidorenkite structure existing in nature, they replaced its elements, constructed more than 270 components and structures, calculated its properties, and screened out several materials:  $\text{Li}_3\text{Mn}(\text{CO}_3)(\text{PO}_4)$ ,  $\text{Li}_2\text{V}(\text{CO}_3)(\text{PO}_4)$ ,  $\text{Li}_3\text{V}(\text{CO}_3)(\text{SiO}_4)$ , etc. [175] Based on theoretical calculations, gerbrand cedar of the University of California, Berkeley and others carried out a comprehensive high-throughput search in five aspects: phase stability, electrochemical stability, chemical stability, ionic conductivity and electronic conductivity, and quickly found suitable coating materials for cathode materials (Fig. 33a). From the results of the author’s study, it is obvious that the selection of coating materials needs to be careful to the specific solid-state electrolyte (SSE)/cathode electrode combination (Fig. 33b). The author believes that lithium borate is recommended regardless of the interface, because lithium borate has good chemical stability and high oxidation limit. Although the results show that  $\text{LiBa}(\text{B}_3\text{O}_5)_3$  has a high migration barrier for lithium ion conduction, other borates with high lithium content may still show high ionic conductivity [176]. Meanwhile, Professor Mo Yifei’s

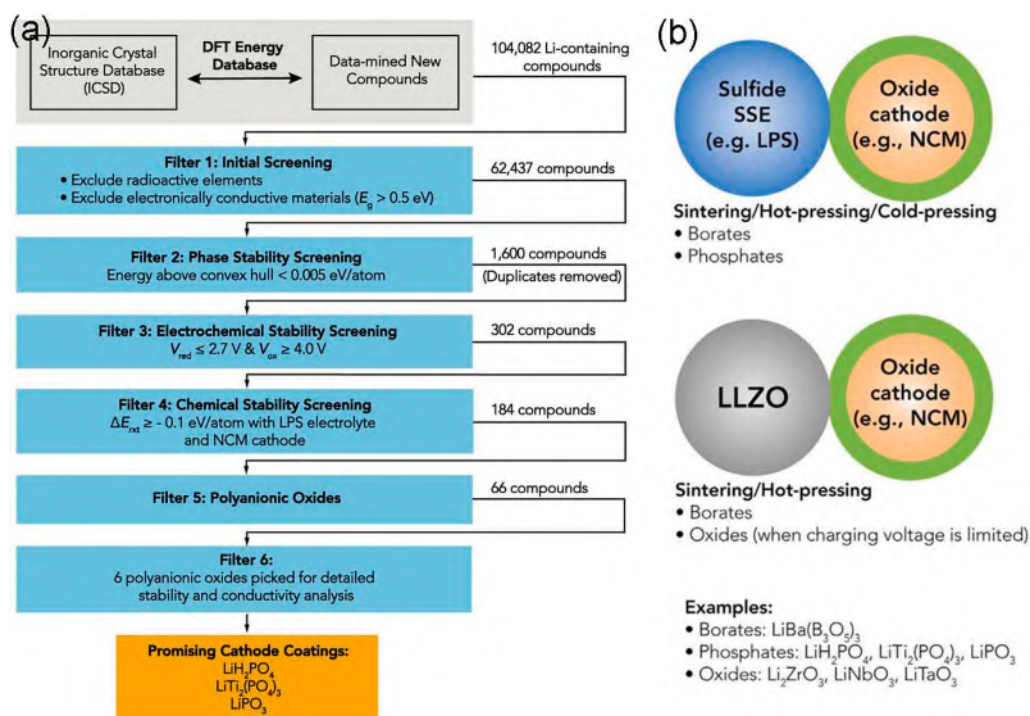


**Fig. 33.** (a) Flowchart describing the computational screening of cathode-coating materials (Following the initial screening, phase stability, electrochemical stability, and chemical stability were used as sequential filters for the high-throughput screening. Eg is the density functional theory (DFT)-calculated Kohn-Sham band gap; Vred and Vox are the reduction and oxidation limits of the electrochemical stability window in V versus Li metal, respectively; DERxt is the reaction energy of the material with the cathode or electrolyte in eV/atom; LPS denotes the SSE material  $\text{Li}_3\text{PS}_4$ ; and NCM denotes the fully lithiated cathode material  $\text{LiNi}_{1/3}\text{Co}_{1/3}\text{Mn}_{1/3}\text{O}_2$ ). (b) Coating Recommendations for Various Cathode/SSE Interfaces under Different Processing Conditions (Oxide cathode/sulfide SSE and Oxide cathode/LLZO). Reproduced with permission. [176] Copyright 2019, American Chemical Society.

team from the University of Maryland studied, analyzed and screened the interaction and interfacial thermodynamic stability of a series of solid compounds for cathode materials of high specific energy lithium-ion batteries through high-throughput thermodynamic calculation. By studying and analyzing the chemical reactions of a large number of compounds on cathode materials, the effects of different material chemistry and components on the interface stability of cathode materials are explained, and the strategy of selecting solid electrolyte and coating materials for different cathode materials is put forward [177].

With the continuous development of material genome and artificial intelligence technology, we believe that it will provide strong guidance for the specific design strategy and material selection of lithium cathode materials such as ternary high nickel. However, at present, the research work on high-throughput screening of lithium battery materials is in its infancy, and there are still the following problems. [178,179] 1) It focuses on the calculation of thermodynamic properties of materials, such as formation energy and thermal stability, and lacks the consideration of lithium ion transport, an important dynamic property; 2) The constraints used in screening are lack of pertinence and hierarchy, resulting in a large number of repeated and unnecessary calculations; 3) The first principle method based on density functional theory is mostly used in the calculation, but it has not been combined with other calculation methods or software; 4) A large number of calculated data have not been effectively mined. However, it can be predicted that in the next few years, the application of high-throughput computing methods, combined with experimental research, will greatly accelerate our R & D of lithium battery materials, deepen our understanding of various problems in lithium batteries, reveal the structure performance relationship and internal physical laws of materials, so as to shorten the whole process from R & D to application. The application of high-throughput computing method to explore and design new lithium battery materials is an important way for future material scientific research and development. It can shorten the whole process from R & D to application, and provide strong support for the development of new battery materials and even battery systems.

## 7. Summary

In summary, the structure, surface properties and electrochemical performance of nickel rich layered oxide cathodes have been preferably awarded and have shown substantial improvements these years. Of course, nickel rich layered oxide cathodes still have numerous challenges related to structural instability, surface side reactions, and safety concerns. Nevertheless, it is believed that unceasing and thorough investigations and honest efforts of the scientific researchers can undeniably inaugurate the application of nickel rich layered oxide cathodes as the next generation of lithium ion batteries high-energy cathode materials in the impending future.

## Declaration of Competing Interest

The authors declare that they have no known competing financial interests or personal relationships that could have appeared to influence the work reported in this paper.

## Acknowledgement

We thank the financial supports from the National Natural Science Foundation of China (51774251), Hebei Natural Science Foundation for Distinguished Young Scholars (B2017203313), Hundred Excellent Innovative Talents Support Program in Hebei Province (SLRC2017057), Talent Engineering Training Funds of Hebei Province (A201802001), and the opening project of the state key laboratory of Advanced Chemical Power Sources (SKL-ACPS-C-11).

## References

- [1] Liu Y, He X, Hanlon D, Harvey A, Khan U, Li Y, et al. Electrical, mechanical, and capacity percolation leads to high-performance  $\text{MoS}_2$ /nanotube composite lithium ion battery electrodes. *ACS Nano* 2016;10(6):5980–90.
- [2] Luo K, Roberts MR, Hao R, Guerrini N, Pickup DM, Liu Y-S, et al. Charge-compensation in 3d-transition-metal-oxide intercalation cathodes through the generation of localized electron holes on oxygen. *Nat Chem* 2016;8(7):684–91.
- [3] Wu T, Fan J, Li Q, Shi P, Xu Q, Min Y. Palladium nanoparticles anchored on anatase titanium dioxide-black phosphorus hybrids with heterointerfaces: highly



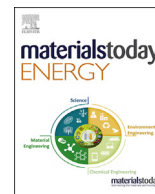
- electroactive and durable catalysts for ethanol electrooxidation. *Adv Energy Mater* 2018;8(1):1701799.
- [4] Xin F, Zhou H, Chen X, Zuba M, Chernova N, Zhou G, et al. Li-Nb-O coating/substitution enhances the electrochemical performance of  $\text{LiNi}_{0.8}\text{Mn}_{0.1}\text{Co}_{0.1}\text{O}_2$  (NMC811) cathode. *ACS Appl Mater Interfaces* 2019;11(38):34889–94.
  - [5] Huang SF, Lv Y, Tie D, Yu Y, Zhao YF. Realizing simultaneously enhanced energy and power density full-cell construction using mixed hard carbon/ $\text{Li}_4\text{Ti}_5\text{O}_{12}$  electrode. *Rare Met* 2021;40(1):65–71.
  - [6] Yu Y, Huang S, Wang B, Tie D, Wang Q, Hou Y, et al. Achieving high energy full-cell lithium storage performance by coupling high capacity  $\text{V}_2\text{O}_5$  with low potential  $\text{Ni}_3\text{P}$  anode. *ACS Appl Mater Interfaces* 2018;11(1):19–25.
  - [7] Chang G, Zhao Y, Dong L, Wilkinson DP, Zhang L, Shao Q, et al. A review of phosphorus and phosphides as anode materials for advanced sodium-ion batteries. *J Mater Chem A* 2020;8(10):4996–5048.
  - [8] Yin X, Sarkar S, Shi S, Huang QA, Zhao H, Yan L, et al. Recent progress in advanced organic electrode materials for sodium-ion batteries: synthesis, mechanisms, challenges and perspectives. *Adv Funct Mater* 2020;30(11):1908445.
  - [9] Ryu HH, Park NY, Seo JH, Yu YS, Sharma M, Mücke R, et al. A highly stabilized Ni-rich NCA cathode for high-energy lithium-ion batteries. *Mater Today* 2020;36:73–82.
  - [10] Yang Y, Xu R, Zhang K, Lee SJ, Mu L, Liu P, et al. Quantification of heterogeneous degradation in Li-ion batteries. *Adv Energy Mater* 2019;9(25):1900674.
  - [11] Kim S, Cho W, Zhang X, Oshima Y, Choi JW. A stable lithium-rich surface structure for lithium-rich layered cathode materials. *Nat Commun* 2016;7(1):1–8.
  - [12] Liu W, Oh P, Liu X, Lee MJ, Cho W, Chae S, et al. Nickel-rich layered lithium transition-metal oxide for high-energy lithium-ion batteries. *Angew Chem Int Ed* 2015;54(15):4440–57.
  - [13] Reddy MV, Subbarao GV, Chowdari BVR. Preparation and characterization of  $\text{LiNi}_{0.5}\text{Co}_{0.5}\text{O}_2$  and  $\text{LiNi}_{0.5}\text{Co}_{0.4}\text{Al}_{0.1}\text{O}_2$  by molten salt synthesis for Li ion batteries. *J Phys Chem C* 2007;111(31):11712–20.
  - [14] Xu S, Du C, Xu X, Han G, Zuo P, Cheng X, et al. A mild surface washing method using protonated polyaniline for Ni-rich  $\text{LiNi}_{0.8}\text{Co}_{0.1}\text{Mn}_{0.1}\text{O}_2$  material of lithium ion batteries. *Electrochim Acta* 2017;248:534–40.
  - [15] Dwivedi D, Gond R, Dayamani A, Araujo RB, Chakraborty S, Ahuja R, et al.  $\text{Na}_{2.32}\text{Co}_{1.84}(\text{SO}_4)_3$  as a new member of the alluaudite family of high-voltage sodium battery cathodes. *Dalton Trans* 2017;46(1):55–63.
  - [16] Fei LF, Sun TY, Lu W, An XQ, Hu ZF, Jimmy CY, et al. Direct observation of carbon nanostructure growth at liquid-solid interfaces. *Chem Commun* 2014;50(7):826–8.
  - [17] Li W, Liu T, Zhang J, Peng N, Zheng R, Yu H, et al. Commercially available InSb as a high-performance anode for secondary batteries towards superior lithium storage. *Sustainable Energy Fuels* 2019;3(10):2668–74.
  - [18] Zhou G, Li F, Cheng HM. Progress in flexible lithium batteries and future prospects. *Energy Environ Sci* 2014;7(4):1307–38.
  - [19] Shi S, Li Z, Sun Y, Wang B, Liu Q, Hou Y, et al. A covalent heterostructure of monodisperse  $\text{Ni}_3\text{P}$  immobilized on N, P-co-doped carbon nanosheets for high performance sodium/lithium storage. *Nano Energy* 2018;48:510–7.
  - [20] Huang S, Li Z, Wang B, Zhang J, Peng Z, Qi R, et al. N-doping and defective nanographitic domain coupled hard carbon nanosheets for high performance lithium/sodium storage. *Adv Funct Mater* 2018;28(10):1706294.
  - [21] Huang S, Wang M, Jia P, Wang B, Zhang J, Zhao Y. N-graphene motivated  $\text{SnO}_2$ @ $\text{SnS}_2$  heterostructure quantum dots for high performance lithium/sodium storage. *Energy Storage Mater* 2019;20:225–33.
  - [22] Whittingham MS. Lithium batteries and cathode materials. *Chem Rev* 2004;104(10):4271–302.
  - [23] Park OK, Cho Y, Lee S, Yoo HC, Song HK, Cho J. Who will drive electric vehicles, olivine or spinel? *Energy Environ Sci* 2011;4(5):1621–33.
  - [24] Yan B, Lin S, Kang L, Song X, Tian Z, Jia K. Spinel structured  $\text{LiMn}_2\text{O}_4$  prepared by laser annealing. *Mater Technol* 2020;35:606–11.
  - [25] Ding Y, Mu D, Wu B, Wang R, Zhao Z, Wu F. Recent progresses on nickel-rich layered oxide positive electrode materials used in lithium-ion batteries for electric vehicles. *Appl Energy* 2017;195:586–99.
  - [26] Hassoun J, Kim J, Lee DJ, Jung HG, Lee SM, Sun YK, et al. A contribution to the progress of high energy batteries: A metal-free, lithium-ion, silicon-sulfur battery. *J Power Sources* 2012;202:308–13.
  - [27] Wang Y, He P, Zhou H. Olivine  $\text{LiFePO}_4$ : development and future. *Energy Environ Sci* 2011;4(3):805–17.
  - [28] Yamada A, Takei Y, Koizumi H, Sonoyama N, Kanno R, Itoh K, et al. Electrochemical, magnetic, and structural investigation of the  $\text{Li}_x(\text{Mn}_y\text{Fe}_{1-y})\text{PO}_4$  olivine phases. *Chem Mater* 2006;18(3):804–13.
  - [29] Tarascon JM, Armand M. Issues and challenges facing rechargeable lithium batteries. *Materials for sustainable energy: a collection of peer-reviewed research and review articles from Nature Publishing Group* 2011:171–9.
  - [30] Ryu HH, Park NY, Yoon DR, Kim UH, Yoon CS, Sun YK. New class of Ni-rich cathode materials  $\text{Li}(\text{Ni}_x\text{Co}_y\text{B}_{1-x-y})\text{O}_2$  for next lithium batteries. *Adv Energy Mater* 2020;10(25):2000495.
  - [31] Ryu HH, Park KJ, Yoon DR, Aishova A, Yoon CS, Sun YK.  $\text{Li}[\text{Ni}_{0.9}\text{Co}_{0.09}\text{W}_{0.01}]\text{O}_2$ : A new type of layered oxide cathode with high cycling stability. *Adv Energy Mater* 2019;9(44):1902698.
  - [32] Aishova A, Park GT, Yoon CS, Sun Y-K. Cobalt-free high-capacity Ni-rich layered  $\text{Li}[\text{Ni}_{0.9}\text{Mn}_{0.1}]\text{O}_2$  cathode. *Adv Energy Mater* 2020;10(4):1903179.
  - [33] Li H, Cormier M, Zhang N, Inglis J, Li J, Dahn JR. Is cobalt needed in Ni-rich positive electrode materials for lithium ion batteries? *J Electrochem Soc* 2019;166(4):A429.
  - [34] Liu A, Zhang N, Li H, Inglis J, Wang Y, Yin S, et al. Investigating the effects of magnesium doping in various Ni-rich positive electrode materials for lithium ion batteries. *J Electrochem Soc* 2019;166(16):A4025–33.
  - [35] Mu L, Zhang R, Kan WH, Zhang Y, Li L, Kuai C, et al. Dopant distribution in Co-free high-energy layered cathode materials. *Chem Mater* 2019;31(23):9769–76.
  - [36] Li W, Lee S, Manthiram A. High-nickel NMA: A cobalt-free alternative to NMC and NCA cathodes for lithium-ion batteries. *Adv Mater* 2020;32(33):2002718.
  - [37] Zhao S, Yan K, Zhang J, Sun B, Wang G. Reaction mechanisms of layered lithium-rich cathode materials for high-energy lithium-ion batteries. *Angew Chem Int Ed* 2021;60(5):2208–20.
  - [38] Sun G, Yu FD, Que LF, Deng L, Wang ZB. Local electronic structure modulation enhances operating voltage in Li-rich cathodes. *Nano Energy* 2019;66:104102.
  - [39] Lee J, Gong Y, Gu L, Kang B. Long-term cycle stability enabled by the incorporation of Ni into  $\text{Li}_2\text{MnO}_3$  Phase in the Mn-based Li-rich layered materials. *ACS Energy Lett* 2021;6(2):789–98.
  - [40] Sicklinger J, Metzger M, Beyer H, Pritzel D, Gasteiger HA. Ambient storage derived surface contamination of NCM811 and NCM111: Performance implications and mitigation strategies. *J Electrochem Soc* 2019;166(12):A2322–35.
  - [41] Xu Z, Jiang Z, Zhao K, Xu R, Qin C, Zhang Y, et al. Charge distribution guided by grain crystallographic orientations in polycrystalline battery materials. *Nat Commun* 2020;11(1):1–9.
  - [42] Brandt LR, Marie JJ, Moxham T, Förstermann DP, Salvati E, Besnard C, et al. Synchrotron X-ray quantitative evaluation of transient deformation and damage phenomena in a single nickel-rich cathode particle. *Energy Environ Sci* 2020;13(10):3556–66.
  - [43] Li S, Yao Z, Zheng J, Fu M, Cen J, Hwang S, et al. Direct observation of defect-aided structural evolution in a nickel-rich layered cathode. *Angew Chem Int Ed* 2020;132(49):22276–83.
  - [44] Park KJ, Hwang JY, Ryu HH, Maglia F, Kim SJ, Lamp P, et al. Degradation mechanism of Ni-enriched NCA cathode for lithium batteries: Are Microcracks Really Critical? *ACS Energy Lett* 2019;4(6):1394–400.
  - [45] Kim UH, Park GT, Son BK, Nam GW, Liu J, Kuo LY, et al. Heuristic solution for achieving long-term cycle stability for Ni-rich layered cathodes at full depth of discharge. *Nat Energy* 2020;5(11):860–9.
  - [46] Xiaoxuan C, Sheng Li, Yonggang HU, Shiyao Z, Yunxuan C, Dongjiang LI, et al. Failure mechanism of  $\text{Li}_{(1-x)}(\text{NCM})_{(1-x)}\text{O}_2$  layered oxide cathode material during capacity degradation. *Energy Storage Science and Technology* 2019;8(6):1003.
  - [47] Qian G, Zhang Y, Li L, Zhang R, Xu J, Cheng Z, et al. Single-crystal nickel-rich layered-oxide battery cathode materials: synthesis, electrochemistry, and intra-granular fracture. *Energy Storage Mater* 2020;27:140–9.
  - [48] Xu X, Huo H, Jian J, Wang L, Zhu H, Xu S, et al. Radially oriented single-crystal primary nanosheets enable ultrahigh rate and cycling properties of  $\text{LiNi}_{0.8}\text{Co}_{0.1}\text{Mn}_{0.1}\text{O}_2$  cathode material for lithium-ion batteries. *Adv Energy Mater* 2019;9(15):1803963.
  - [49] Zou Y, Yang X, Lv C, Liu T, Xia Y, Shang L, et al. Multishelled Ni-rich  $\text{Li}(\text{Ni}_x\text{Co}_y\text{Mn}_z)\text{O}_2$  hollow fibers with low cation mixing as high-performance cathode materials for Li-ion batteries. *Adv Sci* 2017;4(1):1600262.
  - [50] Caballero A, Cruz M, Hernán L, Melero M, Morales J, Castellón ER. Nanocrystalline materials obtained by using a simple, rapid method for rechargeable lithium batteries. *J Power Sources* 2005;150:192–201.
  - [51] Saavedra-Arias JJ, Karan NK, Pradhan DK, Kumar A, Nieto S, Thomas R, et al. Synthesis and electrochemical properties of  $\text{Li}(\text{Ni}_{0.8}\text{Co}_{0.1}\text{Mn}_{0.1})\text{O}_2$  cathode material: Ex situ structural analysis by Raman scattering and X-ray diffraction at various stages of charge-discharge process. *J Power Sources* 2008;183(2):761–5.
  - [52] Xu C, Märker K, Lee J, Mahadevegowda A. Bulk fatigue induced by surface reconstruction in layered Ni-rich cathodes for Li-ion batteries. *Nat Mater* 2021;20(1):84–92.
  - [53] Yang Y, Xu S, Xie M, He Y, Huang G, Yang Y. Growth mechanisms for spherical mixed hydroxide agglomerates prepared by co-precipitation method: A case of  $\text{Ni}_{1/3}\text{Co}_{1/3}\text{Mn}_{1/3}(\text{OH})_2$ . *J Alloy Compd* 2015;619:846–53.
  - [54] Islam N, Li S, Ren G, Zu Y, Warzywoda J, Wang S, et al. High-frequency electrochemical capacitors based on plasma pyrolyzed bacterial cellulose aerogel for current ripple filtering and pulse energy storage. *Nano Energy* 2017;40:107–14.
  - [55] Park KJ, Jung HG, Kuo LY, Kaghazchi P, Yoon CS, Sun Y. Improved cycling stability of  $\text{Li}[\text{Ni}_{0.90}\text{Co}_{0.05}\text{Mn}_{0.05}]\text{O}_2$  through microstructure modification by boron doping for Li-ion batteries. *Adv Energy Mater* 2018;8(25):1801202.
  - [56] Wu F, Liu N, Chen L, Su Y, Tan G, Bao L, et al. Improving the reversibility of the H2-H3 phase transitions for layered Ni-rich oxide cathode towards retarded structural transition and enhanced cycle stability. *Nano Energy* 2019;59:50–7.
  - [57] Wang J, Li C, Xu B. Basic principle, advance and current application situation of sol-gel method. *Chemical Industry and Engineering* 2009;26(3):273–7.
  - [58] Subramaniam CM, Celio H, Shiva K, Gao H, Goodenough JB, Liu HK, et al. Long stable cycling of fluorine-doped nickel-rich layered cathodes for lithium batteries. *Sustainable Energy Fuels* 2017;1(6):1292–8.
  - [59] Lu H, Zhou H, Svensson AM, Fossdal A, Sheridan E, Lu S, et al. High capacity  $\text{Li}[\text{Ni}_{0.8}\text{Co}_{0.1}\text{Mn}_{0.1}]\text{O}_2$  synthesized by sol-gel and co-precipitation methods as cathode materials for lithium-ion batteries. *Solid State Ionics* 2013;249:105–11.
  - [60] Li D, Sasaki Y, Kobayakawa K, Noguchi H, Sato Y. Preparation, morphology and electrochemical characteristics of  $\text{LiNi}_{1/3}\text{Mn}_{1/3}\text{Co}_{1/3}\text{O}_2$  with LiF addition. *Electrochim Acta* 2006;52(2):643–8.
  - [61] Yue P, Wang Z, Peng W, Li L, Chen W, Guo H, et al. Spray-drying synthesized  $\text{LiNi}_{0.6}\text{Co}_{0.2}\text{Mn}_{0.2}\text{O}_2$  and its electrochemical performance as cathode materials for lithium ion batteries. *Powder Technol* 2011;214(3):279–82.

- [62] Ahn W, Lim SN, Jung KN, Yeon SH, Kim KB, Song HS, et al. Combustion-synthesized  $\text{LiNi}_{0.6}\text{Mn}_{0.2}\text{Co}_{0.2}\text{O}_2$  as cathode material for lithium ion batteries. *J Alloy Compd* 2014;609:143–9.
- [63] Nitta N, Wu F, Lee JT, Yushin G. Li-ion battery materials: present and future. *Mater Today* 2015;18(5):252–64.
- [64] Wang L, Li J, He X, Pu W, Wan C, Jiang C. Recent advances in layered  $\text{LiNi}_x\text{Co}_y\text{Mn}_{1-x-y}\text{O}_2$  cathode materials for lithium ion batteries. *J Solid State Electrochem* 2009;13(8):1157–64.
- [65] Ellis BL, Lee KT, Nazar LF. Positive electrode materials for Li-ion and Li-batteries. *Chem Mater* 2010;22(3):691–714.
- [66] Zeng D, Cabana J, Bréger J, Yoon WS, Grey C. Cation Ordering in  $\text{Li}[\text{Ni}_x\text{Mn}_x\text{Co}_{(1-2x)}]\text{O}_2$ -Layered Cathode Materials: A Nuclear Magnetic Resonance (NMR), Pair Distribution Function, X-ray Absorption Spectroscopy, and Electrochemical Study. *Chem Mater* 2007;19(25):6277–89.
- [67] He P, Yu H, Zhou H. Layered lithium transition metal oxide cathodes towards high energy lithium-ion batteries. *J Mater Chem* 2012;22(9):3680–95.
- [68] Koyama Y, Tanaka I, Adachi H, Makimura Y, Ohzuku T. Crystal and electronic structures of super structural  $\text{Li}_{1-x}[\text{Co}_{1/3}\text{Ni}_{1/3}\text{Mn}_{1/3}]\text{O}_2$  ( $0 \leq x \leq 1$ ). *J Power Sources* 2003;119:644–8.
- [69] Myung ST, Lee MH, Komaba S, Kumagai N, Sun YK. Hydrothermal synthesis of layered  $\text{Li}[\text{Ni}_{1/3}\text{Co}_{1/3}\text{Mn}_{1/3}]\text{O}_2$  as positive electrode material for lithium secondary battery. *Electrochim Acta* 2005;50(24):4800–6.
- [70] Chen H, Dawson JA, Harding JH. Effects of cationic substitution on structural defects in layered cathode materials  $\text{LiNiO}_2$ . *J Mater Chem A* 2014;2(21):7988–96.
- [71] Gui S, Zhang Q, Zhuo H, Liu J. Enhancing the electrochemical performance of  $\text{LiNi}_{0.8}\text{Co}_{0.15}\text{Al}_{0.05}\text{O}_2$  by a facile doping method: Spray-drying doping with liquid polyacrylonitrile. *J Power Sources* 2019;409:102–11.
- [72] Wu F, Tian J, Su Y, Wang J, Zhang C, Bao L, et al. Effect of  $\text{Ni}^{2+}$  content on lithium/nickel disorder for Ni-rich cathode materials. *ACS Appl Mater Interfaces* 2015;7(14):7702–8.
- [73] Zhang Q, Su Y, Chen L, Lu Y, Bao L, He T, et al. Pre-oxidizing the precursors of Nickel-rich cathode materials to regulate their  $\text{Li}^+/\text{Ni}^{2+}$  cation ordering towards cyclability improvements. *J Power Sources* 2018;396:734–41.
- [74] Fu C, Li G, Luo D, Li Q, Fan J, Li L, et al. Nickel-rich layered microspheres cathodes: lithium/nickel disordering and electrochemical performance. *ACS Appl Mater Interfaces* 2014;6(18):15822–31.
- [75] Yue P, Wang Z, Peng W, Li L, Guo H, Li X, et al. Preparation and electrochemical properties of submicron  $\text{LiNi}_{0.6}\text{Co}_{0.2}\text{Mn}_{0.2}\text{O}_2$  as cathode material for lithium ion batteries. *Scr Mater* 2011;65(12):1077–80.
- [76] Saadouni I, Delmas C.  $\text{LiNi}_{1-x}\text{Co}_x\text{O}_2$  positive electrode materials: relationships between the structure, physical properties and electrochemical behaviour. *J Mater Chem* 1996;6(2):193–9.
- [77] Chen CY, Xiao SQ, Davis ME. Studies on ordered mesoporous materials III. Comparison of MCM-41 to mesoporous materials derived from kanemite. *Microporous Mater* 1995;4(1):1–20.
- [78] Marom R, Amaraj SF, Leifer N, Jacob D, Aurbach D. A review of advanced and practical lithium battery materials. *J Mater Chem* 2011;21(27):9938–54.
- [79] Mukhopadhyay A, Guo F, Tokranov A, Xiao X, Hurt RH, Sheldon B. Engineering of graphene layer orientation to attain high rate capability and anisotropic properties in Li-ion battery electrodes. *Adv Funct Mater* 2013;23(19):2397–404.
- [80] Shaju KM, Rao GVS, Chowdari BVR. Performance of layered  $\text{Li}(\text{Ni}_{1/3}\text{Co}_{1/3}\text{Mn}_{1/3})\text{O}_2$  as cathode for Li-ion batteries. *Electrochim Acta* 2002;48(2):145–51.
- [81] Thackeray MM. Structural considerations of layered and spinel lithiated oxides for lithium ion batteries. *J Electrochem Soc* 1995;142(8):2558–63.
- [82] Wu F, Li Q, Chen L, Lu Y, Su Y, Bao L, et al. Use of Ce to Reinforce the Interface of Ni-Rich  $\text{LiNi}_{0.8}\text{Co}_{0.1}\text{Mn}_{0.1}\text{O}_2$  Cathode Materials for Lithium-Ion Batteries under High Operating Voltage. *ChemSusChem* 2019;12(4):935–43.
- [83] Zhang C, Liu M, Pan G, Liu S, Liu D, Chen C, et al. Enhanced Electrochemical Performance of  $\text{LiNi}_{0.8}\text{Co}_{0.1}\text{Mn}_{0.1}\text{O}_2$  Cathode for Lithium-Ion Batteries by Precursor Preoxidation. *ACS Applied Energy Materials* 2018;1(8):4374–84.
- [84] Deng D. Li-ion batteries: basics, progress, and challenges. *Energy Sci Eng* 2015;3(5):385–418.
- [85] de Biasi L, Kondrakov AO, Geßwein H, Brezesinski T, Hartmann P, Janek J. Between scylla and charybdis: Balancing among structural stability and energy density of layered NCM cathode materials for advanced lithium-ion batteries. *The Journal of Physical Chemistry C* 2017;121(47):26163–71.
- [86] Manthiram A, Knight JC, Myung ST, Oh SM, Sun Y. Nickel-rich and lithium-rich layered oxide cathodes: progress and perspectives. *Adv Energy Mater* 2016;6(1):1501010.
- [87] Cherkashinin G, Motzko M, Schulz N, Späth T, Jaegermann WJCoM. Electron spectroscopy study of  $\text{Li}[\text{Ni Co Mn}]\text{O}_2$ /electrolyte interface: electronic structure, interface composition, and device implications. *Chem Mater* 2015;27(8):2875–87.
- [88] Gauthier M, Carney TJ, Grimaud A, Giordano L, Pour N, Chang HH, et al. Electrode–electrolyte interface in Li-ion batteries: current understanding and new insights. *J Phys Chem Lett* 2015;6(22):4653–72.
- [89] Chen Z, Zhang C, Zhang Z, Li J. Correlation of intercalation potential with d-electron configurations for cathode compounds of lithium-ion batteries. *PCCP* 2014;16(26):13255–61.
- [90] Reed J, Ceder G. Role of electronic structure in the susceptibility of metastable transition-metal oxide structures to transformation. *Chem Rev* 2004;104(10):4513–34.
- [91] Croguennec L, Bains J, Bréger J, Tessier C, Biensan P, Levasseur S, et al. Effect of aluminum substitution on the structure, electrochemical performance and thermal stability of  $\text{Li}_{1+x}(\text{Ni}_{0.40}\text{Mn}_{0.40}\text{Co}_{0.20-2x}\text{Al}_x)_{1-x}\text{O}_2$ . *J Electrochem Soc* 2011;158(6):A664–70.
- [92] Jung R, Metzger M, Maglia F, Stinner C, Gasteiger H. Oxygen release and its effect on the cycling stability of  $\text{LiNi}_{0.8}\text{Mn}_{0.1}\text{Co}_{0.1}\text{O}_2$  (NMC) cathode materials for Li-ion batteries. *J Electrochem Soc* 2017;164(7):A1361.
- [93] Kim JH, Park KJ, Kim SJ, Yoon CS, Sun YK. A method of increasing the energy density of layered Ni-rich Li  $[\text{Ni}_{1-2x}\text{Co}_x\text{Mn}_x]\text{O}_2$  cathodes ( $x=0.05, 0.1, 0.2$ ). 2019, 7:2694–2701.
- [94] Kim H, Kim MG, Jeong HY, Nam H, Cho J. A new coating method for alleviating surface degradation of  $\text{LiNi}_{0.6}\text{Co}_{0.2}\text{Mn}_{0.2}\text{O}_2$  cathode material: nanoscale surface treatment of primary particles. *Nano Lett* 2015;15(3):2111–9.
- [95] Han B, Xu S, Zhao S, Lin G, Feng Y, Chen L, et al. Enhancing the structural stability of Ni-rich layered oxide cathodes with a preformed Zr-concentrated defective nanolayer. *ACS Appl Mater Interfaces* 2018;10(46):39599–607.
- [96] Zou L, Zhao W, Liu Z, Jia H, Zheng J, Wang G, et al. Revealing cycling rate-dependent structure evolution in Ni-rich layered cathode materials. *ACS Energy Lett* 2018;3(10):2433–40.
- [97] Zhao J, Zhang W, Huq A, Mixture ST, Zhang B, Guo SM, et al. In situ probing and synthetic control of cationic ordering in Ni-rich layered oxide cathodes. *Adv Energy Mater* 2017;7(3):1601266.
- [98] Duan Y, Yang L, Zhang MJ, Chen Z, Bai J, Amine K, et al. Insights into Li/Ni ordering and surface reconstruction during synthesis of Ni-rich layered oxides. *J Mater Chem A* 2019;7(2):513–9.
- [99] Zhang SS. Problems and their origins of Ni-rich layered oxide cathode materials. *Energy Storage Mater* 2020;24:247–54.
- [100] Cho DH, Jo CH, Cho W, Kim YJ, Yashiro H, Sun YK, et al. Effect of residual lithium compounds on layer Ni-rich  $\text{Li}(\text{Ni}_{0.7}\text{Mn}_{0.3})\text{O}_2$ . *J Electrochem Soc* 2014;161(6):A920–6.
- [101] Chen Z, Wang J, Huang J, Fu T, Sun G, Lai S, et al. The high-temperature and high-humidity storage behaviors and electrochemical degradation mechanism of  $\text{LiNi}_{0.6}\text{Co}_{0.2}\text{O}_2$  cathode material for lithium ion batteries. *J Power Sources* 2017;363:168–76.
- [102] Li T, Yuan XZ, Zhang L, Song D, Shi K, Bock C. Degradation mechanisms and mitigation strategies of nickel-rich NMC-based lithium-ion batteries. *Electrochimica Acta* 2020;3(1):43–80.
- [103] Hamam I, Zhang N, Liu A, Johnson MB, Dahn JR. Study of the reactions between Ni-rich positive electrode materials and aqueous solutions and their relation to the failure of Li-ion cells. *J Electrochem Soc* 2020;167(13):130521.
- [104] Azhari L, Zhou X, Sousa B, Yang Z, Gao G, Wang Y. Effects of extended aqueous processing on structure, chemistry, and performance of polycrystalline  $\text{LiNi}_{0.8}\text{Mn}_{0.1}\text{Co}_{0.1}\text{O}_2$  cathode powders. *ACS Appl Mater Interfaces* 2020;12(52):57963–74.
- [105] Hawley WB, Meyer III HM, Li J. Enabling aqueous processing for  $\text{LiNi}_{0.80}\text{Co}_{0.15}\text{Al}_{0.05}\text{O}_2$  (NCA)-based lithium-ion battery cathodes using polyacrylic acid. *Electrochim Acta* 2021;380:138203.
- [106] You Y, Celio H, Li J, Dolocan A, Manthiram A. Modified high-nickel cathodes with stable surface chemistry against ambient air for lithium-ion batteries. *Angew Chem Int Ed* 2018;57(22):6480–5.
- [107] Lee SH, Park GJ, Sim SJ, Jin B, Kim H. Improved electrochemical performances of  $\text{LiNi}_{0.8}\text{Co}_{0.1}\text{Mn}_{0.1}\text{O}_2$  cathode via  $\text{SiO}_2$  coating. *J Alloy Compd* 2019;791:193–9.
- [108] Zhang SS. Understanding of performance degradation of  $\text{LiNi}_{0.80}\text{Co}_{0.10}\text{Mn}_{0.10}\text{O}_2$  cathode material operating at high potentials. *Journal of Energy. Chemistry* 2020;41:135–41.
- [109] Bak SM, Hu E, Zhou Y, Yu X, Senanayake SD, Cho SJ, et al. Structural changes and thermal stability of charged  $\text{LiNi}_x\text{Mn}_y\text{Co}_z\text{O}_2$  cathode materials studied by combined in situ time-resolved XRD and mass spectroscopy. *ACS Appl Mater Interfaces* 2014;6(24):22594–601.
- [110] Nam GW, Park NY, Park KJ, Yang J, Liu J, Yoon CS, et al. Capacity fading of Ni-rich NCA cathodes: Effect of microcracking extent. *ACS Energy Lett* 2019;4(12):2995–3001.
- [111] Ko DS, Park JH, Yu BY, Ahn D, Kim K, Han HN, et al. Degradation of high nickel layered oxide cathodes from surface to bulk: A comprehensive structural, chemical, and electrical analysis. *Adv Energy Mater* 2020;10(36):2001035.
- [112] Yang C, Shao R, Wang Q, Zhou T, Lu J, Jiang N, et al. Bulk and surface degradation in layered Ni-rich cathode for Li ions batteries: Defect proliferation via chain reaction mechanism. *Energy Storage Mater* 2021;35:62–9.
- [113] Cho J, Kim TJ, Kim J, Noh M, Park B. Synthesis, thermal, and electrochemical properties of  $\text{AlPO}_4$ -coated  $\text{LiNi}_{0.8}\text{Co}_{0.1}\text{Mn}_{0.1}\text{O}_2$  cathode materials for a Li-Ion cell. *J Electrochem Soc* 2004;151(11):A1899–904.
- [114] Myung ST, Maglia F, Park KJ, Yoon CS, Lamp P, Kim SJ, et al. Nickel-rich layered cathode materials for automotive lithium-ion batteries: achievements and perspectives. *ACS Energy Lett* 2017;2(1):196–223.
- [115] Noh HJ, Myung ST, Lee YJ, Sun YK. High-energy layered oxide cathodes with thin shells for improved surface stability. *Chem Mater* 2014;26(20):5973–9.
- [116] Yoon SJ, Park KJ, Lim BB, Yoon CS, Sun YK. Improved performances of  $\text{Li}[\text{Ni}_{0.65}\text{Co}_{0.08}\text{Mn}_{0.27}]\text{O}_2$  cathode material with full concentration gradient for Li-ion batteries. *J Electrochem Soc* 2014;162(2):A3059–63.
- [117] Cho Y, Oh P, Cho J. A new type of protective surface layer for high-capacity Ni-based cathode materials: nanoscaled surface pillaring layer. *Nano Lett* 2013;13(3):1145–52.
- [118] Zheng J, Gu M, Xiao J, Polzin BJ, Yan P, Chen X, et al. Functioning mechanism of  $\text{AlF}_3$  coating on the Li- and Mn-rich cathode materials. *Chem Mater* 2014;26(22):6320–7.
- [119] Choi J, Lee SY, Yoon S, Kim KH, Kim M, Hong SH. The role of Zr doping in stabilizing  $\text{Li}[\text{Ni}_{0.6}\text{Co}_{0.2}\text{Mn}_{0.2}]\text{O}_2$  as a cathode material for lithium-ion batteries. *Chem Sus Chem* 2019;12(11):2439–46.

- [120] Gao S, Zhan X, Cheng YT. Structural, electrochemical and Li-ion transport properties of Zr-modified  $\text{LiNi}_{0.8}\text{Co}_{0.1}\text{Mn}_{0.1}\text{O}_2$  positive electrode materials for Li-ion battery. *J Power Sources* 2019;410:45–52.
- [121] Song JH, Bae J, Lee K, Lee I, Hwang K, Cho W, et al. Enhancement of high temperature cycling stability in high-nickel cathode materials with titanium doping. *J Ind Eng Chem* 2018;68:124–8.
- [122] Kong D, Hu J, Chen Z, Song K, Li C, Weng M, et al. Ti-gradient doping to stabilize layered surface structure for high performance high-Ni oxide cathode of Li-ion battery. *Adv Energy Mater* 2019;9(41):1901756.
- [123] Liu Q, Zhao Z, Wu F, Mu D, Wang L, Wu B. The effects of molybdenum doping on  $\text{LiNi}_{0.6}\text{Co}_{0.2}\text{Mn}_{0.2}\text{O}_2$  cathode material. *Solid State Ionics* 2019;337:107–14.
- [124] Xie Q, Li W, Dolocan A, Manthiram A. Insights into boron-based polyanion-tuned high-nickel cathodes for high-energy-density lithium-ion batteries. *Chem Mater* 2019;31(21):8886–97.
- [125] Qiu Z, Liu Z, Fu X, Liu J, Zeng Q. Improving the cycling performance of  $\text{LiNi}_{0.8}\text{Co}_{0.15}\text{Al}_{0.05}\text{O}_2$  cathode materials via zirconium and fluorine co-substitution. *J Alloy Compd* 2019;806:136–45.
- [126] Qiu L, Xiang W, Tian W, Xu CL, Li YC, Wu ZG, et al. Polyanion and cation co-doping stabilized Ni-rich Ni–Co–Al material as cathode with enhanced electrochemical performance for Li-ion battery. *Nano Energy* 2019;63:103818.
- [127] Liu Y, Tang L, Wei H, Zhang X, He Z, Li Y, et al. Enhancement on structural stability of Ni-rich cathode materials by in-situ fabricating dual-modified layer for lithium-ion batteries. *Nano Energy* 2019;65:104043.
- [128] Fan Q, Yang S, Liu J, Liu H, Lin K, Liu R, et al. Mixed-conducting interlayer boosting the electrochemical performance of Ni-rich layered oxide cathode materials for lithium ion batteries. *J Power Sources* 2019;421(1):91–9.
- [129] Zhu J, Li Y, Xue L, Chen Y, Lei T, Deng S, et al. Enhanced electrochemical performance of  $\text{Li}_3\text{PO}_4$  modified  $\text{Li}(\text{Ni}_{0.8}\text{Co}_{0.1}\text{Mn}_{0.1})\text{O}_2$  cathode material via lithium-reactive coating. *J Alloy Compd* 2019;773:112–20.
- [130] Zhang M, Zhao H, Tan M, Liu J, Hu Y, Liu S, et al. Yttrium modified Ni-rich  $\text{LiNi}_{0.8}\text{Co}_{0.1}\text{Mn}_{0.1}\text{O}_2$  with enhanced electrochemical performance as high energy density cathode material at 4.5V high voltage. *J Alloy Compd* 2019;774:82–92.
- [131] Dong S, Zhou Y, Hai C, Zeng J, Sun Y, Shen Y, et al. Ultrathin  $\text{CeO}_2$  coating for improved cycling and rate performance of Ni-rich layered  $\text{LiNi}_{0.7}\text{Co}_{0.2}\text{Mn}_{0.1}\text{O}_2$  cathode materials. *Ceram Int* 2019;45(1):144–52.
- [132] Li YC, Xiang W, Xiao Y, Wu ZG, Xu CL, Xu W, et al. Synergy of doping and coating induced heterogeneous structure and concentration gradient in Ni-rich cathode for enhanced electrochemical performance. *J Power Sources* 2019;423:144–51.
- [133] Chung YM, Ryu SH, Ju JH, Bak YR, Hwang MJ, Kim KW, et al. A surfactant-based method for carbon coating of  $\text{LiNi}_{0.8}\text{Co}_{0.15}\text{Al}_{0.05}\text{O}_2$  Cathode in Li ion batteries. *Bull Korean Chem Soc* 2010;31(8):2304–8.
- [134] Yoon S, Jung KN, Yeon SH, Jin CS, Shin K-H. Electrochemical properties of  $\text{LiNi}_{0.8}\text{Co}_{0.15}\text{Al}_{0.05}\text{O}_2$ -graphene composite as cathode materials for lithium-ion batteries. *J Electroanal Chem* 2012;683:88–93.
- [135] Kong JZ, Chen Y, Cao YQ, Wang QZ, Li AD, Li H, et al. Enhanced electrochemical performance of Ni-rich  $\text{LiNi}_{0.6}\text{Co}_{0.2}\text{Mn}_{0.2}\text{O}_2$  coated by molecular layer deposition derived dual-functional  $\text{C-Al}_2\text{O}_3$  composite coating. *J Alloy Compd* 2019;799:89–98.
- [136] Huang X, Zhu W, Yao J, Bu L, Li X, Tian K, et al. Suppressing structural degradation of Ni-rich cathode materials towards improved cycling stability enabled by a  $\text{Li}_2\text{MnO}_3$  coating. *J Mater Chem A* 2020;8(34):17429–41.
- [137] Su Y, Chen G, Chen L, Lu Y, Zhang Q, Lv Z, et al. High-rate structure-gradient Ni-rich cathode material for lithium-ion batteries. *ACS Appl Mater Interfaces* 2019;11(40):36697–704.
- [138] Fan X, Hu G, Zhang B, Ou X, Zhang J, Zhao W, et al. Crack-free single-crystalline Ni-rich layered NCM cathode enable superior cycling performance of lithium-ion batteries. *Nano Energy* 2020;70:104450.
- [139] Dong P, Wang D, Yao Y, Li X, Zhang Y, Ru J, et al. Stabilizing interface layer of  $\text{LiNi}_{0.5}\text{Co}_{0.2}\text{Mn}_{0.3}\text{O}_2$  cathode materials under high voltage using p-toluenesulfonyl isocyanate as film forming additive. *J Power Sources* 2017;344:111–8.
- [140] Jang SH, Jung K, Yim T. Silyl-group functionalized organic additive for high voltage Ni-rich cathode material. *Curr Appl Phys* 2018;18(11):1345–51.
- [141] Yim T, Kang KS, Mun J, Lim SH, Woo SG, Kim KJ, et al. Understanding the effects of a multi-functionalized additive on the cathode–electrolyte interfacial stability of Ni-rich materials. *J Power Sources* 2016;302:431–8.
- [142] Deng T, Fan X, Cao L, Chen J, Hou S, Ji X, et al. Designing In-Situ-Formed Interphases Enables Highly Reversible Cobalt-Free  $\text{LiNiO}_2$  Cathode for Li-ion and Li-metal Batteries. *Joule* 2019;3(10):2550–64.
- [143] Zhang D, Liu Y, Wu L, Feng L, Jin S, Zhang R, et al. Effect of Ti ion doping on electrochemical performance of Ni-rich  $\text{LiNi}_{0.8}\text{Co}_{0.1}\text{Mn}_{0.1}\text{O}_2$  cathode material. *Electrochim Acta* 2019;328:135086.
- [144] Yan W, Xie Y, Jiang J, Sun D, Ma X, Lan Z, et al. Enhanced rate performance of Al-doped Li-rich layered cathode material via nucleation and post-solvothermal method. *ACS sustainable chemistry & engineering* 2018;6(4):4625–32.
- [145] Kim UH, Park JH, Aishova A, Ribas RM, Monteiro RS, Griffith KJ, et al. Microstructure engineered Ni-rich layered cathode for electric vehicle batteries [J]. *Adv Energy Mater* 2021;11:2100884.
- [146] Zhang C, Xu S, Han B, Lin G, Huang Q, Ivey DG, et al. Towards rational design of high performance Ni-rich layered oxide cathodes: The interplay of borate-doping and excess lithium. *J Power Sources* 2019;431:40–7.
- [147] Woo SU, Park BC, Yoon CS, Myung ST, Prakash J, Sun YK. Improvement of electrochemical performances of  $\text{Li}[\text{Ni}_{0.8}\text{Co}_{0.1}\text{Mn}_{0.1}]\text{O}_2$  cathode materials by fluorine substitution. *J Electrochem Soc* 2007;154(7):A649.
- [148] Qian Y, Niehoff P, Börner M, Grütze M, Mönninghoff X, Behrends P, et al. Influence of electrolyte additives on the cathode electrolyte interphase (CEI) formation on  $\text{LiNi}_{1/3}\text{Mn}_{1/3}\text{Co}_{1/3}\text{O}_2$  in half cells with Li metal counter electrode. *J Power Sources* 2016;329:31–40.
- [149] Sun F, Markötter H, Manke I, Hilger A, Kardjilov N, Banhart JJA, et al. Three-dimensional visualization of gas evolution and channel formation inside a lithium-ion battery. *ACS Appl Mater Interfaces* 2016;8(11):7156–64.
- [150] Wagner MR, Raimann PR, Trifonova A, Möller KC, Besenhard J, Winter M, et al. Dilatometric and mass spectrometric investigations on lithium ion battery anode materials. *Anal Bioanal Chem* 2004;379(2):272–6.
- [151] Zhang SS. Insight into the gassing problem of Li-ion battery. *Front Energy Res* 2014;2:59.
- [152] Fan Q, Lin K, Yang S, Guan S, Chen J, Feng S, et al. Constructing effective  $\text{TiO}_2$  nano-coating for high-voltage Ni-rich cathode materials for lithium ion batteries by precise kinetic control. *J Power Sources* 2020;477:228745.
- [153] Becker D, Börner M, Nölle R, Diehl M, Klein S, Rodehorst UC, et al. Surface modification of Ni-rich  $\text{LiNi}_{0.8}\text{Co}_{0.1}\text{Mn}_{0.1}\text{O}_2$  cathode material by tungsten oxide coating for improved electrochemical performance in lithium-ion batteries. *ACS Appl Mater Interfaces* 2019;11(20):18404–14.
- [154] Yoon M, Dong Y, Hwang J, Sung J, Cha H, Ahn K, et al. Reactive boride infusion stabilizes Ni-rich cathodes for lithium-ion batteries. *Nature Energy*, 202, 6: 362–371.
- [155] Gan Q, Qin N, Zhu Y, Huang Z, Zhang F, Gu S, et al. Polyvinylpyrrolidone-induced uniform surface-conductive polymer coating endows Ni-rich  $\text{LiNi}_{0.8}\text{Co}_{0.1}\text{Mn}_{0.1}\text{O}_2$  with enhanced cyclability for lithium-ion batteries. *ACS Appl Mater Interfaces* 2019;11(13):12594–604.
- [156] Du K, Xie H, Hu G, Peng Z, Cao Y, Yu FJA, et al. Enhancing the thermal and upper voltage performance of Ni-rich cathode material by a homogeneous and facile coating method: spray-drying coating with nano- $\text{Al}_2\text{O}_3$ . *ACS Appl Mater Interfaces* 2016;8(27):17713–20.
- [157] Guo S, Yuan B, Zhao H, Hua D, Shen Y, Sun C, et al. Dual-component silica functional coating in one layer for performance enhanced  $\text{LiNi}_{0.6}\text{Co}_{0.2}\text{Mn}_{0.2}\text{O}_2$  cathode. *Nano Energy* 2019;58:673–9.
- [158] Kim UH, Kim JH, Hwang JY, Ryu HH, Yoon CS, Sun YK. Compositionally and structurally redesigned high-energy Ni-rich layered cathode for next-generation lithium batteries. *Mater Today* 2019;23:26–36.
- [159] Song YM, Kim CK, Kim KE, Hong SY, Choi NS. Exploiting chemically and electrochemically reactive phosphite derivatives for high-voltage spinel  $\text{LiNi}_{0.5}\text{Mn}_{1.5}\text{O}_4$  cathodes. *J Power Sources* 2016;302:22–3.
- [160] Suzuki H, Maruyama S, Ohe K. Polymeric solid electrolyte and lithium secondary cell using the same: U.S. Patent 6,051,343. 2000-4-18.
- [161] Cho JW, Song HY. Dehydrofluorination of a copolymer of vinylidene fluoride and tetrafluoroethylene by phase transfer catalysis reaction. *J Polym Sci, Part A: Polym Chem* 1995;33(13):2109–12.
- [162] Zhang SS, Fan X, Wang C. Enhanced electrochemical performance of Ni-rich layered cathode materials by using  $\text{LiPF}_6$  as a cathode additive. *ChemElectroChem* 2019;6(5):1536–41.
- [163] Bisio M, Colombo R, Uddin MJ, Stanga M, Cho SJ. A rheological behavior of various polyvinylidene difluoride binders for high capacity  $\text{LiNi}_{0.6}\text{Mn}_{0.2}\text{Co}_{0.2}\text{O}_2$ . *Polym Eng Sci* 2016;56(7):760–4.
- [164] Chang B, Kim J, Cho Y, Hwang I, Jung MS, Char K, et al. Highly elastic binder for improved cyclability of nickel-rich layered cathode materials in lithium-ion batteries. *Adv Energy Mater* 2020;10(29):2001069.
- [165] Jang J, Oh J, Jeong H, Jang J, Oh J, Jeong H, et al. A review of functional separators for lithium metal battery applications. *Materials* 2020;13(20):4625.
- [166] Peng L, Kong X, Li H, Wang X, Shi C, Hu T, et al. A rational design for a high-safety lithium-ion battery assembled with a heatproof–fireproof bifunctional separator. *Adv Funct Mater* 2021;31(10):2008537.
- [167] Kim Y, Seong WM, Manthiram A. Cobalt-free, high-nickel layered oxide cathodes for lithium-ion batteries: Progress, challenges, and perspectives. *Energy Storage Mater* 2021;34:250–9.
- [168] Sun YK, Lee DJ, Lee YJJ, Chen Z, Myung ST. Cobalt-free nickel rich layered oxide cathodes for lithium-ion batteries. *ACS Appl Mater Interfaces* 2013;5(21):11434–40.
- [169] Jing L, Cameron AR, Li H, Glazier S, Dahn JR. Comparison of single crystal and polycrystalline  $\text{LiNi}_{0.5}\text{Mn}_{0.3}\text{Co}_{0.2}\text{O}_2$  positive electrode materials for high voltage Li-ion cells. *J Electrochem Soc* 2017;164(7):A1534–44.
- [170] Kim Y. Lithium nickel cobalt manganese oxide synthesized using alkali chloride flux: morphology and performance as a cathode material for lithium ion batteries. *ACS Appl Mater Interfaces* 2012;4(5):2329–33.
- [171] Duan J, Wu C, Cao Y, Huang D, Du K, Peng Z, et al. Enhanced compacting density and cycling performance of Ni-riched electrode via building mono dispersed micron scaled morphology. *J Alloy Compd* 2017;695:91–9.
- [172] Hu G, Tan C, Du K, Peng Z, Cao Y, Liang L, et al. Preparation of high voltage solid nickel rich cathode material  $\text{LiNi}_{0.85}\text{Co}_{0.06}\text{Mn}_{0.06}\text{Al}_{0.03}\text{O}_2$ . *Journal of inorganic chemistry* 2017;33(08):1450–6.
- [173] Liu A, Zhang N, Stark JE, Arab P, Li H, Dahn JR. Synthesis of Co-free Ni-rich single crystal positive electrode materials for lithium ion batteries: part II. one-step lithiation method of Mg-doped  $\text{LiNiO}_2$ . *J Electrochem Soc* 2021;168(5):050506.
- [174] Liu D, Shadik Z, Lin R, Qian K, Li H, Li K, et al. Review of recent development of In situ/operando characterization techniques for lithium battery research. *Adv Mater* 2019;31(28):1806620.
- [175] Hautier G, Jain A, Chen H, Moore C, Ong SP, Ceder G. Novel mixed polyanions lithium-ion battery cathode materials predicted by high-throughput ab initio computations. *J Mater Chem* 2011;21(43):17147–53.
- [176] Xiao Y, Miara LJ, Wang Y, Ceder G. Computational Screening of Cathode Coatings for Solid-State Batteries. *Joule* 2019;3(5):1252–75.



- [177] Nolan AM, Liu Y, Mo Y. Solid-state chemistries stable with high-energy cathodes for lithium-ion batteries. *ACS Energy Lett* 2019;4(10):2444–51.
- [178] Xiao RJ, Li H, Chen LQ. Development of new lithium battery materials by material genome initiative. *Acta Physica Sinica* 2018;67(12):128801.
- [179] Ling SG. Application of high-throughput calculations for screening lithium battery materials. *Materials China* 2015;34(4):272–81.



# Three-dimensional hierarchical porous hard carbon for excellent sodium/potassium storage and mechanism investigation

Shifei Huang<sup>a, b, c, 1</sup>, Yao Lv<sup>a, 1</sup>, Wen Wen<sup>d</sup>, Tao Xue<sup>e</sup>, Peng Jia<sup>c</sup>, Jing Wang<sup>c</sup>,  
Jiujun Zhang<sup>a</sup>, Yufeng Zhao<sup>a, \*</sup>

<sup>a</sup> Institute for Sustainable Energy/College of Sciences, Shanghai University, Shanghai 200444, China

<sup>b</sup> Environmental Science and New Energy Technology Research Center, Tsinghua-Berkeley Shenzhen Institute (TBSI), Shenzhen, 518055, China

<sup>c</sup> Key Laboratory of Applied Chemistry, Yanshan University, Qinhuangdao 066004, China

<sup>d</sup> Shanghai Synchrotron Radiation Facility, Shanghai Advanced Research Institute, Chinese Academy of Sciences, 201204, PR China

<sup>e</sup> Center for Analysis and Tests, Tianjin University, Tianjin 300072, PR China

## ARTICLE INFO

### Article history:

Received 28 December 2020

Received in revised form

29 January 2021

Accepted 1 February 2021

Available online 10 February 2021

### Keywords:

N–P doping

3D hierarchical

Hard carbon

Sodium/potassium-ion batteries

Charge storage mechanism

## ABSTRACT

Hard carbons are one of the most promising anode materials for sodium/potassium-ion batteries (SIBs/PIBs), which demonstrate favorable long charge/discharge plateaus, but suffer from low rate performance. Herein, we report a new design of N–P codoped hard carbon (NPHC) with three-dimensional (3D) hierarchical porous frameworks. Such unique structure provides bicontinuous ion/electron transportation paths, regulated electronic structure, enlarged interlayer spacing, and moderate surface area. The as prepared NPHC demonstrates a high reversible specific capacity (336 mAh g<sup>-1</sup> for SIBs, 339 mAh g<sup>-1</sup> for PIBs), along with a good rate performance of ~5.3 C. Particularly, an in-depth study on the charge storage mechanism for both SIBs and PIBs is conducted by combining in-situ Raman spectra and quasi in-situ synchrotron X-ray diffraction analysis, whereby the coexistence of physical adsorption/graphitic layer intercalation, or intercalation/pore filling within certain potential ranges is detected, and the ion storage behavior at different charge/discharge stages is precisely identified.

© 2021 Elsevier Ltd. All rights reserved.

## 1. Introduction

Sodium/potassium-ion batteries (SIBs/PIBs) are recognized as a potential alternative system for lithium-ion batteries (LIBs) because of the low cost and abundant reserves of sodium/potassium as well as its suitable sodiation/potassiation potential (0.05 Vvs. Na<sup>+</sup>/Na, 0.2 Vvs. K/K<sup>+</sup>) [1–12]. At present, important progress has been made in the research and development of cathode materials for SIBs. But, the search for suitable SIB/PIB anode materials is still ongoing because of the more sluggish diffusion kinetics and a larger radius of Na<sup>+</sup>/K<sup>+</sup> than Li<sup>+</sup> [13–15]. Hard carbons (HCs) comprising interlaced graphite microcrystalline layers and abundant micropores and defects are considered to play an important role in the future commercialization of SIBs because of its high capacity, stable cycling performance, and wide range of precursors [16–18]. However, the very polarized energy storage platform and sluggish ions

diffusion kinetics of HC generally cause limited rate performance [19,20].

It is reported that the fine structure and physicochemical properties, for example, the pore structure, interlayer spacing, and the defects of HCs have a significant effect on their electrochemical performances, and even the charge storage mechanism. Hetero atoms doping (N, P, or S, etc.) or tailoring the porous structure could principally raise the electrochemical performance of amorphous carbon materials, which is generally, however, on the premise of sacrificing the initial columbic efficiency and plateau charge/discharge capacity. For example, an N-doped mesoporous carbon can present a high specific capacity of 462 mAh g<sup>-1</sup>, but with very low initial columbic efficiency [21]. Lu et al. [22] developed a cork-derived HC, which could demonstrate an optimized capacity of 360 mAh g<sup>-1</sup> with well reserved plateau, which, however, suffers from serious capacity decay at high rates. Therefore, a rational design of HCs with modulated structure that can simultaneously improve the rate performance and plateau charge capacity for SIBs/PIBs is urgently demanded. On the contrary, the charge storage behavior of Na/K in HC has been extensively explored [7,22–30].

\* Corresponding author.

E-mail address: [yufengzhao@shu.edu.cn](mailto:yufengzhao@shu.edu.cn) (Y. Zhao).

<sup>1</sup> These authors contributed equally to this work.

The typical sodium storage behavior includes obvious high potential oblique line region ( $>0.1$  V) and low potential plateau region ( $<0.1$  V), indicating that the sodium embedding process has at least two reaction mechanisms. Different researchers have proposed different energy storage mechanism including “layer intercalation-pore filling” [30], “adsorption-intercalation mechanism” [21], “adsorption-hole filling” [31]. Nevertheless, these mechanisms are mainly based on the specific HC structure, and certain in situ or ex situ characterization techniques, which show limitations of single characterization means and inconsistency of test conditions.

In this work, we report a new design of N, P codoped HC (NPHC) with 3D hierarchical ions/electrons bicontinuous porous structure, adjusted electronic structure, and modulated carbon layer spacing, which exhibits a high rate performance, high capacity performance, and good cycle stability for both SIBs and PIBs. More importantly, an in-depth mechanism with combined in-situ Raman combined with in-situ synchrotron X-ray diffraction (XRD) techniques have been conducted. We confirm the coexistence of different charge storage behaviors in certain potential ranges, and a four-step reaction mechanism of “adsorption–adsorption/intercalation–intercalation/pore filling–overpotential deposition” is proposed according to the different charge/discharge stages. The charge storage behaviors for SIBs and PIBs are similar, but vary in some details.

## 2. Results and discussion

### 2.1. Characterization

The NPHC with 3D interconnected channel was synthesized using Artemia cyst shells (Fig. S1) as precursor and N source, and  $\text{H}_3\text{PO}_4$  as P source through a combined preoxidization and high temperature ( $1,300^\circ\text{C}$ ) calcination technique (see more details in the supporting information). The morphology and microstructures of the sample were examined and shown in Figs. 1 and S2. The scanning electronic microscope (SEM) and transition electronic microscope (TEM) images confirm the 3D interconnected microporous carbon framework of as prepared NPHC, with pore sizes around  $120\text{--}150$  nm (Fig. 1a–d), and abundant mesopores can be found on the carbon skeletons (Fig. 1d). This unique structure can not only provide a favorable charge transportation channel for electrolyte, but also can greatly shorten the diffusion path of electrolyte ions and increase the ion diffusion efficiency when applied as battery electrodes. For comparison, the morphology of N-doped hard carbon (NHC) produced with the same precursor (Fig. S2a) and bulk commercial hard carbon (HC-commercial) (Fig. S2d) is also characterized. It is aware that the preoxidation of the carbon precursor may play an important role in decreasing the graphitization degree of the sample, which is confirmed by the high-resolution TEM (HRTEM) images, whereby NPHC shows more disordered microstructure than HC-commercial and NHC (Figs. 1e and S2b&e). This might be due to that the preoxidation could induce the cross-linking of precursor, thus prevent the ordered rearrangement of carbon atoms, meanwhile the as released small molecules (e.g. CO and  $\text{CO}_2$ ) during carbonization can also affect the microstructure of NPHC, increasing the content of defects and micropores. The  $d_{002}$  interlayer spacing of the synthesized materials are measured as  $0.35\text{--}0.4$  nm. According to previous studies, the energy region corresponding to the  $\text{Na}^+$  intercalation into the carbon layer is in the range of  $0.35\text{--}0.47$  nm, HCs with lattice distance  $<0.35$  nm cannot accommodate sodium ions, whereas those  $>0.47$  nm show only adsorption behavior [8]. Note that, the P doping seems be able to enlarge the interlayer spacing of carbon to a certain extent compared with NHC (Fig. S2b) and HC-commercial

(Fig. S2e), which implements multiple storage modes of sodium ions through combined pore filling, defect adsorption, and intercalation within the graphite nanoregion. And the scattered diffraction rings reflected by (002) and (101) crystal planes in selected area electron diffraction (SAED) images (Figs. 1f and S2c&g) verify the low crystallinity of all samples, which is consistent with the HRTEM results. The corresponding energy dispersive X-ray spectroscopy mappings confirm the uniform distribution of C (Fig. 1h), O (Fig. 1i), N (Fig. 1j), and P (Fig. 1k) elements in the skeleton of NPHC. The internal microstructure and composition of the samples were further characterized using XRD, Raman spectroscopy,  $\text{N}_2$  adsorption/desorption isotherms and Density Functional Theory pore-size distribution, as well as X-ray photon spectroscopy (XPS) (Fig. 2). As shown in Fig. 2a, the broadened humps (002) at  $23.48^\circ$  attributed to disordered carbon can be found in the XRD diffraction patterns of NPHC, corresponding to an average d spacing of  $0.380$  nm, which is larger than that of NHC ( $0.372$  nm) and HC-commercial ( $0.378$  nm), which is consistent with HRTEM results. A weak (101) peak appeared at  $44.0^\circ$ , indicating that the graphitized microcrystals formed in the HC had both rhombic phase ( $3R$ ,  $43.4^\circ$ ) and hexagonal phase ( $2H$ ,  $44.7^\circ$ ). Raman spectra of all the samples show the two characteristic peaks of D band (defect) at  $1,330\text{ cm}^{-1}$  and G band ( $\text{E}_{2g}$  lattice vibration) at  $1,593\text{ cm}^{-1}$  (Fig. 2b). The  $I_D/I_G$  values of NPHC, NHC, and HC-commercial calculated from Raman data are 1.17, 1.05, and 1.03, respectively, indicating the more disordered nature because of the increased defect degree of NPHC [32]. The type I isotherm plot from  $\text{N}_2$  adsorption–desorption test (Fig. 2c) indicates the microporous type structure of NPHC [33], with the largest Brunauer–Emmett–Teller (BET) specific surface area (SSA) of  $285.8\text{ m}^2\text{ g}^{-1}$  and pore volume of  $0.197\text{ cm}^3\text{ g}^{-1}$  (Table S1), and the porosity distribution (Fig. 2d) also reveals the microporous structure of NPHC. This moderate SSA will not seriously affect the initial charge–discharge Coulombic efficiency, but can provide more active sites for the storage of sodium/potassium in conjunction with abundant microporous [34,35]. Meanwhile, the tap density of NPHC was detected to be about  $1.2\text{ g cm}^{-3}$ , which is much lower than that of HC-commercial ( $1.6\text{ g cm}^{-3}$ ) and graphite ( $2.2\text{ g cm}^{-3}$ ) because of its large SSA and porous structure. The design of three-dimensional (3D) structure of this material is not conducive to the improvement of volume specific capacity, but it is more conducive to the improvement of mass specific capacity. Fig. 2e shows the XPS survey spectra of NPHC, NHC, and HC-commercial, the contents of C, O, N, and P are 89.3, 7.3, 2.1, and 1.3 at% in NPHC, 85.7 (C), 13.5 (O), and 0.8 at% (N) in NHC, and 94.0 (C) and 6.0 at% (O) in HC-commercial, respectively. The deconvoluted XPS spectra of each element was carried out in Fig. 2f–i. The peaks corresponding to C–P, C–C/C=C, C–N, C–O, and O–C=O were found at 283.7, 284.7, 285.7, 286.2, and 288.9 eV, respectively, of  $\text{C}1s$  spectra (Fig. 2f). Four peaks at 531.3, 532.3, 533.3, and 534.2 eV in  $\text{O}1s$  spectra (Fig. 2g) correspond to C=O, C–OH, C–O–C, and COOH, respectively. There are three classical peaks of pyridine N ( $398.6$  eV), pyrrolidine N ( $400.2$  eV), graphite N ( $401.2$  eV), and one N–O ( $405.1$  eV) in  $\text{N}1s$  spectra [36] (Fig. 2h), and two peaks of P–C ( $133.3$  eV) and P–O ( $135.6$  eV) were also shown in the  $\text{P}2p$  spectra (Fig. 2i). For comparison, the deconvoluted XPS spectra of  $\text{C}1s$ ,  $\text{O}1s$ , and  $\text{N}1s$  of NHC and  $\text{C}1s$ ,  $\text{O}1s$  of HC-commercial spectra were also provided in Fig. S3. The introduction of heteroatoms into HC can change the electronic structure of carbon materials, which can offset the Fermi level guide band of carbon materials. It can not only improve the electronic conductivity of carbon materials, but also provide more active sites of sodium/potassium storage [24,37]. At the same time, the introduction of phosphorus can



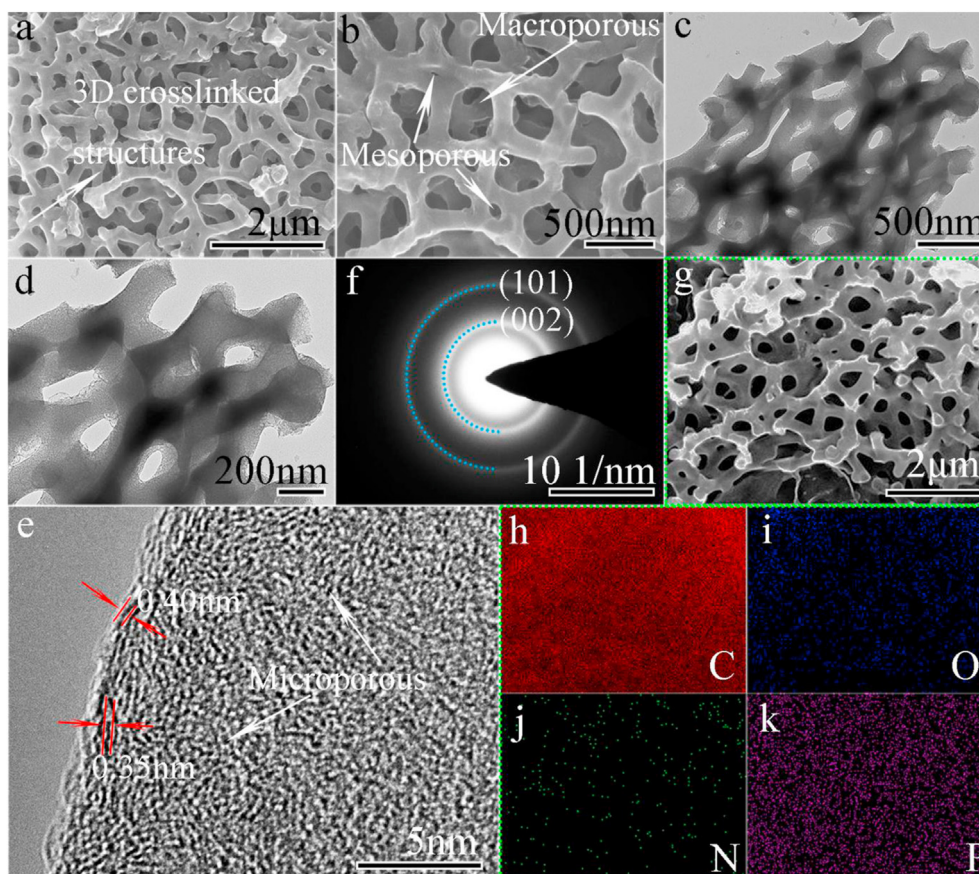


**Fig. 1. Morphological and structural characterizations of NPHC.** (a–b) SEM images of NPHC. (c–d) TEM images of NPHC. (e–f) HRTEM and SAED images of NPHC. (g) SEM images of NPHC and the corresponding element mapping images of C, O, N, P, respectively.

also broaden the graphite layer spacing of carbon materials to a certain extent, and provide favorable conditions for the storage and transport of electrolyte ions [38–40].

## 2.2. Electrochemical performances

The electrochemical performance for Na/K-ion storage of NPHC, NHC, and HC-commercial was investigated by cyclic voltammetry (CV) and galvanic charge–discharge (GCD) test. Fig. 3a–c shows the first five cycles of CV curves of NPHC, NHC, and HC-commercial at the scan rate of  $0.1 \text{ mV s}^{-1}$ . The charge and discharge CV curves are very straight and almost overlapped in the potential interval from 2.5 to 1.5 V, indicating that the adsorption capacity of sodium storage on the surface of carbon materials is limited. When continuous discharge to about 0.2 V, an irreversible region appears relative to the second cycle because of the decomposition of the electrolyte and the formation of solid electrolyte membrane (SEI) on the surface of the carbon materials. The cathodic reduction peaks appear when the discharge potential decreases continuously near 0.01 V. At the same time, the corresponding anodic oxidation peak at  $\sim 0.14 \text{ V}$  was detected during charging process, which can be attributed to the insertion/extraction of sodium ions into the HC graphite layer and the filling of nanopores during the charge–discharge process. In addition, the CV curves of NPHC and NHC overlapped in the following four cycles, but the HC-commercial showed an obvious attenuation of cathodic reduction peak at low potential, which indicates good reversibility and cycle stability of the as synthesized electrode material. The NPHC demonstrates a high reversible specific capacity of  $336 \text{ mAh g}^{-1}$  at

$25 \text{ mA g}^{-1}$ , which is superior to that of NHC ( $292 \text{ mAh g}^{-1}$ ) and HC-commercial ( $268 \text{ mAh g}^{-1}$ ).

At the same time, there is no serious reduction of coulomb efficiency in the first cycle because of its large SSA of NPHC. In fact, the irreversible capacity of NPHC ( $127 \text{ mAh g}^{-1}$ ) is higher than that of NHC ( $108 \text{ mAh g}^{-1}$ ) and HC-commercial ( $72 \text{ mAh g}^{-1}$ ), but it does not increase in proportion to the SSA [3]. Both NPHC and NHC show good rate performance, with 52 and  $48 \text{ mAh g}^{-1}$  at  $3,000 \text{ mA g}^{-1}$ , respectively (Fig. 3d), which can be restored to 281 and  $254 \text{ mAh g}^{-1}$  when the current density is adjusted to  $25 \text{ mA g}^{-1}$ . This indicates that the interconnected hierarchical structure and shorter ion transport path of the prepared 3D HC are more conducive to capacity storage, especially under the higher current density. The electrochemical performance of HC-commercial was also tested for comparison, of which the specific capacities at corresponding current densities are only 268, 37, and  $245 \text{ mAh g}^{-1}$ , respectively. Meanwhile, the capacity of HC-commercial decreases sharply compared with NPHC when the current density increases to 100 and  $200 \text{ mA g}^{-1}$  (Fig. S4), indicating the serious polarization of HC-commercial. We also provide the variation values of platform capacity and slope capacity under different current densities in Table S2.

Promisingly, the samples also exhibit excellent stability in SIBs (Fig. 3e), with no capacity attenuation after 5 and 10 cycles at 25 and  $50 \text{ mA g}^{-1}$ , respectively, and then continued to charge and discharge to 120 cycles at  $100 \text{ mA g}^{-1}$ . More interestingly, both the capacity in the slope ( $107 \text{ mAh g}^{-1}$ ) and platform regions ( $190 \text{ mAh g}^{-1}$ ) have been significantly improved for NPHC as can be seen from the first charge curves (Fig. 3f). The platform region capacity

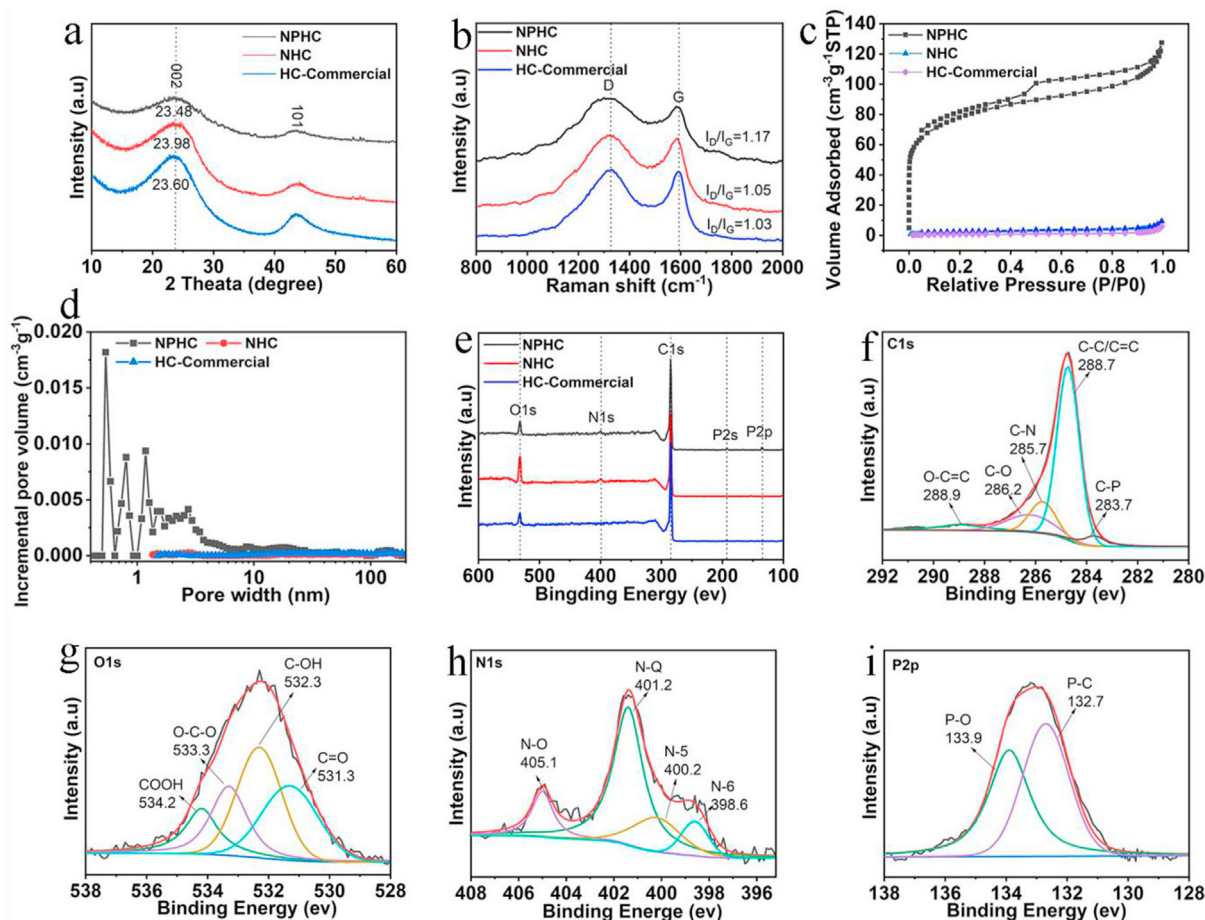


**Fig. 2.** Internal structure characterization and element analysis of NPHC, NHC, and HC-commercial. (a) The XRD, (b) Raman, (c–d) nitrogen adsorption/desorption isotherm plot and Density Functional Theory pore-size distribution, (e) XPS survey spectra and deconvoluted XPS spectra of C1s (f), O1s (g), N1s (h), and P2p (i) of NPHC, respectively.

contribution is 60.3%, 56.9%, and 57.7%, respectively, for NPHC, NHC, and HC-commercial, respectively. This could be due to that, the addition of  $\text{H}_3\text{PO}_4$  during the synthesis would cause activation on NPHC, and increases the defect concentration, which benefits the slope region capacity; however, the heteroatom doping plays an important role in improving the electronic structure of NPHC by increasing the micropore size and broadening the interlayer spacing, which then maximizes the platform region capacity. The capacity of the slope area plays an important role for the rate performance of HC, and a stable long platform is also very conducive to the matching of high energy density full sodium ion cells. To compare the performance of our materials for sodium storage with the state-of-the-art literatures, we conducted a comprehensive investigation and made a detailed comparison in [Tables S3](#) and [S4](#), respectively.

The potential application as PIB electrodes of all the samples was also tested ([Fig. 3g–i](#)). The CV curves show a sharp cathodic reduction peaks near 0.01 V for all samples, and corresponding anodic oxidation peaks of NPHC, NHC, and HC-commercial can be detected at ~0.387 V, 0.544 V, and 0.589 V during discharge and charge process ([Fig. 3g–i](#)). The appearance of redox peaks is due to the intercalation/de-intercalation of potassium ions between the HC graphite layers and the filling/releasing of nanopore during the charge–discharge process. It is noteworthy that the test results also show that the introduction of heteroatoms can effectively alleviate potential hysteresis in PIBs, especially P-doping. At the same time, the effect of the larger radius of potassium ion intercalation on the

internal structure of carbon materials can be effectively alleviated by the enlargement of graphite layer spacing, and so does the 3D skeleton nanoporous structure. The NPHC demonstrates a high reversible specific capacity of  $339 \text{ mAh g}^{-1}$  at  $25 \text{ mA g}^{-1}$ , which is superior to that of NHC ( $290 \text{ mAh g}^{-1}$ ) and HC-commercial ( $217 \text{ mAh g}^{-1}$ ). NPHC also shows good rate performance of  $98 \text{ mAh g}^{-1}$  than NHC ( $78 \text{ mAh g}^{-1}$ ) and HC-commercial ( $67 \text{ mAh g}^{-1}$ ) at  $2,000 \text{ mA g}^{-1}$  (~5.3C) ([Fig. 3j](#)). Promisingly, the samples also exhibit excellent stability in PIBs ([Fig. 3k](#)), with a few capacity attenuations after 5 and 10 cycles at 25 and  $50 \text{ mA g}^{-1}$ , respectively, and then from 21st to 200 cycles at  $100 \text{ mA g}^{-1}$ , the capacity of NPHC, NHC, and HC-commercial also can be maintained at 77.1%, 69.4%, and 65.2%, respectively. From the first GCD curves of NPHC, NHC, and HC-commercial ([Fig. 3l](#)), it can be seen that the plateau potential of PIBs is higher than that of SIBs, and the potential platform is not as obvious as that of SIBs when the voltage is close to 0 V because the larger radius of  $\text{K}^+$  cannot be filled in small nanopores. In addition, it can be seen that the voltage hysteresis of NPHC and NHC has been significantly improved because of the regulation of N, P functional group. To compare the performance of our materials for potassium storage with the state-of-the-art literatures, we conducted a comprehensive investigation and made a detailed comparison in [Table S5](#).

A galvanostatic current intermittent titration test was also performed to determine the ion diffusion coefficient ( $D$ ) of sodium/potassium ions in the prepared HC [[20,40,41](#)]. The galvanostatic intermittent titration technique (GITT) curves ([Fig. 4a](#)) of NPHC,



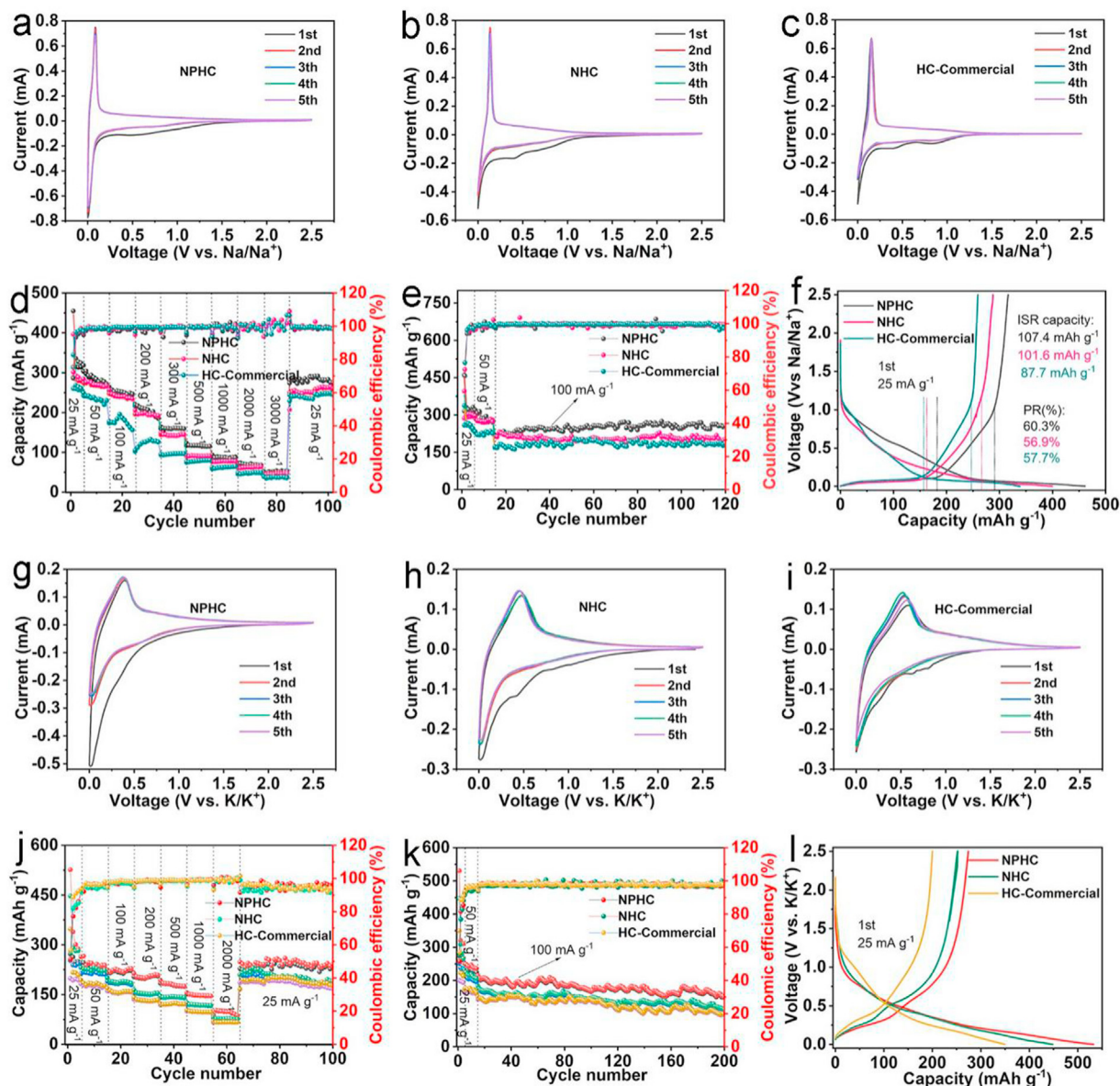


**Fig. 3.** Electrochemical performance of NPHC, NHC, and HC-commercial for SIBs: (a–c) representative CV curves at a scan rate of 0.1 mV s<sup>-1</sup> for the first five cycles; (d) rate performance gradually increasing from 25 to 3,000 mA g<sup>-1</sup>, and then back to 25 mA g<sup>-1</sup>; (e) cycling performance at the current density of 25, 50, and 100 mA g<sup>-1</sup>, respectively; and (f) GCD profiles at the first cycle with the current density of 25 mA g<sup>-1</sup>. Electrochemical performance of NPHC, NHC, and HC-commercial for PIBs: (g–i) representative CV curves at a scan rate of 0.1 mV s<sup>-1</sup> for the first five cycles for PIBs; (j) rate performance gradually increasing from 25 to 3,000 mA g<sup>-1</sup>, and then back to 25 mA g<sup>-1</sup>; (k) cycling performance at the current density of 25, 50, and 100 mA g<sup>-1</sup>, respectively; and (l) GCD profiles at the first cycle with the current density of 25 mA g<sup>-1</sup>.

NHC, and HC-commercial were tested under the pulse current density of 25 mA g<sup>-1</sup> for 0.5 h between rest intervals for 2 h in sodium electric semibattery, respectively. The sodium-ion diffusion coefficient during charging and discharging processes (Fig. 4b and c) can be calculated by Equation S1 [20,33,42]. The  $D$  values for all samples varied in a similar trend in the process of sodiation and desodiation with  $10^{-9}$  cm<sup>2</sup> s<sup>-1</sup> magnitude. The diffusion coefficients of sodium ions gradually decrease with the process of sodiation are relatively gentle. When the discharge reaches about 0.1 V cut-off potential, the diffusion coefficients decrease sharply and recover rapidly, showing a V-shape. It is worth noting that the  $D$  value decreases abruptly at the discharge platform area, indicating it is more prone to polarization under high current in the plateau region. In this region, the  $D$  values follow  $D_{\text{(NPHC)}} > D_{\text{(NHC)}} > D_{\text{(HC-commercial)}}$ , implying that the attenuation of

platform capacity will be in the opposite trend at high rates. At the same time, the diffusion coefficient of Na<sup>+</sup> in the slope area is much larger than that in the platform area with the same sequence of  $D_{\text{(NPHC)}} > D_{\text{(NHC)}} > D_{\text{(HC-commercial)}}$ . The larger diffusion coefficient of Na<sup>+</sup> in this area is the main factor affecting the contribution capacity of HC materials at high rate. During the charging process, the value of Na<sup>+</sup> diffusion coefficient between 0.01 and 0.1 V also shows a V-shaped change trend of first steep decline and rapid recovery, and the value of Na<sup>+</sup> diffusion coefficient decreases slowly as the potential continues to rise. The difference of  $D$  values between slope area and platform area is due to the different binding energy of Na–C, indicating that the sodium storage mechanism of HC in the two areas is completely different. The K<sup>+</sup> diffusion coefficient of all samples was also tested showing a similar trend with that of Na<sup>+</sup> (Fig. 4d–f). However, the K<sup>+</sup> with relatively larger ion radius cannot



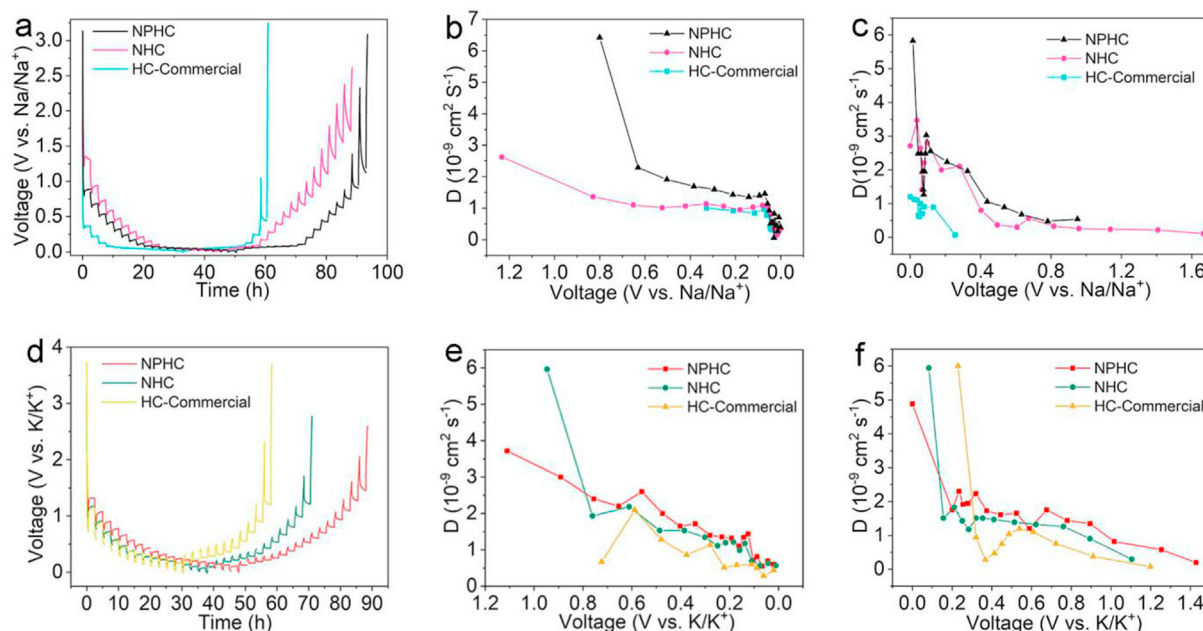


**Fig. 4.** GITT tests and ion diffusion coefficient calculations of NPHC, NHC and HC-commercial. (a) GITT potential profiles of NPHC, NHC and HC-commercial for sodiation and desodiation during the second cycle, (b–c) Na ion apparent diffusion coefficients calculated from the corresponding GITT potential profiles for sodiation and desodiation during the second cycle, respectively; (d) GITT potential profiles of NPHC, NHC and HC-commercial for potassiation and depotassiation during the second cycle, (e–f) K ion apparent diffusion coefficients calculated from the corresponding GITT potential profiles for potassiation and depotassiation during the second cycle, respectively.

embed or fill in the smaller graphite layers and nanopores like  $\text{Na}^+$ , resulting in the less obvious platform area, which also has a negative impact on the assembly of high-energy potassium battery. This is due to the difference in ion diffusion activation energy caused by the difference in electron density between Na and K, and the difference in binding energy between  $\text{Na}^+$  and  $\text{K}^+$  with the active sites of carbon materials, respectively.

### 2.3. In situ electrochemical study

Raman spectroscopy can provide important information about vibration and structural details of carbon materials [43–48]. Thus, in-situ Raman characterization was conducted to reveal the sodium/potassium storage mechanism of NPHC during the real-time charging/discharging process (Fig. S5). The Raman signal of the electrode material at different potential states can be obtained by synchronizing the charge and discharge with the Raman test. Fig. 5a shows the charge and discharge curves of NPHC at the current density of  $100 \text{ mA g}^{-1}$  in the sodium half-cell. Two characteristic peaks, D band at  $1350 \text{ cm}^{-1}$  and G band at  $1580 \text{ cm}^{-1}$  are detected in open circuit (OCV), and also shows a gradual change during the charging/discharging process. Interestingly, during the OCV  $\sim 0.01 \text{ V}$  discharge in the first cycle, the signal strength of D and G peaks begins to increase and then gradually decreases and finally the two peaks disappear (Fig. 5b1–b3). Specifically, from OCV to  $2.0 \text{ V}$ , the initial increase of D and G peak strength may be caused by the greater influence of polarization current on the potential of electrode materials. Then the peak strength of D and G decreases slowly from  $2.0$  to  $1.0 \text{ V}$ , implying that the interaction between Na and C atoms at this stage shows weak influence on the vibration strength, which is attributed to the physical adsorption of sodium ions on the surface of carbon materials. The D-peak sharply decreases from  $1.0$  to  $0.5 \text{ V}$  and disappears when continues to discharge to  $\sim 0.15 \text{ V}$ , which indicates that sodium ion has gradually occupied the defect site in the carbon material at this stage, and has a greater influence on the respiration vibration of carbon atoms at

the edge, making the Raman scattering signal decreases till it disappears. At the potential of  $0.5 \text{ V}$ , G peak shifts left to  $1556 \text{ cm}^{-1}$ , indicating the intercalation of Na into the carbon layer at this potential. When continued discharging to  $0 \text{ V}$ , the G-peak is further shifted or even disappeared, indicating that sodium ions continue to be embedded in the carbon layer at this stage and formed  $\text{NaCx}$  (“x” gradually decreases) [49,50]. We further conducted a quasi in situ synchrotron X-ray radiation study to double check the products upon charge/discharge by collecting the XRD data at several certain potentials. The existence of elemental sodium within the potential of  $0.128 \sim 0 \text{ V}$  stage (Fig. 5c and d) was detected from the XRD patterns, indicating that sodium was continuously filling in the carbon nanopore during this stage. Note that, the half-cell test system with discharge above  $0 \text{ V}$  cannot completely show the sodium storage characteristics of HC materials in full-cells. We therefore overcharged the half-cell to below  $0 \text{ V}$ , the discharge curve shows the same trend, until a polarization potential of  $-0.0375 \text{ V}$  appears, the voltage then gradually stabilizes at  $-0.0329 \text{ V}$  and a stable platform appears under this depolarization potential. During this process, we detected a large increase of metallic Na signal, which also indicated that the HC material reached saturation after discharging to  $-0.0375 \text{ V}$ , and began to precipitate (over-potential deposition) on the surface of the electrode material. In particular, this kind of HC with 3D hierarchical porous structure can reduce the local current density, thus inhibiting the formation of sodium dendrite at low potential. A large number of  $\text{Na}_2\text{CO}_3$  may be formed by the conversion of some Na elements in contact with air (caused by leakage of polyacetylimide membrane), and the presence of NaOH and NaCl might be the main inorganic substances of SEI membranes. Meanwhile, the Raman curves show a relatively symmetric change trend during the charging process, which also indicates the good sodium storage reversibility of the NPHC. At this point, we can conclude that the HC electrode material shows empirical adsorption under high potential ( $2.5\text{--}1.0 \text{ V}$ ) in the process of sodium storage, defect adsorption under medium potential ( $1.0\text{--}0.128 \text{ V}$ ), and the beginning of

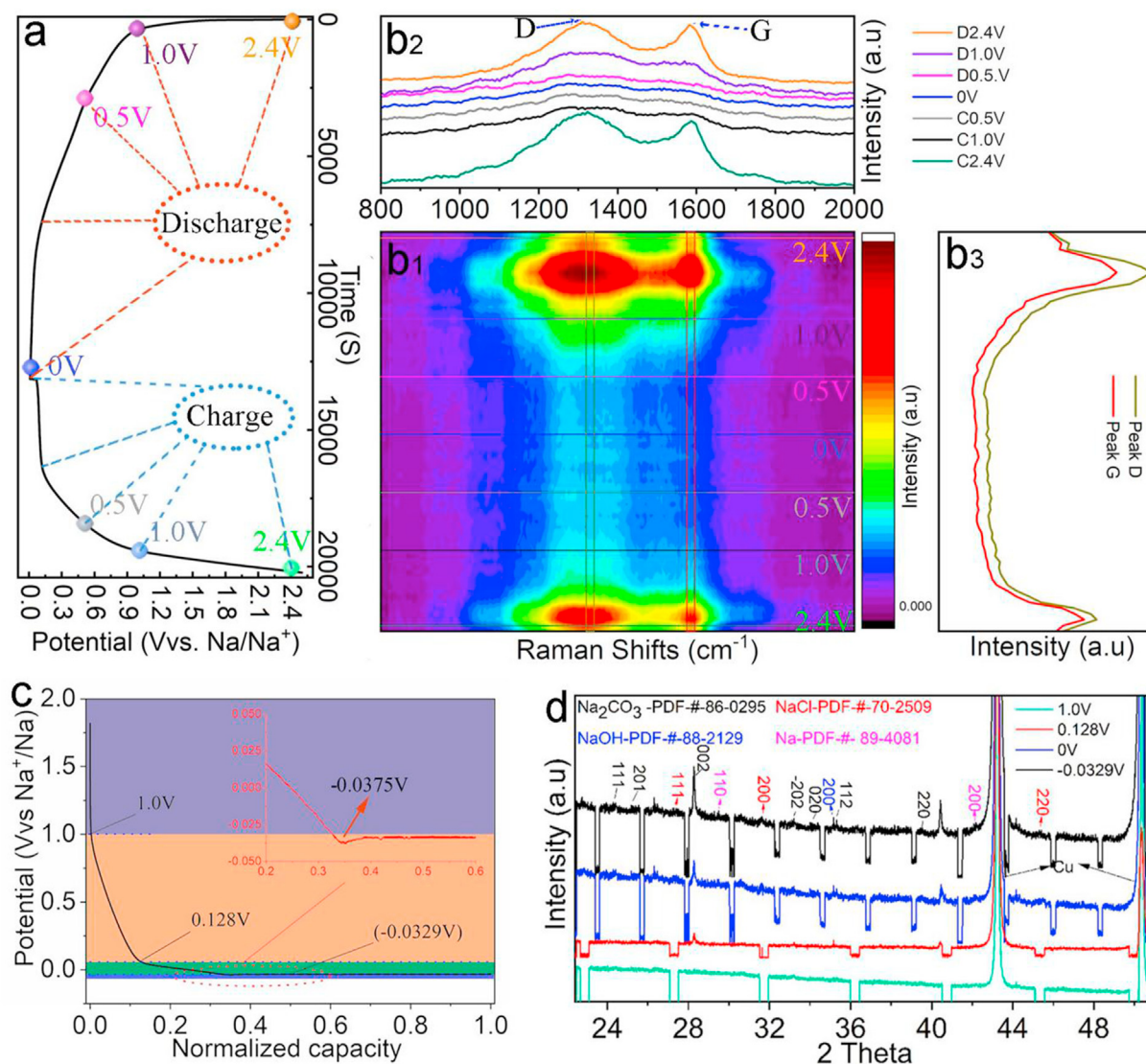


**Fig. 5.** In-situ Raman and quasi in-situ Synchrotron Radiation XRD (SR-XRD) test of NPHC for SIBs. (a) Discharge-charge profiles at the first cycle of NPHC for SIBs with current density of 100 mA g<sup>-1</sup>, (b1) the corresponding in-situ Raman curves, (b2) the Raman curves corresponding to charge and discharge to 2.4, 1.0, 0.5, and 0 V, (b3) the intensity change of D and G peaks in Raman curves at different test potentials, (c) the over-discharge curve of NPHC in sodium half-cell, (d) the quasi in-situ SR-XRD curves corresponding to discharge to 1.0 V, 0.128 V, 0 V, and -0.0329 V of NPHC, respectively.

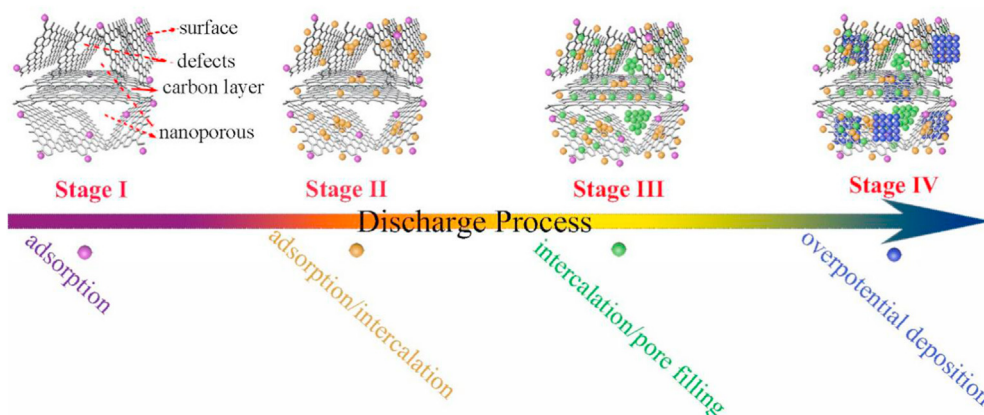


**Fig. 6.** Schematic diagram of four different stages of the discharge process.

graphite layer embedding, graphite layer embedding and nanopore filling under low potential ( $0.128 \sim -0.0375$  V), and surface overpotential deposition ( $-0.0329$  V). Therefore, the mechanism of HC sodium storage can be simply attributed to the model (Fig. 6) of “adsorption (OCV  $\sim 1.0$  V, stage I)—adsorption/intercalation ( $1.0\text{--}0.128$  V, stage II)—intercalation/pore filling ( $0.128\text{--}-0.0375$  V, stage III)—overpotential deposition ( $-0.0329$  V, stage IV)”

Similar tests were performed on the electrochemical process of NPHC in a PIB half-cell as in SIBs. It can be seen that the Raman curves change significantly during charging/discharging process (Fig. 7a and Fig. 7b1–b3). Two typical characteristic peaks of amorphous carbon materials, D peak at  $1350\text{ cm}^{-1}$  and G peak at  $1589\text{ cm}^{-1}$ , can be detected under the state of open circuit (OCV). Interestingly, the intensity and the position of D and G peaks did not change significantly during the first discharge potential from OCV to  $1.2$  V, indicating that there is no K ion embedding in the graphite layer of NPHC, nor is there any storage of defect site, but the adsorption process of a small amount of K ion at the surface site of NPHC. However, the position of D and G peaks shift to the left obviously, and two characteristic peaks ( $1266\text{ cm}^{-1}$  and  $1555\text{ cm}^{-1}$ ) were detected at  $0.25$  V, which were in good agreement with the Raman spectra of  $\text{KC}_8$  reported in the literature [51,52], indicating that  $\text{K}^+$  intercalation occurred in the graphite layers at this stage, and the disappearance of the D peak also indicated that  $\text{K}^+$  ion was adsorbed by defect sites at the same time.

With the discharge process going on, the response signal at  $1555\text{ cm}^{-1}$  is stronger and stronger, which indicates that  $\text{K}^+$  continues to be embedded in the carbon layer ( $\text{KC}_{8-x}$  may be formed). Meanwhile, the existence of K element is detected at  $0$  V in the ex-situ synchrotron radiation XRD curves (Fig. 7c and d). It also indicates that the filling process of potassium in carbon nanopores occurs at this stage. However, the larger radius of  $\text{K}^+$  makes it unable to fill in the smaller graphite layers and smaller nanopores like  $\text{Na}^+$ , so the discharge platform at low potential is not as obvious as that in sodium battery. When continue discharge to negative voltage, the charge–discharge curve still shows the same discharge trend, until a polarization potential of  $-0.0546$  V appears, then the voltage gradually stabilizes at  $-0.044$  V. When the discharge continues to negative voltage, the charge–discharge curve still shows the same discharge trend, until a polarization potential of  $-0.0546$  V appears, the voltage gradually stabilizes at  $-0.044$  V (Fig. 7c). In this process, we detected a large amount of K element increase, which also indicated that the HC materials reached full saturation after discharging to  $-0.0546$  V, and began to deposit on the surface of electrode materials (overpotential deposition). At the same time, the symmetrical change trend of Raman curves in the charging process also shows that the NPHC has good reversibility of potassium storage. Therefore, the mechanism of HC potassium storage also can be simply attributed to the model of “adsorption (OCV  $\sim 1.2$  V, stage I)—adsorption/intercalation

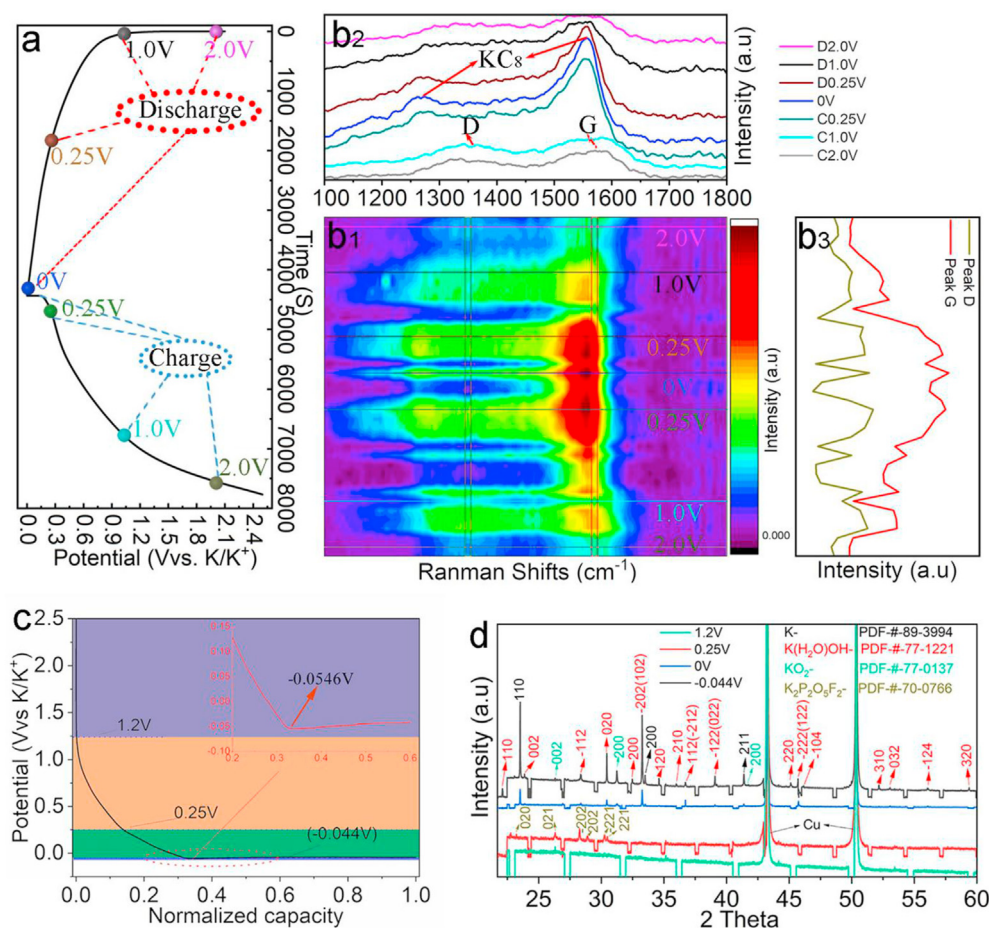


**Fig. 7.** In-situ Raman and quasi in-situ synchrotron radiation XRD (SR-XRD) test of NPHC for PIBs. (a) Discharge–charge profiles at the first cycle of NPHC for PIBs with current density of  $250\text{ mA g}^{-1}$ , (b1) the corresponding in-situ Raman curves, (b2) the Raman curves corresponding to charge and discharge to  $2.0, 1.0, 0.25,$  and  $0\text{ V}$ , (b3) the intensity change of D and G peaks in Raman curves at different test potentials, (c) the overdischarge curve of NPHC in potassium half-cell, (d) the quasi in-situ SR-XRD curves corresponding to discharge to  $1.2\text{ V}, 0.25\text{ V}, 0\text{ V}$  and  $-0.044\text{ V}$  of NPHC, respectively.



(1.2–0.25 V, stage II)—intercalation/pore filling (0.25 ~ –0.0546 V, stage III)—overpotential deposition (–0.044 V, stage IV)" too. Although the process of potassium storage is similar to that of sodium storage, there are obvious differences in details.

### 3. Conclusions

In this work, a novel 3D NPHC anode material with high capacity, high rate performance, and cycle stability was obtained using the biomass precursor with 3D connected pore structure. The maximum discharge specific capacities of NPHC for sodium and potassium storage reached 335.6 and 338.9 mAh g<sup>−1</sup>, respectively. In addition, the combined in-situ Raman and quasi in-situ synchrotron XRD study confirms the coexistence of physical adsorption and graphitic layer intercalation, and the coexistence of intercalation and pore filling within certain potential ranges. In conclusion, this study further reveals the energy storage mechanism of HCs during the charge–discharge process of SIBs/PIBs.

### 4. Experimental section

#### 4.1. Materials preparation

Preparation:

1. Precursor pretreatment: The Artemia cyst shells were washed with tap water for several times, then washed with distilled water for three times, placed in a drying oven, dried at 80 °C, milled at 300 r min<sup>−1</sup> for 6 h to obtain carbon source precursor.
2. Precursor preoxidized: Firstly, the milled precursor powder was put into a muffle furnace and heated to 200 °C at a heating rate of 0.5 °C min<sup>−1</sup> for 6 h. Then, 5.0 g of the obtained precursor was immersed in a dilute solution containing 2 ml phosphoric acid and stirred for 12 h. Finally, the paste was evaporated in a water bath at 80 °C and dried in a drying oven at 80 °C. The control group was not treated with phosphoric acid;
3. High temperature pyrolysis and carbonization: Firstly, the pre-treated precursor powder was put into a tubular furnace, heated to 350 °C at a heating rate of 0.5 °C min<sup>−1</sup> and kept for 6 h. Then, it was heated to 1,300 °C at a heating rate of 0.5 °C min<sup>−1</sup>, and then held for 6 h. Finally, the samples were treated with concentrated nitric acid and then washed and dried.

#### 4.2. Characterization

Raman spectra were recorded on a Renishaw inVia Raman microscope with an Ar-ion laser at the excitation wavelength of 532 nm. Powder XRD patterns between 10 and 60° (2θ) were collected by Rigaku D/MAX-2500 powder diffractometer with Cu-Kα radiation (λ = 0.154 nm) operated at 40 kV, 200 mA. Hitachi XPS was measured by a VG ESCALAB MKII X-ray photoelectron spectrometer using Mg-Kα as the exciting source (1,253.6 eV). The SSA and pore size of the materials were measured using a micro-meritics (ASAP 2020 V4.00 (V4.00 H)). Carl Zeiss SUPRA 55 SAP-PHIRE field-emission scanning electron microscope (Germany, 15 kV), Hitachi-7650 TEM (Japan, 80 kV), and HRTEM (JEOL JEM-3000F) were used to investigate the morphology and microstructure.

#### 4.3. Electrochemical measurements

The working electrodes were prepared by a mixture of 80 wt% synthesized active materials, 10 wt% acetylene carbon black, and 10 wt% polyvinylidene fluoride (PVDF) binder in N-methyl-2-

pyrrolidone onto a Cu foil, and then dried in a vacuum furnace at 120 °C for 12 h. The 675 μm glass fiber isolation membrane (GF/D) and Na/K metal was used as separator and counter electrodes, respectively, when assembled into a stainless-steel coin cell (2032) in an Ar-filled glovebox (both O<sub>2</sub> and H<sub>2</sub>O levels below 0.1 ppm). The electrochemical measurements were tested in 1 M NaClO<sub>4</sub> solution in a mixture (1:1, in vol%) of EC and DEC for SIBs and 0.8 M KPF<sub>6</sub> solution in a mixture (1:1, in vol%) of EC and DEC for PIBs. CV curves were measured at different scanning rate of 0.1 mV s<sup>−1</sup>, respectively. The CV was test on CHI 650e electrochemical workstation (Chenhua, China). The constant current charge–discharge and GITT tests were performed with a computer controlled cycling equipment (Land CT2001A, China) in the potential range of 0.01–2.5 V.

#### 4.4. In-situ characterization

The in-situ Raman curves were recorded on a Renishaw inVia Raman microscope with an Ar-ion laser at the excitation wavelength of 532 nm through an in-situ Raman steel shell cell (Raman tests while the workstation is charged and discharged). The quasi in-situ synchrotron radiation XRD was carried out at BL14B1 line station of Shanghai light source. Electrode treatment in quasi in situ testing: After the electrodes are charged and discharged to the corresponding potential, the electrodes are relaxed at constant voltage for 30 min. The electrodes are removed in the glove box, washed with organic solvents, and sealed with polyacetylimide film after drying.

### credit author statement

**Shifei Huang:** Synthesis, test and original draft preparation. **Yao Lv.:** Writing- Original draft preparation. **Wen Wen:** In-situ XRD and data analysis. **Tao Xue:** In-situ Raman spectra. **Peng Jia:** TEM analysis. **Jing Wang:** Reviewing and Editing. **Jiujun Zhang:** Reviewing and Editing. **Yufeng Zhao:** Supervision, Writing- Reviewing and Editing.

### Declaration of competing interest

The authors declare that they have no known competing financial interests or personal relationships that could have appeared to influence the work reported in this paper.

### Acknowledgements

The authors thank the financial supports from the National Natural Science Foundation of China (51774251), Shanghai Science and Technology Commission's "2020 science and technology innovation action plan" (20511104003), Hebei Natural Science Foundation for Distinguished Young Scholars (B2017203313), Hundred Excellent Innovative Talents Support Program in Hebei Province (SLRC2017057), Scientific Research Foundation for the Returned Overseas Chinese Scholars (CG2014003002) and the open funding of state key laboratory of advanced chemical power sources (SKL-ACPS-C-11). They also thank beamline BL14B1 of the Shanghai Synchrotron Radiation Facility for providing the beamtime.

### Appendix A. Supplementary data

Supplementary data to this article can be found online at <https://doi.org/10.1016/j.mtener.2021.100673>.

## References

- [1] L. Xiao, H. Lu, Y. Fang, M.L. Sushko, Y. Cao, X. Ai, H. Yang, J. Liu, *Adv. Energy Mater.* 8 (20) (2018) 1703238.
- [2] S. Shi, C. Sun, X. Yin, L. Shen, Q. Shi, K. Zhao, Y. Zhao, J. Zhang, *Adv. Funct. Mater.* 30 (2020) 1909283.
- [3] L. Shen, S. Shi, S. Roy, X. Yin, W. Liu, Y. Zhao, *Adv. Funct. Mater.* 31 (4) (2021) 2006066.
- [4] H. Hou, X. Qiu, W. Wei, Y. Zhang, X. Ji, *Adv. Energy Mater.* 7 (24) (2017) 1602898.
- [5] S. Shi, Z. Li, L. Shen, X. Yin, Y. Liu, G. Chang, J. Wang, S. Xu, J. Zhang, Y. Zhao, *Energy Storage Mater.* 29 (2020) 78–83.
- [6] Y. Zheng, Y. Wang, Y. Lu, Y.S. Hu, J. Li, *Nano Energy* 39 (2017) 489–498.
- [7] M. Chen, W. Wang, X. Liang, S. Gong, J. Liu, Q. Wang, S. Guo, H. Yang, *Adv. Energy Mater.* 8 (19) (2018) 1800171.
- [8] S. Huang, M. Wang, P. Jia, B. Wang, J. Zhang, Y. Zhao, *Energy Storage Mater.* 20 (2019) 225–233.
- [9] Y. Li, Q. Shi, X. Yin, J. Wang, J. Wang, Y. Zhao, J. Zhang, *Chem. Eng. J.* 402 (2020) 126181.
- [10] W.C. Chang, J.H. Wu, K.T. Chen, H.Y. Tuan, *Adv. Energy Mater.* 6 (9) (2019) 1801354.
- [11] R. Rajagopalan, Y. Tang, X. Ji, C. Jia, H. Wang, *Adv. Funct. Mater.* 30 (12) (2020) 1909486.
- [12] N. Wang, C. Chu, X. Xu, Y. Du, J. Yang, Z. Bai, S. Dou, *Adv. Energy Mater.* 8 (27) (2018) 1801888.
- [13] D. Tie, G. Gao, F. Xia, R. Yue, Q. Wang, R. Qi, B. Wang, Y. Zhao, *ACS Appl. Mater. Interf.* 11 (7) (2019) 6978–6985.
- [14] C. Chen, Y. Yang, X. Tang, R. Qiu, M. Zhang, *Small* 15 (10) (2019) 1804740.
- [15] S. Shi, Z. Li, Y. Sun, B. Wang, Q. Liu, Y. Hou, S. Huang, J. Huang, Y. Zhao, *Nano Energy* 48 (2018) 510–517.
- [16] Z.L. Yu, B. Qin, Z.Y. Ma, J. Huang, S.C. Li, H.Y. Zhao, H. Li, Y.B. Zhu, H.A. Wu, S.H. Yu, *Adv. Mater.* 31 (23) (2019) 1900651.
- [17] J.L. Xia, D. Yan, L.P. Guo, X.L. Dong, A.H. Lu, *Adv. Mater.* 32 (21) (2020) 2000447.
- [18] R. Guo, C. Lv, W. Xu, J. Sun, Y. Zhu, X. Yang, J. Li, J. Sun, L. Zhang, D. Yang, *Adv. Energy Mater.* 9 (2020) 1903652 (2020).
- [19] Z. Li, Z. Jian, X. Wang, I.A. Rodríguez-Pérez, C. Bommier, X. Ji, *Chem. Commun.* 53 (17) (2017) 2610–2613.
- [20] Z. Jian, Z. Xing, C. Bommier, Z. Li, X. Ji, *Adv. Energy Mater.* 6 (3) (2016) 1501874.
- [21] H. Huang, R. Xu, Y. Feng, S. Zeng, Y. Jiang, H. Wang, W. Luo, Y. Yu, *Adv. Mater.* 32 (8) (2020) 1904320.
- [22] Y. Li, Y. Lu, Q. Meng, A.C.S. Jensen, Q. Zhang, Q. Zhang, Y. Tong, Y. Qi, L. Gu, M. Titirici, Y. Hu, *Adv. Energy Mater.* 9 (48) (2019) 1902852.
- [23] Q. Meng, Y. Lu, F. Ding, Q. Zhang, L. Chen, Y.-S. Hu, *ACS Energy Lett.* 4 (11) (2019) 2608 (2019).
- [24] S. Huang, Z. Li, B. Wang, J. Zhang, Y. Zhao, *Adv. Funct. Mater.* 28 (10) (2018) 1706294.
- [25] G. Wang, M. Shao, H. Ding, Y. Qi, F. Huo, *Angew. Chem. Int. Ed.* 58 (38) (2019) 13718.
- [26] N. Sun, Z. Guan, Y. Liu, Y. Cao, Q. Zhu, H. Liu, Z. Wang, P. Zhang, B. Xu, *Adv. Energy Mater.* 9 (32) (2019) 1901351.
- [27] X. Dou, I. Hasa, D. Saurel, C. Vaalma, L. Wu, D. Buchholz, D. Bresser, S. Komaba, S. Passerini, *Mater. Today* 23 (2019) 87–104.
- [28] Y. Li, Y. Yuan, Y. Bai, Y. Liu, Z. Wang, L. Li, F. Wu, K. Amine, C. Wu, J. Lu, *Adv. Energy Mater.* 8 (18) (2018) 1702781.
- [29] H. Lu, F. Ai, Y. Jia, C. Tang, X. Zhang, Y. Huang, H. Yang, Y. Cao, *Small* 14 (39) (2018) 1802694.
- [30] D.A. Stevens, J.R. Dahn, *J. Electrochem. Soc.* 147 (4) (2000) 1271–1273.
- [31] B. Zhang, C.M. Ghimbeu, C. Laberty, C. Vix-Guterl, J.-M. Tarascon, *Adv. Energy Mater.* 6 (1) (2016) 1501588.
- [32] H.D. Asfaw, C.W. Tai, M. Valvo, R. Younesi, *Materials Today Energy* 18 (2020) 100505.
- [33] Y. Li, Y.S. Hu, M.M. Titirici, L. Chen, X. Huang, *Adv. Energy Mater.* 6 (18) (2016) 1600659.
- [34] X. Wu, C.W.K. Lam, N. Wu, S.-S. Pang, Z. Xing, W. Zhang, Z. Ju, *Materials Today Energy* 11 (2019) 182–191 (2019).
- [35] R. Muruganantham, T.-H. Hsieh, C.-H. Lin, W.-R. Liu, *Materials Today Energy* 14 (2019) 100346.
- [36] C. Yang, J. Xiong, X. Ou, C.-F. Wu, X. Xiong, J.-H. Wang, K. Huang, M. Liu, *Materials Today Energy* 8 (2018) 37–44.
- [37] Z. Hong, Y. Zhen, Y. Ruan, M. Kang, K. Zhou, J.M. Zhang, Z. Huang, M. Wei, *Adv. Mater.* 30 (29) (2018) 1802035.
- [38] Kuan-Wei Tseng, Sheng-Bor Huang, Wei-Chung Chang, Hsing-Yu Tuan, *Chem. Mater.* 30 (13) (2018) 4440.
- [39] W. Chen, M. Wan, Q. Liu, X. Xiong, F. Yu, Y. Huang, *Small Methods* 3 (4) (2018) 1800323.
- [40] Q. Zhang, X. Deng, M. Ji, Y. Li, Z. Shi, *Ionics* 26 (2020) 4523–4532.
- [41] M.H. Han, E. Gonzalo, G. Singh, T. Rojo, *Energy Environ. Sci.* 8 (1) (2014) 81.
- [42] H. Zhan, H. Ming, W. Zhang, G. Cao, Y. Yang, *ACS Appl. Mater. Inter.* 9 (28) (2017) 23766–23774.
- [43] L. Yokokura, Y. Hagiwara, J. Yamamoto, *J. Raman Spectrosc.* 51 (6) (2020) 997–1002.
- [44] Z. Li, Y. Chen, Z. Jian, H. Jiang, J. Razink, *Chem. Mater.* 30 (14) (2018) 4536–4542.
- [45] V.G. Hadjiev, M.N. Iliev, S. Arepalli, P. Nikolaev, B.S. Files, *Appl. Phys. Lett.* 78 (21) (2001) 3193–3195.
- [46] T. Zhang, J. Mao, X. Liu, M. Xuan, K. Bi, X.L. Zhang, J. Hu, J. Fan, S. Chen, G. Shao, *RSC Adv.* 7 (66) (2017) 41504.
- [47] F. Tuinstra, *J. Chem. Phys.* 53 (3) (1970) 1126–1130.
- [48] A.V. Baranov, A.N. Bekhterev, Y.S. Bobovich, V.I. Petrov, *Optic Spectrosc.* 62 (1987) 612.
- [49] M. Anji Reddy, H. Maria Joseph, A. Gross, M. Fichtner, H. Euchner, *ACS Energy Lett.* 3 (12) (2018) 2851–2857 (2018).
- [50] J.S. Weaving, A. Lim, J. Millichamp, T.P. Neville, D. Ledwoch, E. Kendrick, P.F. McMillan, P.R. Shearing, C.A. Howard, D.J.L. Brett, *ACS. Appl. Energy Matter.* 3 (8) (2020) 7474–7484.
- [51] P. Vecera, J.C. Chacón-Torres, T. Pichler, S. Reich, A. Hirsch, *Nat. Commun.* 8 (2017) 15192.
- [52] J. C. Chacón-Torres, T. Pichler, *Phys. Status Solidi* 248 (11) 2744–2747.